Understanding the Origins of Strong Multivalent Cooperativity

Isabell Grübner

Lady Margaret Hall

University of Oxford

A thesis submitted for the degree of

Doctor of Philosophy

Trinity 2019

Acknowledgements

First and foremost, I would like to thank Prof. Harry L. Anderson for his support and constant encouragement as a supervisor, regardless of positive or negative research outcomes. The dedication and time Harry invests in every single one of his group members is remarkable and deserves great appreciation. I must also take the opportunity to thank Prof. Pablo Ballester and Prof. Chris Hunter for allowing me to do experiments in their research groups.

This thesis was funded by the European Union's Horizon 2020 research and innovation programme under the Marie Skłodowska-Curie grant agreement MULTI-APP. Additional funding came from Lady Margaret Hall and the Department of Chemistry (Oxford) and computational time was generously provided by the Oxford Advanced Research Computing Facility. Without such generous contributions, none of this work would have been possible.

Special thanks go to Prof. Harry L. Anderson, Dr. Martin Peeks, Dr. James Thomas, Dr. Bart Limburg, Dr. Keith Andrews, Dr. Michel Rickhaus, Dr. Virginia Wycisk, and Mr. Connor Patrick for the dedicated proofreading of parts of this thesis. Your patience and effort (despite the occasional short notice) is greatly appreciated. Thanks are owed to everyone in G1 and G2; I am very grateful for working in such an exceptional group. The friendly atmosphere, and the immense knowledge every group member contributes, created an exceptional environment. My time in Oxford was shaped by every single one of you, both past and present members (in vaguely chronological order): Martin, Dan, Jonathan, Renee, Yaoyao, Cécile, Nun, Przemek, Takayuki, Ibo, Anjul, Andreas, Sabine, Huawei, James, Bart, Michel, Will, Michael, Steffen, Lara, Pernille, Wenjun, Lorel, Keith, Andrew, Virginia, Kenny, Boom, Joe, and Connor. Thank you for the lab chats, the (always on time) lunch breaks, and (one more time) gym sessions.

Particular thanks must go to Martin, for answering all of my questions throughout the last three and a half years no matter the time or continent, and Dan and Jonathan, for settling me into the lab, for all the advice and for the enormous encouragement over my first two years.

During my time in Oxford, my friends outside the lab were a constant source of support and encouragement. In particular: Emma Barlow, for an amazing first year in Oxford and all the times ever since that you mastered this 24 h journey; Kirstie McLoughlin, for all the patiently spent evenings calming me down and being my comfort and; Romina Salak, for the last 15 years listening to any issue no matter how small. I have no words to describe how much I appreciate your friendship.

Finally, I would like to thank my family: Ich bin unglaublich dankbar für die niemals endende Unterstützung und die Geduld, die ihr mir stets entgegengebracht habt. Thank you for your love and support.

Abstract

This thesis presents a combined experimental and computational evaluation of chelate cooperativity. The principal result from the thesis is that host-guest design cannot be limited to chemical intuition. By using a combination of theoretical approaches, we determined a procedure for a qualitative prediction of chelate cooperativity.

Chapter 1 briefly reviews the concepts of supramolecular chemistry and cooperativity, its different types and presents experimental methods used to quantify cooperativity.

In Chapter 2, host-guest are designed to probe different influences on chelate cooperativity. The synthesis of the studied host-guest library is presented.

In Chapter 3 we show whether cooperativity can be predicted based on simple molecular structures. Therefore, we determined binding constants for the selected systems and compared the chelate cooperativity strength qualitative and quantitative. Our conclusion is that even systems only exhibiting chelate cooperativity are too complex to base cooperativity prediction exclusively on molecular structure.

In Chapter 4, the cooperativity study of the presented host-guest systems is extended and contributions of entropy and enthalpy on chelate cooperativity are separated. The results have shown that the intramolecular process is driven by favourable entropy, but additional factors such as solvation lead to entropy-enthalpy compensation.

In Chapter 5, computational results on the prediction of effective molarities and cooperativity strength are presented. A benchmark compares different methods on the evaluation of supramolecular systems. The results have shown that theoretical methods allow a qualitative prediction of chelate cooperativity strength. A comparison of different solvation models revealed a procedure to reproduce experimental results.

Supplement to Statement of Authorship

In Chapter 4, the **Zn_2-P6** porphyrin nanoring was synthesised by Pernille Bols (under the supervision of Prof. H. L. Anderson).

In Chapter 5, a solvation study is presented. The experimental *EM* values were determined by Anne Jeppesen (under the supervision of Prof. H. L. Anderson and Prof. M. Pittelkow, University of Copenhagen).

Contents

List of Publications

1. R. Haver, L. Tejerina, H.-W. Jiang, M. Rickhaus, M. Jirasek, I. Gruebner, H. J. Eggimann, L. M. Herz and H. L. Anderson, 'Tuning the Circumference of Six-Porphyrin Nanorings', *J. Am. Chem. Soc.*, 2019, jacs.9b02965

2. M. Rickhaus, A. Vargas Jentzsch, L. Tejerina, I. Grübner, M. Jirasek, T. D. Claridge and H. L. Anderson, 'Single-Acetylene Linked Porphyrin Nanorings', *J. Am. Chem. Soc.*, 2017, **139**, 16502–16505

List of Abbreviations

Abbreviations

A	hydrogen bond acceptor
D	hydrogen bond donor
ADF	Amsterdam density functional
AIBN	azobisisobutyronitrile
Ar	aryl
BSSE	basis set superposition error
COSMO-RS	conductor-like screening model for real solvents
DABCO	1,4-diazabicyclo[2.2.2]octane
DFT	density functional theory
DMC	double mutant cycle
DoF	degrees of freedom
DPM	dipyrrolmethane
EBS	effective binding sites
EDTA	ethylenediaminetetraacetic acid
EM	effective molarity
FM	flexible molecule
GGA	generalized-gradient approximation
GPC	gel permeation chromatography
HF	Hartree-Fock
IO	independent optimisation
ITC	isothermal titration calorimetry
IUPAC	International Union of Pure and Applied Chemistry
KNF	Koshland–Nemethy–Filmer
KS-DFT	Kohn-Sham density functional theory
KSCN	potassium thiocyanate
LDA	local density approximation
LR	long range
LSDA	local spin density approximation
MAD	mean absolute deviation
MWC	Monod–Wyman–Changeux
NIR	near IR
py	pyridine
RPA	random phase approximation
RRHO	rigid rotor, harmonic oscillator
SE	statistically equivalent
SH	sterically hindered
SIE	self-interaction error
SR	short range
SSQ	sum-of-squares of deviations
SVD	singular value decomposition
TBAF	tetra-*n*-butylammonium fluoride
THS	trihexylsilyl
TM	titration mode
UV	ultraviolet

1 Introduction

Contents

1.1 Outline

This thesis explores the origins of chelate cooperativity in multivalent supramolecular systems. The introduction covers nomenclature used in this thesis, *e.g.* supramolecular chemistry, the host-guest relationship, and different types of cooperativity. A detailed discussion of chelate cooperativity is given in Chapter 2. A brief introduction is given on the determination of cooperativity including common experimental techniques and further details will be discussed in the Chapter 3 and Chapter 4. Theoretical chemistry concepts are excluded from the introduction but will be discussed in Chapter 5.

1.2 Supramolecular Chemistry

In modern days, the term 'Supramolecular Chemistry' describes the chemistry of molecular assemblies and (non-covalent) intermolecular bonds. This definition was introduced by Lehn[1] in 1978, and since then a variety of different descriptions of supramolecular chemistry have evolved, including 'chemistry beyond the molecule', 'the chemistry of the non-covalent bond', and even 'Lego chemistry'.

The foundation of supramolecular chemistry is formed by the relationship of two different type of components, the host and the guest molecule. A precise definition of host–guest relationship has been defined by Donald Cram,[2] which can be summarised as: the host molecule is classically defined as a large molecule or aggregate possessing convergent binding sites (*e.g.* Lewis basic donor atoms, hydrogen-bond donors, etc.). The counterpart is formed by the guest molecule, which possesses divergent binding sites. A binding site is defined in both, host and guest, as a region able to exhibit non-covalent interactions.

The understanding of supramolecular host-guest chemistry is based on a few key concepts, originating from the ongoing exploration of biological receptor–substrate supramolecular chemistry, including Paul Ehrlich concept of a receptor, and a generalisation of Alfred Werner's 1893 theory of coordination chemistry. A milestone is the recognition by Emil Fischer in 1894 that binding must be selective, which he phrased as the lock-and-key concept. For a binding event, a certain geometric size or shape complementarity is required between the host and the guest, forming the basis for molecular recognition. This idea has been further developed by Koshland's 'induced fit' model in 1958. Given a certain degree of flexibility in the host-guest components, the unbound molecular structure allows distortion to form a host-guest complex.[3] This formed the basis for modern days host-guest design rules and will be discussed in Chapter 2.

1.3 Cooperativity

The underlying concept for understanding molecular recognition and supramolecular self-assembly is cooperativity.[4–7] The term cooperativity is a thermodynamic concept used in chemistry and biology with several different meanings depending on the context. In a broader definition, systems that involve multiple interactions show cooperativity if the

system as a whole behaves differently than the individual interactions in isolation.[7] However, because of the broad range of subjects within which cooperativity is used as a term, an exact definition is challenging. Traditionally, the definition of cooperativity was limited to the interactions between substrate sites in allosteric enzymes.[8] Meanwhile, cooperativity evolved to be an umbrella term for a range of scientific concepts and systems (*e.g.* preorganisation, avidity, allostery and some types of assembly). A student's first encounter of the term cooperativity is generally one of the following archetypical three archetypal examples: the binding of oxygen to hemoglobin;[4] the folding of biopolymers (*e.g.* protein folding and the Levinthal's paradox, DNA or RNA double strand formation);[9] and the higher complex affinity of multidentate ligands within coordination chemistry.[10]

While all of these systems exhibit cooperativity, the fundamental thermodynamic basis varies. Putting the focus on thermodynamic effects, cooperative processes can be characterised as interactions or binding events that involve multiple steps, whereby the free energy change (ΔG) of the first step differs from the sequential ones. The change in free energy can either decrease (positive cooperativity) or increase (negative cooperativity). In he absence of cooperativity, each step(s) is equal to the next one in energy and the isolated interactions behave identically to the interlinked system.[11]

The effect of cooperativity can be separated into two sub-types, namely allosteric and chelate cooperativity.[7,12] The former phenomenon describes (traditionally) an induced shift in binding affinity based on a guest binding to one site on a host molecule and thereby affecting the properties of another binding site on the same host. The latter arises from one or multiple intramolecular interactions and is related to the chelate effect (termed multivalency in supramolecular chemistry). A detailed description of these two types of cooperativity and their thermodynamic basis can be found in the literature review by Hunter and Anderson.[7]

1.3.1 Allosteric cooperativity

Comparing chelate and allosteric cooperativity, allosteric cooperativity is better understood. Two traditional models to describe allosteric cooperativity are the Monod–Wyman–Changeux (MWC)[13] and Koshland–Nemethy–Filmer (KNF)[14] model, involving concerted and sequential subunit transitions, respectively. The models were derived to explain the steady-state sigmoidal profile of oxygen binding to hemoglobin, a well-studied example of allosteric

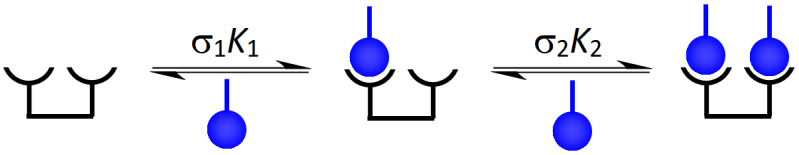

Figure 1.1: Binding of a monovalent ligand (blue) to a divalent host (black) to illustrate allosteric cooperativity.

cooperativity. Hemoglobin consists of four subunits, each equipped with a binding site. The binding of a first O_2 molecule leads to a conformational change in the protein structure and increases the binding strengths of the following oxygen molecule.[4] The MWC and the KNF model considers the binding of one ligand to result in a structurally transmitted induced change at a distant binding site. This change in the other vacant binding sites increases or decreases the binding affinity in subsequent binding steps, in comparison to a isolated binding event. However modern biochemistry moved beyond these simplified models to describe hosts as an ensemble of dynamically interchangeable conformers.

The simplest system manifesting allosteric cooperativity is a a divalent host binding two monovalent ligands (also referred to as a 1:2 complex) (Fig. 1.1). The first binding influences the binding strength of the second ligand by inducing an electronic change of the host binding site. Allosteric cooperativity can be quantified (for identical binding sites and ligands) by comparing the ratio of the two statistically corrected intrinsic binding constants (divided by the statistical factor σ_1, σ_2, respectively) to each other. In the absence of cooperativity, the binding constant of the first binding event (K_1) would be identical to the second binding affinity (K_2). If the first binding event influences the second one, a difference in binding affinity would be observed. Therefore, allosteric cooperativity can be expressed as an interaction parameter defined as the ratio of $\alpha = K_2/K_1$. This interaction parameter is usually termed as cooperativity factor α. For $\alpha > 1$, positive cooperativity is observed, while $\alpha < 1$ describes negative cooperativity.

1.3.2 Chelate cooperativity

The second type is chelate cooperativity, which describes the effect observed in protein folding or DNA duplex formation. While the assessment and quantification of allosteric cooperativity is well established, the multivalent nature of chelate cooperativity creates an additional issue. This issue manifests itself even in the most simple system able to exhibit

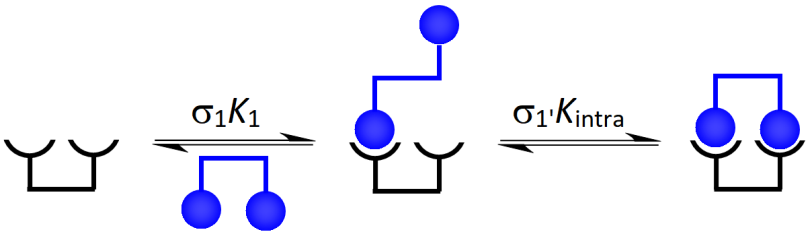

Figure 1.2: Binding of a divalent ligand (blue) to a divalent host (black) to illustrate chelate cooperativity.

chelate cooperativity: a divalent host binding a divalent guest (Fig. 1.2). This system is more complicated than the allosteric systems in Figure 1.1 because there are more possible bound states (*e.g.* the formation of oligomeric structures). For now, we will focus on the two complexes displayed in Figure 1.2, the partially-bound and fully-bound state. Again, two binding events occur but in contrast to the allosteric system, only the first step is inter- and the second step is intramolecular, leading to the fully-bound 1:1 complex. The cooperative allosteric system can be directly related to a (fictional) non-cooperative 1:2 system, in which the binding of the first ligand does not induce a conformational change on the vacant binding site. However, multivalent interactions are fundamentally different from monovalent interactions, and a non-cooperative reference is harder to define.[15]

A fictional non-cooperative reference system requires the two ligand interactions to be independent. To achieve such a non-correlated interaction, the two binding groups of the divalent ligand need to be separated and result in two monovalent ligands. However, a direct comparison of a fully bound 1:1 complex and a non-cooperative 1:2 complex involves different numbers of compounds. Therefore, a thermodynamic parameter is required to account for the difference in dimensions between the actual and the reference system. The most commonly used thermodynamic parameter for quantifying the cooperativity strength is the effective molarity (*EM*) in the unit of concentrations which determines the threshold concentration, at which a multivalent complex opens and/or forms oligomers. EM relates the intermolecular binding constant of an equivalent reference process to the intramolecular one. In a multi-step binding event, every binding interaction except the first leads to an individual *EM*.

While the importance of chelate cooperativity is well known, the understanding, quantification and especially prediction of intramolecular cooperativity is an ongoing challenge due to a large number of influences and a combination of intra- and intermolecular effects.[11] A detailed discussion of this issue can be found in Chapter 3.

1.4 Determination of Cooperativity

Due to the nature of the interactions, the determination of cooperativity is not a straightforward task. To determine cooperativity strength and its origins, a comparison between the isolated individual interactions (of a non-cooperative system) and a cooperative system is required. Therefore, the reference binding strengths of a fully isolated interaction has to be known. This isolated interaction needs to be incorporated into a (non-cooperative) model system, and its binding affinity will be tested against the (potentially) cooperative system. Any deviation between the two systems quantifies the cooperativity strength.[16]

Generally, the experimental technique should be chosen based on the thermodynamic parameter of interest, *e.g.* association constants, Gibbs energy, enthalpy, and entropy. The technique has to be chosen accordingly to the expected association constant(s) and the expected physical changes upon complexation. The association constant limits the feasible experimental concentration range. Wilcox uses the probability of binding as a criteria to determine the experimental concentration.[17] Concerning the physical observable, the time scale of the experiment needs to be compared to the time scale of the binding process. Therefore, the relationship between the association constant and the kinetic on/off rates requires investigation. In reality, the chosen technique is contexts to practical limitations, such as the amount of material required, duration and cost of conducting the experiment. The most commonly used titration methods are NMR, UV-Vis, CD and fluorescence spectroscopy, and isothermal titration calorimetry (ITC), which will be discussed briefly. Interested readers are referred to reviews by Pall Thordarson, which discuss concepts and practical advice and examples on supramolecular chemistry titrations and the determination of cooperativity.[11,18,19]

1.4.1 NMR Titration Experiments

The most popular and highly informative technique regarding structural changes within supramolecular chemistry is ^{1}H NMR titration experiments. NMR experiments enable the simultaneous analysis of multiple components. Especially important are the relative shifts and the changes in symmetry, which can deliver insights in the host-guest stoichiometry and the type of binding interaction. Modern NMR instruments enable observation of concentration ranges from higher millimolar to sub-millimolar, allowing the determination of association

constants up to 10^6 M^{-1}.[17] For intramolecular systems exhibiting chelate cooperativity, issues can arise since the kinetic processes behind these interactions can fall in the slow exchange regime. Such processes result increasing complexity of the spectrum.[11,18,19]

1.4.2 UV-vis-NIR Titration Experiments

UV-vis-NIR titration experiments are the second most commonly used methods. Compared to NMR, UV-vis-NIR measurements are less rich in structural information, however these experiments allow for thermodynamic analysis of complex equilibria involving multiple species.[20] UV-vis-NIR require the presence of a suitable chromophore (typically the host molecule), which displays a significant change in the absorption spectra upon binding. High absorptive chromophores (for example porphyrins) allow experimental settings within the sub-micromolar range enabling the determination of association constants up to 10^8 M^{-1}. The advantage of these very dilute experimental conditions is the suppression of aggregation in either host or guest. Additionally, these low concentrations allow the assumption of ideal conditions resulting in activity coefficients equal to 1, which results in a more realistic description using simple binding models. The accessible experimental concentration of the chromophore is limited by the Lambert-Beer Law ($A = d \times \epsilon \times c$, with ϵ as extinction coefficient, d the length of the corvette and c the chromophore concentration), and requires a sample absorption between 0.1 and 0.9 OD. If the host is used as chromophore, the guest should not possess absorption within the same range (which is luckily the case for most host-guest systems due to the difference in size between host and guest).

The biggest source of error for UV-vis-NIR is the vulnerability towards dilution, evaporation, and temperature effects. While all methods are affected by these effects, the impact is most significant for UV-vis and especially for highly dilute samples, which require precise weighing out of the sample.[11,18]

1.4.3 Fluorescence spectroscopy

The third most of popular method to determine cooperativity is fluorescence spectroscopy. With the potentially highest sensitivity, fluorescence measurements requires very low concentration ranges between sub-micromolar and nanomolar, and allows the determination of very high binding constants (above 10^6 M^{-1}). The ideal concentration range is determined by the absorbance at the excitation wavelength (which should be less than 0.05). Higher

concentrations result in a deviation from linearity between the absorbed light and the fluorescence response. This technique is particularly useful when either the free host or guest is fluorescently inactive, resulting in a total fluorescence that it either turned off or on upon binding.[11,18]

1.4.4 Isothermal titration calorimetry

Isothermal titration calorimetry (ITC) experiments exceed any other technique in terms of information density as it delivers information about the association stoichiometry n, the formation constant K_f, the Gibbs free formation energy ΔG, the formation enthalpy ΔH, and the formation entropy ΔS of the system in a single experiment.[21] As a calorimetric technique, ITC measures the heat change occurring during the complex formation directly and non-invasively. Due to the simplicity of the binding experiment, ITC is increasingly used in the determination of stoichiometry for multiple binding events, such as the formation of multiprotein complexes[22] or the binding of multivalent ligands.[23,24] However, ITC experiments are structure insensitive, meaning that additional experiments are required to complement the binding process on a molecular level. Despite the number of advantages, this method is rarely used in supramolecular chemistry and will be discussed in detail in Chapter 4.

2

Origins of Chelate Cooperativity

Contents

2.1 Abstract

This chapter focuses on the design and synthesis of a host-guest library to study chelate cooperativity. Based on the presented literature review on non-covalent host-guest systems exhibiting chelate cooperativity, two potential systems are found: a hydrogen-bonded tetramer

with nucleic acid base-pairs and a porphyrin nanoring (***c*-P6•T6**) binding a hexadentate guest. Due to its well-known behaviour and the high variability, the ***c*-P6•T6** system was chosen.

Based on this nanoring, three different guest series were designed. The guests were optimised to fit to the ***c*-P6** binding pocket via DFT geometry optimisations. The synthesis of the hosts followed published procedures, and the synthesis of the guests was optimised and is presented in this chapter.

2.2 Introduction

Chelate cooperativity describes the energetic difference between intramolecular interactions and the corresponding sum of intermolecular interactions. Explicitly, the formation of multiple (intramolecular) interactions between two molecules leads to an increase in binding affinity compared with multiple monovalent interactions.[7] The term 'chelate' originates from the chelate effect, first used by Morgan and Drew in 1920 in the field of coordination chemistry, specifically the observation that metal centres are often coordinated with higher affinity by di- or multivalent ligands with covalently connected electron-donating groups.[25] Investigating the binding event in a stepwise process, after formation of the first contact, point all further interactions are effectively intramolecular. Chelate cooperativity is closely related to multivalency, describing the simultaneous interactions of multiple binding sites. Many factors are responsible in the enhanced stability provided by multivalent chelating ligands, including (system-dependent) both thermodynamic and kinetic effects. From the thermodynamics side, an early explanation was the reduced cost of entropy combining two vs. multiple components. As a result, intramolecular interactions are not simply additive. The classic multivalent ligand is ethylenediaminetetraacetic acid (EDTA) with its four carboxylates and two amino groups participating in binding. Chemists have investigated this hexavalent system for over half a century and recent studies of Toone *et al.*[26] showed an enthalpic origin of the binding enhancement.

Chelate cooperativity is quantified by effective molarities (EM).[7] The EM reflects the difference in binding efficiency for formation of a single-site complex and a chelate complex, and determines the threshold concentration above which a multivalent complex begins to open and/or form oligomers. The mathematical definition of EM is the ratio between the intramolecular and the intermolecular binding constant:

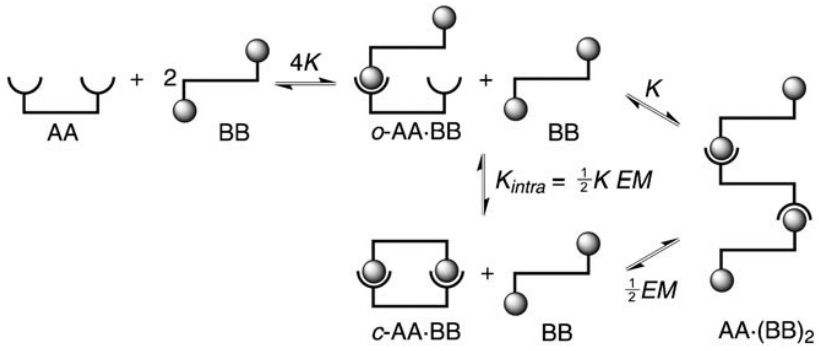

Figure 2.1: Binding of a divalent ligand BB to a divalent receptor AA, assuming the absence of allosteric effects and $[BB_0] \gg [BB_0]$. Reprinted with permission from Reference [16].

$$EM = \frac{K_{\text{intra}}}{K_{\text{inter}}} \tag{2.1}$$

To understand chelate cooperativity, we examine the most simple model system able to exhibit chelate cooperativity: a divalent guest (BB) binding to a divalent host (AA) (Fig 2.1).[16] A key assumption in our model system is that an excess of the guest molecule is present (*e.g.* one guest will not bind to two hosts) and no allosteric effects are introduced by any type of binding.

In this scenario, the host can exist in four different states: fully unbound AA, a partially bound complex *o*-AA•BB, the fully bound cyclic intramolecular complex *c*-AA•BB and the fully bound 1:2 complex AA•$(BB)_2$. If K is the binding constant for a single intermolecular binding interaction of a monovalent host and a monovalent guest, the apparent formation constant for the *o*-AA•BB complex is four times K due to the different possible combinations of binding sites. From *o*-AA•BB onwards, there are two different options for the next binding interaction; either a second guest molecule binds and forms AA•$(BB)_2$ (with binding constant K) or an intramolecular process can occur, forming *c*-AA•BB. The likelihood with which this process occurs is determined by the EM value for this specific system.

The concept of effective molarities originates from covalent bond formation in intramolecular processes (*e.g.* ring closure reactions, intramolecular S_N2) and has been subject of various reviews.[27–30] Thereby, kinetic effective molarities were used to quantify the rate acceleration of an intramolecular bond formation *vs.* an intermolecular one. A collection of these EM values for covalent bond formation by Kirby showed a broad distribution, from weak ($\overline{EM} = 10^{-2}$ M) to extremely strong ($\overline{EM} = 10^{13}$ M) (Fig. 2.2).[31,32] Assuming that translational and rotational motion is the major source of the entropic advantage

for an intra- vs. an intermolecular system, Page and Jencks estimated the theoretical EM maximum value under standard state conditions for gas phase reactions as $\overline{EM} = 10^8$ M (or 40–50 cal mol^{-1}).[33] However, as the collection of Kirby's EM values demonstrates, this approximation is not sufficient for EM values determined for reactions in solution.

By extending the concept of effective molarities to non-covalent systems, chelate cooperativity strength could be determined in supramolecular self-assembly and biological systems. However, EM values for non-covalent systems are narrowly distributed, ranging from from 10^{-5} to 10^3 M and have an average around 100 mM.[30] The largest values of EM found for supramolecular systems are in the most rigid highly preorganised assemblies and it is therefore assumed that multivalent supramolecular systems could attain similarly large values.[32]

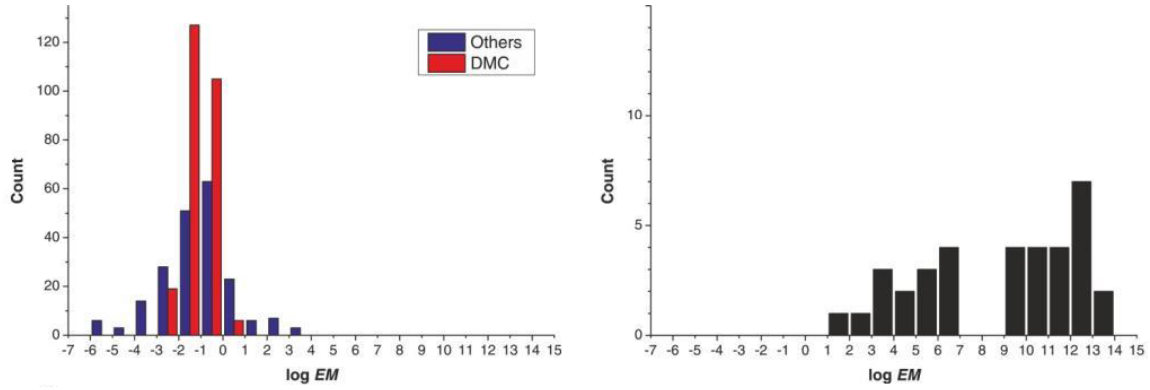

Figure 2.2: Distribution of thermodynamic EM values for non-covalent bond (left determined via DMC or another method) and for covalent bond formation (right). Reprinted with permission from Reference [30].

Understanding the reasons for the differences between these two distributions would be significant progress in not only understanding the thermodynamics behind cooperativity but moreover a breakthrough in the design and synthesis of supramolecular systems.

2.2.1 Chelate Cooperativity in Non-Covalent Systems

Cooperativity is a key concept regulating processes in molecular recognition, supramolecular self-assembly and regulates biological processes. Even though this phenomenon is essential in biology, the cooperativity strength is usually orders of magnitude weaker compared to covalent interactions. A variety of different non-covalent systems exist in literature, and Hunter and co-workers classified approximately 500 reliably determined EM values in dependency of their determination method, whereby the vast majority was determined by double mutant cycles (DMC).

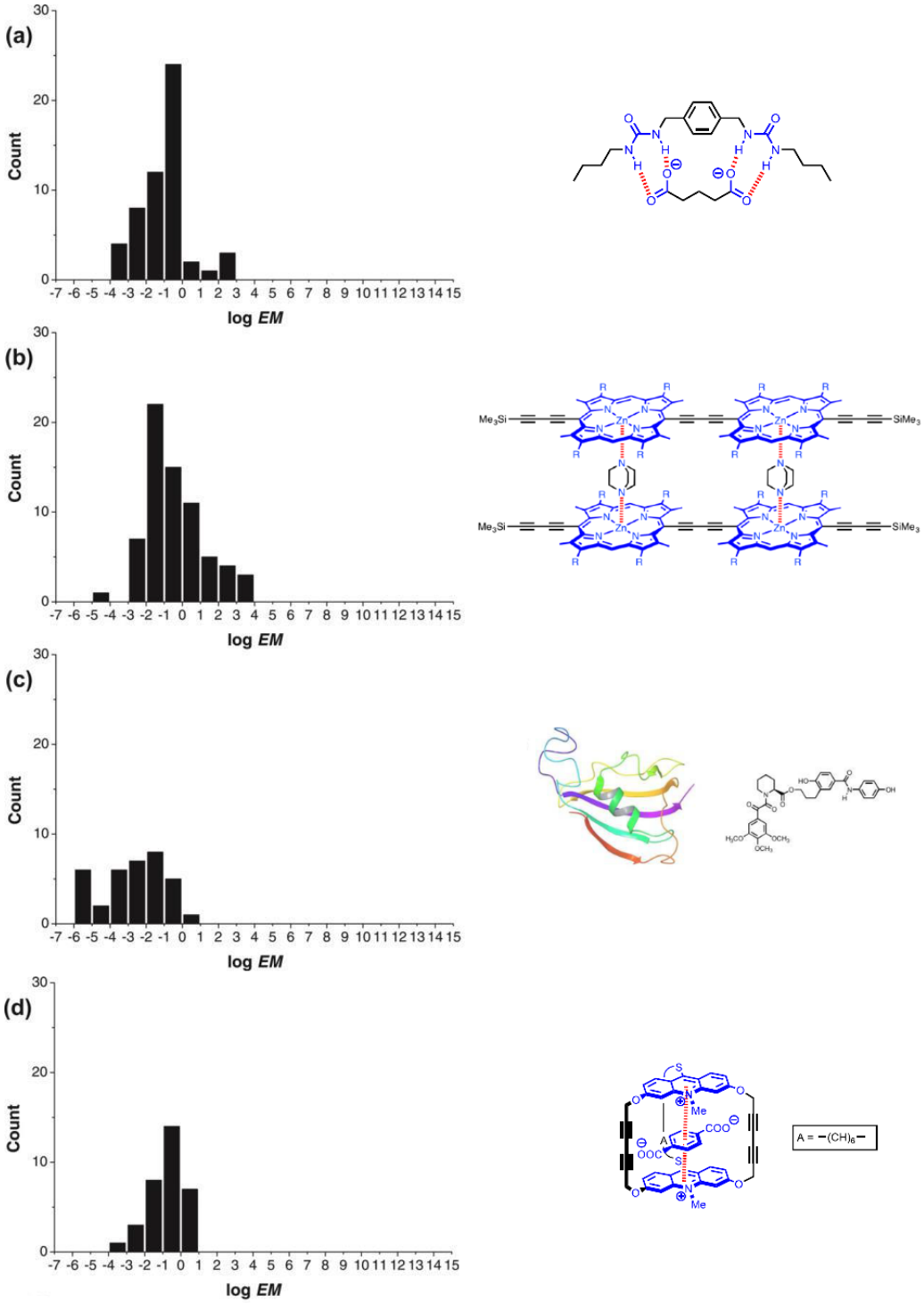

Figure 2.3: Distribution of EM values for different types of supramolecular complexes: (a) H-bonding (Hamilton's bis-urea receptors for dicarboxylates[34]), (b) metal coordination (Anderson's double stranded porphyrin ladder[35]), (c) larger protein-based, biomolecular complexes (small molecules binding to the FK506 protein[36]), and (d) electrostatic effects (Lehn's bis-intercaland receptors binding aromatic anions[37]). Reprinted with permission from Reference [30].

The collected EM values were analysed based on the type of interaction: H-bonding, metal coordinated, biomolecular complexes, and electrostatic effects (Fig. 2.3). The individual distributions show that the type of interaction is a limiting factor for EM values. Complexes based on H-bonding and metal coordination (Fig. 2.3 a and b) reach higher EM values than those based on electrostatic effects (Fig. 2.3 d). It is not surprising that larger protein-based, hydrophobic biomolecular complexes only reach lower ranges of EM values (Fig. 2.3 c).

A possible reason for this observation could be a dependency of the reference intermolecular association constant (K_{ref}) and the obtained EM value. However, an analysis of this relationship gave no clear defined trend.[30] Particularly, the very high values of EM ($\log(\overline{EM}) > 1$) are distributed across a wide range of association constant values ($\log(K_{ref}) = 0 - 5$). To choose an appropriate system for this study, we will analyse the non-covalent systems exhibiting high EM values.

2.2.2 Host-Guest Systems with High EMs

To understand the thermodynamic reasons behind high chelate cooperativity strength, we need to design a host-guest library allowing us to probe specific properties. The two systems exhibiting the highest EM values across the non-covalent complexes are a hydrogen-bonded tetramer with nucleic acid base-pairs (**cGC$_4$**)[38] and the zinc-porphyrin nanoring (***c*-P6**)[39,40] which will be discussed in the following.

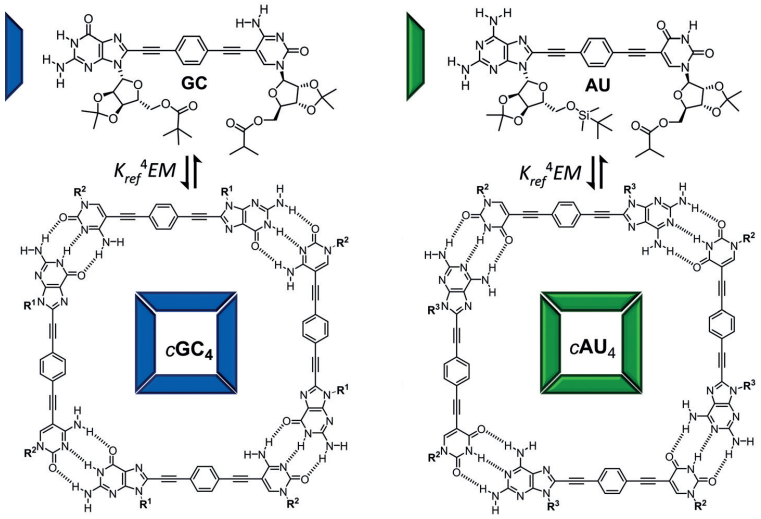

Figure 2.4: Structure of two lipophilic dinucleoside monomer units (**GC** with $K_{ref} = 2.8 \times 10^4$, and **AU** with $K_{ref} = 2.5 \times 10^2$, in chloroform respectively) and their respective formed cyclic tetramers (**cGC$_4$**, and **cAU$_4$**). Reprinted with permission from Reference [41].

The former is shown in Figure 2.4 and reaches a EM value of 910 M in chloroform. The thermodynamic and kinetic stability of the self-assembled tetramer was tested over a broad concentration range and several different solvents. González-Rodríguez and co-workers observed remarkable stability in the presence of a competitive solvent environment (33 % dimethylsulfoxide in chloroform).

Further studies on related systems have shown a dramatic effect of the symmetry of the binding interaction on the magnitude of EM. Changing the types of base pairs from guanine-cytosine **GC** to aminoadenine-uracil **AU** base-pairs, which preserve the number of intramolecular hydrogen bonds, leads to an EM value of 100 mM resulting in an decrease of cooperativity by several orders of magnitude. The monomeric units hold a rigid structure optimised to form the square-shaped assembly in absence of any strain or significant conformational entropy loss. The overall molecular symmetry of all monomeric units is C_1, and all cyclic tetramers result in C_4 symmetry. However, a significant difference between the monomeric units is the symmetric *vs.* antisymmetric pattern of hydrogen bond donor (D) and acceptor (A) within each binding site. For the **AU** monomer, the hydrogen bond pattern is *DAD-ADA*, leading to two different dimeric complexes, the Watson–Crick or reverse Watson–Crick conformers, which can be formed with comparable energy. This leads to a higher number of (linear oligomeric) binding possibilities for the **AU** monomer which are competing with the cyclic tetramer (*e.g.* oligomeric structures *vs.* the cyclic tetramer). The result is a macroscopic loss of entropy which needs to be paid by the cyclic tetramer and therefore reduces the EM value dramatically.[41]

The other system is the zinc-porphyrin nanoring (***c*-P6**) binding to the six pyridine groups of the **T6** template (Fig. 2.5). This example of metal coordination shows with an EM of 126 M (in chloroform) not only an exceptionally high chelate cooperativity but also an impressively strong binding constant ($K_f \approx 10^{36}$ M^{-1}).[39,40] This strong cooperativity is persistent over different solvents and reflects the high preorganisation, rigidity and the favourable entropy of the binding process. The **T6** template has an excellent shape-complementary to the ***c*-P6** nanoring. The comparison of the cyclic ***c*-P6** host and the ***l*-P6** linear analogue illustrates this effect; the geometric average EM for the linear host is with 0.03 M several orders of magnitude smaller.[40] To investigate this effect more carefully, the stepwise EM values for each of the 5 intramolecular interactions were determined. While the

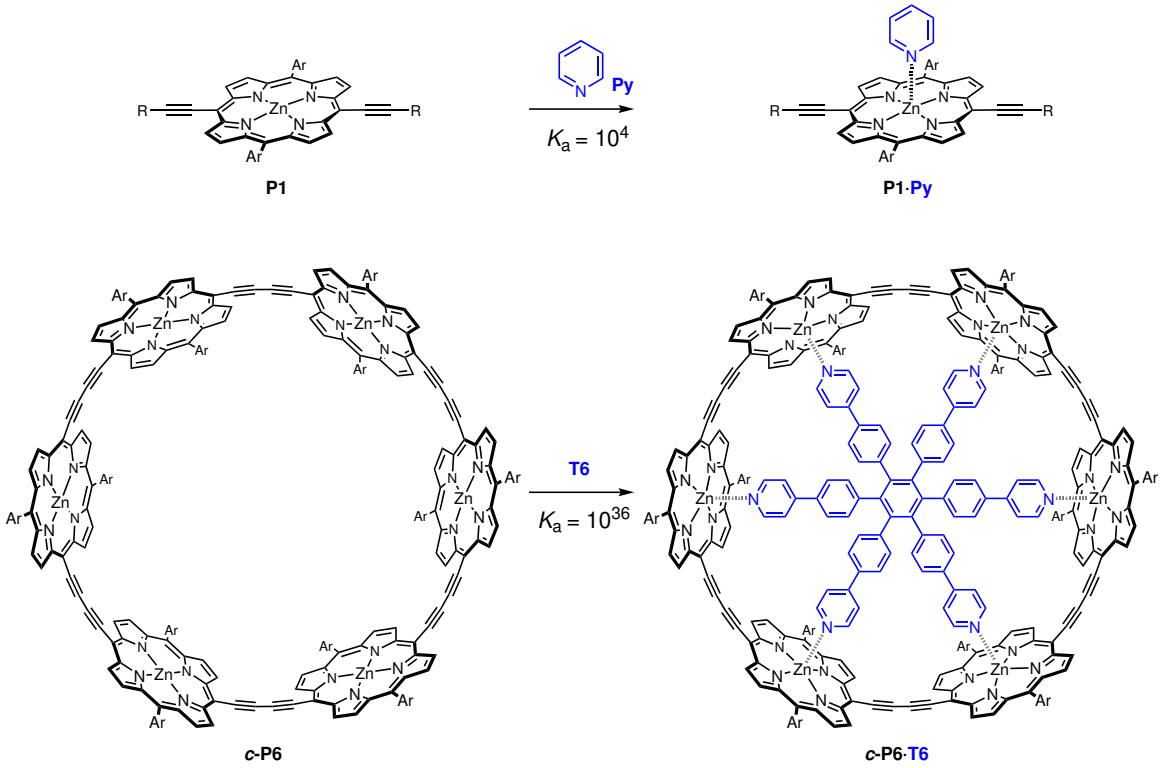

Figure 2.5: The [6]-porphyrin nanoring ***c*-P6** binding to the hexadentate template **T6**, and the the reference binding constants for a porphyrin monomer (**P1**) to pyridine.[39,40]

linear oligomers show almost the same stepwise effective molarities for all 5 intramolecular interactions, the cyclic hexamer leads to a drastic increase of the effective molarity with the third binding event. The first intramolecular bond freezes a rotational degree of freedom, as the two connection points between the guest and the host do not allow the rotation of the guest any more. This suggests that the entropic gain by any intramolecular interaction beyond 2 can be generalised with the first three binding interactions.

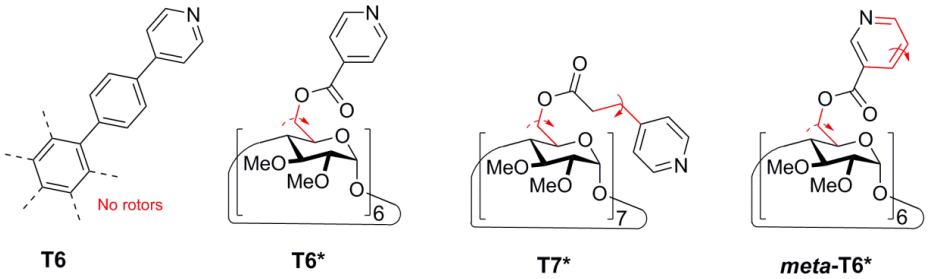

Figure 2.6: Alternative templates, varying in the number of free rotors to be frozen in the template-nanoring complex.

Recent studies addressed whether the rigidity of the template has a significant effect on the cooperativity strength. Therefore, three flexible guests were designed and their

cooperativity strength was tested (Fig. 2.6). The average EM value for ***c*-P6•T6*** is in a similar range to the rigid **T6** guest ($\overline{EM} = 74\,\mathrm{M}$). The rotational degree of freedom which is frozen by complexation is already hindered in the unbound state of the guest due to the sterically demanding ester group. Contrary to that, the more flexible guest **T7*** has two rotational degrees of freedom lost upon complex formation which are less hindered in the unbound state. The geometric average EM is with 0.7 M drastically lower. This entropic loss does not scale linearly with the number of rotations, suggesting that not only the degrees of freedom but also the reduced preorganisation is a significant factor affecting cooperativity.[42] A similarly restricted but less preorganised guest (***meta*-T6***) did not show effective binding.[42] However, the presented guest systems show several changes at once, making it harder to understand the factors in detail.

Due to the well-known behaviour of the system and the general robustness of cooperativity against modifications, the host-guest library designed in this study focussed on the ***c*-P6•T6** complex. The advantage of the systems chosen is the absence of any allosteric effects, since binding one porphyrin centre does not electronically affect the binding strength of another porphyrin centre. This is also true for the pyridine based guest molecules.[39,43,44] In contrast to the **cGC$_4$** tetramer, the host-guest ***c*-P6•T6** is a 1:1 complex with a clear distinction between host and guest. Therefore, modifications of either guest or host can be used to distinguish between the geometric average effective molarity (involving all binding sites) and the stepwise EM values (the individual stepwise contributions of the multivalent system).

To address the effect of preorganisation and shape-complementary, linear porphyrin oligomers were used as flexible host and the cyclic nanoring as rigid preorganised hosts for this study. Moreover, this system allows us to study the effect of enthalpy optimisation, as the complex formation of the linear hosts introduces strain.[26]

2.2.3 Porphyrins as a Host

Porphyrins are a key element in a variety of organic compounds, including chlorophyll, heme, and the cytochrome proteins. The simplest porphyrin is the porphine **1** shown in Figure 2.7. The atomic positions of porphine can be identified by the IUPAC nomenclature, which is illustrated with compound (**1**). Alternatively, the common nomenclature can be used, whereby the methines are referred to as the *meso* positions, the pyrrole C−Hs are referred to as the β positions, and the quaternary pyrrole carbons are the α positions (compare TPP **2** in Fig. 2.7).

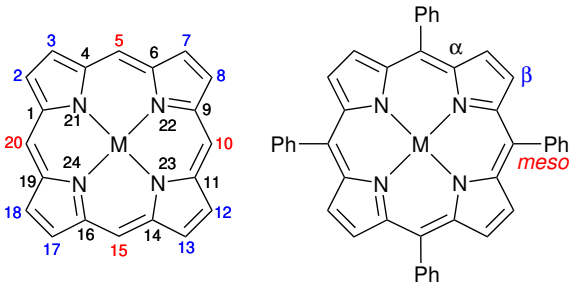

Figure 2.7: Porphine indicating **1** IUPAC atom numbering and tetraphenylporphyrin (TPP, **2**) showing the 'common names' for the atomic positions.

The four nitrogen atoms in the porphyrin unit can coordinate to a metal atom, turning the porphyrin into a square planar tetradentate chelate ligand. A variety of different central metal atoms can be inserted into the porphyrin; suitable atoms for coordination include Zn(II), Ni(II), Cu(II), Mg(II).[45,46] The central atom allows modulation of the porphyrin's properties and has been heavily used in supramolecular coordination chemistry. Depending on the central metal atom, an axial ligand can coordinate to the metal atom, creating a pentacoordinated complex. This coordination is generally rapid and reversible. Due to its easy adaptability, porphyrins have become an interesting host-guest system in self-assembly, and molecular recognition patterns. Especially the binding between a Zn(II) porphyrin and and an amine is a commonly used combination for porphyrin assemblies and will be discussed in the following section.[47] An additional sixth coordination in Zn(II) porphyrins is rare, although it has been observed in the solid state[48] or under specific conditions as a consequence of a chelate effect.[49]

2.2.3.1 Binding Strength of the Axial Coordination

The dependence of axial thermodynamic stability of porphyrins on different central metal atoms has been intensively studied.[50–52] Replacing hydrogens in the porphyrin by alkanes, alkenes, or alkynes generally lead to no or small changes in the binding constant.[52] However, a significant dependency of association constant was found to the metal atom and the solvent. The investigation of zinc, cadmium, mercury and copper metallo-porphyrin derivatives showed dependencies of the thermodynamic complex stability with basicity and steric hindrance of the ligands.[51,52] However, the observed trends are not universal across all metal atoms. Magnesium(II) and some Fe(II) porphyrin derivatives show an decrease in

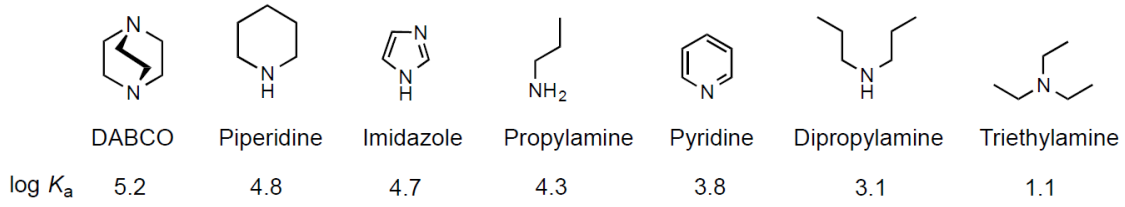

Figure 2.8: Logarithmic association constants for nitrogen-based ligands binding to Zn(II) 5,10,15,20-tetraphenyl porphyrin (ZnTPP) in toluene at 298 K.[55–57]

stability as the ligand basicity increases,[53] while zinc(II) porphyrins show a constructive correlation between basicity and binding affinity.[54]

Overall, the binding motif of nitrogen-based ligands to Zn(II) porphyrins is well studied.[45] The association constants K_a can range widely from 10 to 10^5 M^{-1}, decreasing with steric hindrance and increasing with ligand basicity. This dependency is illustrated in Figure 2.8.

Comparing the primary to the secondary and tertiary amines, a significant decrease of binding affinity is found due to the sterically demanding substituents. Especially the sterically hindered triethylamine shows a very low binding constant. The weak inductive effects, which increase the basicity on the nitrogen atom, are not strong enough to compensate the steric clash. For the cyclic amines, the difference in steric interference becomes less significant, so the binding is dominated by the increase in basicity. This is shown by the more basic imidazole which exceeds the binding constant of pyridine by a factor of 10.

Additional factors controlling the binding affinities are solvent and temperature. Generally, increasing the polarity of the solvent or the temperature decreases the binding constant. As an example, the association constants of a Zn(II) porphyrin monomer binding to pyridine were studied in dependency of the solvent at 20 °C, showing a decrease in the order of cyclohexane $>$ dichloromethane $\approx$ toluene $>$ chloroform.[58]

The binding constant has a significant effect on the supramolecular architectures that can be constructed. While higher binding constants allow greater stability for arrays which helps forming strongly coordinated assemblies, lower binding constants allow dynamic systems forming several competing species and can be used to control reaction processes and shift equilibria.[59]

2.2.3.2 Zinc-porphyrin Oligomers

As mentioned above, the Zn(II) porphyrin binding motif is extensively used in supramolecular chemistry and assembly. This thesis focuses on butadiyne-linked zinc-porphyrin oligomers.

The first documented preparation was attempted by Arnold in 1978.[60] Since then, extensive studies were carried out on these systems.[35,61–64] While Arnold's group focused mainly on the physical properties of shorter oligomers (*e.g.* porphyrin dimers),[65] the Anderson group utilised longer porphyrin oligomers to build supramolecular structures, including porphyrin ladders,[20] the previously mentioned nanoring-template complex ***c*-P6•T6**,[40] and an axially elongated nanoring tube ***t*-P12** (Figure 2.9).[66] The synthesis, characterisation and molecular properties of these systems have been subject to several studies and were reviewed in related publications and theses.[59,67–71]

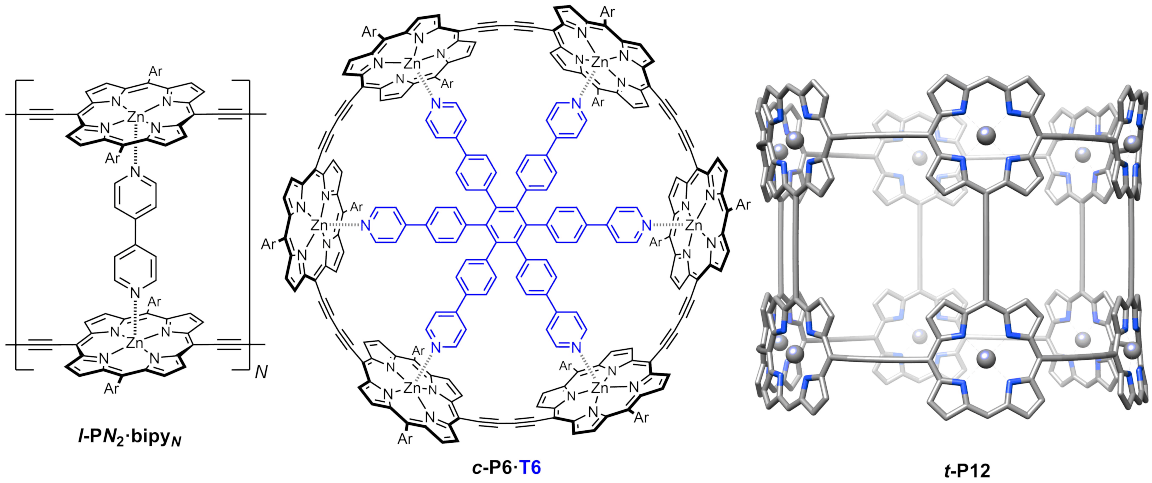

Figure 2.9: An example of porphyrin based supramolecular architectures, showing a double-stranded porphyrin ladder,[20] ***c*-P6•T6**,[40] and ***t*-P12**.[66,70] Reprinted with permission from Reference [70].

Among all the properties butadiyne-linked porphyrin oligomers possess, two distinct ones are important for this thesis: the high absorption coefficients and the low torsional barrier. The former often motivate comparisons to the light harvesting complexes in green plants,[72,73] but it also provides an important tool to analyse host-guest systems. Due to the high absorptivity, UV-vis-NIR titrations are enabled at very low concentrations (µM range) avoiding a variety of unwanted macroscopic effects (*e.g.* aggregation, insolubility and other non-ideal behaviour). The torsional rotation in a butadiyne-linked porphyrin dimer between the two porphyrins is about 2 kJ mol^{-1}.[74,75] Therefore, the system can easily adopt a coplanar conformation without steric hindrance.[70]

2.2.4 Choice of the Host

From the variety of existing porphyrin oligomers, we are most interested in the following four: ***l*-P1**, ***l*-P2**, ***l*-P3**, and ***c*-P6** (Fig. 2.10). As explained in subsection 2.2.2, ***c*-P6**

represents an ideal host to study chelate cooperativity. The high absorption coefficient allows UV-vis-NIR titrations at very dilute concentrations. The flexible, linear oligomers ***l*-P2** and ***l*-P3** enable the comparison to a shape-complementary, preorganised host (***c*-P6**). Moreover, the observed change in cooperativity strength depending on the number of

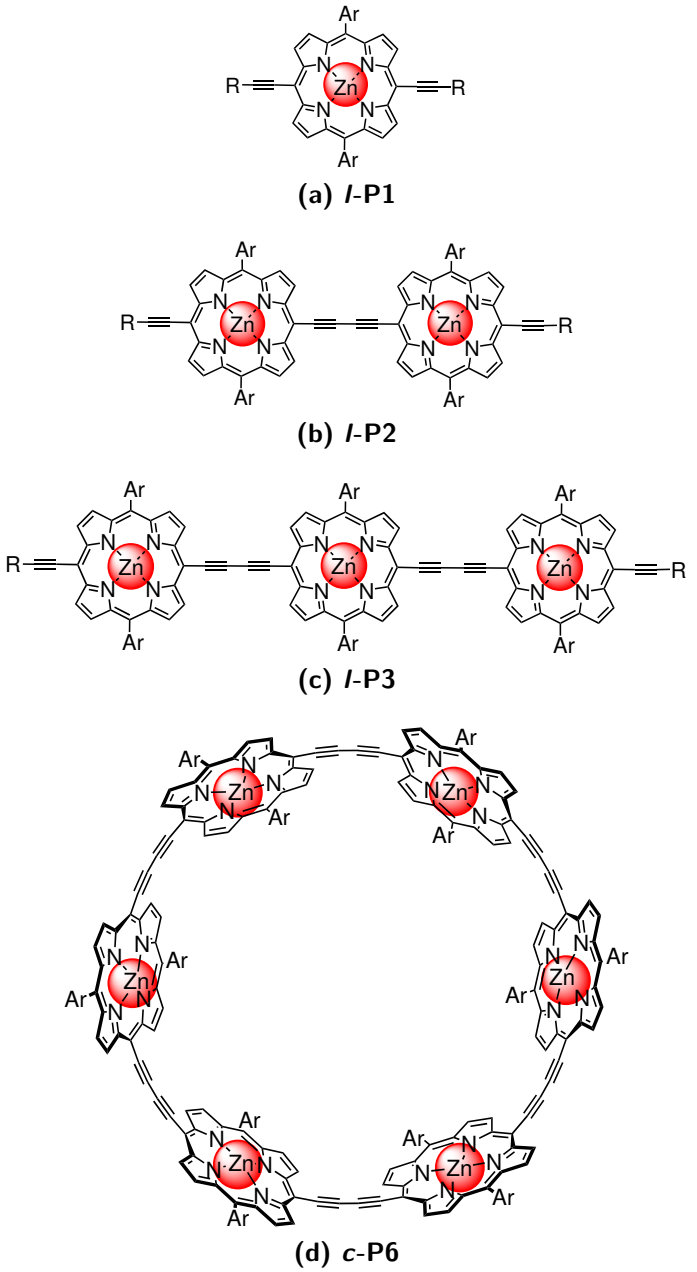

Figure 2.10: Host structures used in this study. Ar = (3,5-bis(trihexylsilyl))phenyl and (3,5-bis(*tert*-butyl))phenyl, R = trihexylsilyl group.

interactions can be studied with these hosts. The significant change in cooperativity was observed between the first and the second intramolecular interaction. Therefore, it is sufficient to study the porphyrin dimer and trimer.[39]

Due to the large size of these nanorings, all porphyrin oligomers require solubilising groups at the *meso* positions perpendicular to the butadiyne linkers. Various groups are reported in literature, and the two most suitable ones for this study are (3,5-bis(*tert*-butyl))phenyl (tBu)[40,74,76] and (3,5-bis(trihexylsilyl))phenyl (THS).[77] The advantage of the small tBu solubilising group is the minimal steric hindrance of solubilising group and a guest molecule. However, the biggest disadvantage is the higher potential of aggregation. While aggregation is not observed in the µM range and therefore not in UV-vis-NIR titration experiments, binding experiments requiring higher concentrations (such as ITC or NMR titrations) would potentially show a significant amount of aggregation affecting the determined binding constants. Therefore, (3,5-bis(trihexylsilyl))phenyl (THS) solubilising groups were used in Chapter 4. While these solubilising groups guarantee the absence of any aggregation, the flexible and large THS groups can both sterically interact with guest molecules but also change the solvation environment and can therefore highly influence the binding energy. Therefore, the host series was synthesised with both types of solubilising groups and studied in comparison.

2.2.5 Design Rules

In the following sections, we discuss the molecular modelling and the synthesis of guests as well as the synthesis of the hosts. The design of the guests follows general design principles to manipulate chelate cooperativity. Different factors are discussed in literature influencing chelate cooperativity. However, a strong controversy exists about the importance of each factor.

2.2.5.1 Preorganisation and Complementary

Two fundamental concepts thought to impact chelate cooperativity, and widely used in new host-guest design, are the principles of complementarity and preorganisation. While closely related, these two concepts address two distinct effects.[78] Both principles were defined by Cram and are reviewed in detail in his Nobel Lecture.[79] Cram's statement of the principle of complementary is that 'to complex, hosts must have binding sites which can simultaneously contact and attract the binding sites of the guests without generating internal strains or strong non-bonded repulsions'.[80] While complementarity is an essential component for structural recognition between molecules, it does not need to correlate directly to the complex association strength. As a thought experiment, we will compare

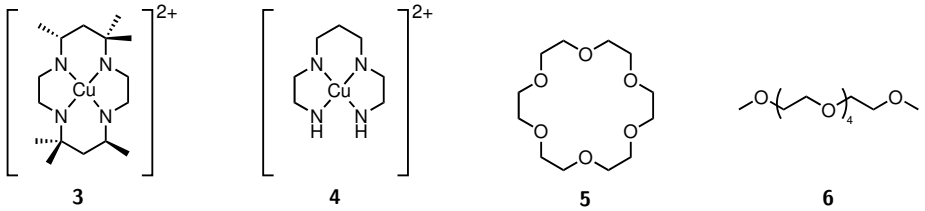

Figure 2.11: Examples to demonstrate the concepts of preorganisation and shape-complementary: amino copper(II) complexes (**3** and **4**) and oligo ethers (**5** and **6**) .[81,82]

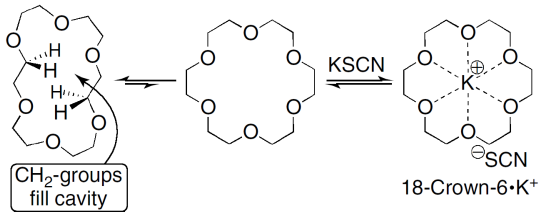

Figure 2.12: Illustration of the conformational change of 18-crown-6 required to bind potassium cations.[78,83] Reprinted with permission from Reference [78].

two hosts, each possessing one single conformation corresponding to a specific guest. In the unbound state, the hosts differ significantly, as one host is rigid and only exists in one ground-state conformation. On the contrary, the other host is very flexible and exists in numerous conformations. By restricting the flexible host to a single conformation, the formation of a host-guest complex requires more energy (entropy and enthalpy-wise) through conformational change and reduces the overall association strength in comparison to the rigid host. To differentiate between the two hosts, the concept of preorganisation is necessary. Cram defined preorganisation as 'the more highly hosts and guests are organized for binding and low solvation prior to their complexation, the more stable will be their complexes.'[80]

Several examples illustrate these effects. One of the most simple and well-known examples is the stability comparison between the two amino copper(II) complexes **3** and **4**. Both amino-based ligands are identical in the number of binding interactions and lead to the same complex geometry. However, the binding affinity of the macrocyclic ligand is 104 times higher than for the linear analogue **5**.[81] This behaviour is relatively independent of the nature of interaction, as the comparison between the 18-crown-6 ether (**5**) and the linear oligo ether (**6**) shows, whereby the binding constant of the macrocyclic system is several orders of magnitude higher than the linear one.[82]

18-crown-6 ether provides an excellent example to illustrate difference between preorganisation and complementary. In the presence of potassium thiocyanate (KSCN), 18-crown-6 undergoes a conformational change adapting its conformation to bind a potassium cation

(Fig. 2.12). The resulting complex (18-crown-6 · K^+) shows higher stabilities than any other alkali cation due to the excellent shape complementary. However, the 18-crown-6 host is required to adopt a single conformation significantly different to the unbound lowest-energy ground state conformation. This example illustrates the effect of shape-complementary in absence of preorganisation, whereby binding is enhanced by minimising energy-consuming conformational changes during complexation.[83]

2.2.5.2 Flexibility / Rigidity

A lot of new host-guest design in supramolecular chemistry is based on the principles of preorganisation and complementary. Related to the effect of preorganisation is the host flexibility. Correctly designed, conformationally non-flexible spacers can lead to very stable host-guest complexes with only a small entropic loss and minimal enthalpic strain.[84,85] Multiple examples exist in the literature, exploring the balance of flexibility *vs.* perfect shape-complementary, as the series of heterodivalent pseudorotaxanes in dependency of linker length.[86] A very prominent example is the cucurbit[n]uril (CB[n] with (n = 5, 6, 7, 8, 10)) family of macrocycles which demonstrates the strong effect of rigidity on binding.[29,87,88] This host family is built from fused five- and eight-membered rings, turning the hosts into very rigid and preorganised containers. As illustrated in Figure 2.13, the curcubit[6]uril (CB[6]) is an ideal host for binding the cationic hexanediammonium ion **7** with an impressively strong binding constant of $K_a = 4.5 \times 10^8$ M^{-1} (50 mM acetate-buffered D_2O, pH = 4.74) based on a combination of hydrophobic effects, H-bonding, and ion–dipole interactions.[88] The hexanediammonium ion **7** represents a flexible guest, that can easily adapt to the binding pocket. However, adjusting the guest to a more rigid molecule shows the downside of rigidity as a design principle. The cyclopentylmethylammonium guest **8** (cavity volume of 86 Å^2) fits satisfyingly into the binding pocket, resulting in a strong binding constant ($K_a = 3.3 \times 10^5$ M^{-1}) although somewhat weaker than the flexible one (**7**). Slight changes in the rigid guest geometry, as the example of *p*-methylanilinium ion (**9**, cavity volume of 89 Å^2) decreases the binding by a factor of 1000.[89] Overall, the cucurbit[n]uril series of molecular containers demonstrate that high selectivity is required for molecular recognition, but also the sensitivity of chelate cooperativity towards the lack of adaptability.

While these examples illustrate the potential of rigid systems, it should be highlighted that nature (very efficiently) uses more flexible building blocks. An analysis of a guest series

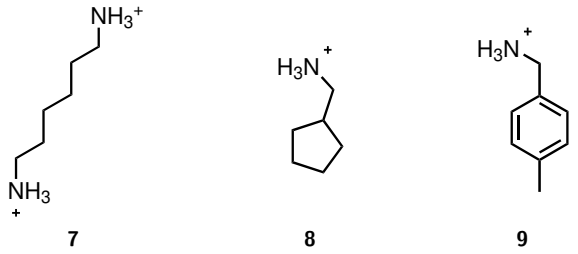

7 8 9

(a) Ammonium based guests for CB[6].

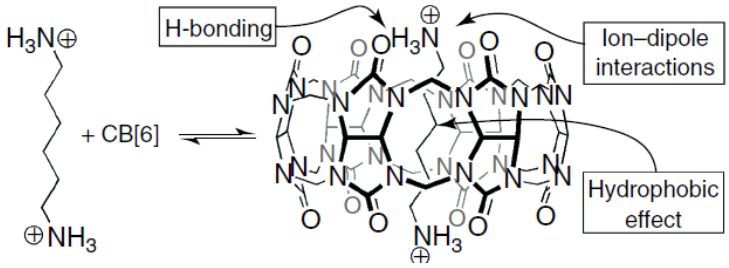

(b) Ammonium based guests for CB[6].

Figure 2.13: Illustration of the non-covalent interactions driving forces for the binding of a hexanediammonium ion to CB[6] (a) and different guests (b).[29,78,87,89] Reprinted with permission from Reference [78].

with varying spacer length and rigidity has shown that, while too long spacers reduce chelate cooperativity significantly, flexible guests show chelate cooperativity exceeding the rigid analogue due to the higher adaptability for geometric mismatch. These examples clearly indicate the delicate balance of preorganisation and adaptability for multivalent complexes.[90]

2.2.5.3 Rotational Restrictions

As the discussion of flexibility has already indicated, the downside of high adaptability in a system is the high entropic cost associated with reducing the number of accessible conformations significantly upon binding. For covalent systems, the cost of losing a rotational degree of freedom is approximately 5 to 6 kJ mol^{-1}. For non-covalent systems, the loss of conformational flexibility can be less dramatic and ranges between 0.5 to 5 kJ mol^{-1}.[91] This is reflected in the chelate cooperativity of non-covalent systems. A study on 12 different systems with varying numbers of restricted rotors upon complexation (between 5 to 20) has shown that the variation in EM is remarkably small for all 12 complexes (0.1–0.9 M). It is assumed that the loss of conformational flexibility is compensated by the increase in binding affinity, improving the preorganisation of the binding sites.[92] It should be noted that this observation is system dependent. Another study has shown that the values of EM for the flexible ligands are an order of magnitude lower than for the corresponding rigid ligands.[91]

2.2.5.4 Solvation and Single-Site Binding Strength

Another aspect of the enthalpic and entropic cost associated with host–guest complexation is the effect of desolvation. Poorly solvated, unbound hosts and guests require less energy for desolvation, due to the smaller number of interactions which need to be broken. The comparison of acyclic and macrocyclic hosts illustrates this, as macrocyclic hosts usually possess a lower surface area for solvation.[93] Studies of encapsulation processes in molecular recognition patterns have shown that in host molecules with internal cavities, binding a guest inside this cavity leads to the strongest host-guest complexes if the packing coefficient (guest volume to host volume) ranges around 55 %.[94]

However, the importance of this aspect is disputed in the literature. As studies on a variety of systematically varied H-bonding systems have shown, supramolecular EMs were found to be very weakly affected by solvent and intrinsic H-bond strength.[95] Further studies have indicated that a strong direct interaction between solvent and the host-guest system is able to affect chelate cooperativity.[96]

2.3 Aim of this Thesis

In general, the principles important in designing a host-guest system are dependent of each other. For example, designing a rigid guest leads to small entropic losses but requires the host to be shape-complementary. Equally, preorganisation is influenced by the desolvation of the unbound components and resolvation of the host-guest complex. This raises the question as to whether the design of host-guest systems can be rationalised in a straightforward way.

The aim of this thesis is to answer basic molecular design questions, which are the following:

1. Can the host-guest binding affinity and therefore chelate cooperativity be predicted just from molecular structures? This question will be discussed in Chapter 3.

2. Can the separation of entropic and enthalpic contributions in the host-guest systems reveal the foundation for chelate cooperativity? This will be addressed in Chapter 4.

3. Can we predict chelate cooperativity in supramolecular systems theoretically (Ch. 5)?

4. Can we determine additional influences and estimate the effect, such as solvation (Ch. 5)?

2.4 Molecular Design of the Guests

All guests are based on the **T6** guest presented above. The hexagon pattern of phenyl groups allows the guest to connect the individual binding sites perfectly to match the porphyrin units. Moreover, modifications can be made without significant effect on basicity or steric hindrance in binding. Since the second intramolecular binding step leads to a significant increase in cooperativity, the guests were designed to allow the stepwise analysis of the first and second intramolecular binding step. We tried to keep the changes systematic and independent of each other. We designed three different guest series, each allowing a stepwise analysis of the binding sites (Fig. 2.14): the blue series, representing a highly preorganised system that loses no internal rotational degrees of freedom; the green series, which shows no preorganisation, but allows a higher flexibility and; the red series, which is equivalent to the green series in terms of preorganisation and loss of degrees of freedom, but is very rigid.

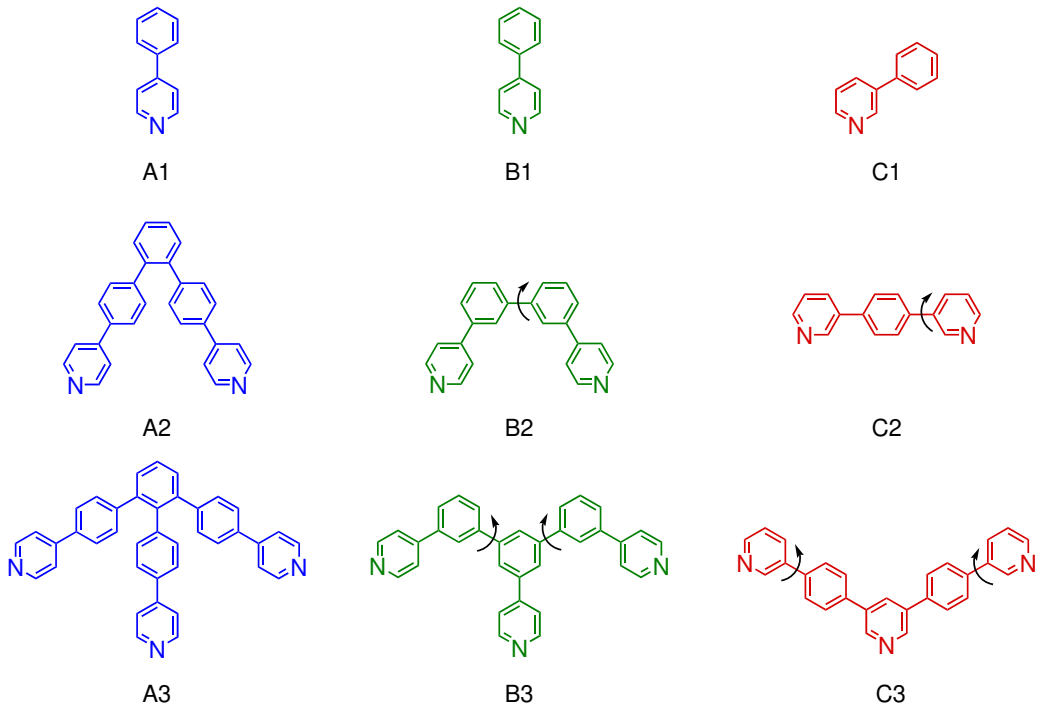

Figure 2.14: Structures of the guests used in this study.

All guests were optimized on B3LYP/6-31G* level to fit into the ***c*-P6** binding pocket (solubilising groups and acetylene protection groups were replaced by hydrogen to reduce the computational cost). The performance of B3LYP to predict binding energies and crystal structures is explored and validated in Chapter 5. The molecular structures, and the corresponding zinc–nitrogen axial bond lengths are shown in Figure 2.15. Additionally, the

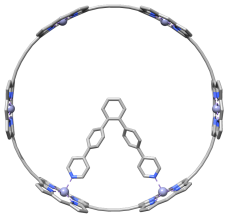

Zn–N: 2.171 Å

N–N: 10.4 Å

(a) *c*-P6•A2

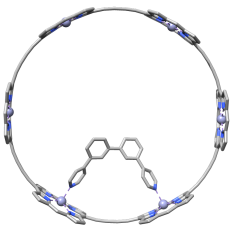

Zn–N: 2.171 Å

N–N: 10.3 Å

(b) *c*-P6•B2

Zn–N: 2.187 Å

N–N: 10.0 Å

(c) *c*-P6•C2

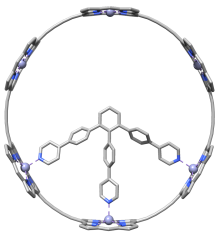

$Zn–N_1$: 2.175 Å

$Zn–N_2$: 2.177 Å

$N_1–N_2$: 10.2 Å

(d) *c*-P6•A3

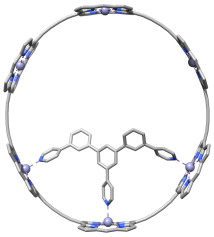

$Zn–N_1$: 2.173 Å

$Zn–N_2$: 2.177 Å

$N_1–N_2$: 10.2 Å

(e) *c*-P6•B3

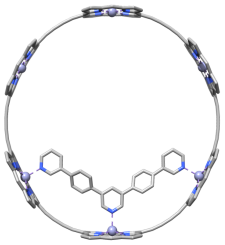

$Zn–N_1$: 2.186 Å

$Zn–N_2$: 2.180 Å

$N_1–N_2$: 10.0 Å

(f) *c*-P6•C3

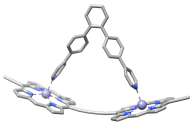

Zn–N: 2.173 Å

N–N: 11.3 Å

(g) *l*-P2•A2

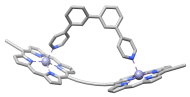

Zn–N: 2.184 Å

N–N: 10.7 Å

(h) *l*-P2•B2

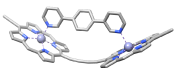

Zn–N: 2.188 Å

N–N: 10.0 Å

(i) *l*-P2•C2

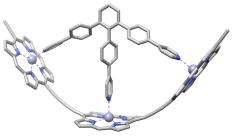

$Zn–N_1$: 2.163 Å

$Zn–N_2$: 2.173 Å

$N_1–N_2$: 10.5 Å

(j) *l*-P3•A3

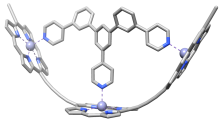

$Zn–N_1$: 2.185 Å

$Zn–N_2$: 2.183 Å

$N_1–N_2$: 10.2 Å

(k) *l*-P3•B3

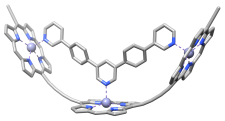

$Zn–N_1$: 2.199 Å

$Zn–N_2$: 2.187 Å

$N_1–N_2$: 10.0 Å

(l) *l*-P3•C3

Figure 2.15: Optimised molecular geometries of the host-guest complexes on B3LYP/6-31G* level. Given values describe the zinc–nitrogen axial coordination bond length (Zn–N for the divalent systems, $Zn–N_1$ for the central and $Zn–N_2$ for the outer axial coordination for the trivalent systems), the distance between the nitrogens in the guests ($N_1–N_2$ gives the distance between the central and an outer nitrogen in the trivalent systems).

distance between the nitrogens (in the trivalent systems N_1–N_2 gives the distance from the inner to outer nitrogen) in the guests are given. To evaluate the binding geometries, the respective single-site binding geometry was optimised using the guests **A1** and **C1** binding to ***I*-P1** (Fig. 2.16). Both guest series **A** and **B** share the same single-site reference (4-phenyl pyridine), while 3-phenyl pyridine was used as reference for series **C.** The nitrogen–zinc bond length is slightly elongated in the ***I*-P1•C1** complex, which results in a slightly weaker binding constant (*vide infra* Chapter 3).

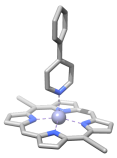

Zn–N: 2.164 Å

(a) *I*-P1•A1

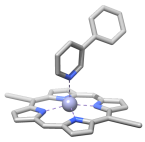

Zn–N: 2.172 Å

(b) *I*-P1•C1

Figure 2.16: Optimised molecular geometries of the host-guest single-site references on B3LYP/6-31G* level. Given values describe the zinc–nitrogen axial coordination bond length.

The optimised host-guest complexes clearly illustrate the different degrees of flexibility for each guest series. The very rigid **C** series shows in all complexes the same nitrogen–nitrogen distance (10.0 Å), requiring the host molecules instead to adjust the binding pocket accordingly. As a result, the Zn–N bond length is elongated in all host-guest complexes compared to the single-site reference. Upon complex formation, the guest **C2** loses one and the guest **C3** two rotational degrees of freedom (rotation of the pyridyl groups, see illustration in Fig. 2.14). In combination with the rigidity of the guest series, it is assumed that series **C** shows the weakest cooperativity strength of the host-guest library. Series **B** has the rigid aromatic phenyl units connected in *meta* position, increasing the flexibility of the guest to adjust its binding geometry. This is supported by the higher variation of N–N distances in the different host-guest complexes formed by series **B.** However, series **B** is identical to series **C** in the unfavourable loss of entropy upon complexation. Hence, the cooperativity strength is assumed to be slightly higher.

The strongest cooperative effect is expected for series **A.** This guest series is perfectly preorganised for the complexation, and shows the most favourable binding entropy. Moreover, guest series **A** displays the highest flexibility, as illustrated by the broad range of N–N

distances ranging from 10.2 to 11.3 Å. The large N–N distance in ***I*-P2•A2** shows the amount of strain induced by bending the acetylene linkers, which must be compensated by the binding energy. With exception of the Zn–N_1 bond length in complex ***I*-P3•A3** (Fig. 2.15j), all axial bond lengths are slightly elongated, indicating a certain degree of strain. However, a slight elongation of the Zn–N bond in comparison to the reference is observed in all host-guest complexes, which might be a consequence of the porphyrin bending. This question will be addressed in Section 4.4.1. These results are a preliminary analysis of the binding geometries and do not take into account any additional effects like solvation. While the comparison of bond length can be a helpful illustrative quantity, it is more an estimate for the binding energy and hence cooperativity than a quantitative measure. A detailed discussion of theoretical approaches addressing binding energies and cooperativity is shown in Chapter 5.

The molecular modelling has shown that all individual components of the host-guest library are expected to form stable complexes. Generally, the binding geometry seems to be reasonable to form intramolecular complexes in an 'all-or-nothing'process, without the formation of intermolecular complexes in a significant amount. As strain is induced in the bending of the linear systems, a lower binding energy is expected.[39] However, within the linear and the cyclic host-guest complexes, the amount of strain is similar between the different guests and the Zn–N bond lengths are close enough to the single-site reference to assume that any observed changes in energy are of entropic nature.

2.5 Synthesis of the Host-Guest Library

2.5.1 Guest Synthesis

Compounds **A1** or **B1**, and **C1** are commercially available. The commercial compounds **A1** or **B1** were purified by recrystallisation, yielding white crystals. The synthesis of **A2** and **A3** requires three steps, involving the formation of the boronic ester precursor **10**, as shown in Figure 2.17. The first step is a Suzuki coupling forming **11**, followed by a Miyaura borylation reaction.[97] Due to the high steric hindrance, the final ligands are formed by a Suzuki coupling using SPhos to activate the catalyst.[98] The final reaction conditions were adapted from similar known compounds.[99] The final reaction step (iii) forms **A2** in 64 % yield, while the yield for **A3** of 4 % is significantly lower. A possible explanation is a competing reductive elimination, reducing the 1-iodo-2,6-dibromo-benzene to the debrominated or

deiodated species. To minimise side-product formation, lower temperatures were chosen for the reaction conditions. Despite these attempts, significant side product formation was still observed, as exemplified in the purification process.

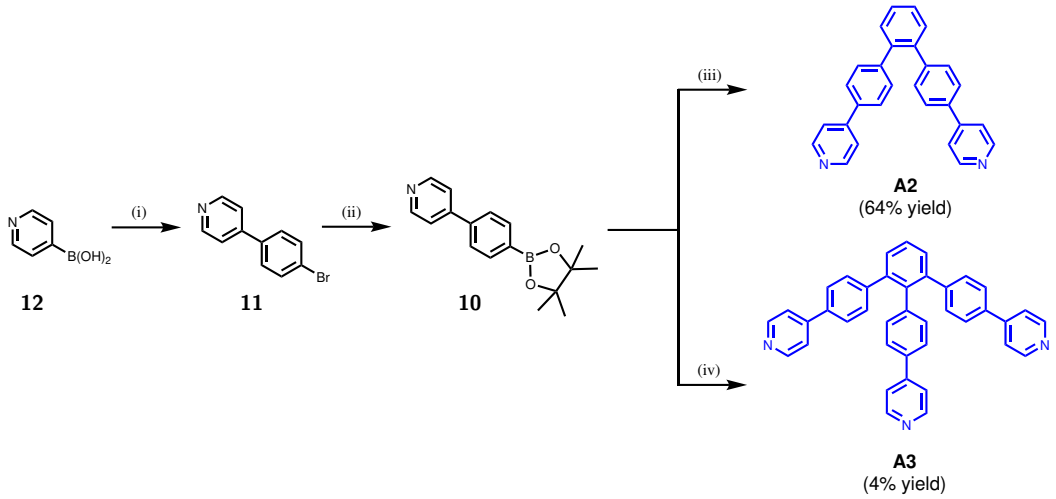

Figure 2.17: i) 1-bromo-4-iodobenzene, $Pd(PPh_3)_2Cl_2$, Na_2CO_3, H_2O, THF, EtOH, 60 °C, 24 h, 43%, ii) $B_2(pin)_2$, $Pd(dppf)Cl_2$, KOAc, DMF, 80°C, 3 h, 80%, iii) 1,2-dibromo-benzene, $Pd(OAc)_2$, Cs_2CO_3, SPhos, toluene, EtOH, H_2O, 70°C, 24 h, 64%, iv) 1-iodo-2,6-dibromo-benzene, $Pd(OAc)_2$, Cs_2CO_3, SPhos, toluene, EtOH, H_2O, 70°C, 72 h, 4%.

Based on the synthesis of **A3**, similar reaction conditions were selected for the synthesis of **C3** (Fig. 2.18). With each Suzuki coupling in *meta* position to a nitrogen, lower reaction yields were observed. The reduced yield might be caused by potential site reactions, most likely by protodeboronation, a site reaction observed in electron-poor arylboronic acids under basic conditions. Fortunately, the coupling sites in **C3** are further apart than in **A3**, leading to a sufficient reaction yield of 33 %. The formation of **C2** was performed in a single step Suzuki coupling (Fig. 2.19) and the desired product was obtained in 70 % yield.

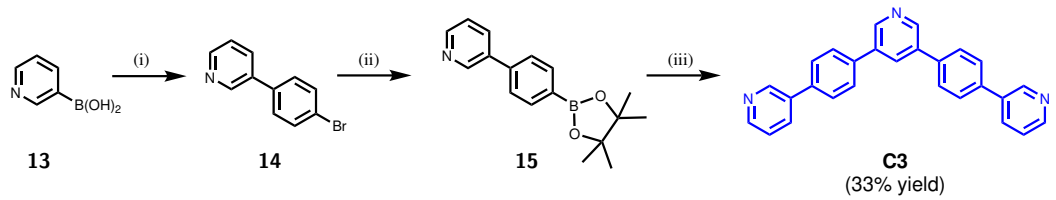

Figure 2.18: 1-bromo-4-iodobenzene, $Pd(PPh_3)_2Cl_2$, Na_2CO_3, H_2O, THF, EtOH, 60 °C, 24 h, 98%, ii) $B_2(pin)_2$, $Pd(dppf)Cl_2$, KOAc, DMF, 80°C, 3 h, 80%, iii) 3,5-dibromo-pyridine, $Pd(OAc)_2$, Cs_2CO_3, SPhos, toluene, EtOH, H_2O, 80°C, 24 h, 66%.

For the synthesis of **B2**, a two-step procedure was required (Fig. 4). The first step followed a literature procedure,[100] yielding 22 % of the desired product **16**. For the second

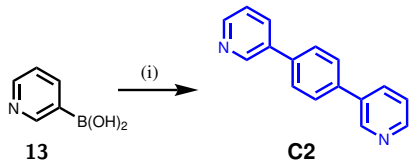

Figure 2.19: i) 1,4-diiodobenzene, $Pd(PPh_3)_2Cl_2$, Na_2CO_3, H_2O, THF, EtOH, 60 °C, 24 h, 70%.

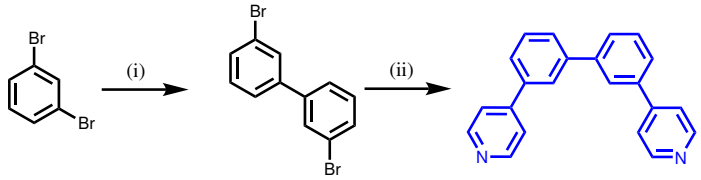

Figure 2.20: 1,3-dibromobenzene, *n*-BuLi, EtO_2, -78 °C, $CuCl_2$ 16 h, 23%, ii) **12**, $Pd(PPh_3)_2Cl_2$, Na_2CO_3, H_2O, THF, EtOH, 70 °C, 72 h, 12%.

reaction step, standard Suzuki-coupling conditions were used and after recrystallisation the product was obtained in 12 % yield.

The synthetic route to the precursor **18** of **B3** is shown in Figure 2.21. In the first step, dibromophenyl-pyridine was formed via Suzuki coupling of 1,3,5-tribromobenzene with 4-phenyl boronic acid. The reaction conditions were adapted from a literature procedure[101] and gave the desired product in a low yield of 27 % due to multi coupling as a competing side reaction. The second reaction step (ii) forms the precursor stage for **B3** with a yield of 65 %.

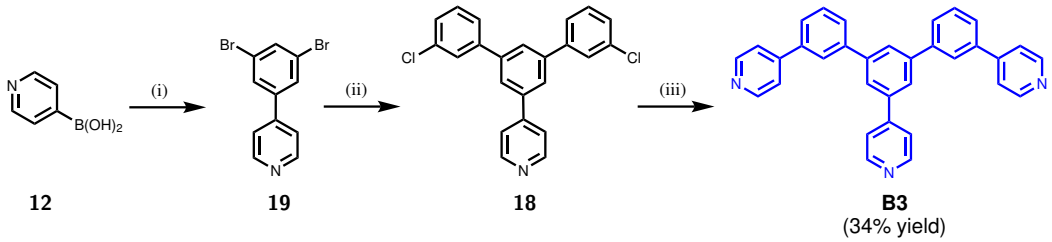

Figure 2.21: i) 1,3,5-tribromobenzene, $Pd(dppf)Cl_2$, Na_2CO_3, dioxane, H_2O, 70°C, 16 h, 27%, ii) : 3-chlorophenylboronic acid, $Pd(PPh_3)_2Cl_2$, Na_2CO_3, H_2O, THF, EtOH, 70 °C, 18 h, 65%, iii) **12**, 3,5-dibromo-pyridine, $Pd(OAc)_2$, Cs_2CO_3, SPhos, toluene, EtOH, H_2O, 80°C, 24 h, 34%.

The final reaction step of the **B3** ligand (iii) was challenging due to the lower reactivity of the chloride groups. Suzuki couplings with chloroaryl compounds require a balance of high reaction temperature and a high catalyst activity. In order to increase the reactivity, several reaction conditions were trialled.[44,102–105] An overview of the tested reaction conditions is presented in Table 2.1. Attempts to improve the reaction yield included variation of the amount and type of base, the solvent composition as well as the reaction

temperature. However, none of these led to the desired product due to side reactions (deborylation etc.) or recovery of the starting material. During the reaction, the formation of a metallic layer on the flask was observed, indicating that the catalyst undergoes a decomposition/deactivation process. Stoichiometric amounts of catalyst gave the desired product in a satisfying yield (34 %).

Table 2.1: Reaction condition screening for the **B3** ligand.

Exp. No.	Catalyst	Base	Solvent	Temperature	Yield
1[44]	$Pd(OAc)_2$, 0.2 eq.; SPhos, 0.4 eq.	Cs_2CO_3; 20 eq.	toluene, EtOH, H_2O; 5 : 1 : 1	75 °C up to 95 °C	0%
2[104,105]	$Pd(OAc)_2$, 0.2 eq.; SPhos, 0.4 eq.	K_3PO_4; 6 eq.	dioxane	100 °C	0%
3	$Pd(OAc)_2$, 0.2 eq.; SPhos, 0.4 eq.	K_3PO_4; 6 eq.	dioxane, H_2O; 5 : 1	100 °C	0%
4[103,104]	$Pd_2(dba)_3$, 0.2 eq.; SPhos, 0.5 eq.	K_3PO_4; 5 eq.	toluene	110 °C	0%
5	$Pd(OAc)_2$, 0.5 eq.; SPhos, 1.0 eq.	Cs_2CO_3; 20 eq.	toluene, EtOH, H_2O; 5 : 1 : 1	105 °C	≈10%
6	$Pd(OAc)_2$, 1 eq.; SPhos, 2.0 eq.	Cs_2CO_3; 20 eq.	toluene, EtOH, H_2O; 5 : 1 : 1	115 °C	34%

2.5.2 Host Synthesis

The synthesis of the porphyrin oligomers was based on published procedures with yields matching those reported in the literature.[40,43,74,76,77,106] For Chapter 3 and Chapter 5, all porphyrins were synthesised with (3,5-bis(*tert*-butyl))phenyl (tBu) groups[40,74,76] in the *meso* position. For Chapter 4, which involves ITC binding experiments and therefore higher concentrated samples, (3,5-bis(trihexylsilyl))phenyl (THS)[43,77,106]
solubilising groups were used. However, both types of porphyrins were synthesised via the general route explained on the example of tBu porphyrins.

The preparation of a porphyrin monomer with acetylene linkers is shown in Figure 2.22. Dipyrrolmethane (DPM) was combined with the aldehyde bearing the solubilising group. In a condensation reaction (iii), the porphyrin with protons at the *meso* positions is formed. Bromination of these positions (iv) allows for a Sonogashira coupling between trihexylsilylacetylene and the brominated porphyrin. The trihexylsilyl groups were removed in a statistical deprotection by addition of tetra-n-butylammonium fluoride (TBAF), forming the mono- and the fully deprotected porphyrin monomers. Combining partially protected and fully deprotected monomer in a coupling reaction led to the formation of a series of oligomers (Fig. 2.23), which could be separated via recycling gel permeation chromatography (GPC).

The synthesis of the ***c*-P6** host requires a template approach. Therefore, the template **T6** was synthesised following the literature publications.[74] Combining the **T6** and the fully

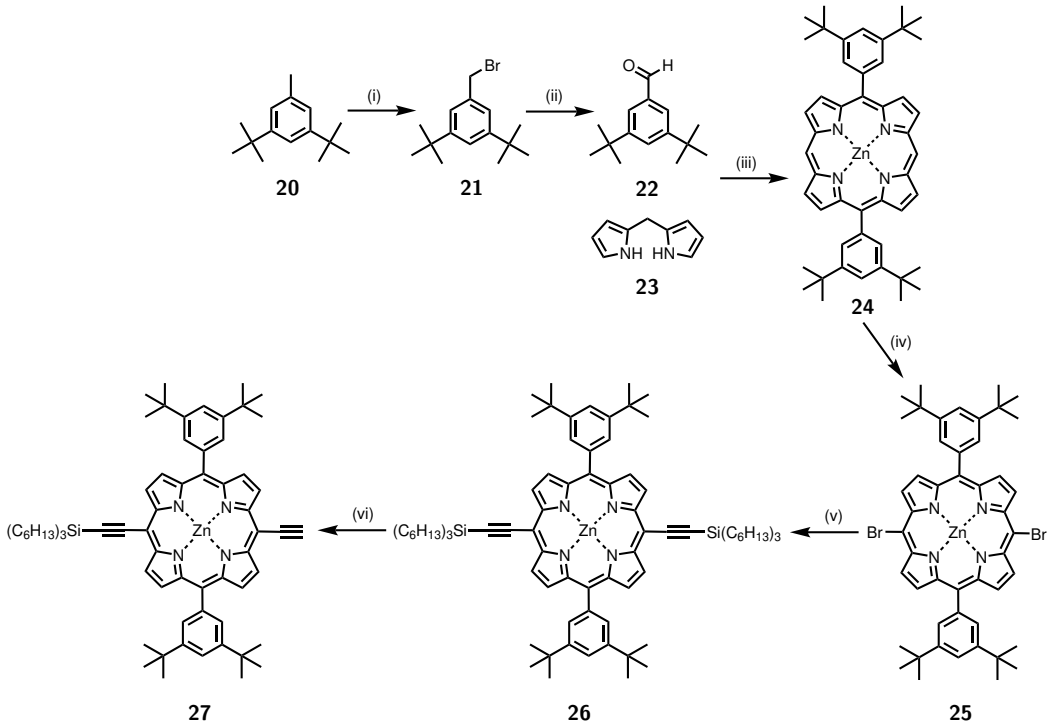

Figure 2.22: (i) NBS, AIBN, benzene, 80 °C, 4 h.; (ii) hexamethylenetetramine, HCl, EtOH/H_2O, reflux, 4 h., 44%; (iii) TFA, DDQ, CH_2Cl_2, rt, 4 h., $Zn(OAc)_2$, $CHCl_3$/MeOH, rt, 1 h., 51%; (iv) NBS, CH_2Cl_2/pyridine, -10 °C rt, 40 min., 76%; (v) $Pd_2(dba)_3$, CuI, PPh_3, trihexylsilylacetylene, toluene/DIPA, 50 °C, 3 h., 95%; (vi) TBAF, CH_2Cl_2/$CHCl_3$/pyridine, rt, 30 min., 38%.

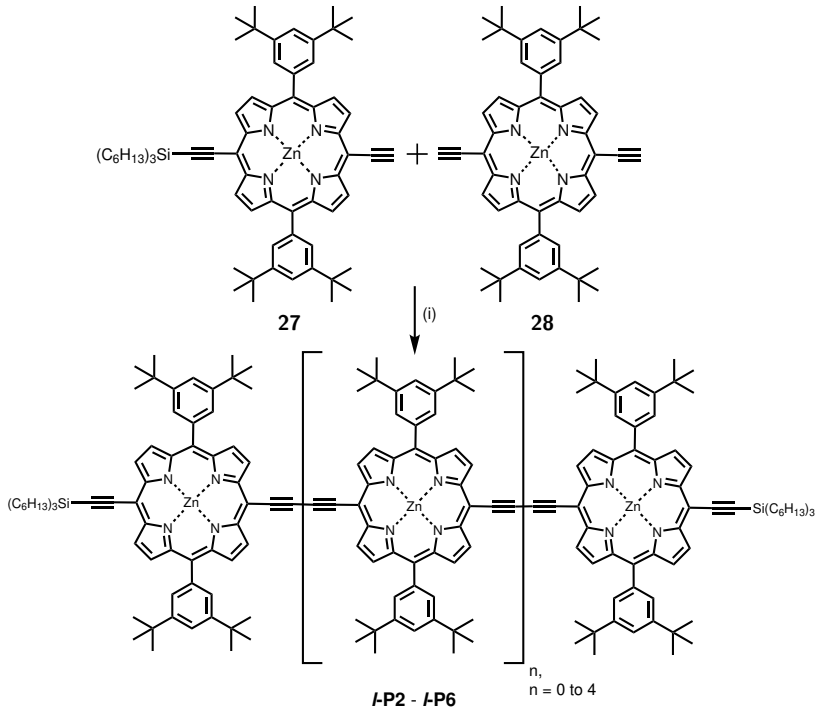

Figure 2.23: (i) $PdCl_2(PPh_3)_2$, CuI, 1,4-benzoquinone, $CHCl_3$/DIPA, rt, 1 h.

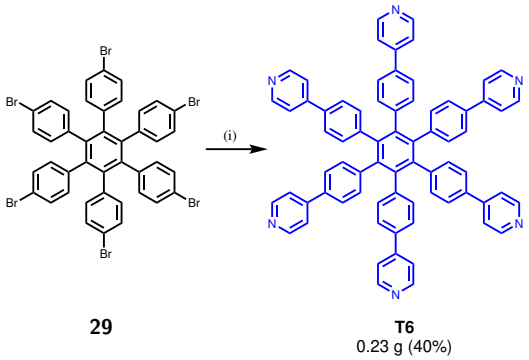

Figure 2.24: i) **12**, $Pd(PPh_3)_2Cl_2$, $NaHCO_3$, THF, DME, H_2O, 70°C, 6 days, 40%.

deprotected porphyrin dimer (***l*-P2**) forms in situ a 3:1 complex, which can be coupled via Glaser-Hay coupling (Fig. 2.25). To remove the **T6** template, ***c*-P6•T6** was demetallated by addition of acid, and remetallated with zinc, yielding the template-free ***c*-P6** host.

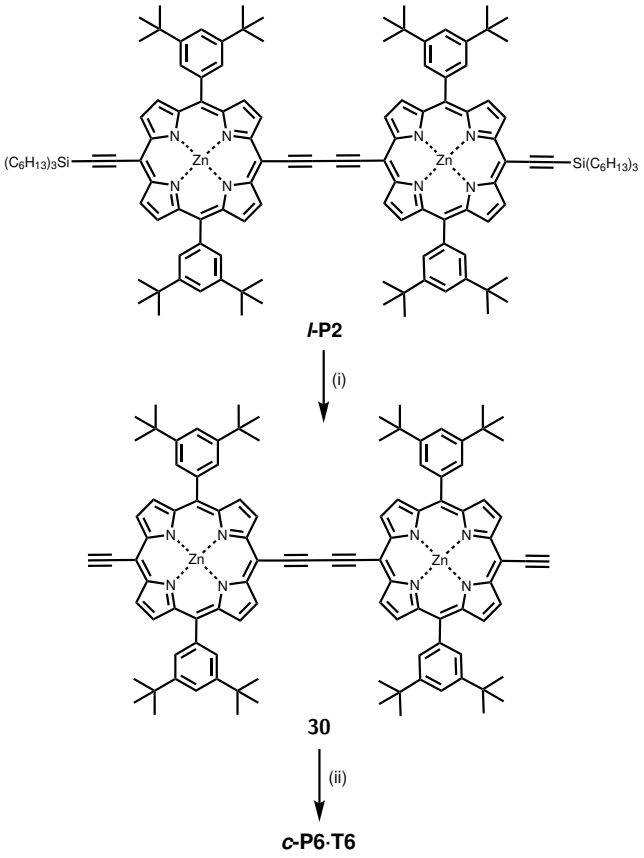

Figure 2.25: (i) TBAF, CH_2Cl_2, rt, 15 min., 76%, (ii) $PdCl_2(PPh_3)_2$, CuI, 1,4-benzoquinone, **T6**, $CHCl_3$/DIPA, rt, 16 h, 36%.

2.6 Appendix – Experimental Procedures

2.6.1 General Methods

The synthesis and characterisation of the used compounds is described in the following section. The host molecules are literature known and synthesised following literature procedures. At the minimum, intermediates and precursors (for simple reaction steps) for the host compounds were checked via proton NMR. Proton NMR gives clear indication of product formation, since each reaction step shows clear differences between starting material and product. Complicated reaction steps were checked with at least one additional characterisation method such as mass spectrometry. The final host molecules were purified via GPC. Proton resonances, mass spectra, and UV-vis were compared with literature values for all host molecules. Detailed characterisation can be obtained via the cited references.

The guest molecules include known and novel compounds. All known molecules were synthesised following literature procedures and compared with the receptive characterisation, which includes ^{1}H, and ^{13}C NMR and mass spectrometry. The final guest compounds were additionally characterised with melting points. Proton NMR spectra are shown for all host and guest compounds used further in this study.

Solvents were dried by passing the solvents through columns of activated alumina. Diisopropylamine (DIPA) was distilled from CaH_2 and kept over activated molecular sieves (3 Å, 8–12 mesh). Unless specified otherwise, all other solvents were used as commercially supplied. Flash chromatography was carried out on silica gel 60 under positive pressure. Analytical thin-layer chromatography was carried out on aluminum-backed silica gel 60 F254 plates. Unless stated otherwise, ^{1}H/^{13}C NMR spectra were recorded at 298 K using Bruker AV400 (400/100 MHz) instrument. ^{1}H, and ^{13}C NMR spectra are reported in ppm; coupling constants are given in Hertz, to the nearest 0.1 Hz based on the recorded spectrum. MALDI-TOF mass spectra were carried out using Waters MALDI Micro MX spectrometer. ESI-TOF were carried out using the Agilent single quadrupole with CTC-PAL spectrometer.

2.6.2 Synthetic Procedures for Guests

11[97]

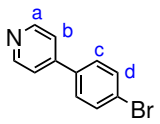

Compound **12** was dried under high vacuum overnight. In a 250 mL two necked round bottom flask, sodium carbonate (1.96 g, 18.4 mmol, 1.3 eq.) was dissolved in water (10 mL). To the suspension, 1-bromo-4-iodobenzene (4.00 g, 14 mmol, 1.0 eq.), **12** (2.44 g, 19.6 mmol, 1.4 eq.), $PdCl_2(PPh_3)_2$ (520 mg, 1.4 mmol, 0.05 eq.), THF (20 mL) and ethanol (20 mL) was added. The resulting reaction mixture was degassed via three freeze-pump-thaw cycles and stirred at 80 °C for 2 days. The product was isolated by column chromatography (hexane : EtOAc 3:1) affording a pale white solid. The solid was washed with petrol ether yielding a white solid (1.43 g, 6.02 mmol, 43% yield).

^{1}**H-NMR** ($CDCl_3$, 400 MHz) δ/ppm: 8.65 (d, J = 5.2 Hz, 2H, a), 7.55 (d, J = 8.0 Hz, 2H, b), 7.47 (d, J = 8.0 Hz, 2H, c), 7.44 (d, J = 5.2 Hz, 2H, d).

^{13}**C-NMR** ($CDCl_3$, 400 MHz) δ/ppm: 150.4, 147.1, 137.0, 132.3, 132.3, 128.5, 123.6, 121.3.

m/z (ESI-ToF) : 234.0 M^+, ($C_{11}H_9BrN$, M^+ requires 233.9).

10[97]

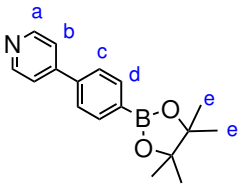

A 50 mL two necked round bottom flask was charged with **11** (200 mg, 0.92 mmol, 1.0 eq.), bis(pinacolato)diboron (264 mg, 1.04 mmol, 1.1 eq.), potassium acetate (288 mg, 2.94 mmol, 3.0 eq.) and $Pd(dppf)Cl_2$ (40 mg, 0.05 mmol, 0.05 eq.). The apparatus was dried and put under argon and dry DMF (5 mL) was added by syringe. The resulting reaction mixture was stirred at 80 °C for 3.5 h. The reaction progress was monitored by TLC. After reaction completion, DMF was removed under high vacuum. The product was isolated by column chromatography (petrol : EtOAc 3:1). Small residual bis(pinacolato)diboron impurities are removed by layer addition recrystallisation (CH_2Cl_2/petrol ether) affording a pale white powder (200 mg, 0.69 mmol, 80% yield).

^{1}**H-NMR** ($CDCl_3$, 400 MHz) δ/ppm : 8.67 (dd, J = 4.6 Hz, J = 1.5 Hz, 2H, a), 7.92 (d, J = 8.1 Hz, 2H, b), 7.64 (d, J = 8.2 Hz, 2H, c), 7.52 (d, J = 4.6 Hz, $J_{H,H}$ = 1.5 Hz, 2H, d), 1.36 (s, 12H, e).

^{13}**C-NMR** ($CDCl_3$, 400 MHz) δ/ppm: 150.4, 148.2, 140.7, 135.6, 129.2, 127.1, 126.3, 121.8, 84.3, 25.0.

m/z (ESI-ToF) : 282.6 M^+, ($C_{11}H_9BrN$, M^+ requires 281.2).

A2

In a 25 mL two necked round bottom flask, caesium carbonate (326 mg, 1.0 mmol, 10 eq.) was dissolved in water (0.5 mL). To the solution, 1,2-dibromobenzene (13 µl, 0.1 mmol, 1 eq.), **10** (112.5 mg, 0.4 mmol, 4.0 eq.), $Pd(OAc)_2$ (4.5 mg, 0.02 mmol, 0.2 eq.), toluene (2.5 mL), and ethanol (0.5 mL) was added. The reaction mixture was degassed by four freeze-pump-thaw cycles and stirred at 70 °C for 24 h. The reaction progress was monitored by TLC. After the reaction completed, the product was extracted five times with $CHCl_3$. The combined organic layer was washed with water and brine and dried over $MgSO_4$. After reducing the solution to approximately 5 mL, the product was precipitated by adding petrol ether. Recrystallisation by layer addition (CH_2Cl_2/petrol ether) afforded a white powder (25 mg, 64% yield).

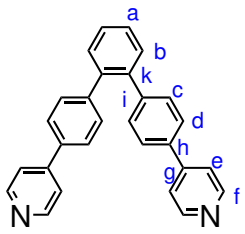

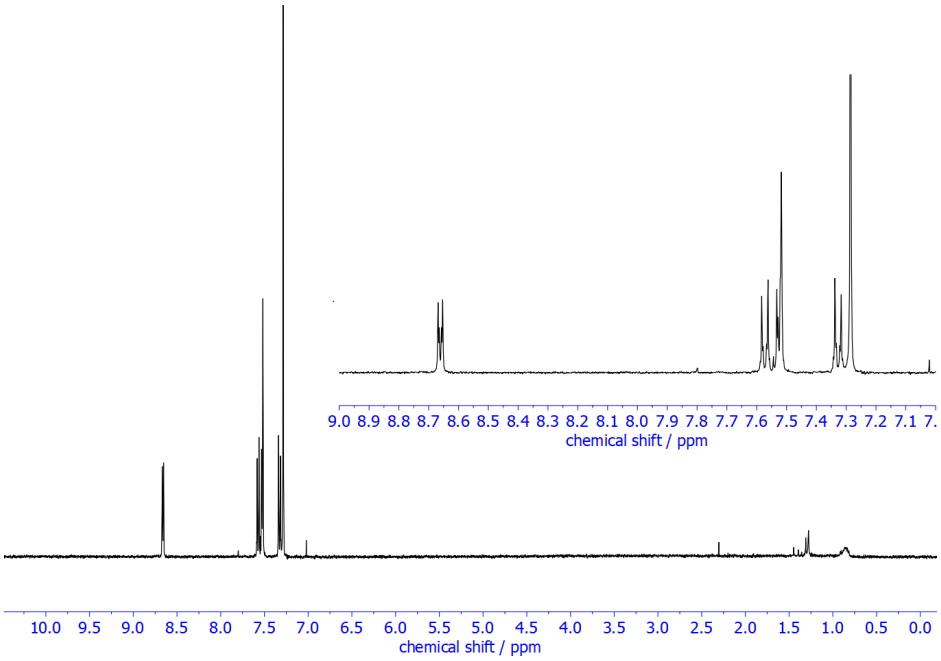

Figure 2.26: ^{1}H-NMR of **A2**.

^{1}**H-NMR** ($CDCl_3$, 400 MHz) δ/ppm : 8.66 (dd, J = 6.4 Hz, J = 1.4 Hz, 4H, f), 7.57 (d, J = 8.3 Hz, 4H, d), 7.52 (m, 8H, a,c,e), 7.33 (d, J = 8.4 Hz, 4H, b).

^{13}**C-NMR** ($CDCl_3$, 100 MHz) δ/ppm : 150.4 (f), 147.4 (g), 142.6 (i), 139.9 (k), 136.3 (h), 130.8 (b), 130.7 (c), 128.2 (a), 126.9 (d), 121.6 (e).

m/z (ESI-ToF) 385.2 M^+, 193.1 M^{2+} ($C_{17}H_{20}BNO_2$, M^+ requires 384.16).

M.P. 218-220 °C.

A3

In a 50 mL Schlenk tube, Cs_2CO_3 (326 mg, 1.0 mmol, 10 eq.) was dissolved in water (0.5 mL). To the solution, 2,6-dibromoiodobenzene (36 mg, 0.1 mmol, 1 eq.), **10** (169 mg, 0.6 mmol, 6.0 eq.), $Pd(OAc)_2$ (4.5 mg, 0.02 mmol, 0.2 eq.), SPhos (16 mg, 0.04 mmol, 0.4 eq.), toluene (2.5 mL), and ethanol (0.5 mL) was added. The reaction mixture was degassed via freeze-pump-thaw and stirred at 70 °C for 72 h. After the reaction completed, the product was extracted five times with $CHCl_3$. The combined organic layer was washed with water and brine and dried over $MgSO_4$. The product was isolated by column chromatography (DCM:MeOH:Net_3 with a gradient from 20:1:0.1 to 10:1:0.1). Recrystallisation by layer addition (CH_2Cl_2/petrol ether) afforded a white powder (14 mg, 4% yield).

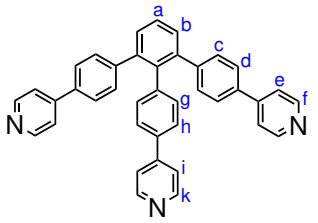

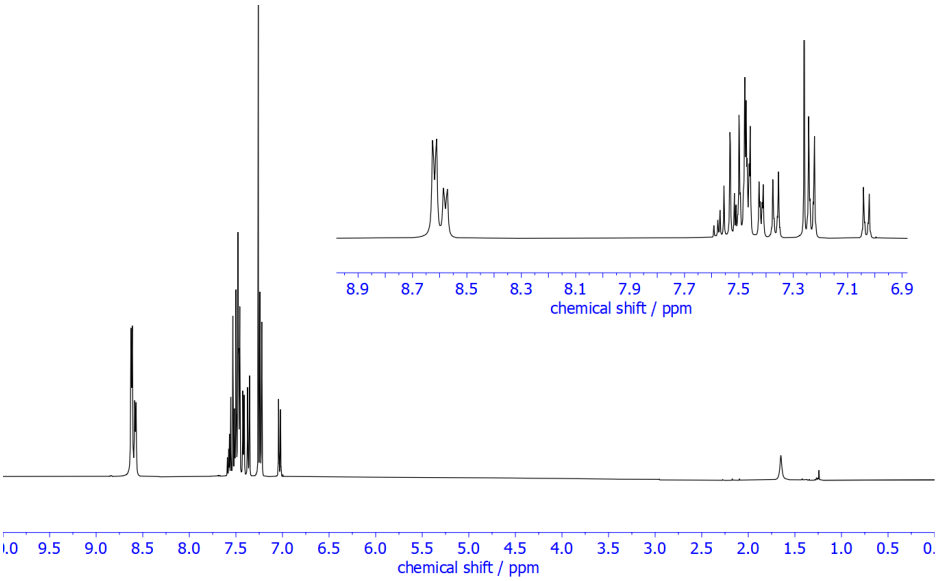

Figure 2.27: ^{1}H-NMR of **A3**.

^{1}**H-NMR** ($CDCl_3$, 400 MHz) δ/ppm : 8.62 (d; J = 5.8 Hz; 4H; f), 8.58 (d; J = 5.8 Hz; 2H; k), 7.53 (m; 3H; a,b), 7.48 (d; J = 8.4 Hz; 4H; d), 7.46 (d; J = 6.2 Hz, 4H; e), 7.41 (dd; J = 4.5, 1.6 Hz; 2H; i), 7.36 (d; J = 8.4 Hz; 2H; h), 7.23 (d; J = 8.4 Hz; 4H; c), 7.03 (d; J = 8.4 Hz; 2H; g).

^{13}**C-NMR** ($CDCl_3$, 100 MHz) δ/ppm : 150.4 (f), 150.4 (k), 132.6 (g), 130.8 (c), 130.3 (a,b), 126.5 (e), 126.5 (d), 121.4 (i), 126.2 (h).

m/z (ESI-ToF) 279.1 M^{2+} ($C_{39}H_{27}N_3$, M^+ requires 537.65).

M.P. 251-253 °C.

14[97]

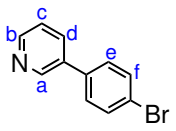

A 250 mL two necked round bottom flask was charged with 1-bromo-4-iodobenzene (5.00 g, 17.7 mmol, 1. eq.), 3-pyridinylboronic acid (3.04 g, 24.7 mmol, 1.4 eq.), $PdCl_2(PPh_3)_2$ (0.62 g, 0.88 mmol, 0.05 eq.), Na_2CO_3 (2.81 g, 26.5 mmol, 1.5 eq.), THF (50 mL), ethanol (50 mL) and H_2O (25 mL). The resulting suspension was degassed by freeze-pump-thaw (3 cycles) and then stirred at 60 °C for 24 h. The reaction mixture was extracted with EtOAc five times. The combined organic phases were washed with water and brine, dried over anhydrous $MgSO_4$ and concentrated under reduced pressure. The product was passed through a plug (petroleum ether (40-60):EtOAc 6:1) to give a yellow wax (3.38 g, 15.0 mmol, 85 % yield).

^{1}**H-NMR** ($CDCl_3$, 400 MHz) δ/ppm : 8.83 (dd; J = 8.8, 1. Hz; 1H; a), 8.55 (dd; J = 6.3, 1.6 Hz; 1H, b), 7.78 (d; J = 7.8 Hz; 1H; d), 7.55 (d; J = 8.5 Hz; 1H; f), 7.38 (d; J = 8.5 Hz; 1H; e), 7.31 (dd; J = 7.9 Hz; 1H; d).

^{13}**C-NMR** ($CDCl_3$, 100 MHz) δ/ppm : 148.9, 148.1, 136.7, 135.5, 134.1, 132.2, 128.7, 123.6, 122.5.

m/z (ESI-ToF) : 235.2 M^+, ($C_{11}H_9BrN$, M^+ requires 233.9).

15[97]

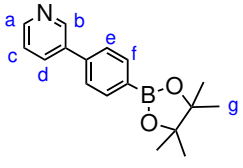

A 100 mL Schlenk tube was charged with **14** (2.0 g, 9.1 mmol, 1.0 eq.), bis(pinacolato)diboron (2.3 g, 10.7 mmol, 1.05 eq.), potassium acetate (2.7 g, 27.3 mmol, 3.0 eq.) and $Pd(dppf)Cl_2$ (0.4 mg, 0.5 mmol, 0.05 eq.). After vacuuming overnight, the apparatus was put under argon and dry DMF (30 mL) was added by syringe. The resulting reaction mixture was stirred

at 80 °C for 3.5 h. The reaction progress was monitored by TLC. After reaction completion, DMF was removed under high vacuum. The product was isolated by column chromatography (petrol : EtOAc 3:1). Small residual bis(pinacolato)diboron impurities are removed by storing the waxy substance for several days in the freezer followed by layer addition recrystallisation (CH_2Cl_2/petrol ether) affording an pale white powder (1.9 g, 64% yield).

^{1}**H-NMR** ($CDCl_3$, 400 MHz) δ/ppm : 8.87 (dd; J = 3.2, 1.0 Hz; 1H; b), 8.61 (dd; J = 4.8, 1.6 Hz; 1H, a), 7.92 (d; J = 8.3 Hz; 2H; c), 7.89 (dd; J = 2.3, 1.6 Hz; 1H; d), 7.60 (d; J = 8.2 Hz; 2H; e), 7.38 (ddd; J = 7.8, 4.8 0.6 Hz; 1H; f), 1.37 (s; 12H; g).

^{13}**C-NMR** ($CDCl_3$, 100 MHz) δ/ppm : 148.7, 148.3, 140.4, 136.5, 135.5, 134.4, 126.4, 123.5, 83.9, 24.8.

m/z (ESI-ToF) : 282.6 M^+, ($C_{17}H_{20}BNO_2$, M^+ requires 281.2).

C3[108]

In a 10 mL Schlenk flask, caesium carbonate (326 mg, 1.0 mmol, 10 eq.) was dissolved in water (0.5 mL). To the solution, 3,5-dibromo-pyridine (24.7 mg, 0.1 mmol, 1 eq.), **14** (112.5 mg, 0.4 mmol, 4.0 eq.), toluene (2.5 mL) and ethanol (0.5 mL) was added. The suspension was degassed by freeze-pump-thaw (3 cycles) stirred at 65 °C for 20 h. The reaction mixture was extracted with DCM and EtOAc and the combined organic layers were washed with water and brine, dried over $MgSO_4$ and the solvent was removed by rotor evaporator. The solid was dissolved in $CHCl_3$ and filtered via a micro filter to remove any solids. Recrystallisation by layer addition of petrol ether to a solution of $CHCl_3$ with 10% methanol afforded a white powder (20 mg, 66% yield).

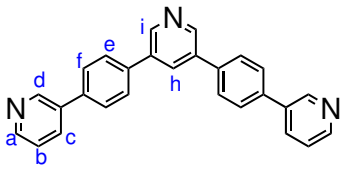

^{1}**H-NMR** ($CDCl_3$, 400 MHz) δ/ppm : 8.92 (dd; J = 8.5, 2.0 Hz; 4H; d,i), 8.64 (dd; J = 4.8, 1.4 Hz; 2H; a), 8.15 (t; J = 2.1; 1H; h), 7.96 (td; J = 7.9, 1.9 Hz; 2H; c), 7.78 (m; 8H; e,f), 7.42 (dd; J = 7.8, 4.9 Hz; 2H; b).

^{13}**C-NMR** ($CDCl_3$, 100 MHz) δ/ppm : 148.0, 147.4, 146.4, 137.4, 137.1, 136.3, 136.1, 134.8, 133.1, 127.9, 127.8, 123.9.

m/z (ESI-ToF) 386.2M^+ ($C_{27}H_{19}N_3$, M^+ requires 385.46).

M.P. 297-301 °C.

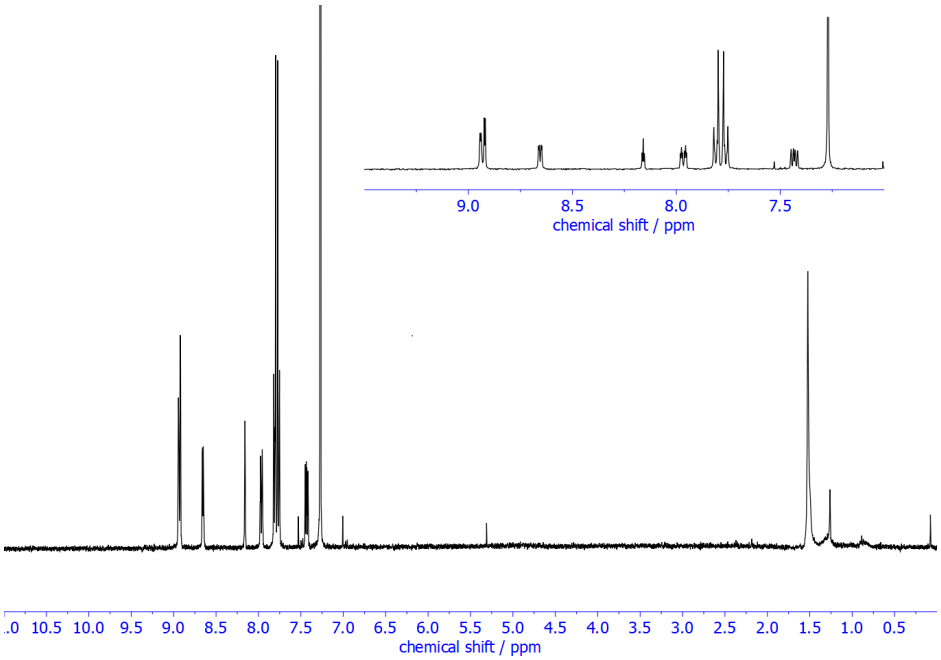

Figure 2.28: ^{1}H-NMR of **C3**.

C2[107]

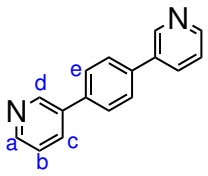

1,4-Dibromo benzene (0.5 g, 2.12 mmol), **13** (0.78 g, 6.35 mmol), tris(dibenzylideneacetone)dipalladium(0) (50 mg, 0.05 mmol), and triphenyl phosphine (120 mg, 0.46 mmol) were dissolved in 75 mL toluene, 10 mL methanol and 10 mL 2M Na_2CO_3 under inert conditions. The mixture was heated for 20 h at 70 °C. The organic phase was separated and the water phase was extracted three times with 25 mL dichloromethane. The combined organic phases were dried over $MgSO_4$, filtered off and the solvent was removed. The crude product was purified by column chromatography (dichloromethane/ethyl acetate 1:1) and recrystallised in cyclohexane yielding 227 mg (46 %) of slight yellowish crystalline plates.

^{1}**H-NMR** ($CDCl_3$, 400 MHz) δ/ppm: 8.80 (d, J = 2.4 Hz, 2H, d), 8.49 (d, J = 4.8 Hz, 2H, a), 7.90 (d, J = 2.4 Hz, 2H, c) 7.63 (s, 4H, e), 7.29 (d, J = 7.9 Hz, 2H, b).

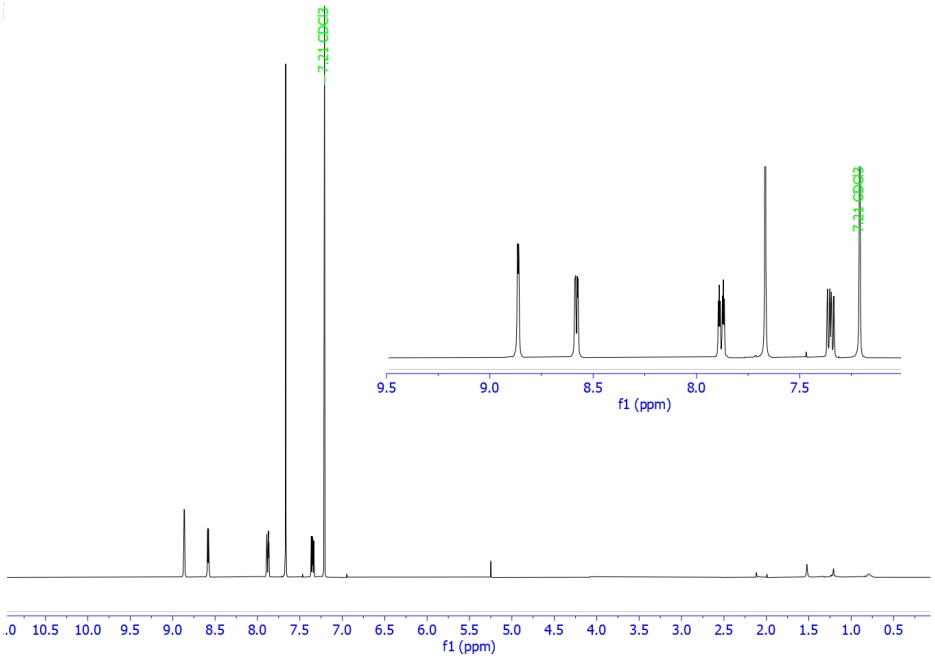

Figure 2.29: ^{1}H-NMR of **C2**.

^{13}**C-NMR** ($CDCl_3$, 100 MHz) δ/ppm : 148.8, 148.2, 137.6, 135.7, 134.1, 127.7, 123.6.

m/z (ESI-ToF) : 234.2 M^+, ($C_{16}H_{12}N_2$, M^+ requires 233.1).

M.P. 125.8-127.1 °C.

16[100]

In a 100 mL two-necked round bottom flask, 1,3-dibromobenzene (2.95 g, 12.5 mmol, 1 eq.) was dissolved in dried diethylether (40 mL). The solution was cooled to -78 °C via a dry ice/acetone bath and *n*-butyl lithium (5 mL) was added over 30 minutes via a dropping funnel. Under vigorous stirring, $CuCl_2$ (1.85 g, 13.8 mmol, 1.1 eq.) was added. After the reaction mixture come to room temperature, the solution was stirred overnight. The mixture was washed three times with a 10% NH_4OH solution, water and brine. The organic layer was washed with water and brine and dried over $MgSO_4$. The product was isolated by column chromatography (DCM:hexane 1:1), affording yellow crystals (0.87 g, 23%).

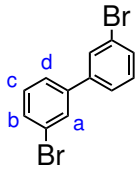

^{1}**H-NMR** ($CDCl_3$, 400 MHz) δ/ppm : 7.70 (t; J = 1.7 Hz; 2H; a), 7.50 (m; 4H; b,c), 7.32 (m; 2H; b).

^{13}**C-NMR** ($CDCl_3$, 100 MHz) δ/ppm : 141.9, 130.9, 130.5, 130.3, 125.9, 132.1

m/z (ESI-ToF) : 312.0 M^+, ($C_{12}H_8Br_2$, M^+ requires 309.9).

B2

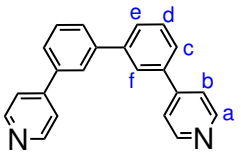

In a 100 mL Schlenk tube, sodium carbonate (102 mg, 0.96 mmol, 1.5 eq.) was dissolved in water (2.5 mL). To the solution, **16** (200 mg, 0.64 mmol, 1 eq.), pyridineboronic acid (236 mg, 1.92 mmol, 3 eq.), $PdCl_2(PPh_3)_2$ (42 mg, 0.06 mmol, 0.1 eq.), THF (5 mL), and ethanol (5 mL) was added. The reaction mixture was degassed by four freeze-pump-thaw cycles and stirred at 70 °C for 72 h. The reaction progress was monitored by ESI-MS. After the reaction completed, the product was extracted five times with $CHCl_3$. The combined organic layer was washed with water and brine and dried over $MgSO_4$. The product was isolated by column chromatography (DCM:MeOH 30:1). Recrystallisation by layer addition (CH_2Cl_2/petrol ether) afforded a white powder (21 mg, 12% yield).

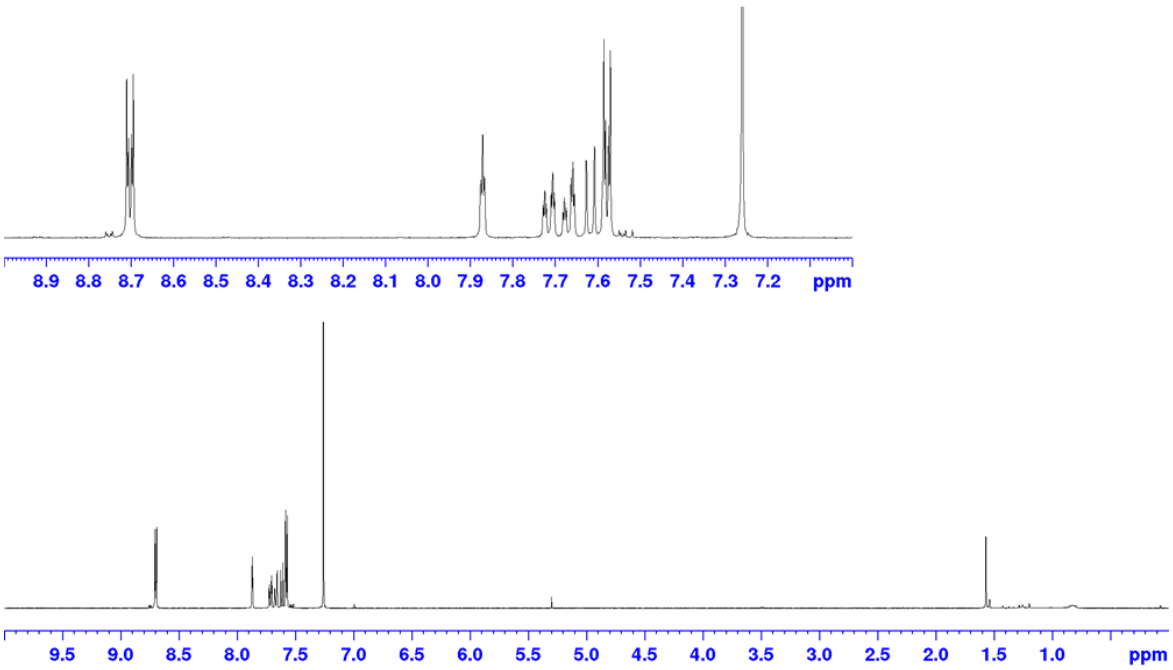

Figure 2.30: ^{1}H-NMR of **B2**.

^{1}H-NMR ($CDCl_3$, 400 MHz) δ/ppm : 8.70 (dd; J = 4.5, 1.6 Hz; 4H; a), 7.87 (m; 1H; f), 7.71 (m; 2H; c), 7.66 (m; 2H; e), 7.62 (m; 2H; d), 7.58 (m; 4H; b).

^{13}C-NMR ($CDCl_3$, 100 MHz) δ/ppm : 150.5 (a), 129.9 (d), 128.1 (c), 126.5 (e), 126.2 (f), 121.9 (b).

m/z (ESI-ToF) 305.2 M^+ ($C_{22}H_{16}N_2$, M^+ requires 304.38).

M.P. 155.0-157.7 °C.

19[101]

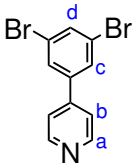

In a 250 mL Schlenk tube, sodium carbonate (5.30 g, 50.0 mmol, 10 eq.) was dissolved in water (70 mL). To the solution, 1,3,5-tribromoiodobenzene (1.57 g, 5.0 mmol, 1 eq.), **12** (0.77 g, 6.3 mmol, 1.25 eq.), $PdCl_2$(dppf) (0.20 g, 0.3 mmol, 0.05 eq.) and dioxane (70 mL) was added. The reaction mixture was degassed by three freeze-pump-thaw cycles and stirred at 70 °C for 16 h. The reaction progress was monitored by TLC. After the reaction completed, the product was extracted five times with DCM. The combined organic layer was washed with water and brine and dried over $MgSO_4$. The product was isolated by column chromatography (DCM:MeOH:NEt_3 with a gradient from 10:0:0 to 10:1:0.1), affording a white powder (0.42 g, 27%).

^{1}**H-NMR** ($CDCl_3$, 400 MHz) δ/ppm : 8.70 (dd; J = 4.5, 1.6 Hz; 2H; a), 7.74 (t; J = 1.7 Hz; 1H; d), 7.70 (d; J = 1.7 Hz; 2H; c), 7.44 (dd; J = 4.4, 1.7 Hz; 2H; b).

^{13}**C-NMR** ($CDCl_3$, 100 MHz) δ/ppm : 149.5, 147.1, 142,5, 135.5, 131.5, 122.1, 119.5.

m/z (ESI-ToF) 313.9 M^+ ($C_{22}H_{16}N_2$, M^+ requires 312.9).

18

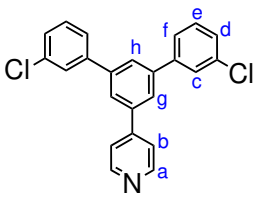

In a 50 mL Schlenk tube, sodium carbonate (0.68 g, 6.4 mmol, 5 eq.) was dissolved in water (5 mL). To the solution, **19** (0.40 g, 1.3 mmol, 1 eq.), (3-chlorophenyl)boronic acid (0.60 g, 3.8 mmol, 6.0 eq.), $Pd(PPh_3)_2Cl_2$ (0.22 g, 0.3 mmol, 0.25 eq.), THF (10 mL), and ethanol (10 mL) was added. The reaction mixture was degassed by three freeze-pump-thaw cycles and stirred at 70 °C for 18 h. The reaction progress was monitored by ESI-MS. After the reaction completed, the product was extracted five times with DCM. The combined organic layer was washed with water and brine and dried over $MgSO_4$. The product was isolated by column chromatography (DCM:MeOH:pyridine with a gradient from 3:1:0.1 to 5:3:0.2). Recrystallisation by layer addition (CH_2Cl_2/petrol ether) afforded a pale white powder (312 mg, 65% yield).

^{1}**H-NMR** ($CDCl_3$, 400 MHz) δ/ppm : 8.72 (dd; J = 4.5, 1.4 Hz; 2H, a), 7.76 (s; 3H; f,h), 7.50 (t; J = 1.5 Hz; 2H; c,d,e,f), 7.60 (dd; J = 4.6, 1.5 Hz; 2H; b), 7.55 (m; 2H; c,d,e,f), 7.40 (m; 4H; c,d,e,f).

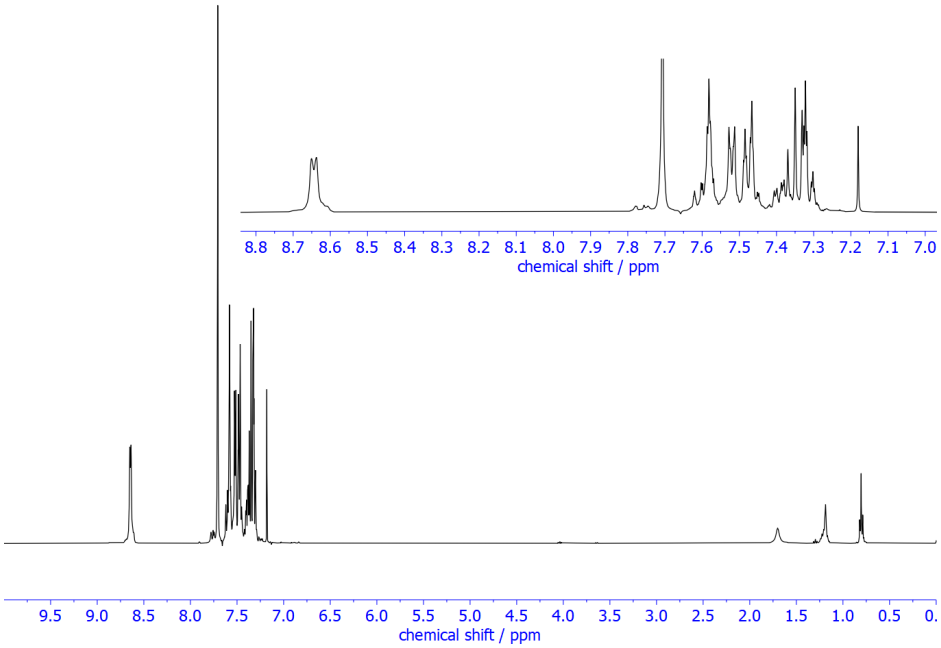

Figure 2.31: ^{1}H-NMR of **18**.

^{13}**C-NMR** ($CDCl_3$, 100 MHz) δ/ppm : 150.5 (a), 126.7 (h), 125.38 (g), 121.9 (b).

m/z (ESI-ToF) 376.0 M^+ ($C_{22}H_{15}N_1Cl_2$, M^+ requires 376.28).

B3

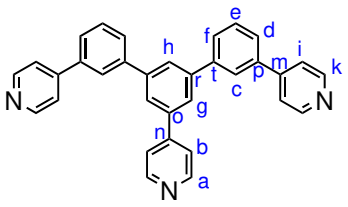

In a 50 mL Schlenk tube, caesium carbonate (515 mg, 2.6 mmol, 20 eq.) was dissolved in water (2 mL). **18** (50 mg, 0.14 mmol, 1 eq.), **12** (164 mg, 1.33 mmol, 10.0 eq.), $Pd(OAc)_2$ (24.4 mg, 0.07 mmol, 0.5 eq.) and SPhos (57 mg, 2.66 mmol, 1 eq.) were dissolved in toluene (10 mL) and ethanol (2 mL). The reaction mixtures were combined and degassed by three freeze-pump-thaw cycles and stirred at 110 °C for 24 h in a sealed Schlenk tube. Afterwards, $Pd(OAc)_2$ (24.4 mg, 0.07 mmol, 0.5 eq.) and SPhos (57 mg, 2.66 mmol, 1 eq.) were added and the reaction was continued for another 24 h. The solvents were removed and the product was isolated by column chromatography (toluene:MeOH with a gradient from 100:5 to 100:15). Recrystallisation in Et_2O/PE afforded a white powder (22 mg, 34% yield).

^{1}**H-NMR** ($CDCl_3$, 400 MHz) δ/ppm : 8.73 (dd; J = 4.5, 1.4 Hz; 2H, a), 8.70 (dd; J = 4.5, 1.4 Hz; 2H, k), 7.92 (m; 3H; c+h), 7.88 (m, 2H, g), 7.77 (m; 2H; f), 7.70 (m; 2H; d), 7.65 (m; 4H; b+e), 7.59 (m; 4H; i) .

^{13}**C-NMR** ($CDCl_3$, 100 MHz) δ/ppm : 150.35 (a), 150.26 (k), 148.13 (m,n), 142.52 (o), 141.51 (p), 139.06 (r,t), 129.83 (e) 128.06 (f), 126.95 (d), 126.60 (h), 126.07 (c), 125.36 (g), 121.88 (b), 121.79 (i).

m/z (ESI-ToF): 462.2 M^+ ($C_{33}H_{23}N_3$, M^+ requires 462.2)

M.P. 207 °C.

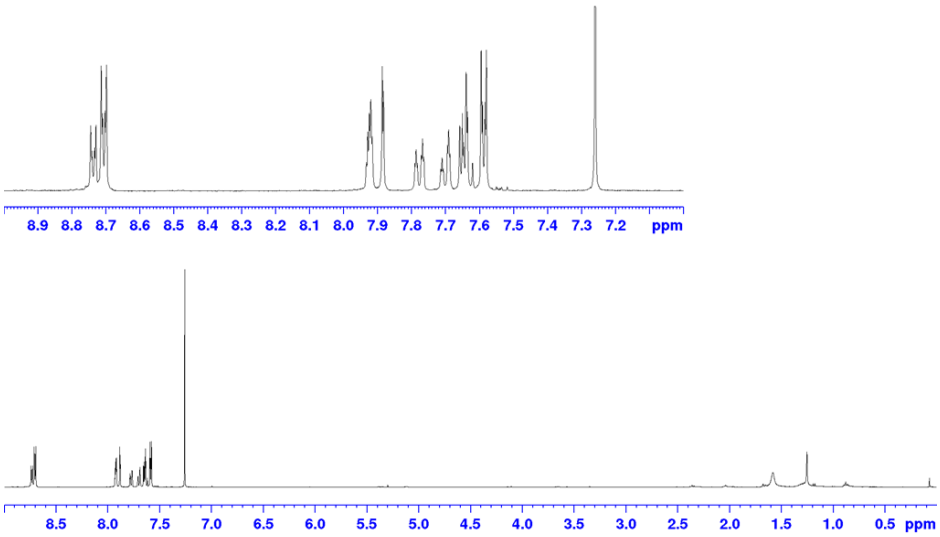

Figure 2.32: ^{1}H-NMR of **B3**.

2.6.3 Synthesis of Porphyrin Oligomers (tBu)

3,5-Di-*tert*-butylbenzaldehyde (22)[109]

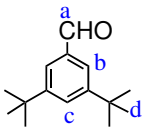

A round bottom flask was charged with a solution of 3,5-di-tert-butyltoluene (**20**) (25.0 g, 0.122 mol, 1 eq.), *N*-bromosuccinimide (33.0 g, 0.185 mol, 1.5 eq.), and azobisisobutyronitrile (AIBN) (0.900 g, 5.5 mmol, 0.05 eq.) in benzene (50 mL). The mixture was heated slowly to gently reflux under magnetic stirring. The mixture was heated to reflux for 4 h, then cooled and filtered through paper, and the solvents were removed under reduced pressure. The residue was dissolved in 70 mL of a solvent mixture composed of EtOH/H_2O (1:1, v/v). Hexamethylenetetramine (50.0 g, 0.357 mol, 2.9) was added to the solution. The solution was heated at reflux for 4 h. Concentrated HCl was added (21 mL), and heating at reflux was continued for 30 min. After the reaction was finished, the ethanol was removed under reduced pressure, and the remaining aqueous layer was extracted with ether. The ether layer was dried over Na_2SO_4 and the solvent was removed. Recrystallisation from EtOH afforded 3,5-bis(*tert*-butyl)benzaldehyde (**22**) as colourless crystals (7.85 g, 31% yield).

^{1}**H NMR** ($CDCl_3$) δ/ppm : 10.01 (s, 1H, C*H*O, a), 7.72 (d, J = 8.5 Hz, 2H, H^{ortho} b), 7.71 (m, J = 8.5 Hz,1H, H^{para} , c), 1.36 (s, 18H, CH_3, d).

Dipyrromethane (DPM, 23)[110]

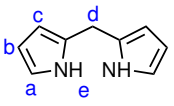

Formaldehyde (33% w/w solution in water, 5.4 mL, 60 mmol) was added to pyrrole (100 mL, 1.44 mol) and the solution degassed by repeated evacuation and stirring under N_2. Trifluoroacetic acid (0.54 mL, 3.09 mmol) was added by syringe under vigorous stirring and in the N_2 atmosphere. The reaction was allowed to proceed for 5 minutes before CH_2Cl_2 (100 mL) was added, followed immediately by Na_2CO_3 (aq., sat. solution, 100 mL). The organic layer was washed with Na_2CO_3 (aq., sat. solution, 2 $\times$ 100 mL) and water (100 mL), then dried over Na_2SO_4. The solvent and excess pyrrole were removed on the rotor evaporator. Distillation of the oily residue in a Kugelrohr apparatus (180 °C, 0.6 mbar) yielded the product as a white crystalline solid (2.61 g, 31%).

^{1}**H NMR** (250 MHz, $CDCl_3$) δ/ppm : 3.96 (s, 2H, CH_2, d), 6.06 (m, 2H, pyrrole-H^β, c), 6.17 (m, 2H, pyrrole-H^β, b), 6.66 (m, 2H, pyrrole-H^α, a), 7.88 (br s, 2H, NH, e).

Zinc 5,15-bis(3,5-bis(*tert*-butyl)phenyl)porphyrin (24)[111]

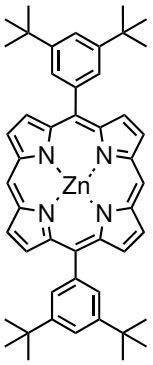

3,5-Bis(*tert*-butyl)benzaldehyde (**22**) (2.81 g, 12.9 mmol) and dipyrromethane (**23**) (1.88 g, 12.9 mmol) were placed in a dry flask under N_2 and dissolved in fresh Winchester bottle of CH_2Cl_2 (2.5 L). The solution was degassed three times by repeated evacuation and stirring under nitrogen. Trifluoroacetic acid (0.62 mL, 8.0 mmol) was added and the reaction mixture stirred in the dark for 3 h. DDQ (3.72 g, 16.4 mmol) was added and stirring continued for 0.5 h. After quenching of the acid by addition of triethylamine (12.5 mL) the mixture was concentrated to a volume of about 300 mL on the rotary evaporator, passed over a silica plug (CH_2Cl_2), dried and redissolved in $CHCl_3$ (300 mL). $Zn(OAc)_2 \cdot 2H_2O$ (3.17 g, 14.46 mmol) was dissolved in methanol (30 mL) and added to a solution of free-base porphyrin. The reaction was stirred at room temperature for 1 hour. The mixture was passed through a short plug of silica gel using CH_2Cl_2. The crude product was recrystallized by layer addition (CH_2Cl_2 / MeOH) to give **24** as a purple powder (2.8 g, 58 %).

^{1}**H NMR** (400 MHz, $CDCl_3$ + 1% pyridine-d5) δ/ppm : 1.59 (s, 36H, ^{t}Bu-H, 5), 7.86 (t, 2H, J = 2.0 Hz, Ar-H^{ortho}, 6), 8.17 (d, 4H, J = 2.0 Hz, Ar-H^{ortho}, 4), 9.23 (d, 4H, J = 4.5 Hz, H^β, 3), 9.45 (d, 4H, J = 4.5 Hz, H^β, 2), 10.36 (s, 2H, H^{meso}, 1).

Zinc 5,15-bis-(3,5-bis-tert-butyl-phenyl)-10,20-dibromo-porphyrin[111]

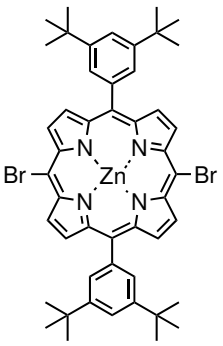

To a solution of **24** (2.1 g, 2.8 mmol) in CH_2Cl_2 (345 mL) and pyridine (6 mL) cooled to -10°C or lower temperature, was added freshly recrystallized N-bromosuccinimide (1.0 g, 5.6 mmol) in one portion. After stirring in the dark for 10 minutes, the reaction was allowed to warm to room temperature and stirred for 40 minutes. Then petroleum ether (207 mL) was added and the mixture was filtered through a short silica plug, the silica was previously treated with pyridine

(8 mL) in a mixture of Petrol/CH_2Cl_2 1/1 (207 mL). The silica
was flushed with a mixture 1/1 Petrol/CH_2Cl_2 to recover the entire product. The solvents were removed by rotary evaporation. The crude product recrystallized from CH_2Cl_2/MeOH to give the dibromoporphyrin (**25**) as a purple solid (1.68 g, 68%).

^{1} **H NMR** (400 MHz, $CDCl_3$ + 1% pyridine-d_5): δ_H = 1.54 (s, 36H), 7.79 (t, J = 1.8 Hz, 2H), 7.98 (d, J = 1.8 Hz, 4H), 8.90 (d, J = 4.6 Hz, 4H), 9.65 (d, J = 4.6 Hz, 4H).

I-P1 (26)[111]

Tris-(Dibenzylideneacetone)-di-palladium(0) (105 mg, 0.11 mmol), copper(I) iodide (46 mg, 0.23 mmol), triphenylphosphine (36 mg, 0.23 mmol) and dibromoporphyrin (**25**) (1.048 g, 1.15 mmol) were dried in a Schlenk tube under argon. Toluene (74 mL), $^iPr_2NH$ (40 mL) and pyridine (2.1 mL) were added and the reaction mixture deoxygenated via 3 vacuum freeze/thaw cycles.

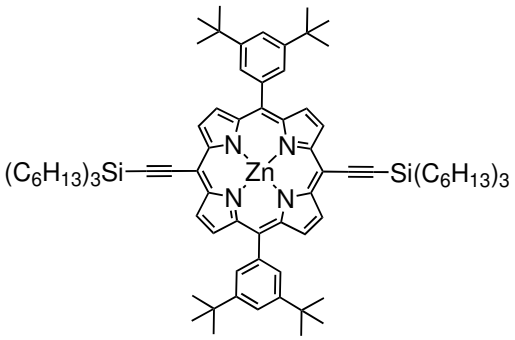

Trihexylsilyl acetylene (1.4 mL, 3.4 mmol) was added by syringe. The reaction mixture was stirred at 50 °C for 3 hours, and the reaction progress was monitored by TLC. Solvents were removed and the residue passed through a short silica gel column using CH_2Cl_2. The recrystallisation was performed by layer addition (CH_2Cl_2 / MeOH) yielding **26** as a green solid (1.17 g, 7%).

^{1}**H NMR** (400 MHz, $CDCl_3$ + 1% pyridine-d_5) δ/ppm: 0.90 (t, 18H, J = 7.0 Hz, CH_3), 1.02 (m, 12H, CH_2), 1.39 (m, 24H, CH_2), 1.58–1.51 (m, 48H, CH_2, ^{t}Bu-H), 1.77 (m, 12H, CH_2), 7.83 (t, 2H, J = 1.5 Hz, Ar-H^{para}), 8.06 (d, 4H, J = 1.5 Hz, Ar-H^{ortho}), 8.98 (d, 4H, J = 4.5 Hz, H^{β}), 9.74 (d, 4H, J = 4.5 Hz, H^{β}).

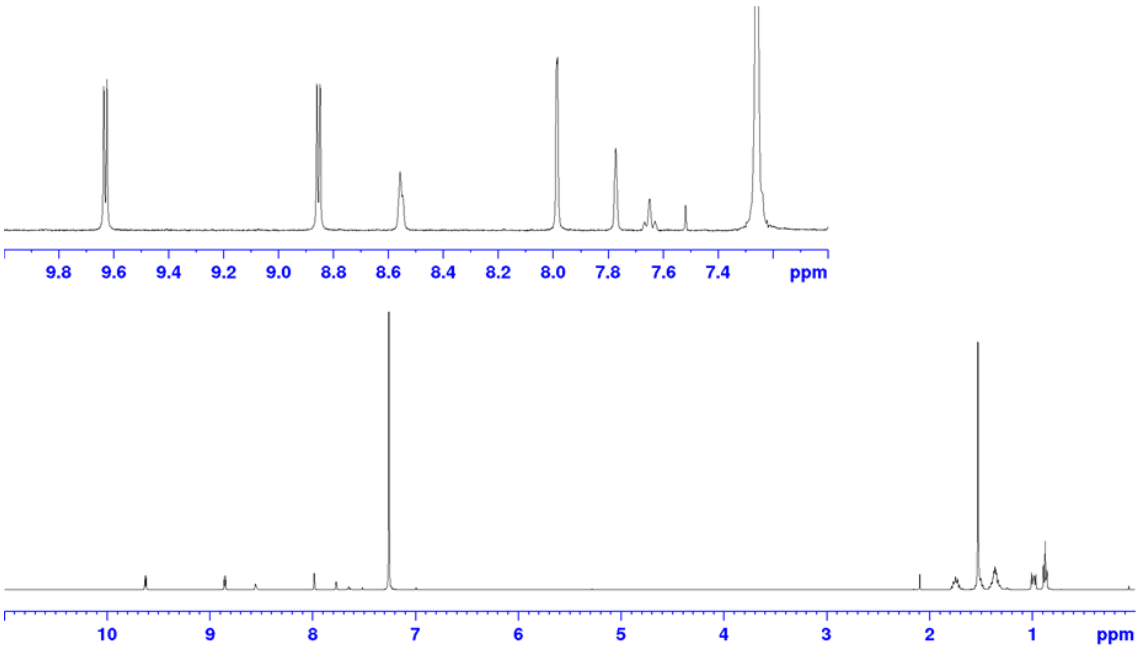

Figure 2.33: ^{1}H-NMR of ***l*-P1**.

***l*-P1$_{MD}$ (27) and *l*-P1$_{FD}$ (28)[74]**

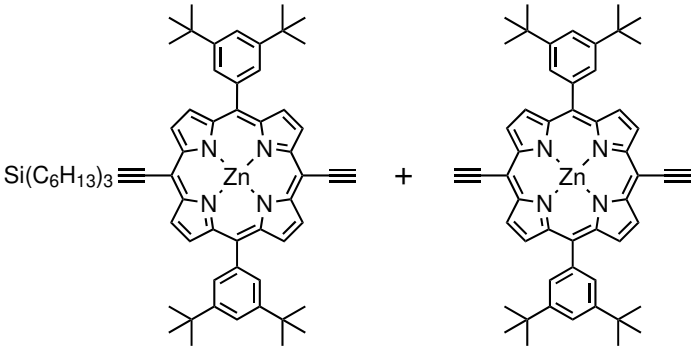

Protected porphyrin monomer ***l*-P1** (**26**) (1.54 g, 1.13 mmol) was dissolved in CH_2Cl_2 (280 mL), $CHCl_3$ (280 mL) and pyridine (5.3 mL). Tetra-*n*-butylammonium fluoride (1.7 mL, 1.0 M solution in THF, 1.7 mmol) was added in small portions (0.2 mL) to the stirred solution. The progress of the reaction was monitored by TLC until an optimal product mixture was reached (begin of the formation of fully deprotected porphyrin). The mixture was passed immediately through a short plug of silica gel (CH_2Cl_2). Column chromatography (50:1:1, petrol:EtOAc:pyridine) gave mono-deprotected (**27**, 306 mg, 24%), fully-deprotected porphyrin (**28** 13 mg, 1%) and recovered starting material (1.16 g, 75%).

Mono-deprotected *l*-P1$_{MD}$ (27): (306 mg, 24%).

^{1}H NMR (400 MHz, $CDCl_3$) δ/ppm: 0.91 (t, 9H, $J = 7.0$ Hz, CH_3), 1.01–1.05 (m, 6H, CH_2), 1.37–1.44 (m, 12H, CH_2), 1.52–1.57 (m, 42H, -CH_2, ^{t}Bu-H), 1.76–1.81 (m, 6H, CH_2), 4.15 (s, 1H, ≡CH), 7.81 (t, 2H, $J = 2.0$ Hz, Ar-H^{para}), 8.03 (d, 4H, $J = 2.0$ Hz, Ar-H^{ortho}), 8.92 (m, 4H, H_β), 9.68 (m, 4H, H_β).

Fully deprotected *I*-P1$_{FD}$ (28): (13 mg, 1%).

^{1}H NMR (400 MHz, $CDCl_3$) δ/ppm: 1.55 (s, 36H, ^{t}Bu-H), 4.15 (s, 2H, ≡CH), 7.79 (t, 2H, $J = 1.5$ Hz, Ar-H^{para}), 8.01 (d, 4H, $J = 1.5$ Hz, Ar-H^{ortho}), 8.91 (d, 4H, $J = 4.5$ Hz, H^β), 9.67 (d, 4H, $J = 4.5$ Hz, H^β).

I-P2, *I*-P3, *I*-P4, *I*-P5[74]

$Pd(PPh_3)_2Cl_2$ (21.9 mg, 0.03 mmol), CuI (21.6 mg, 0.11 mmol) and 1,4-benzoquinone (64.4 mg, 0.57 mmol) were dissolved in dry $CHCl_3$ (15.9 mL) and $^i Pr_2NH$ (0.84 mL). The resulting catalysts mixture was added to a solution of *mono*-deprotected porphyrin monomer (**27**) (184.1 mg, 0.17 mmol) and *fully*-deprotected porphyrin monomer (**28**) (45.13 mg, 0.06 mmol) in $CHCl_3$ with 1% pyridine (85 mL). The reaction mixture was stirred at room temperature for 1 h and passed through a short silica gel column using $CHCl_3$ with 1% pyridine. Size exclusion chromatography on Biobeads SX–1 using toluene was performed to separate monomer and benzoquinone, followed by GPC separation and recrystallisation by layer addition (CH_2Cl_2 / MeOH). (***I*-P2**: 80.2 mg; ***I*-P3**: 31 mg; ***I*-P4**: 17.5 mg; ***I*-P5**: 9.5 mg)

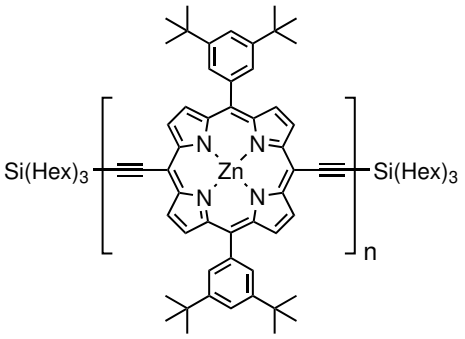

***I*-P2**

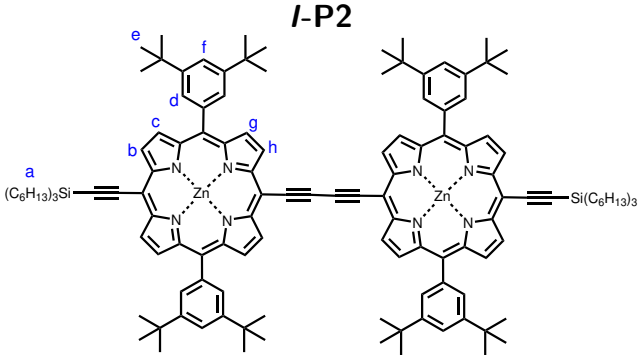

^{1}H NMR (400 MHz, $CDCl_3$) δ/ppm: 0.92 (m, 20H, Ha), 1.04 (m, 13H, Ha), 1.41 (m, 30H, Ha), 1.59 (s, 84H, He), 1.78 (m, 11H, Ha), 7.86 (m, 4H, Hf), 8.11 (broad d, $J = 1.8$ Hz, 8H, Hd), 8.99 (d, $J = 4.6$ Hz, 4H, Hc), 9.10 (d, $J = 4.6$ Hz, 4H, Hg), 9.75 (d, $J = 4.6$ Hz, 4H, Hb), 9.99 (d, $J = 4.6$ Hz, 4H, Hh).

m/z (MALDI-ToF) 2158.48 ($C_{140}H_{178}N_8Si_2Zn_2$, M^+ requires 2159.23).

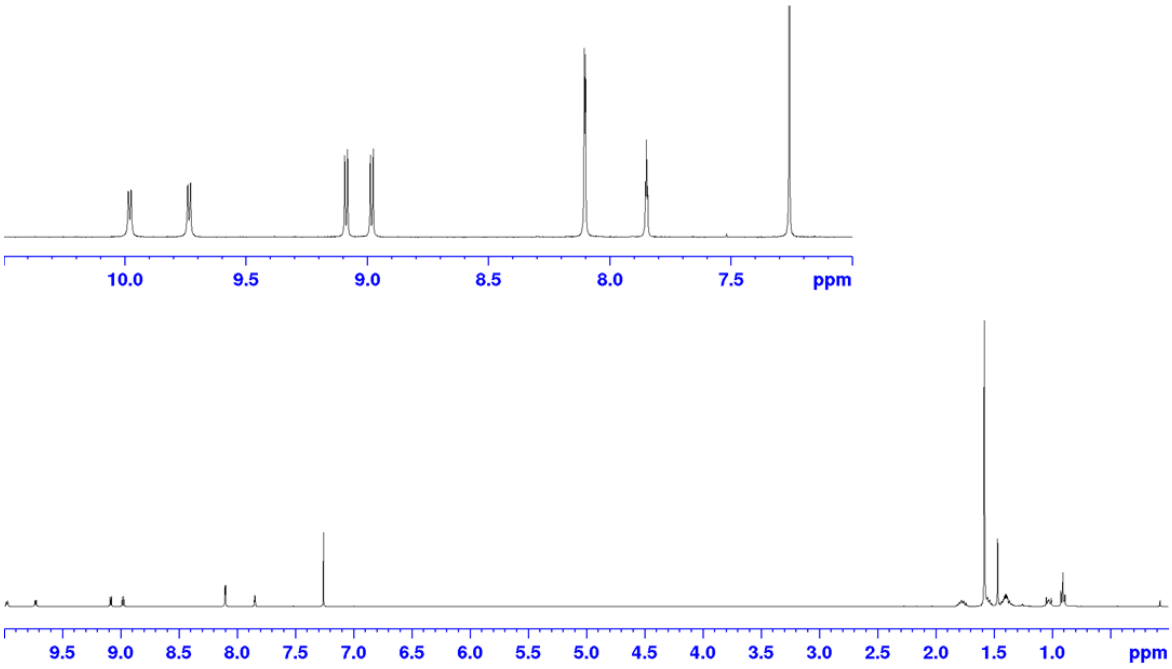

Figure 2.34: ^{1}H-NMR of ***I*-P2**.

***I*-P3**

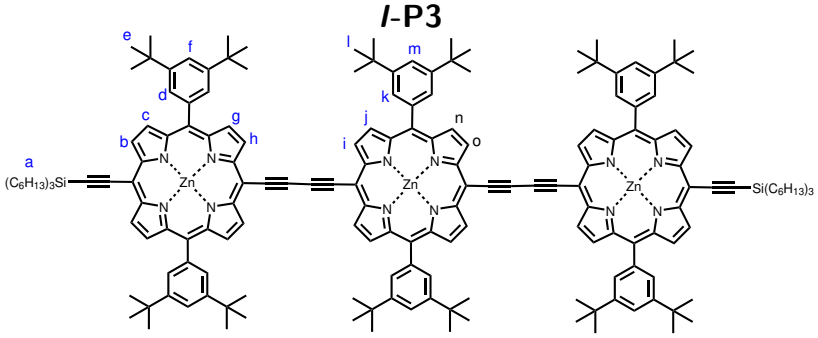

^{1}H NMR (400 MHz, $CDCl_3$ + 1% pyridine) δ/ppm: 0.90 (m, 18H, Ha), 1.02 (m, 12H, Ha), 1.39 (m, 28H, Ha), 1.56 (m, 18H, Ha), 1.57 (s, 72H, He), 1.59 (s, 36H, Hl), 1.77 (m, 13H, Ha), 7.81 (m, 4H, Hf), 7.83 (m, 2H, Hm), 8.05 (m, 8H, Hd), 8.09 (m, 4H, Hk), 8.89 (d, J = 4.4 Hz, 4H, Hc), 8.99 (d, J = 4.6 Hz, 8H, Hg + Hj), 9.66 (d, J = 4.6 Hz, 4H, Hb), 9.90 (d, J = 4.6 Hz, 8H, Hh + Hi).

m/z (MALDI-ToF) 2954.40 ($C_{192}H_{228}N_{12}Si_2Zn_3$, M^+ requires 2955.56).

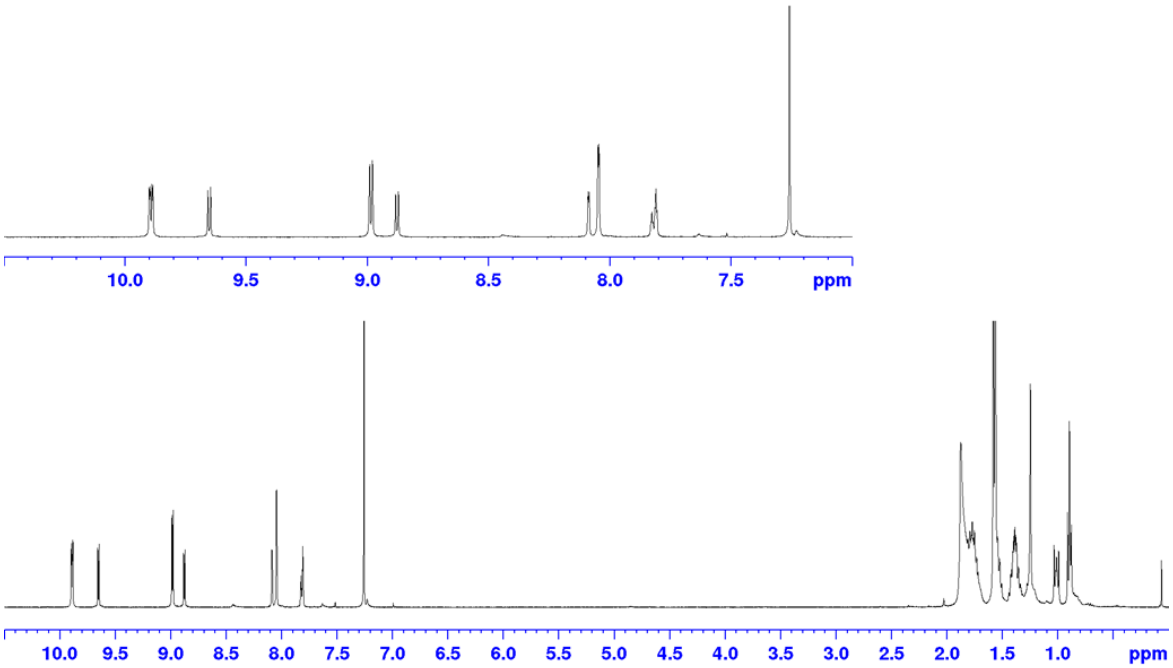

Figure 2.35: ^{1}H-NMR of ***I*-P3**.

***I*-P4**

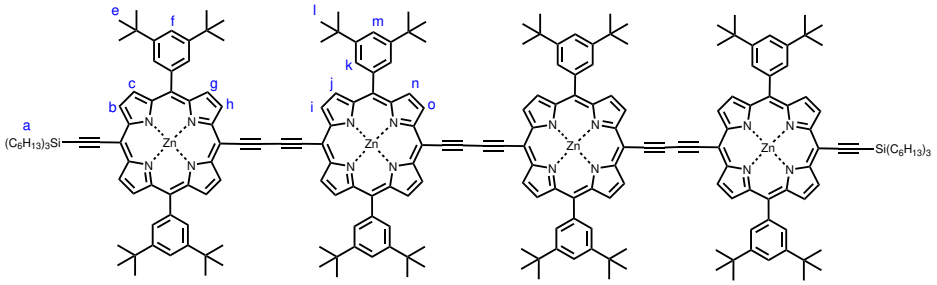

^{1}**H NMR** (400 MHz, $CDCl_3$ + 1% pyridine) δ/ppm: 0.91 (m, 18H, Ha), 1.02 (m, 12H, Ha), 1.39 (m, 27H, Ha), 1.57 (s, 72H, He), 1.59 (s, 72H, Hl), 1.77 (m, 14H, Ha), 7.82 (m, 4H, Hf), 7.84 (m, 4H, Hm), 8.06 (m, 8H, Hd), 8.10 (m, 8H, Hk), 8.89 (d, J = 4.5 Hz, 4H, Hc), 9.00 (m, 12H, Hg, j, n), 9.66 (d, J = 4.6 Hz, 4H, Hb), 9.91 (m, 12H, Hh, I, o).

m/z (MALDI-ToF) 3748.60 ($C_{244}H_{278}N_{16}Si_2Zn_4$, M^+ requires 3751.90).

***I*-P5**

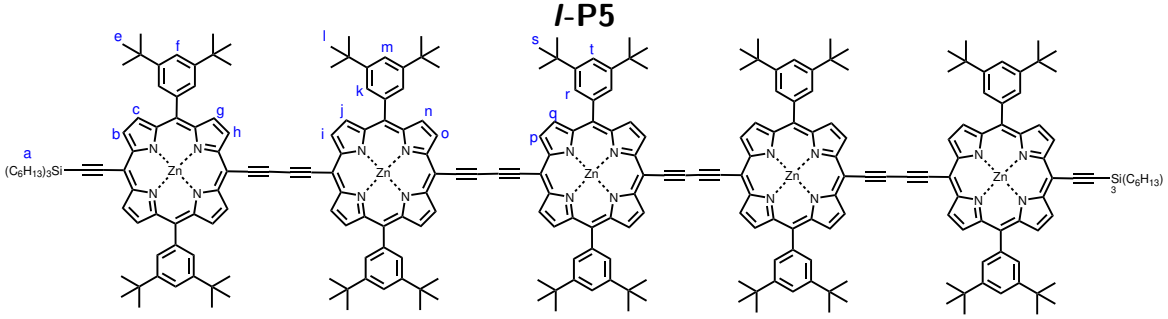

^{1}H NMR (400 MHz, $CDCl_3$ + 1% pyridine) δ/ppm: 0.90 (m, 20H, Ha), 1.02 (m, 13H, Ha), 1.39 (m, 32H, Ha), 1.57 (s, 72H, He), 1.59 (s, 72H, Hl), 1.60 (s, 36H, Ht), 1.77 (m, 15H, Ha), 7.82 (m, 4H, Hf), 7.84 (m, 6H, Hm, t), 8.05 (m, 8H, Hd), 8.10 (m, 12H, Hk, r), 8.89 (d, J = 4.5 Hz, 4H, Hc), 9.01 (m, 16H, Hj, n, q), 9.66 (d, J = 4.5 Hz, 4H, Hb), 9.91 (m, 16H, Hi, o, p).

m/z (MALDI-ToF) 4538.04 ($C_{296}H_{328}N_{20}Si_2Zn_5$, M^+ requires 4548.23).

Hexa(4-(pyridine-4-yl)phenyl)benzene (T6)[74]

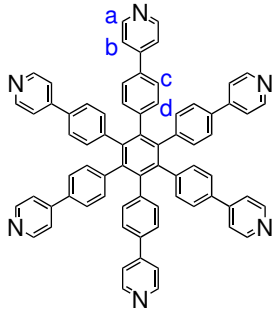

To a solution of hexakis-(4-bromophenyl)benzene (0.60 g, 0.60 mmol, 6 eq.) in THF (42 mL) and dimethoxyethane (18 mL) was added $PdCl_2(PPh_3)_2$ (0.08 mg, 0.11 mmol, 1.1 eq.). After addition of water (24 mL) $NaHCO_3$ (0.90 g, 10.7 mmol, 108 eq.) and 4-pyridineboronic acid (1.76 g, 14.4 mmol, 145 eq.) the mixture was deoxygenated and stirred at 70 °C for 6 days. Solvents were removed and the crude product was purified by column chromatography on flash silica gel (CH_2Cl_2: MeOH : NEt_3 gradient 100:1:0.25 to 100:10:0.5) to give the template as a white solid. The solid product was washed with methanol, redissolved in $CHCl_3$ and washed with water. After drying under high vacuum, the compound was a white powder (0.23 g, 40%, around 20% in a mixed fraction).

^{1}H-NMR ($CDCl_3$, 400 MHz) δ/ppm : 7.01 (d, J = 8.3 Hz, 12H, a), 7.25 (d, J = 8.5 Hz, 12H, b), 7.32 (d, J = 6.1 Hz, 12H, c), 8.53 (d, J = 6.4 Hz, 12H, d)

c-P6•T6[40]

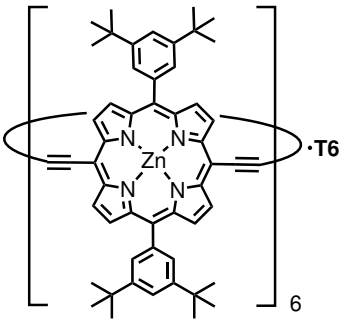

Hexadentate template (**T6**) (13 mg, 0.013 mmol) and deprotected porphyrin dimer ***I*-P2$_{FD}$** (**30**) (64 mg, 0.040 mmol) were dissolved in dry $CHCl_3$ (65 mL) and sonicated for 2 h. A catalyst solution was prepared by dissolving dichlorobis(triphenylphosphine)-palladium(II) (14 mg, 0.019 mmol), CuI (19 mg, 0.010 mmol) and 1,4-benzoquinone (20 mg, 0.200 mmol) in dry $CHCl_3$ (11 mL) and of freshly distilled diisopropylamine (0.5 mL). The template and porphyrin monomer mixture cooled to room temperature and

the catalysts solution was added. The reaction mixture was stirred vigorously at room temperature overnight under argon. The reaction mixture was passed through a plug of alumina using $CHCl_3$ as eluent, then through a SEC column with toluene as the eluent (to remove benzoquinone and traces of dimer). Separation of the crude was done by recycling GPC in toluene with 1% pyridine with a flow rate of 3.5 mL/min. The separation gave ***c*-P6•T6** as brown solid (16 mg, 22%).

^{1}H NMR (400 MHz, $CDCl_3$) δ/ppm: 1.54 (s, 108H, ^{t}Bu-*H*), 1.58 (s, 108H, ^{t}Bu-*H*), 2.33 (d, J = 7.0 Hz, 12H, pyridyl-H^β), 5.00 (d, J = 7.0 Hz, 12H, pyridyl-H^β), 5.48 (d, J = 9.0 Hz, 12H, Ar-*H*), 5.52 (d, J = 9.0 Hz, 12H, Ar-*H*), 7.81 (s, 12H, Ar-H^{para}), 7.86 (s, 12H, Ar-H^{ortho}), 8.05 (s, 12H, Ar-H^{ortho}), 8.81 (d, J = 4.5 Hz, 24H, H^β), 9.59 (d, J = 4.5 Hz, 24H, H^β).

c-P6[76]

***c*-P6•T6** (6 mg, 2.0 μmol) was dissolved in a in a 1 M solution of 1,4-diazabicyclo[2.2.2]octane (DABCO) in toluene (0.2 mL). The solution was passed through a silica coulmn using 1 M DABCO solution in toluene as eluent. The colored fraction was collected, and the solvent evaporated by blowing with N_2. The sample was dissolved in $CHCl_3$, and stirred with a saturated aqueous potassium hydrogen phthalate solution. The product was precipitated from DCM/MeOH to give ***c*-P6** as solid (2.3 mg, 86%).

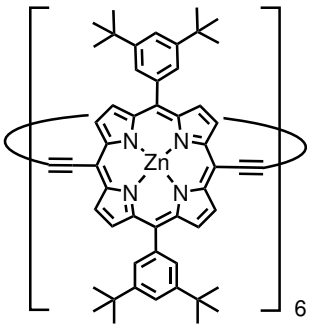

^{1}H NMR (400 MHz, $CDCl_3$) δ/ppm: 1.54 (s, 108H, ^{t}Bu-*H*), 1.58 (s, 108H, ^{t}Bu-*H*), 7.84 (s, 12H, Ar-H^{ortho}), 8.10 (s, 12H, Ar-H^{ortho}), 9.00 (m, 24H, H^β), 9.91 (d, J = 4.5 Hz, 24H, H^β).

m/z (MALDI-ToF) 4763.3 ($C_{312}H_{300}N_{24}Zn_6$, M^+ requires 4765.90).

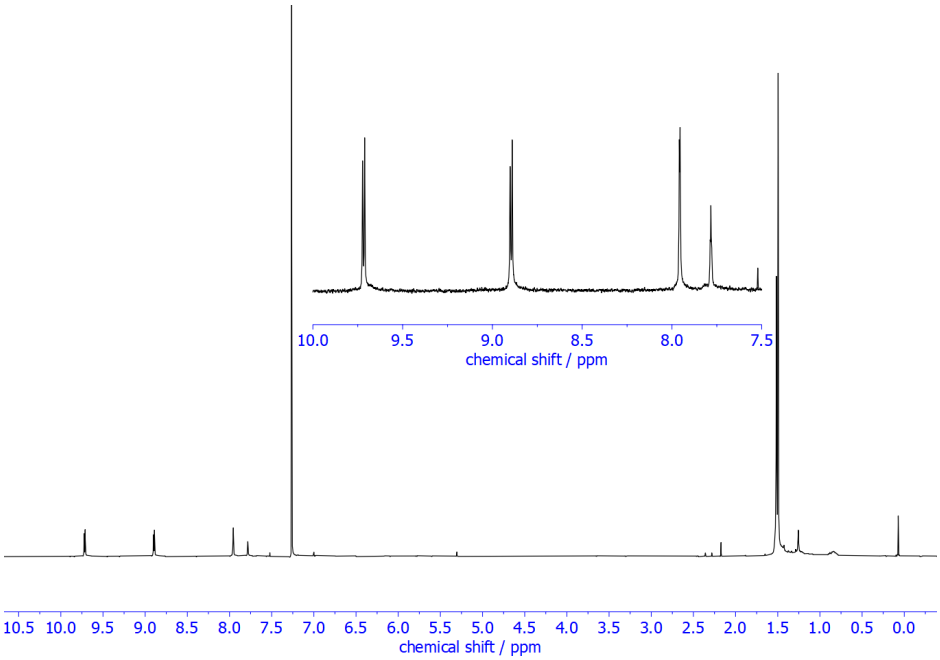

Figure 2.36: ^{1}H-NMR of ***c*-P6**.

2.6.4 Synthesis of Porphyrin Oligomers (THS)

3,5-Bis(trihexylsilyl)benzaldehyde[77]

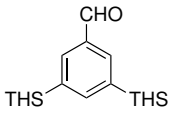

To a stirring solution (or suspension) of 1,3,5-tribromobenzene (5.00 g, 15.8 mmol) in Et_2O (125 mL) at -20 °C (acetone/dry ice), was added *n*-butyl lithium (1.6 M in hexane, 20.8 mL, 33.3 mmol) dropwise, under inert atmosphere. The solution was stirred for 90 min before adding trihexylsilylchloride (13.5 mL, 34.9 mmol) dropwise via a syringe. The solution was allowed to warm to room temperature. After stirring for another 90 min, the reaction mixture was washed with water, dried over $MgSO_4$ and filtered. The solution was concentrated and passed through a silica plug with petrol (PE: 40-60 °C). The solvent was removed to give 10.5 g of a mixture of 3,5-bis(trihexylsilyl)bromobenzene and 1,3,5-tris(trihexylsilyl)-benzene.

This crude product was dried and used without further purification. *n*-Butyl lithium (1.6 M in hexane, 27.5 mL, 44 mmol) was added dropwise via a pressure-equalising dropping funnel to a solution of 3,5-bis(trihexylsilyl)bromobenzene (10.5 g, 14.4 mmol) in dry Et_2O (70 mL) under Ar at 0 °C. The solution was stirred at this temperature for 30 min and then at room temperature for 90 min. *N,N*-Dimethylformamide (5.3 mL, 70 mmol) was added and the mixture was stirred for 1 hr. Aqueous saturated ammonium chloride solution

(100 mL) was added and the organic layer was separated. The aqueous layer was extracted with Et_2O. The combined organic layer was washed with an aqueous solution of $NaHCO_3$ and with water, dried over $MgSO_4$ and filtered. The crude product was purified by column chromatography on silica gel eluting with a gradient of CH_2Cl_2 and petrol (starting from 0% to 10% CH_2Cl_2). The solvent was removed to give 3,5-bis(trihexylsilyl)benzaldehyde (2.1 g, 19% over two steps) as a pale-yellow oil.

^{1}**H NMR** (400 MHz, $CDCl_3$) δ/ppm :10.04 (s, 1H), 7.93 (s, 2H), 7.85 (s, 1H), 0.81–1.31 (m, 78H).

5,15-Bis(3,5-bis(trihexylsilyl)phenyl)porphyrin[77]

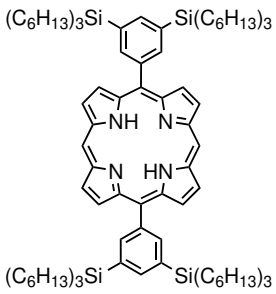

3,5-Bis(trihexylsilyl)benzaldehyde (2.5 g, 3.8 mmol) and dipyrromethane (**23**) (0.56 g, 3.8 mmol) were dissolved in CH_2Cl_2 (700 mL). The solution was saturated with nitrogen, then TFA (0.50 mL, 7.6 mmol) was added and the mixture was stirring for 3 hrs in the dark. DDQ (1.5 g, 6.6 mmol) was added and the mixture was stirred for a further 20 min. Finally, triethylamine (3.8 mL) was added to quench the acid. The solution was concentrated and passed through a short silica plug eluting with a mixture of petrol and CH_2Cl_2 (4:1). The solvent was removed to give the free base porphyrin (2.3 g, 41%) as red-purple oily semi-solid.

^{1}**H NMR** (400 MHz, $CDCl_3$) δ/ppm : 10.35 (s, 2H), 9.40 (d, $J = 4.5$ Hz, 4H), 9.09 (d, $J = 4.5$ Hz, 4H), 8.37 (s, 4H), 8.02 (s, 2H), 0.87–1.52 (m, 156H), -3.03 (s, 2H).

Zinc 5,15-bis(3,5-bis(trihexylsilyl)phenyl)porphyrin[77]

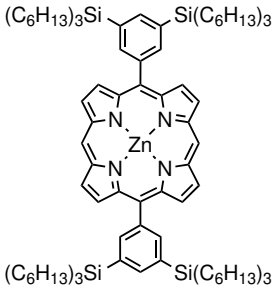

A solution of $Zn(OAc)_2 \cdot 2H_2O$ (1.7 g, 7.8 mmol) in MeOH (10 mL) is added to a solution of 5,15-bis[3,5(trihexylsilyl)phenyl]porphyrin (2.3 g, 1.4 mmol) in $CHCl_3$ (70 mL). The mixture was stirred at 40 °C and monitored by TLC. Metallation is generally complete after 30 min, but it can take up to 2 hours. The solution was evaporated and passed through a short silica plug, eluting with a mixture of petrol and CH_2Cl_2 (80/20). The solvent was removed to give the zinc porphyrin (1.56 g, 70%) as pink crystals.

^{1}H NMR (400 MHz, $CDCl_3$) δ/ppm : 10.39 (s, 2H),9.47 (d, J= 4.5 Hz, 4H), 9.17 (d, J = 4.5 Hz, 4H), 8.37 (s, 4H), 8.03 (s, 2H), 0.82-1.52 (m, 156H).

Zinc 5,15-bis(3,5-bis(trihexylsilyl)phenyl)-10,20-dibromoporphyrin[77]

A solution of *N*-bromosuccinimide (0.33 g, 1.8 mmol) in $CHCl_3$ (90 mL) was added dropwise over 10 min to a stirred solution of porphyrin (1.5 g, 1.8 mmol) in pyridine (0.6 mL) and $CHCl_3$ (42 mL). The reaction mixture was stirred at room temperature for 15 min before adding acetone (0.9 mL) to quenched any excess *N*-bromosuccinimide. The solution was concentrated and passed through a short silica plug eluting with a mixture of petrol and CH_2Cl_2 (80/20). The solvent was removed to give the dibromoporphyrin (1.62 g, 98%) as purple crystals.

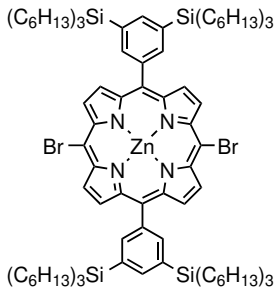

^{1}H NMR (400 MHz, $CDCl_3$) δ/ppm : 9.74 (d, J = 4.8 Hz,4H), 8.95 (d, J = 4.8 Hz, 4H), 8.25 (s, 4H), 8.01 (s, 2H), 0.87–1.51 (m, 156H).

I-P1[77]

(5,15-Bis(3,5(trihexylsilyl)phenyl)10,20-dibromo- porphyrinato)zinc(II) (1.62 g, 0.82 mmol), tris-(dibenzylideneacetone)-di-palladium(0) (72 mg, 78 μmol), copper(I) iodide (30 mg, 156 μmol) and triphenylphosphine (41 mg, 156 μmol) were dissolved in a mixture of toluene (35 mL) and ^{i}Pr$_2$NH (35 mL) and the solution was degassed by several freeze-pump-thaw cycles. Trihexylsilylacetylene (0.91 mL, 2.3 mmol) was added by syringe and the mixture was stirred at 50 °C for 2 hours. TLC indicated full conversion. The reaction mixture was filtered over a plug of silica eluting with petrol / DCM 4:1. Purification by column chromatography on silica gel (gradient of petrol / CH_2Cl_2 100:0 to 100:6) yielded ***I*-P1** (1.48 g, 64 μmol, 83%) as a green oil.

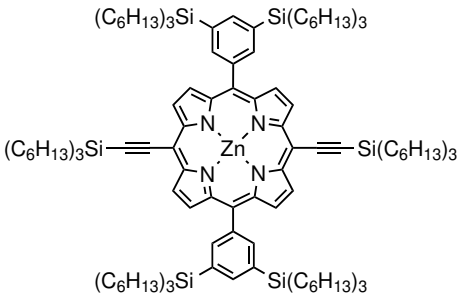

^{1}H-NMR (400 MHz, $CDCl_3$) δ/ppm : 9.74 (d, ^3J = 4.7 Hz, 4H, H^{β}), 8.90 (d, ^3J = 4.7 Hz, 4H, H^{β}), 8.25 (m, 4H, H^{ortho}), 8.00 (m, 2H, H^{para}), 1.82-1.69 (m, 12H, CH_2), 1.59-1.44 (m, 36H, CH_2), 1.44-1.25 (m, 96 H, CH_2), 1.06-0.98 (m, 12 H, CH_2), 0.98-0.91 (m, 24 H, CH_2), 0.91-0.83 (m, 54 H, CH_3).

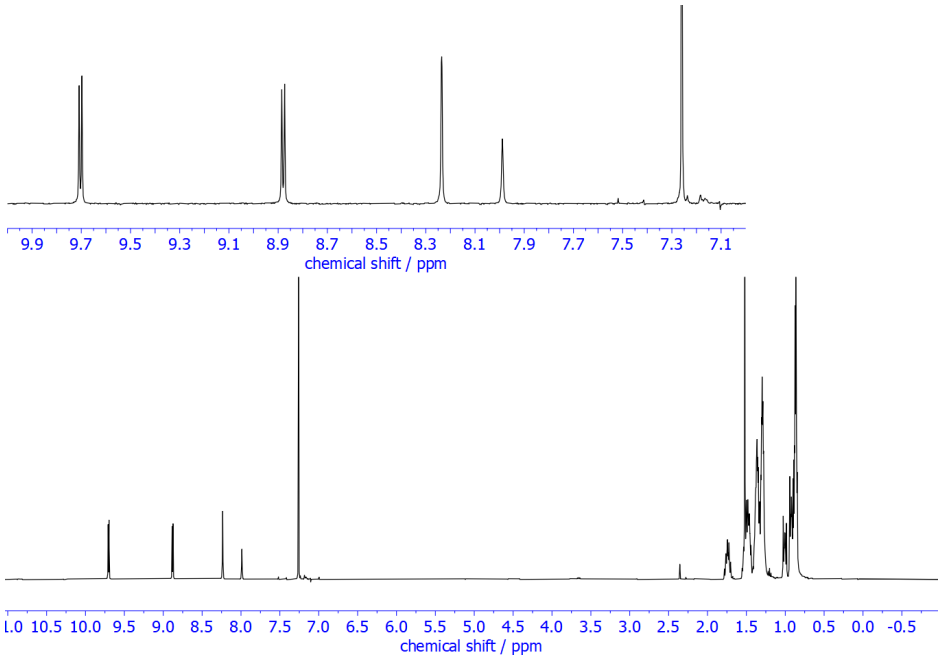

Figure 2.37: ^{1}H-NMR of ***l*-P1**.

***l*-P1$_{MD}$ and *l*-P1$_{FD}$[77]

***l*-P1** (863.4 mg, 0.380 mmol) was dissolved in CH_2Cl_2 (60 mL), chloroform (30 mL) and pyridine (7 mL). The solution was deoxygenated by bubbling argon through the solution. The solution was cooled in a water-ice bath and TBAF (570 μL, 1.0 M in THF) was added. The mixture was stirred and frequently monitored by TLC (petrol : CH_2Cl_2 20:1). As soon as the preferred ratio of deprotection was reached the reaction was quenched with acetic acid (4.2 μL) and the mixture was filtered through a short column of silica gel (CH_2Cl_2 with 1% pyridine). Separation by column chromatography on silica gel (gradient of petrol to petrol : CH_2Cl_2 10:1, always with 1% pyridine) yielded green waxy solids. (recovered ***l*-P1** 133 mg, 15.4%).

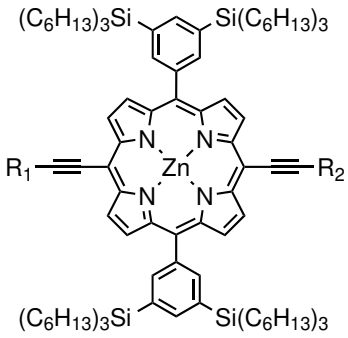

***l*-P1$_{MD}$**: R_1=H, R_2=H
***l*-P1$_{MD}$**: R_1=H, R_2=Si(C_6H_{13})$_3$

***l*-P1$_{MD}$**: (370 mg, 48 %).

^{1}H-NMR (400 MHz, $CDCl_3$) δ/ppm : 9.73 (m, 4H, H_β), 8.93 (m, 4H, H_β), 8.26 (m, 4H, Ar-H^{ortho}), 8.00 (m, 2H, Ar-H^{para}), 4.18 (s, 1H, CH), 1.76 (m, 6H, CH_2), 1.59-1.43 (m, 30 H, CH_2),1.43-1.22 (m, 84 H, CH_2), 1.06-0.98 (m, 6 H, CH_2), 0.98-0.90 (m, 24 H, CH_2), 0.90-0.84 (m, 45 H, CH_3).

MS (MALDI-ToF) m/z : 1989.0 (m/z_{calc} for $[M+H]^+$ 1987.5).

***I*-P1$_{FD}$**: (232 mg, 35 %).

^{1}H NMR (400 MHz, $CDCl_3$) δ/ppm : 9.75 (d, J = 4.8 Hz, 4H), 8.96 (d, J = 4.8 Hz, 4H), 8.27 (s, 4H), 8.01 (s, 2H), 4.19 (s, 2H), 0.86-1.50 (m, 156H).

MS (MALDI-ToF) m/z : 1703.02 (m/z_{calc} for $C_{108}H_{172}N_4Si_4Zn$ $[M+H]^+$: 1701.19).

I-P2[43,77]

***I*-P1$_{MD}$** (20 mg, 9.9 μmol) was dissolved in dry toluene (1 mL). $PdCl_2(PPh_3)_2$ (0.4 mg, 0.5 μmol), copper(I) iodide (1.0 mg, 5 μmol), and 1,4-benzoquinone (2.2 mg, 20 μmol) were dissolved in a mixture of dry toluene (1 mL) and dry $^iPr_2NH$ (0.5 mL) and added. The reaction was monitored by TLC. After 45 min, all ***I*-P1$_{MD}$ (THS)** had reacted. The volume was reduced and the mixture was filtered through a short column of silica gel (CH_2Cl_2 and 1 % pyridine). The mixture was passed through a SEC column (toluene). Recrystallisation of the dimer by layer addition (CH_2Cl_2 /methanol) yielded ***I*-P2 (THS)** (17 mg, 87 %).

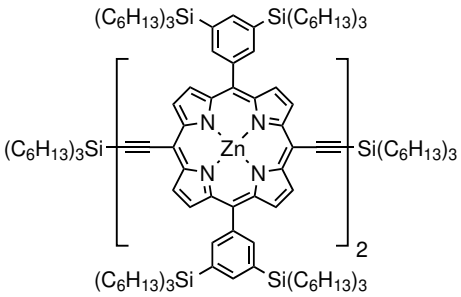

^{1}**H-NMR** (400 MHz, $CDCl_3$) δ/ppm : 9.94 (d, J = 4.7 Hz, 4H, H^{β}), 9.72 (d, J = 4.7 Hz, 4H, H^{β}), 9.00 (d, J = 4.7 Hz, 4H, H^{β}), 8.92 (d, J = 4.7 Hz, 4H, H^{β}), 8.30 (m, 8 H, Ar-H^{ortho}), 8.02 (m, 4 H, Ar-H^{para}), 1.83-1.70 (m, 12 H, CH_2), 1.57-1.46 (m, 60 H, CH_2), 1.44-1.23 (m, 168 H, CH_2), 1.08-1.00 (m, 12 H, CH_2), 1.0-0.92 (m, 48 H, CH_2), 0.92-0.85 (m, 90 H, CH_3).

MS (MALDI-ToF) m/z : 3974.4 (m/z_{calc} for $[M+H]^+$: 3972.9).

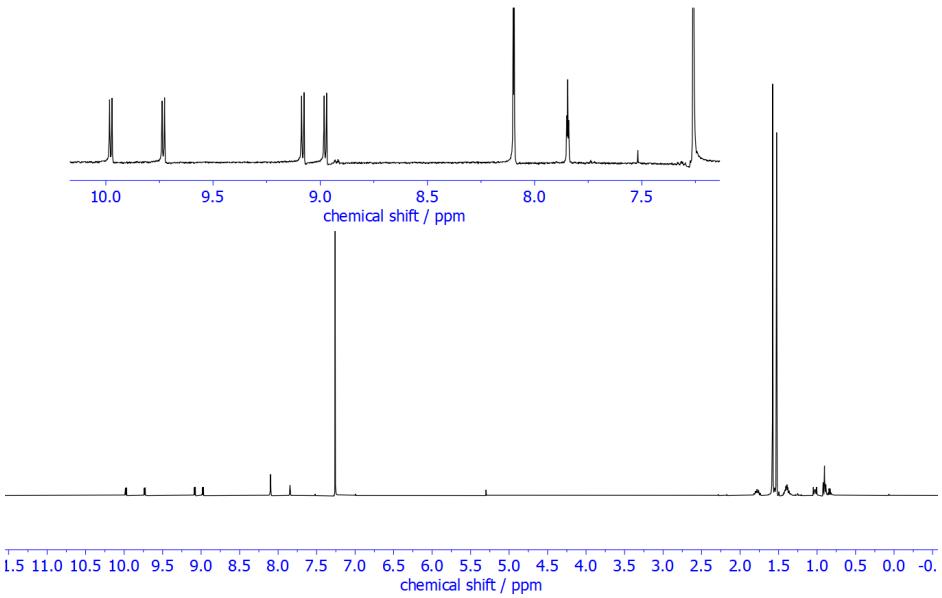

Figure 2.38: ^{1}H-NMR of ***l*-P2**.

***l*-P3**[43,77]

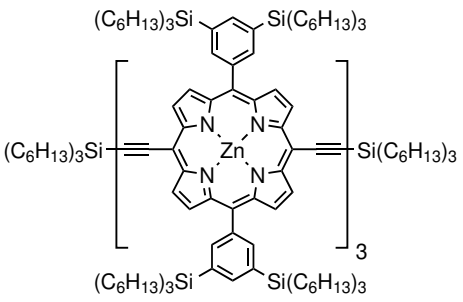

A mixture of ***l*-P1$_{MD}$** (300 mg, 150 µmol) and ***l*-P1$_{FD}$** (64 mg, 38 µmol) was dissolved in toluene (25 mL). $PdCl_2(PPh_3)_2$ (15.8 mg, 22 µmol), copper(I) iodide (43 mg, 220 µmol), and 1,4-benzoquinone (33 mg, 300 µmol) were dissolved in a mixture of toluene (10 mL) and DIPA (2.5 mL) and added. The mixture was stirred overnight at room temperature. The reaction mixture was concentrated and filtered through a short column of silica gel (CH_2Cl_2). The mixture was passed through a SEC column (toluene) and then the oligomers were separated by preparative GPC (toluene/pyridine 10/1). Recrystallisation of the GPC fractions by layer addition (CH_2Cl_2/methanol) yielded ***l*-P2** (66 mg, 22%), ***l*-P3** (37 mg, 9%).

^{1}H NMR (400 MHz, $CDCl_3$) δ/ppm: 9.95 (d, ^{3}J = 4.6 Hz, 4H; ArHβ), 9.94 (d, ^{3}J = 4.6 Hz, 4H; ArHβ), 9.72 (d, ^{3}J = 4.6 Hz, 4H; ArHβ), 9.02 (d, ^{3}J = 4.6 Hz, 4H; ArHβ), 9.01 (d, ^{3}J = 4.6 Hz, 4H; ArHβ), 8.91 (d, ^{3}J = 4.6 Hz, 4H; ArHβ), 8.35 (m, 4H; ArH$_{ortho}$), 8.31 (m, 8H; ArH$_{ortho}$), 8.05 (m, 2H; ArH$_{para}$), 8.03 (m, 4H; ArH$_{para}$), 1.83–1.70 (m, 12H; CH2), 1.60–1.46 (m, 84H; CH_2), 1.44–1.23 (m, 240H; CH_2), 1.08–1.00 (m, 12H; CH2), 1.0–0.92 (m, 72H; CH_2), 0.92–0.85 (m, 126H; CH_3).

MS (MALDI-ToF) *m/z* : calcd. M+ for $C_{360}H_{588}N_{12}Si1_4Zn_3$: 5674.08; found: 5674.1.

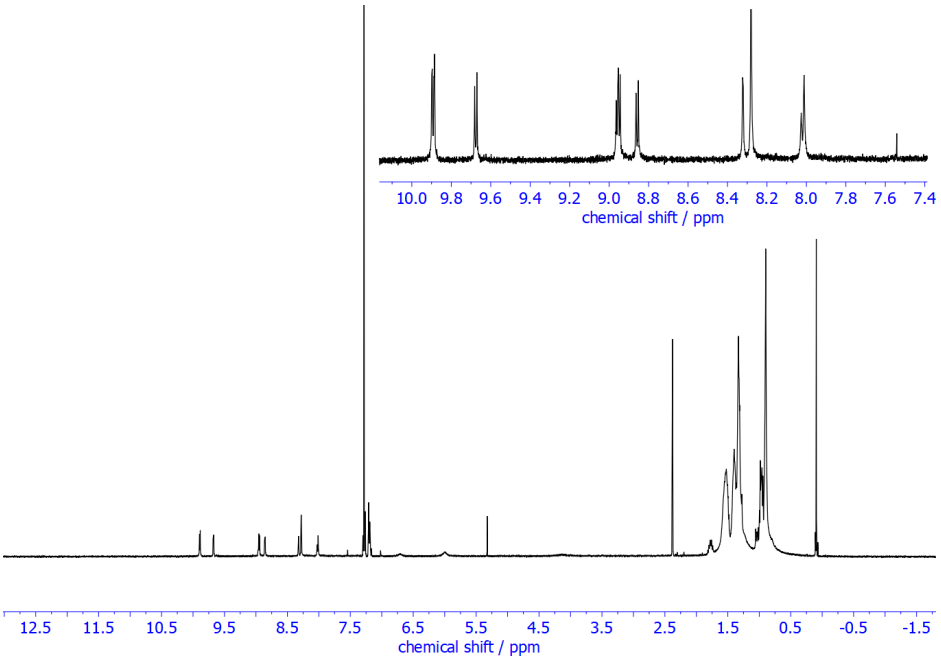

Figure 2.39: ^{1}H-NMR of ***l*-P3**.

***c*-P6•T6^{77,106}**

***l*-P1$_{FD}$** (200 mg, 0.12 mmol) and template **T6** (26 mg, 29 μmol) were dissolved in $CHCl_3$ (133 mL) by sonication for 2 h. A solution of $Pd(PPh_3)_2Cl_2$ (27 mg, 39 μmol), copper(I) iodide (37 mg, 0.19 mmol) and 1,4-benzoquinone (89 mg, 0.80 mmol) in $CHCl_3$ (18 mL) and DIPA (0.25 mL) was added to the porphyrin mixture at r.t. The mixture was stirred at r.t. overnight, open to air. The reaction mixture was partially concentrated and passed over a plug of alumina ($CHCl_3$). The mixture was purified by SEC (toluene) to remove benzoquinone, then passed over another alumina plug to remove polymer (toluene + 1% pyridine). Purification by preparative recycling GPC (toluene + 1% pyridine) afforded ***c*-P6•T6** (78 mg, 36%) as a brown solid.

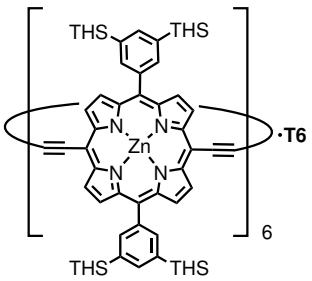

^{1}**H NMR** (400 MHz, $CDCl_3$) δH, ppm: 9.54 (d, J = 4.2 Hz, 24H), 8.72 (d, J = 4.2 Hz, 24H), 8.30 (bs, 12H), 7.98 (bs, 12H), 7.97 (bs, 12H), 5.52 (d, J = 8.5 Hz, 12H), 5.45 (d, J = 8.5 Hz, 12H), 4.98 (d, J = 6.1 Hz, 12H), 2.41 (d, J = 5.8 Hz, 12H), 1.54–1.41 (m, 144H), 1.41–1.17 (m, 432H), 0.98–0.77 (m, 360H)

MS (MALDI-TOF) m/z: calc. M+ for $C_{720}H_{1068}N_{30}Si_{24}Zn_6$: 11211; found: 11207.

***c*-P6^{77,106}**

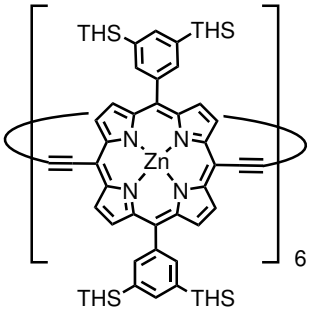

***c*-P6•T6** (5.4 mg, 0.48 µmol) was dissolved in CH_2Cl_2 (5 mL) and trifluoroacetic acid (50 µL, 0.65 mmol) was added. The mixture was stirred for 5 min. at room temperature then pyridine (0.5 mL) was added and the mixture was immediately filtered over a short column of silica gel (CH_2Cl_2). Removing the solvent yielded a green solid. The solid was dissolved in CH_2Cl_2 (10 mL) and a solution of $Zn(OAc)_2 2H_2O$ (50 mg, 228 µmol) in methanol (2 mL) was added. The mixture was stirred over night at room temperature then filtered through a short column of silica gel (CH_2Cl_2). Recrystallization by layer addition (CH_2Cl_2/methanol) yielded ***c*-P6** (4.9 mg, 100 %) as a brown solid.

^{1}H NMR (400 MHz, $CDCl_3$) δH, ppm: 9.67 (d, J = 4.6 Hz, 24H), 8.81 (d, J = 4.6 Hz, 24H), 8.16 (m, 24H), 7.91 (m, 12H), 1.50–1.37 (m, 144H; CH2), 1.37–1.12 (m, 432H; CH2), 0.94–0.84 (m, 144H; CH2), 0.84–0.72 (m, 216H; CH3).

MS (MALDI-TOF) m/z: calc. M+ for $C_{648}H_{1020}N_{24}Si_{24}Zn_6$: 10214; found: 10211.

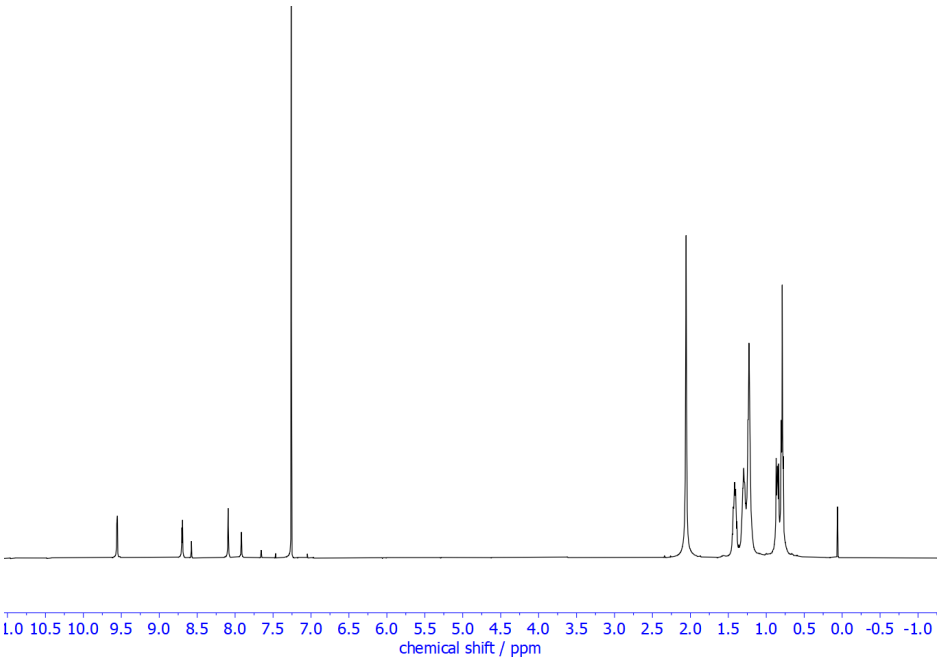

Figure 2.40: ^{1}H-NMR of ***c*-P6**.

3

Titration Experiments and Exploration of Binding Models

Contents

3.1 Abstract

Reliable design of synthetic supramolecular assemblies requires the precise prediction of thermodynamic properties. Especially for large multivalent systems, where the highly organised intramolecular complex competes with an intermolecular one, a potent way to predict chelate cooperativity is not straight-forward. Here, we used the host-guest library presented in Chapter 2 (Fig. 3.1) to explore the relationship between chelate cooperativity strength and molecular structures.

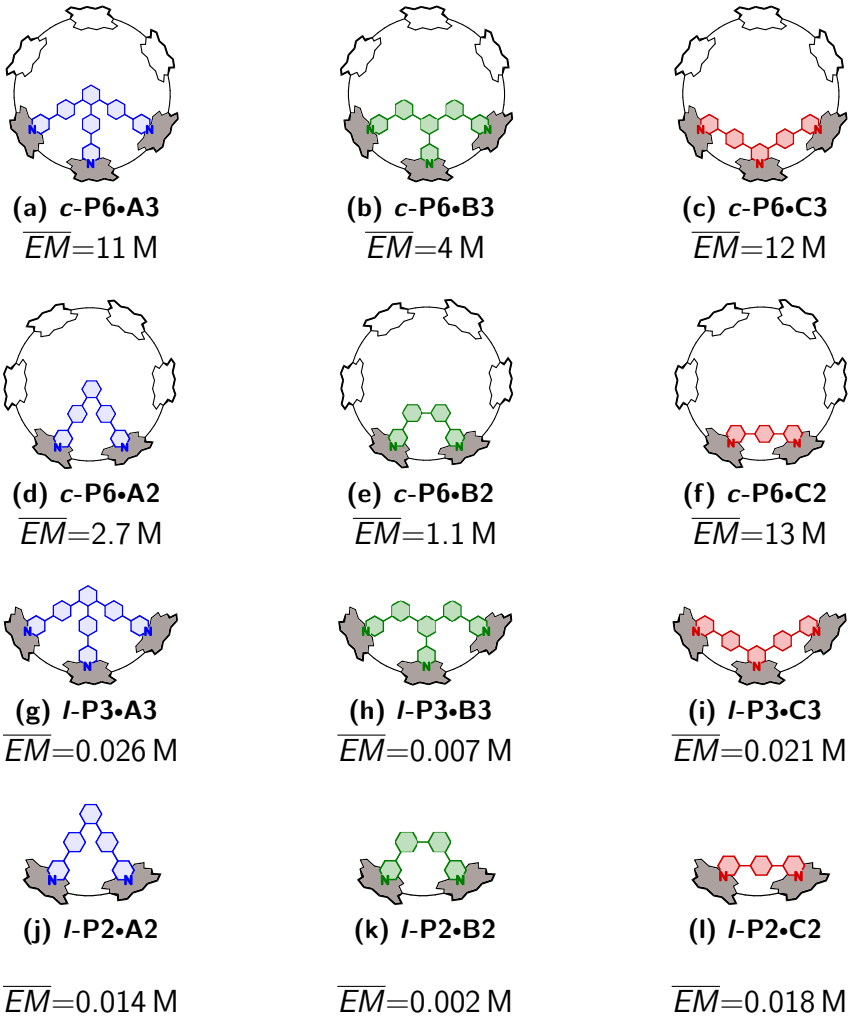

Figure 3.1: Comparison of the experimentally determined effective molarities (EM). 298 K, toluene, Ar=tBu as solubilising group.

As a quantification parameter, effective molarities were determined via binding constants derived by UV-vis-NIR titrations. Direct determination for association constants was only possible for the linear divalent host (***l*-P2**), while binding constants for the strongly bound

systems were determined via competition experiments. Due to the formation of higher order complexes (up to 1:3), different binding models were compared to determine the formation constant. The experimentally determined $\overline{EM}$ values showed the expected trend for guest series **A** and **B**. However, guest series **C** exhibits a surprisingly strong chelate cooperativity, which contradicts the molecular structure design approach. Therefore, we concluded that a prediction based on molecular structure is not sufficient and additional dependencies needs to be explored.

3.2 Introduction

Chelate cooperativity is an effect arising from the presence of two or more intramolecular binding interactions involving a polyvalent host and guest. It is assumed that the initial binding event preorganises the other binding sites on the polyvalent ligand for binding and thereby favours the second binding event. Thermodynamically, the first binding event combines the two components into one, and restricts the total number of (translational) degrees of freedom. Any additional binding in this combined component does not require further loss of translational degrees of freedom, as any further interaction occurs intramolecular.[7,12] However, entropic contributions are difficult to partition. Experimental attempts to quantify the loss of translational degrees of freedom vary considerably, are highly dependent on the medium, and changes in entropy cannot be determined directly.[112] The entropic contributions of rotational and vibrational degrees of freedom are generally smaller than for translational degrees of freedom.[113] For intramolecular processes with multiple anchor points, the sum of rotational and vibrational restrictions can add up to significantly affect the binding energy.[114,115]

The host-guest systems in this study are derived from the famous ***c*-P6•T6** complex (Fig. 3.2a), exhibiting one of the highest effective molarities ($\overline{EM} = 180$ M) reported to date for supramolecular systems.[40,76] Due to the high effective molarities, an 'all-or-nothing' behaviour is observed, meaning that a multivalent ligand is only bound with all binding sites and partially bound intermediates are not formed in significant concentrations. The explanation for this strong chelate cooperativity is based on molecular structure design rules; high preorganisation, rigidity and the favourable entropy of the binding process are thought to cause this strong complexation. Contradicting the molecular structure approach

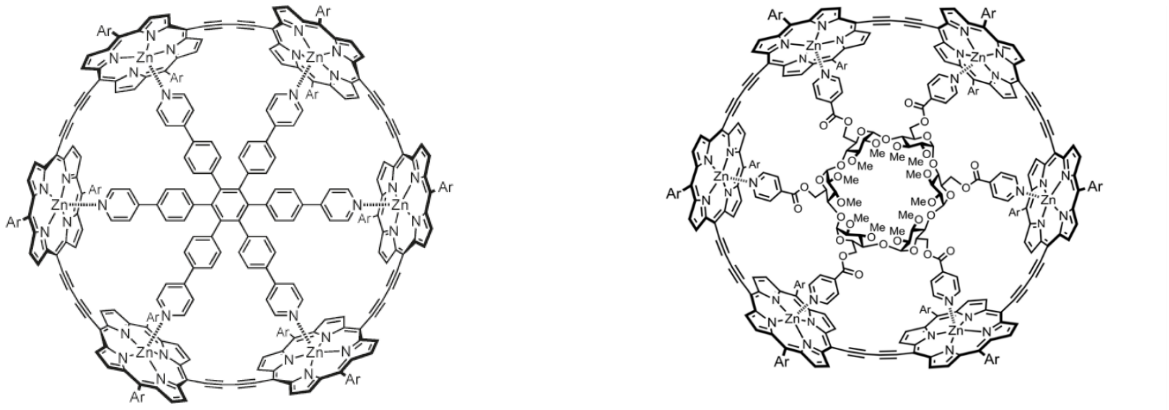

(a) ***c*-P6•T6**[40,76] **(b)** ***c*-P6•T6***[42,116]

Figure 3.2: Illustration of the discussed complexes ***c*-P6•T6** and ***c*-P6•T6***, Ar is an aromatic solubilising group.

is the finding of a recent study. This has shown that a higher flexibility in the core of the template has a surprisingly small effect on the binding affinity. The more flexible template (Fig. 3.2b) still exhibits a strong binding constant of $K_f \approx 10^{29}$ M^{-1} ($\overline{EM} = 74$ M).[42,116]

The presented systems are an ideal model to study chelate cooperativity in the absence of other effects. Previous studies have proven the absence of any allosteric effects, since binding one porphyrin centre does not electronically affect the binding strength of another porphyrin centre. This is equally true for the guest molecule.[39,43,44] All guests were optimised to fit into the ***c*-P6** binding pocket. The guests were designed to analyse the stepwise effective molarities independently (see Chapter 1). Based on the work done by Hogben *et al.*, it seems reasonable that enthalpic contributions to the cooperativity can be neglected and all differences observed in Gibbs energy are of entropic origin. Therefore, the question arises if effective molarities can be used as an reasonable estimate of cooperativity.

An important feature related to cooperativity is the degeneracy of bound states affecting entropy. This is illustrated by the example of the hydrogen-bonded tetramer with nucleic acid base-pairs studied by González-Rodríguez and coworkers. The cooperativity strength of this tetramer is with an $\overline{EM}$ value of 860 M is impressively high for a non-covalently bound system.[38] A comparison of a symmetric and an unsymmetric binding motif of this tertamer has shown that the unsymmetric derivative demonstrates higher stabilities due to the higher number of degenerated states.[41]

Therefore, an accurate and consistent evaluation of cooperative effects requires the determination of the degeneracy of bound states which are affecting the apparent binding

constant. As the example of a divalent host binding two monovalent guests illustrates, the probability of the first guest binding to either side is four times as high as for the second guest (Fig. 3.3). The scenario can be adapted to a divalent guest, binding stepwise to a divalent host.

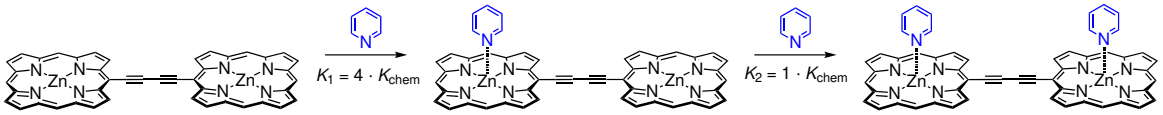

Figure 3.3: Illustration of statistical impacts of a divalent host binding two monovalent guests.

To quantify the cooperativity strength, the differences arising from statistical factors between the cooperative host-guest-system and the reference need to be eliminated. The experimentally accessible apparent binding constant K_{app} and the intrinsic binding constant K_{chem} are related via a statistical factor K_σ. The relationship is illustrated in Equation 3.1. Dividing the apparent stability constant by the statistical entropic component (K_σ), the experimental binding constant can be translated into a comparable quantity (*e.g.* K_{chem}).

$$a\,\mathrm{A} + b\,\mathrm{B} \overset{K_{app} = K_\sigma K_{chem}}{\rightleftharpoons} c\,\mathrm{C} + d\,\mathrm{D} \tag{3.1}$$

It is generally accepted that the determination of statistical factors in host-guest chemistry and self-assembly processes is of great importance when evaluating the absence or presence of cooperative effects. However, several different approaches to calculate statistical factors have been reported in literature. The most commonly used are Benson's symmetry number method[117,118] and the direct-count method by Bishop and Laidler.[119] The symmetry number method uses the following equation:[117,120]

$$K_\sigma = \frac{\sigma_{reactants}}{\sigma_{products}} = \frac{\sigma_{\mathrm{A}}^{a}\sigma_{\mathrm{B}}^{b}}{\sigma_{\mathrm{C}}^{c}\sigma_{\mathrm{D}}^{d}} \tag{3.2}$$

The individual symmetry numbers (σ) comprises the external (σ_{ext}), and the internal (σ_{int}) symmetry number. The former is calculated from the point group of the molecule and its internal symmetry number (σ_{int}). The latter is calculated from the number of degenerate internal rotors.

The external symmetry number is defined as the number of different, but indistinguishable atomic arrangements, which can be obtained by rotating the given molecule as a whole.

Table 3.1: Correlation of Symmetry and external symmetry number.

Point Group	σ_{ext}
C_1, C_i, C_s, $C_{\infty v}$	1
C_n, C_{nv}, C_{nh}, S_{2n}	n
$D_{\infty h}$	2
D_n, D_{nd}, D_{nh}	$2n$
T_d	12
O_h	24
I_h	60

Therefore, the external symmetry number can be directly related to the point group of the molecule (Table 3.1).

Correspondingly, the internal symmetry number is defined as the number of atomic arrangements that can be obtained by internal rotations around single bonds. It has been argued by Monahan[121] and DeTar[122] that internal rotations should only be considered if the rotation barrier is close to RT.[123] However, if the time scale of the measurement determining the equilibrium is much slower than the time scale of internal rotations, all conformational isomers can be accessed and therefore all internal rotations contribute to the partition function independent of the barrier height of the internal rotations.[124] By such a procedure the partition function for hindered rotation is inversely proportional to σ_{int}.

There are often many rotations that give equivalent structures, but only the rotations that are changed by the complex formation affect K_σ. The rotations that are unaffected by the binding processes are identical in the bound and unbound state and cancel each other out.[39]

Similar to determining the internal rotations, another issue is encountered for dynamic fluxional molecules, such as NH_3. Analogous to σ_{int}, a fluxional symmetry number σ_{flux} must be considered, defined as the the number of different, but indistinguishable atomic arrangements that can be obtained by intramolecular dynamic processes (*e.g.* inversion and pseudorotation).[124] For reactions involving a mixture of different isomers (i), an apparent symmetry number must be determined using the symmetry numbers of the individual isomers (σ_i):[124]

$$\sigma_{app} = \frac{1}{\sum_i \frac{1}{\sigma_i}} \tag{3.3}$$

If all isomers show the same symmetry number, the apparent symmetry number is the symmetry number of the isomers (σ) divided by the number of isomers (n):

$$\sigma_{app} = \frac{\sigma}{n} \tag{3.4}$$

Bishop and Laidler[119] suggested a direct count method, where the number of microspecies in an equilibrium is counted. Considering an equilibrium reaction of two components (A and B) forming two products (C and D); l is the number of chemically plausible different sets (microspecies) of C + D that can be formed if all identical atoms in A and B are labelled, and r as the number of chemically plausible different sets of A + B that can be formed if all identical atoms in C and D are labelled.

$$a\,\mathrm{A} + b\,\mathrm{B} \overset{K_\sigma = l/r}{\rightleftharpoons} c\,\mathrm{C} + d\,\mathrm{D} \tag{3.5}$$

Bishop and Laider state that the statistical factor for an equilibrium is given as the ratio of l and r and proved that the ratio l/r is equal to the ratio of symmetry numbers, $\sigma_A\sigma_B/\sigma_C\sigma_D$. If the stoichiometry of the starting materials and the products differs from 1, a (factorial) correction for the redundancy of microspecies must be considered.

Both methods result in the same statistical factors. While the symmetry number method delivers an easy and fast evaluation of statistical factors, the results can be counterintuitive. In complicated host-guest systems with higher stoichiometries, both methods should be used to validate the determined factors.

Here, we use the host-guest systems presented in Chapter 2 to study chelate cooperativity isolated from allosteric effects. The host-guest systems are designed to evaluate the cooperative effect of each binding site by determination of the stepwise *EM* values. We start with the determination of statistical factors. All presented binding constants are determined via UV-vis-NIR titrations and, in contrast to previous studies, obtained via multi-wavelength analysis. Association constants for the complexes of monovalent ligands are determined, used as a reference to evaluate cooperativity. This is followed by the determination of the association constants for the multivalent, intramolecular complexes. Different binding models and ways to analyse the data are discussed and the statistical significance is compared between different options. Finally, the effective molarities are determined and discussed.

3.3 Experimental Methods

The porphyrin compounds were prepared as described in Chapter 2. All porphyrin compounds in this chapter contain *tert*-butyl (tBu) solubilising groups on the *meso*-aryls. Experiments were performed under very dilute conditions (10^{-6} M). The UV-vis-NIR titration experiments were performed at 298 K and toluene was used as solvent. The spectra were recorded using a Perkin-Elmer Lambda 20 spectrometer with a 1 cm quartz cuvette.

All titration experiments were conducted using a constant total host concentration. The advantage of a constant host concentration is that isosbestic points - wavelengths at which different species exhibit identical absorption coefficients - can be determined easily. These points indicate that very few species are involved in the titration process as the probability of observing an isosbestic point decreases drastically as the number of species increases.

The absorption spectra were analysed via non-linear regression using a global analysis multiple regression to model the entire spectrum simultaneously (ReactLab EQUILIBRIA software by Jplus Consulting). This allowed us to determine both the binding constants (expressed as $\log(K_f)$) and the various species involved in the equilibrium processes. Different reasonable models were tested and the best matching fit was determined via a statistical approach (extra sum-of-squares F test)[125] and the Akaike information criterion.[126] The models used to analyse the individual titrations are described in each section.

3.4 Calculation of Statistical Factors

For host-guest systems forming 1:1 complexes, without significant formation of any partially bound species, the determination of the statistical factors is straight-forward. Benson's symmetry number method was used to determine the symmetry numbers of the individual components involved in the 1:1 complexes (see Table 3.2).

The determination of statistical factors for host-guest systems with higher stoichiometries is challenging, due to the high number of microspecies involved. For the tridentate guests, a 1:1 and a 1:2 complex can be formed. Similarly, the denaturation process can be stepwise as one of the two multivalent guests can be exchanged by three monovalent ligands while the second multivalent guest remains in the complex. For the symmetry number method, a schematic thermodynamic cycle is shown in Figure 3.4a. By forming the 1:1 complex, the

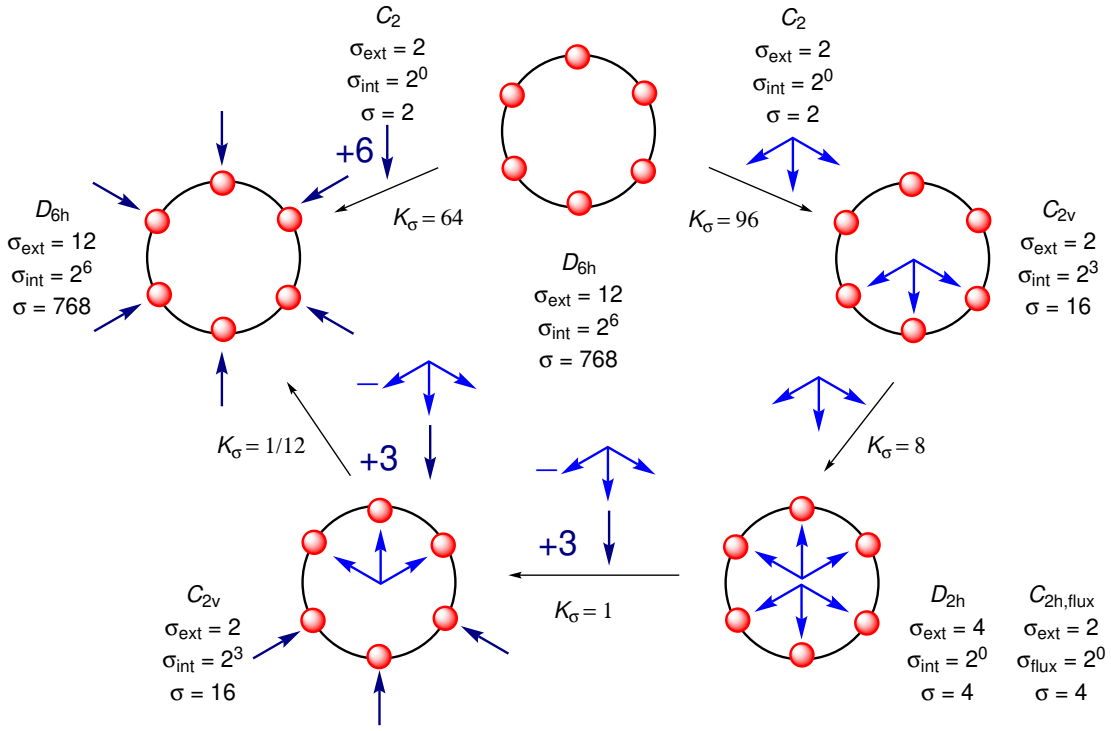

(a) Symmetry Number Method

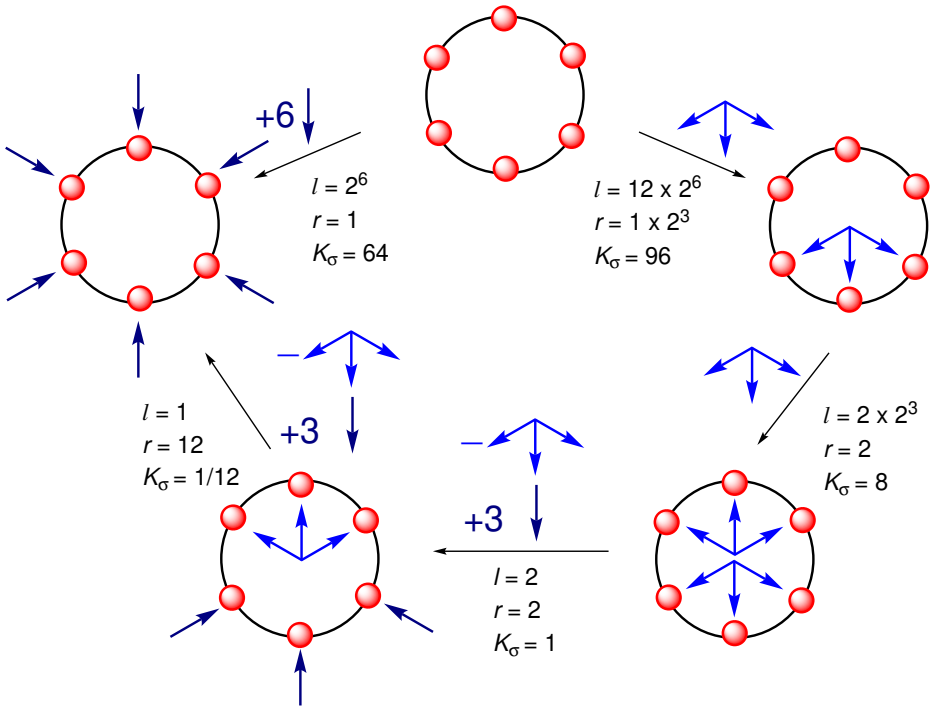

(b) Direct Count Method

Figure 3.4: Statistical factors for the thermodynamic cycle for the tridentate ligands binding to ***c*-P6**.

Table 3.2: Internal, external and total symmetry numbers for each component. (The internal rotations unaffected by the complex formation are ignored.)

Component	Point group	σ_{ext}	σ_{int}	Free rotations	σ
C1	C_1	1	1	0	1
py, **A1**, **B1**	C_{2v}	2	1	0	2
A2, **B2**, **C2**	C_2	2	1	0	2
A3, **B3**, **C3**	C_2	2	1	0	2
***l*-P1**	D_{2h}	4	1	0	4
***l*-P2**	D_{2h}	4	2	1	8
***l*-P3**	D_{2h}	4	4	2	16
***c*-P6**	D_{6h}	12	64	6	768
***l*-P1•C1**	C_1	1	2	1	2
***l*-P1•A1**, ***l*-P1•B1**, ***l*-P1•py**	C_{2v}	2	2	1	4
***l*-P2•A2**, ***l*-P2•B2**, ***l*-P2•C2**	C_{2v}	2	1	0	2
***l*-P3•A3**, ***l*-P3•B3**, ***l*-P3•C3**	C_{2v}	2	1	0	2
***c*-P6•A2**, ***c*-P6•B2**, ***c*-P6•C2**	C_{2v}	2	16	4	32
***c*-P6•A2$_2$**, ***c*-P6•B2$_2$**, ***c*-P6•C2$_2$**	C_{2v}; D_{2h}	2; 4	4	2	16/3
***c*-P6•A2$_3$**, ***c*-P6•B2$_3$**, ***c*-P6•C2$_3$**	D_{3h}	6	1	0	6
***c*-P6•A2$_2$py$_2$**, ***c*-P6•B2$_2$py$_2$**, ***c*-P6•C2$_2$py$_2$**	C_{2v}; D_{2h}	2; 4	4	2	16/3
***c*-P6•A2py$_4$**, ***c*-P6•B2py$_4$**, ***c*-P6•C2py$_4$**	C_{2v}	2	16	4	32
***c*-P6•A3**, ***c*-P6•B3**, ***c*-P6•C3**	C_{2v}	2	8	3	16
***c*-P6•A3$_2$**, ***c*-P6•B3$_2$**, ***c*-P6•C3$_2$**	D_{2h}	4	1	0	4
***c*-P6•A3py$_3$**, ***c*-P6•B3py$_3$**, ***c*-P6•C3py$_3$**	C_{2v}	2	8	3	16
***c*-P6•py$_6$**	D_{6h}	12	64	6	768

symmetry of the D_{6h} ***c*-P6** nanoring is decreased to C_{2v}. The binding of the second guest increases the symmetry again to D_{2h}. As a result, the binding of the first ligand is 12 times more likely than the second binding event. Denaturating the 1:2 complex with a monovalent ligand decreases the statistical factor again by forming a complex with a higher stoichiometry. Replacing the last multivalent guest with three monovalent guests restores the D_{6h} symmetry.

The schematic model gives the same statistical factors as the actual molecular structures for the guests **B3** and **C3**. However, the ***c*-P6•A3** complex loses the D_{2h} symmetry due to the ligand overlap, forming a 1:2 complex in C_{2h} symmetry (Fig. 3.5). Both isomers interconvert, increasing the symmetry to an effective planar D_{2h} symmetry. This is represented with the fluxional symmetry number σ_{flux} of 2 for both isomers. Therefore, all tridentate ligands show the same symmetry numbers for the 1:1 and 2:1 complexes as well as the denaturation intermediates.

The direct count method was also used (Fig. 3.4b). As the molecular geometry can

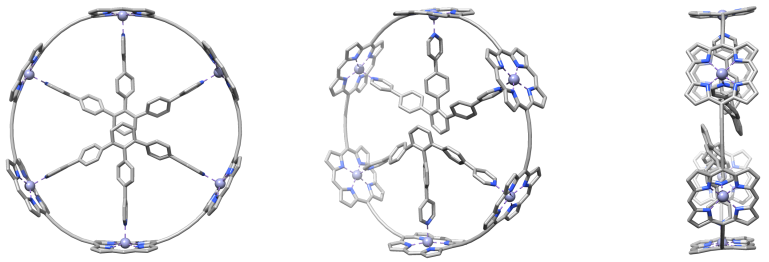

Figure 3.5: Different perspectives of the ***c*-P6•A3$_2$** complex. Binding the second guest breaks the D_{2h} symmetry.

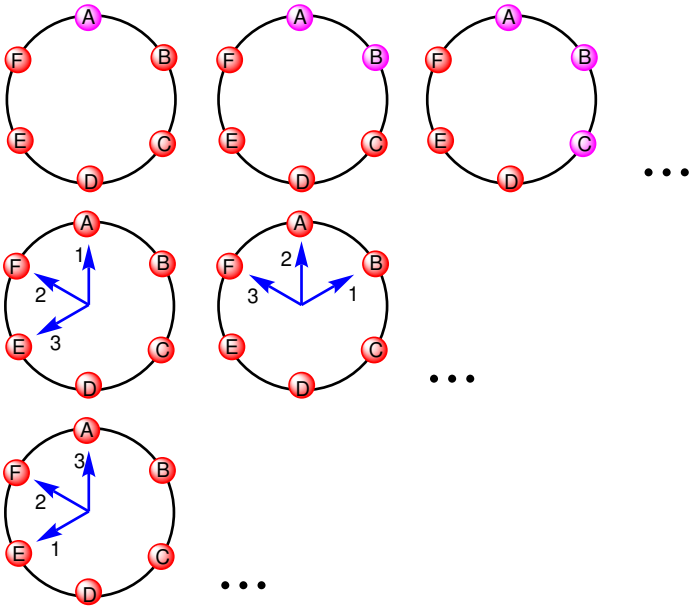

Figure 3.6: Illustration of possible microspecies of ***c*-P6** and binding positions for a tridentate ligand.

be neglected for the direct count method, the analysis of the schematic representation is sufficient. Analysing the first reaction step, the number of all microspecies formed in the forward direction is 768. By labelling all atoms in the molecule, each porphyrin provides two binding sides (Fig. 3.6), resulting in 2^6 arrangements of all porphyrin units, meaning every porphyrin can be up (red) or down (pink). The first tridentate ligand can bind in 12 different combinations (6 binding sites times two faces) to the six porphyrin units. Marking each porphyrin alphabetically emphasises the different binding combinations; from the three binding positions a tridentate has, the two outer ones can bind to each of the six porphyrin units. Therefore, the total number for l in this reaction step is the product of 12 and 2^6. The backwards reaction (r) involves 2^3 different microspecies, namely all combinations of up and down of the three unbound porphyrin units. As a result, the statistical factor

for this reaction is 96. The same approach can be used for the second ligand forming the ***c*-P6•X$_2$** complex, which gives 8 as the statistical factor.

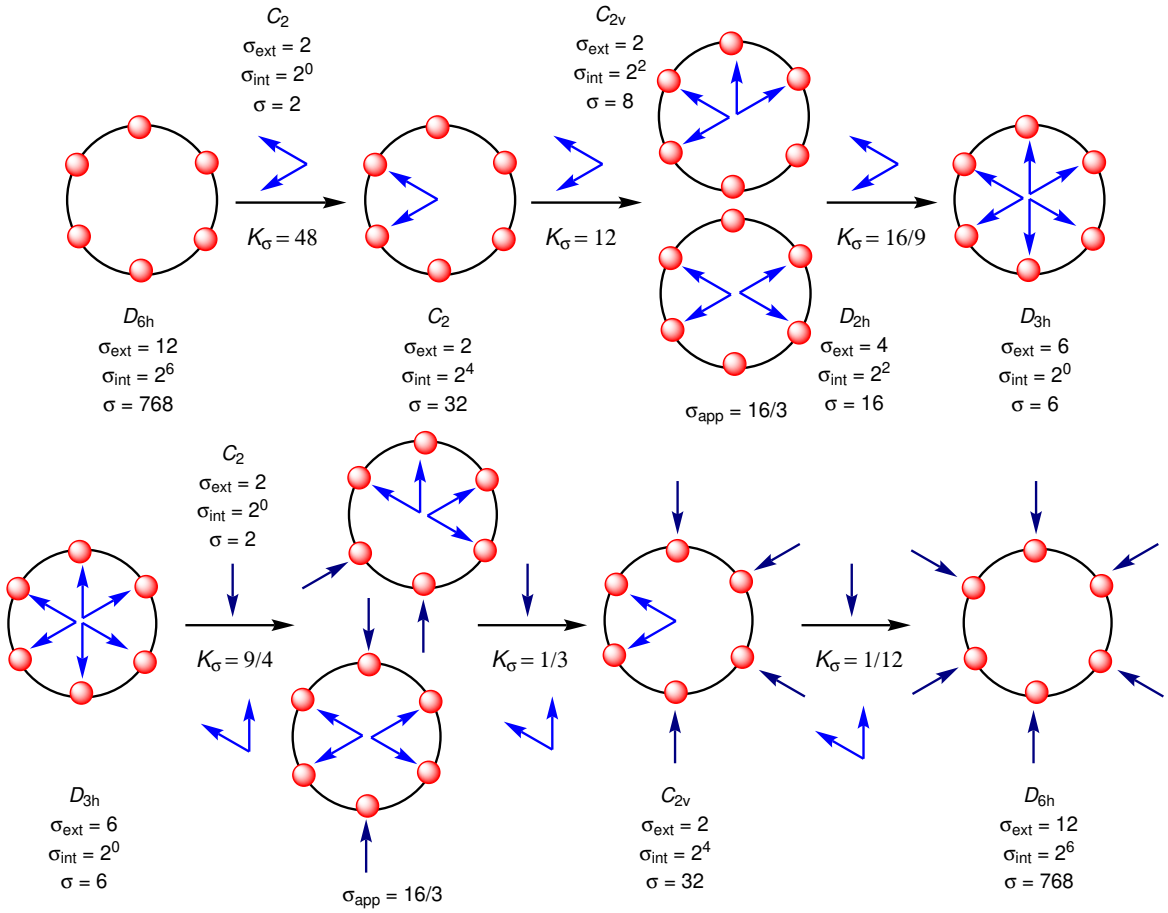

Figure 3.7: Symmetry numbers for ***c*-P6** and the bidentate ligands.

Introducing a competing monovalent guest increases the number of species. It should be noted that a monovalent ligand can be positioned inside or outside. Due to the free rotation of the porphyrin units, the resulting 8 different microspecies are equivalent to each other within the time-scale of the experiment. Therefore, the forward reaction of the first denaturation step involves two species, identical to the backward reaction. The same procedure is used for the second denaturation step.

Both methods are in agreement and result in the same statistical factors for the individual species. For the analysis of the bidentate ligands, the symmetry number method alone was used, as more steps are involved in the thermodynamic cycle. Extending the procedure described above for the tridentate ligands, a schematic representation with an effective planar symmetry through all six zinc centres (for the sterically demanding ligand) is reasonable. The schematic thermodynamic cycle is shown in Figure 3.7. The

formation of the 1:1 complex is four times more likely than the formation of the 1:2 complex, due to the formation of several species and the decreasing symmetry in the first binding step. With the 1:2 complex, two different isomers are possible with different symmetry numbers. By binding the third ligand, higher symmetry is restored (D_{3h}), resulting in an decreased likelihood to form the 1:3 complex. The first denaturation step also forms two isomers, which influences the statistical factor.

An overview of all statistical factors for the individual components is shown in Table 3.2. These numbers were used to determine the overall statistical factors for the individual reaction steps.

3.5 Determination of Reference Binding Strength

3.5.1 Linear porphyrin oligomers

Binding constants for the non-cooperative reference system were determined via the porphyrin monomer ***l*-P1**, with tBu solubilising groups and THS protection groups on the acetylenes, and the cyclic host ***c*-P6**, with tBu solubilising groups, in combination with the monodentate guests **A1** and **C1**. The binding constant for pyridine binding to each host was also determined. As previously reported, binding a monovalent ligand to one porphyrin unit in an oligomer does not influence the binding strength of the remaining poprhyrin units.[20] The UV-vis-NIR titration of ***l*-P2** binding the monovalent ligand quinuclidine shows no isosbestic points, and therefore provides enough information to separate the first and second binding constant. This experiment verifies the absence of allosteric effects for the linear oligomers and the same behaviour can be expected for cyclic oligomers.[20]

For the porphyrin monomer ***l*-P1** host, the analysed data of the individual titrations are shown in Figure 3.8. Each titration experiment was analysed using a multiwavelength, multivariant global fit using a simple 1:1 binding model. The experimental matrix of absorbances can be deconvoluted into different spectral components and a concentration profile. By conducting a titration experiment with known total concentrations of the host and the guest at any point, the concentration-dependent change in the absorption spectra can be used to determine the individual components contributing to the total absorption. Therefore, the molar absorptivity for each species at each measured wavelength can be determined.

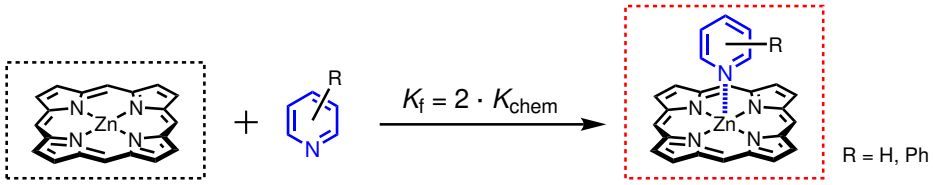

(a) Titration experiment for ***l*-P1** and a monovalent guest.

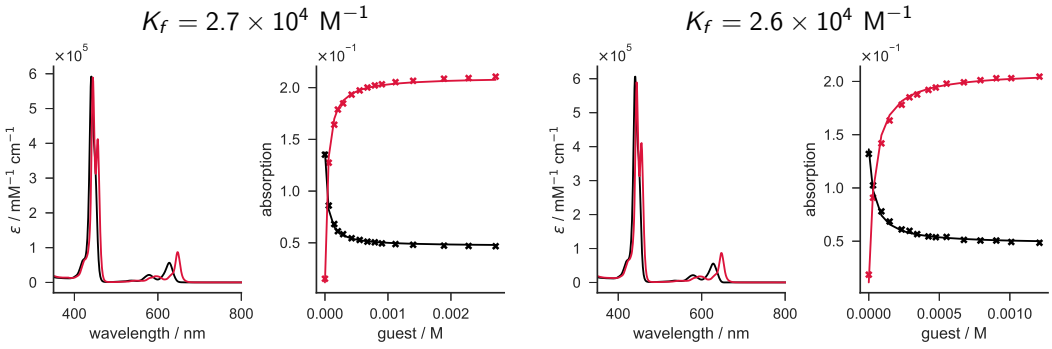

(b) First formation of ***l*-P1•py**

(c) Second formation of ***l*-P1•py**

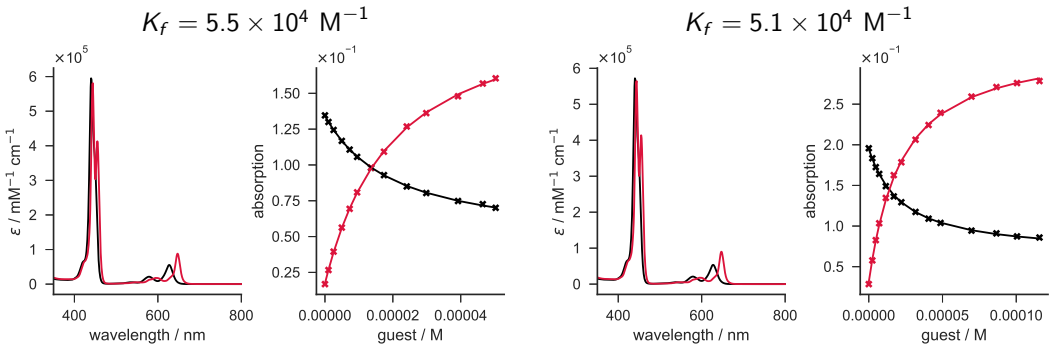

(d) First formation of ***l*-P1•A1**

(e) Second formation of ***l*-P1•A1**

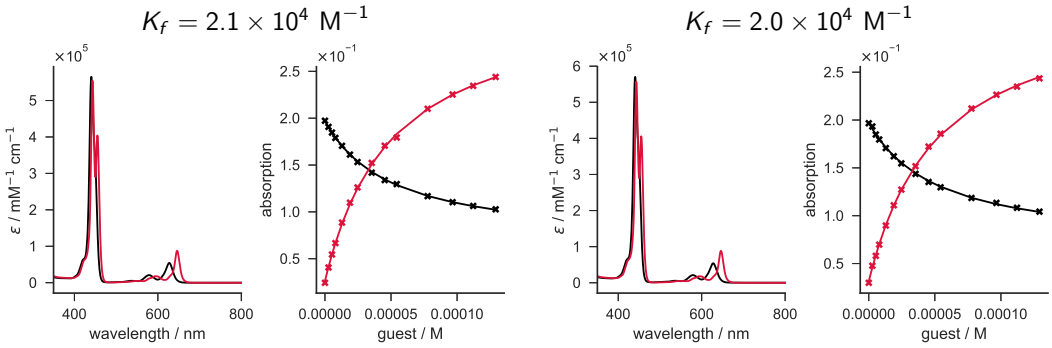

(f) First formation of ***l*-P1•C1**

(g) Second formation of ***l*-P1•C1**

Figure 3.8: Multivariant global fit results of two UV-vis-NIR titration experiment showing the single components of the absorption spectra (unbound host in black, host-guest complex in red) and the experimental point and the fitted binding isotherm of two characteristic wavelengths (629 nm in black, 646 nm in red), respectively. (toluene, 298 K, [***l*-P1**] = 2.48 µM).

In addition to the calculated extinction coefficients, the binding constant(s) relating the host and guest concentration are calculated by iteratively solving a non-linear regression problem. The presented data analysis shows the two coloured components contained in the titration data (unbound host in black, host-guest complex in red) and the experimental points in comparison with the fitted binding isotherm at two characteristic wavelengths (629 nm in black, 646 nm in red).

3.5.2 Cyclic porphyrin oligomer

The determination of binding constants for the multivalent host ***c*-P6** is more complicated. Since all monovalent guests show a relatively weak binding strength, all possible complexes are formed in the process (*e.g.* ***c*-P6•py**, ***c*-P6•py$_2$**, ***c*-P6•py$_3$**, ***c*-P6•py$_4$**...). As determined for the linear oligomers, we expect the individual statistically corrected binding constants to be identical. There are no sharp isosbestic points observed in the titration, indicating that the absorption spectra of partially bound complexes are not exactly a linear combination of free and fully bound species. Different methods can be used to determine the binding constant. The simplest model would treat the individual porphyrin faces as fully independent and therefore the change in absorption additive upon complex formation. Therefore, the actual host concentration can be multiplied with the number of binding sites, treating the system as six porphyrin monomers. The binding isotherm related to this model sufficiently reproduces the experimental data (Fig. 3.9a) and the binding constant is very close to the monomer binding constant ($K_{chem} = 1.5 \times 10^4$ M^{-1}).

A similar binding constant can be obtained by fitting one statistically corrected binding constant, in a system of linear equations describing each complex with the apparent binding constant. The statistical factors for the formation of all multivalent complexes are shown in Figure 3.10a. Thereby, two options are possible: the spectra can be expressed as a linear combination of the absorption spectra of the unbound and the fully bound complex (*e.g.* the final spectrum of the titration) or the spectra can be optimised independently. Determining the binding constant with the linear combination of spectra gives a slightly higher binding constant and a higher least-square error (Fig. 3.9b). The increased fitting error despite the number of fitted parameters remaining constant indicates that the change in absorption of the individual species is non-linear.

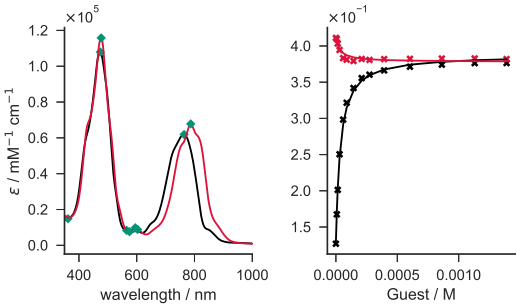

(a) Host concentration correction by multiplication with binding sites ($K_{chem} = 1.5 \times 10^4$ M^{-1})

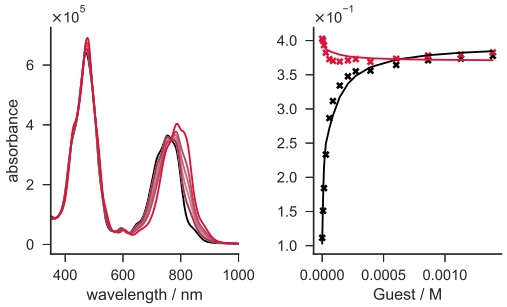

(b) Identical binding interactions, spectra as a linear combination ($K_{chem} = 2.5 \times 10^4$ M^{-1})

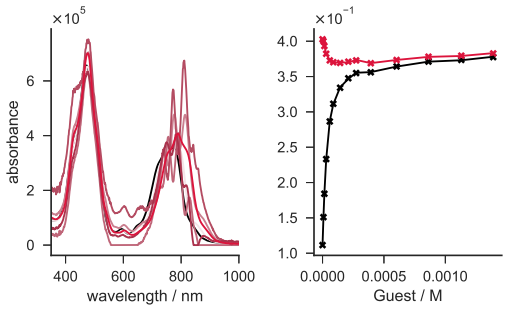

(c) Identical binding interactions, independent spectra ($K_{chem} = 1.6 \times 10^4$ M^{-1})

Figure 3.9: Comparison of different binding models to analyse the ***c*-P6•py** UV-vis-NIR titration experiment, showing the single components of the absorption spectra (unbound host in black, host-guest complex in red) and the experimental point and the fitted binding isotherm of two characteristic wavelengths (758 nm in black, 820 nm in red), respectively. (toluene, 298 K, [***c*-P6**] = 1.11 µM).

Treating the spectra as individual optimised parameters is difficult. Performing a singular value decomposition (SVD) of the titration data matrix showed that two species contribute significantly to the change in absorption. The SVD is a model-free analysis, and delivers a good estimate of how reliable the fit of a certain model will be. As expected, fitting the absorption contribution of each species independently results in a better fit, but the calculated extinction coefficients show that the model has too many variables and the result is overfitted (Fig. 3.9). However, the binding constant is within the experimental error with the concentration model ($K_{chem} = 1.6 \times 10^4$ M^{-1}). Based on these results, the most reliable estimation of binding constants is done using the concentration model, *e.g.* assuming that all six sites act independent and identically.

The fits for the multivalent ***c*-P6** host binding the monodentate guests **py**, **A1**, and **C1** is shown in Figure 3.10. The unbound host is shown in black and the host-guest complex in red. The experimental points are compared with the fitted binding isotherms for two characteristic wavelengths (758 nm in black, 820 nm in red).

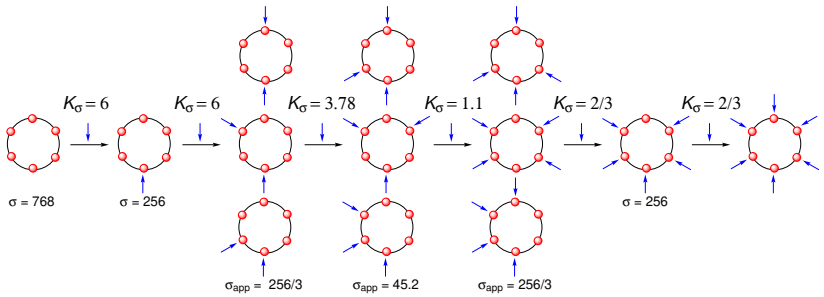

(a) Symmetry numbers for ***c*-P6** and a monovalent guest.

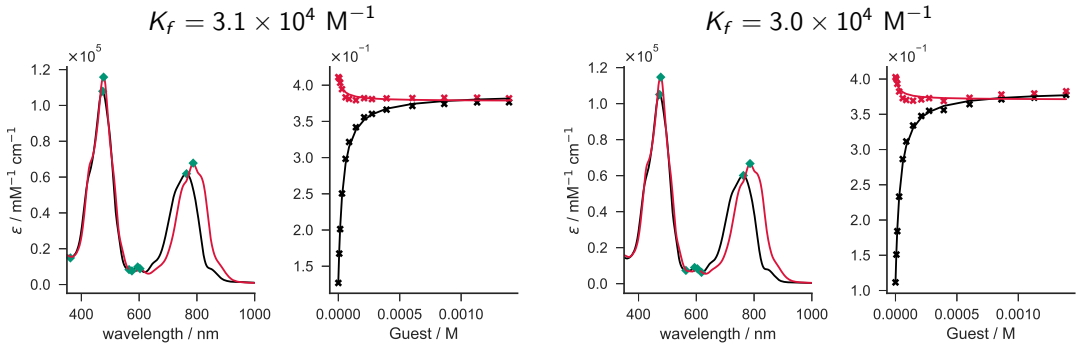

(b) First formation of ***c*-P6•py**

(c) Second formation of ***c*-P6•py**

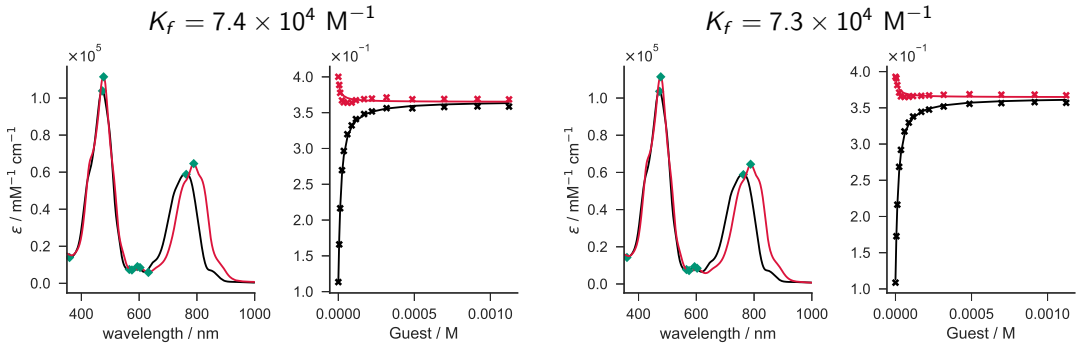

(d) First formation of ***c*-P6•A1**

(e) Second formation of ***c*-P6•A1**

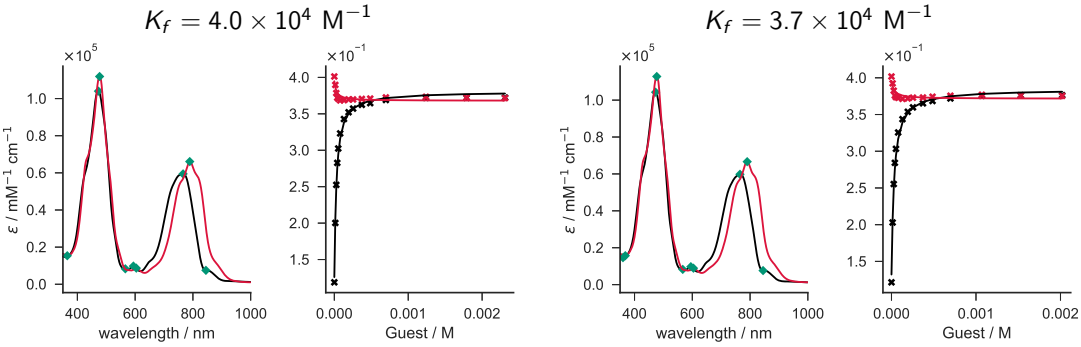

(f) First formation of ***c*-P6•C1**

(g) Second formation of ***c*-P6•C1**

Figure 3.10: Multivariant global fit results of two UV-vis-NIR titration experiment showing the single components of the absorption spectra (unbound host in black, host-guest complex in red) and the experimental point and the fitted binding isotherm of two characteristic wavelengths (758 nm in black, 820 nm in red), respectively. All data were fitted to a 1:1 model with an effective host concentration (6× [***c*-P6**]). Characteristic points of the spectra were used to validate the concentration of the individual measurements (green diamonds). (toluene, 298 K, [***c*-P6**] = 1.11 µM).

Table 3.3: Overview of reference binding constants (toluene, 298 K, Ar = tBu, *effective concentration as analysis method used).

Complex	$K_f(M^{-1})$	K_σ	$K_{chem}(M^{-1})$
***l*-P1•py**	$(2.7 \pm 0.2) \times 10^4$	2	1.3×10^4
***l*-P1•A1**	$(5.3 \pm 0.5) \times 10^4$	2	2.7×10^4
***l*-P1•C1**	$(2.2 \pm 0.2) \times 10^4$	2	1.1×10^4
c*-P6•py	$(3.0 \pm 0.3) \times 10^4$	2	1.5×10^4
c*-P6•A1	$(7.3 \pm 0.7) \times 10^4$	2	3.7×10^4
c*-P6•C1	$(3.8 \pm 0.3) \times 10^4$	2	1.9×10^4

An overview of the reference binding constants determined in this section is shown in Table 3.3. The binding constant for pyridine to ***l*-P1** and ***c*-P6** is within the experimental error tolerance of 10 %. However, the larger guests **A1** and **C1** show an increase of binding strength from ***l*-P1** to ***c*-P6**. The difference in binding constant between the two hosts is small, but still outside the experimental error, suggesting that this observation is real.

3.6 Binding Strength for 1:1 Complexes

3.6.1 Effect of Number of Binding Sites on the Binding Isotherm

All linear oligomers form 1:1 complexes with the bidentate and tridentate guests. The formation titration curves clearly exhibit different shapes for the complexes. While an excess of the monodentate guests is required to saturate all hosts, the binding of the multidentate guests is stronger and gives sharp end points. With the stronger (cooperative) binding, stoichiometric amounts of guests are sufficient to saturate all binding sites.

As an example, the UV-vis-NIR spectra and the single wavelength binding isotherm of ***l*-P1** with **A1**, ***l*-P2** with **A2**, and ***l*-P3** with **A3** are shown in Table 3.4. The binding of a guest to a porphyrin unit leads to a red shift in the absorption maxima in the Soret- and Q-bands. Due to the accessibility of a wide range of torsional states,[75] the unbound ***l*-P2** shows a broad absorption in the Q-band region. Forming the ***l*-P2•A2** complex, leads to narrowing of the absorption maxima in the B- and Q-band regions, since the torsional degrees of freedom are reduced (Fig. 3.4b). This behaviour is even more dramatic in the ***l*-P3•A3** complex (Fig. 3.4c).

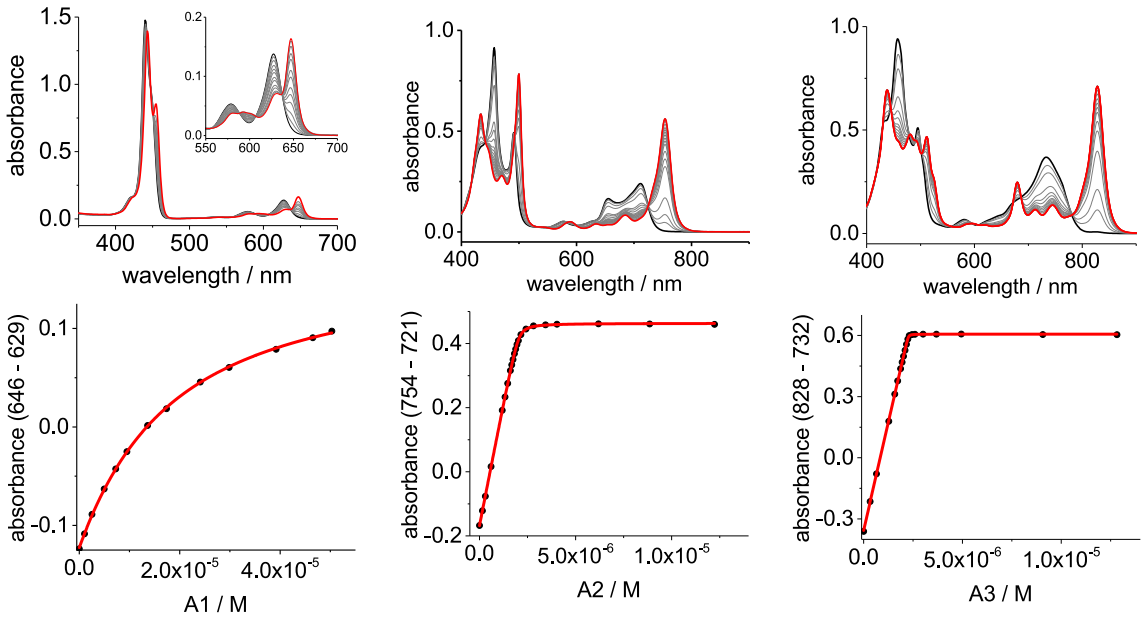

(a) ***I*-P1** with **A1** **(b)** ***I*-P2** with **A2** **(c)** ***I*-P3** with **A3**

Table 3.4: UV-vis-NIR spectra and titration curves. The black spectra show the unbound porphyrin. The red spectra correspond to the host-guest complex. The graphs below show the binding isotherms (toluene, 298 K, [***I*-P1**] = 2.48 µM, [***I*-P2**] = 1.85 µM, and [***I*-P3**] = 1.84 µM).

3.6.2 Determination of K_f via Direct Titration Experiments

The fits for the ***I*-P2** host binding the bidentate guests **A2**, **B2**, and **C2** are shown in Figure 3.11. Each formation titration was repeated several times and the experimental data for each guest were combined for a global analysis of each guest.

The slope around the inflection point on binding isotherms is relatively gradual for ***I*-P2•B2** and ***I*-P2•C2**, resulting in sufficient data points to characterise the binding constant. However, the binding constant for ***I*-P2•A2** is very high, and only a few points can be used to determine the binding strengths. For binding constants $K_f > 5 \times 10^7$ M^{-1}, the determination of the binding constant using a formation titration is unreliable.[39] This is why the binding constants have to be determined by competition experiments.

3.6.3 Determination of K_f via Competition Experiments

Competition experiments are performed by titrating a large excess of pyridine as a competing ligand into a solution of a 1:1 complex (*e.g.* ***I*-P2•A2**). This leads to a displacement of the multidentate ligand (**A2**) at a specific concentration of monodentate guest. The denaturation constant (K_{dn}) is related to the formation constant K_f via the independently

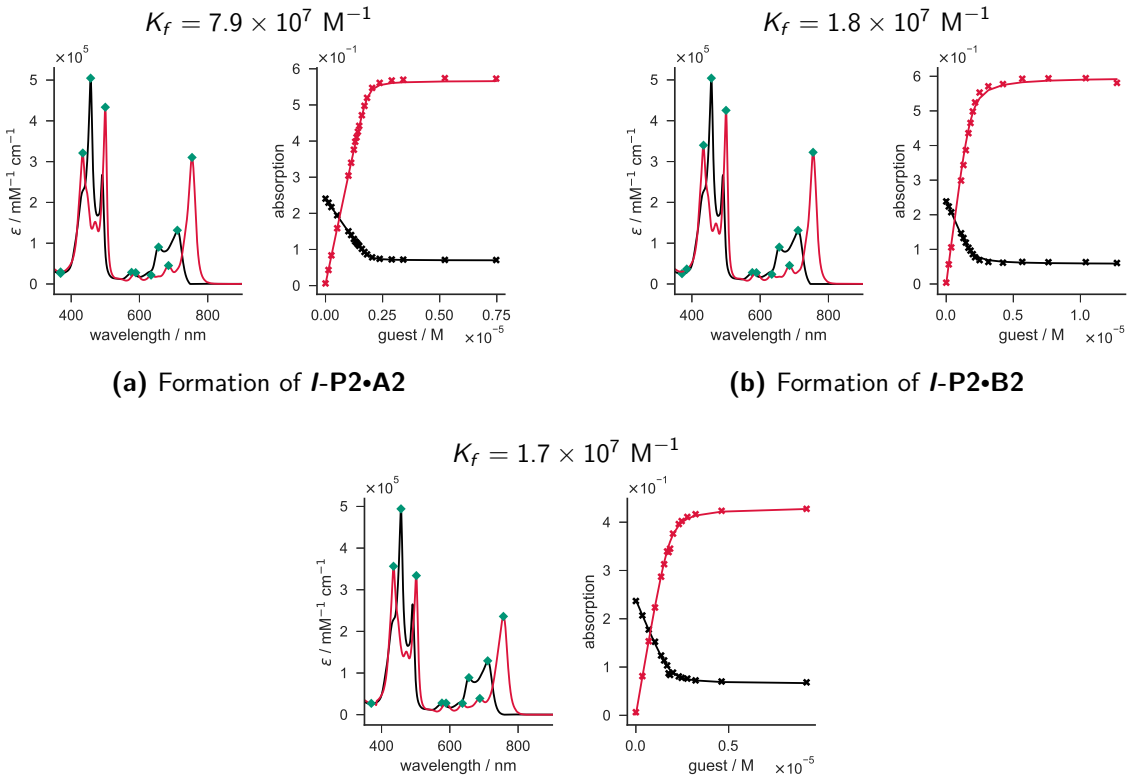

(a) Formation of ***I*-P2•A2**

(b) Formation of ***I*-P2•B2**

(c) Formation of ***I*-P2•C2**

Figure 3.11: Multivariant global fit results of multiple UV-vis-NIR titration experiment showing the single components of the absorption spectra (unbound host in black, host-guest complex in red) and the experimental point and the fitted binding isotherm of two characteristic wavelengths (712 nm in black, 755 nm in red), respectively. Characteristic points of the spectra were used to validate the concentration of the individual measurements (green diamonds). (toluene, 298 K, [***I*-P2**] = 1.85 µM).

determined reference binding constant of pyridine to a zinc porphyrin unit (K_{Py}) (Eq. 3.6, N is the number of binding sites).

$$K_f = \frac{K_{Py}^N}{K_{dn}} \tag{3.6}$$

The thermodynamic cycle for the ***I*-P2•A2** denaturation titration is shown in Figure 3.12 as an example.

The isosbestic nature of the titration suggest that the denaturation processes follows an 'all-or-nothing' two-state equilibrium without forming any partially denatured species in significant concentration. This behaviour is supported by the good reproduction of the experimental absorption points by the calculated binding isotherm for the simple two-state equilibrium (see Appendix, Fig. 3.38 and 3.39). The denaturation fits for ***I*-P2•A2** and the ***I*-P3** host complexes are shown in Figure 3.13.

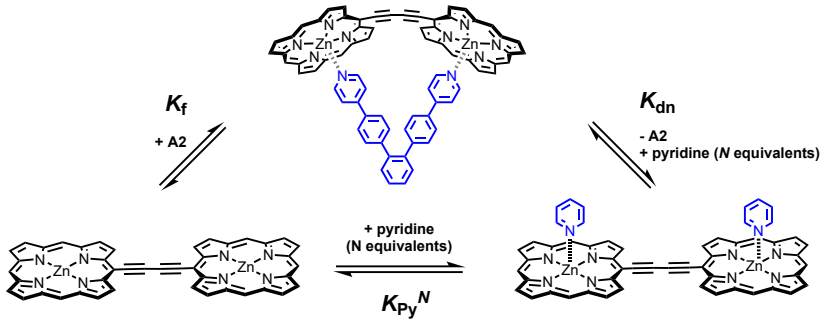

Figure 3.12: Thermodynamic cycle for the formation and the denaturation of the ***I*-P2•A2** complex.

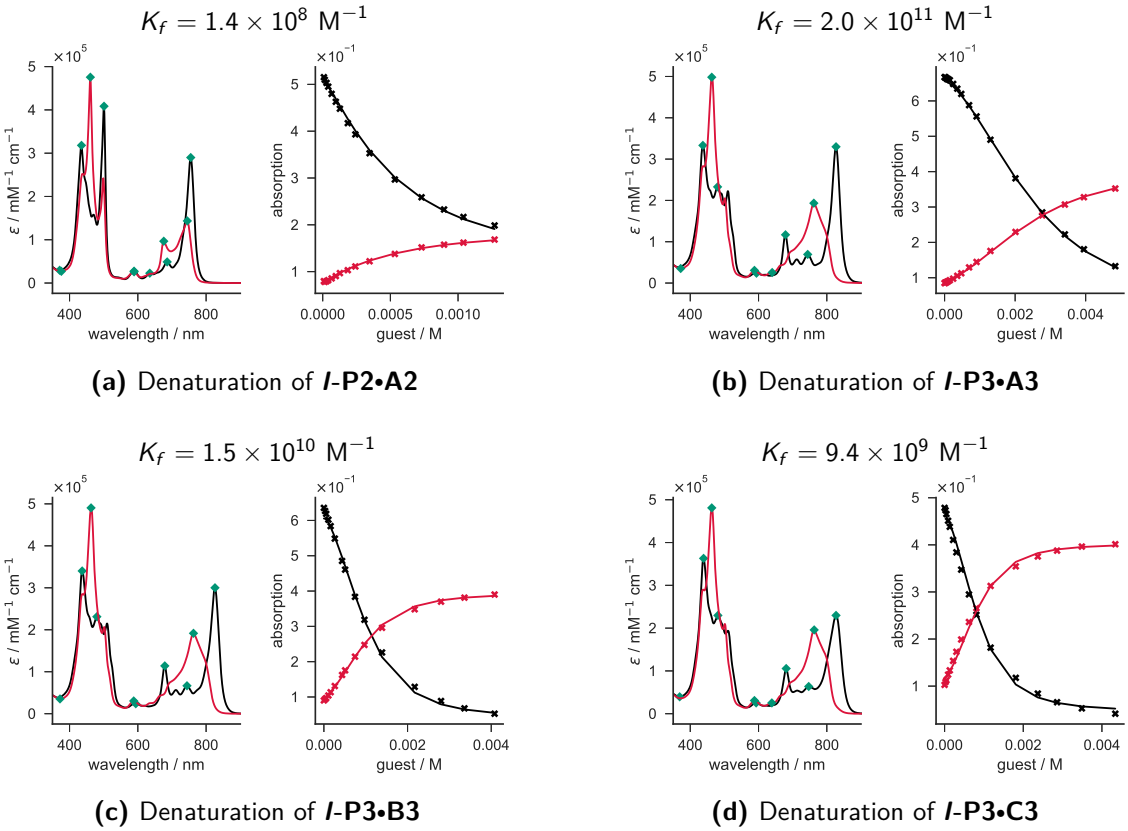

(a) Denaturation of ***I*-P2•A2**

(b) Denaturation of ***I*-P3•A3**

(c) Denaturation of ***I*-P3•B3**

(d) Denaturation of ***I*-P3•C3**

Figure 3.13: Multivariant global fit results of multiple UV-vis-NIR titration experiment showing the single components of the absorption spectra (host-guest complex in black, pyridine bound host in red) and the experimental point and the fitted binding isotherm of two characteristic wavelengths (824 nm in black, 762 nm in red), respectively. Characteristic points of the spectra were used to validate the concentration of the individual measurements (green diamonds). Experimental conditions were 298 K, toluene as a solvent, [***I*-P2**] = 1.85 µM, and [***I*-P3**] = 1.84 µM.

Each denaturation titration was repeated several times and the experimental data were combined for global analysis of each guest. The indirect determined binding constant for ***l*-P2•A2** is slightly higher than the one obtained by direct formation titration values. However, this example illustrates the limitation of the competition method. Very low pyridine concentrations are sufficient to completely displace the divalent guest **A2**, which leads to a smaller slope around the point of inflection. As a result, the determined denaturation constant is less accurate and propagates this error to the formation constant. This is why direct formation titrations were chosen for the determination of the ***l*-P2•A2**, ***l*-P2•B2** and ***l*-P2•C2** binding constants. The trend for the bidentate binding constants was verified by formation titration experiments with weaker binding hosts (see Chapter 4) and DFT calculations (see Chapter 5). The denaturation constants for the tridentate host-guest systems are more characteristic and improve the reliability of the calculated formation constants. All formation constants are within the typical range and follow the expected trend of decreasing stability with ***l*-P3•A3**, followed by ***l*-P3•B3** and finally ***l*-P3•C3**.

3.7 Complexes with Higher Order Stoichiometries

3.7.1 Determination of Stoichiometry

The multivalent cyclic hosts ***c*-P6** can bind up to two tridentate and up to three bidentate guests. To confirm the stochiometry, formation titrations were done. The concentration of the ***c*-P6** was confirmed by the use of extinction coefficients. However, residual amounts of pyridine have a significant impact in the extinction coefficient increasing the uncertainty of the concentration. Therefore, the concentration ***c*-P6** was confirmed by a formation titration with the hexadentate ligand **T6** and the **T6** concentration was cross-validated by formation titration using the linear oligomers ***l*-P2** and ***l*-P3**. The cross-validation method is very reliable due to the high binding constants and sharp end points in the binding isotherms for all involved complexes. The formation curves for ***c*-P6** binding to the bi- and tridenate guests are shown in Figure 3.14. A single wavelength (830 nm for the bidentate, 850 nm for the tridentate) was fitted to a 1-to-1 binding isotherm with an effective host concentration depending on the number of binding sites.

All guests show sharp end points, demonstrating a strong binding behaviour, with stepwise binding constants larger than $K_f > 5 \times 10^7$ M^{-1}. All tridentate guests form 1:2

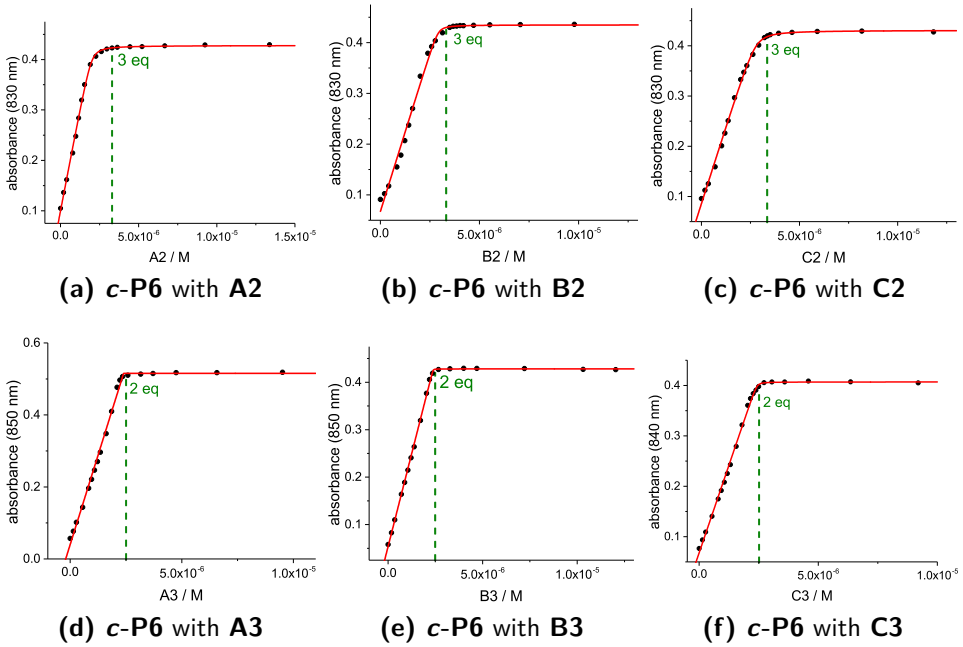

Figure 3.14: UV-vis-NIR spectra and titration curves. The black spectra show the unbound porphyrin. The red spectra correspond to the formed complex. The graphs below show the binding isotherms (toluene, 298 K, [***c*-P6**] = 1.11 µM).

complexes, while the bidentate guests form 1:3 complexes. The complex formation for guest **A2** shows a less steep slope between 2 and 3 guest equivalents, indicating that the third stepwise binding constant might be weaker than the first two. However, the formation titrations only give a result for the average behaviour. The individual, stepwise formation constants were analysed in a competition experiment with a monovalent guest.

3.7.2 Complexes involving Tridentate Guests

3.7.2.1 Comparison of Binding models

To determine the individual binding constants of the 1:1 and 1:2 complexes for ***c*-P6** binding **A3**, **B3**, or **C3**, denaturation titrations were done, in which multiple species are formed (Fig. 3.15).

Based on the conclusion from the determination of reference constants, each porphyrin unit in ***c*-P6** is assumed to bind a (monodentate) ligand with identical strength, such that the axial coordination of one porphyrin unit does not affect the pyridine binding strength of the neighbouring ones. Moreover, an 'all-or-nothing' behaviour can be assumed for each multidentate ligand, meaning that a multivalent ligand is only bound with all binding sites and partially bound intermediates are not formed in significant concentrations.

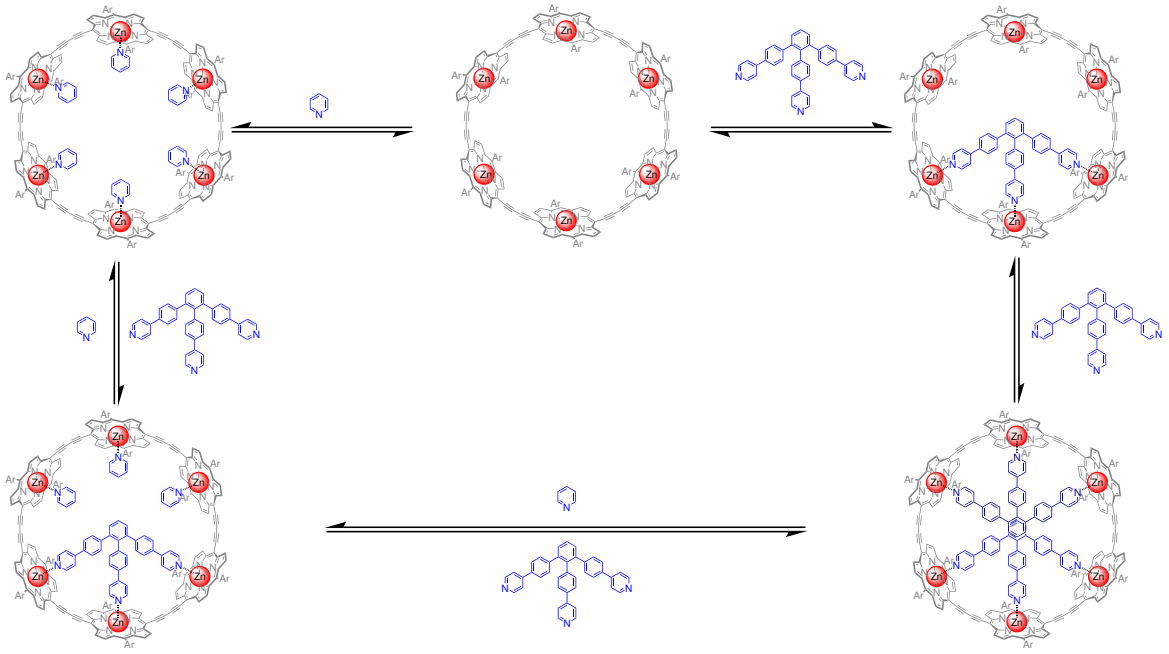

Figure 3.15: Thermodynamic cycle of the formation and denaturation of a ***c*-P6** and **A3** complex with pyridine as competing monovalent guest.

However, the apparent formation constants (K_f) for the 1:1 and the 1:2 complexes are not identical due to statistical factors. If the first ligand does not influence the second one, the statistical correction would lead to identical chemical binding constants (K_{chem}). Therefore, an observed difference between the first and the second binding event is related to the number of free binding sites per host molecule. However, the binding of the first ligand could sterically hinder the binding of the second ligand, leading to a difference in the statistically corrected binding constant between the first and the second ligand.

To determine the first and the second binding constant, different binding models were tested:

- **Effective binding sites**: Assuming that the binding of the first guest does not affect the binding of the second guest and that the host can be represented as trimer (twice the concentration of the actual ***c*-P6** host). Then, the data can be fitted to a simple 1:1 'all-or-nothing' denaturation process involving only two species: The ***c*-P6•A3** complex and the ***c*-P6•py$_3$** complex.

- **Statistically equivalent**: Even though the statistically corrected binding constants are identical, the two absorption spectra for ***c*-P6•A3** and ***c*-P6•A3$_2$** might not be well represented by an average effective spectrum. The former method requires

that the spectra of the actual denaturated complex ***c*-P6•A3py$_3$** can be represented as a linear combination of the two species ***c*-P6•A3$_2$** and ***c*-P6•py$_3$**. By explicitly defining all species, the number of variables is increased as each species contributes independently to the total absorption. If the binding constants are identical, the thermodynamic cycle can be expressed as a system of linear equations relating both formation constants to one statistically corrected binding constant K_{chem} via the statistical factors (see Section 3.4). Using the system of linear equations shown in Figure 3.16, K_1 is set equal to K_2.

***c*-P6** + **A3**	$\rightleftharpoons$	***c*-P6•A3**	$96 \times K_1$
***c*-P6** + 2 **A3**	$\rightleftharpoons$	***c*-P6•A3$_2$**	$768 \times K_1 \times K_2$
***c*-P6** + **A3** + 3 **py**	$\rightleftharpoons$	***c*-P6•A3py$_3$**	$768 \times K_1 \times K_{py}^3$
***c*-P6** + 6 **py**	$\rightleftharpoons$	***c*-P6•py$_6$**	$64 \times K_{py}^6$

Figure 3.16: System of linear equations.

- **Sterically hindered**: If the statistically corrected binding constants are not identical, the same system of linear equations can be used as for the statistically equivalent case with K_1 not equal to K_2.

- **Independent optimisation**: The two apparent binding constants for the formation of the 1:1 and the 1:2 complexes were independently optimised from the titration data. This fit procedure has the same number of variables and should lead to the same solution as the 'sterically hindered' model. By relating the different processes via statistical factors, the flexibility of the optimisation algorithm is reduced. However, if the statistical corrections are a valid representation of the experimental system, the solution should be identical.

The models above were tested with the UV-vis-NIR titration data for the denaturation of complexes of ***c*-P6** with tridentate guests. Each denaturation titration was repeated several times and the experimental data were combined for a global analysis for each guest. The results for the 'effective binding sites' model are shown in Figure 3.17. Clearly, the model shows a significant deviation between the experimental and the calculated change in absorption. While ***c*-P6•A3** and ***c*-P6•B3** show an overestimation of the

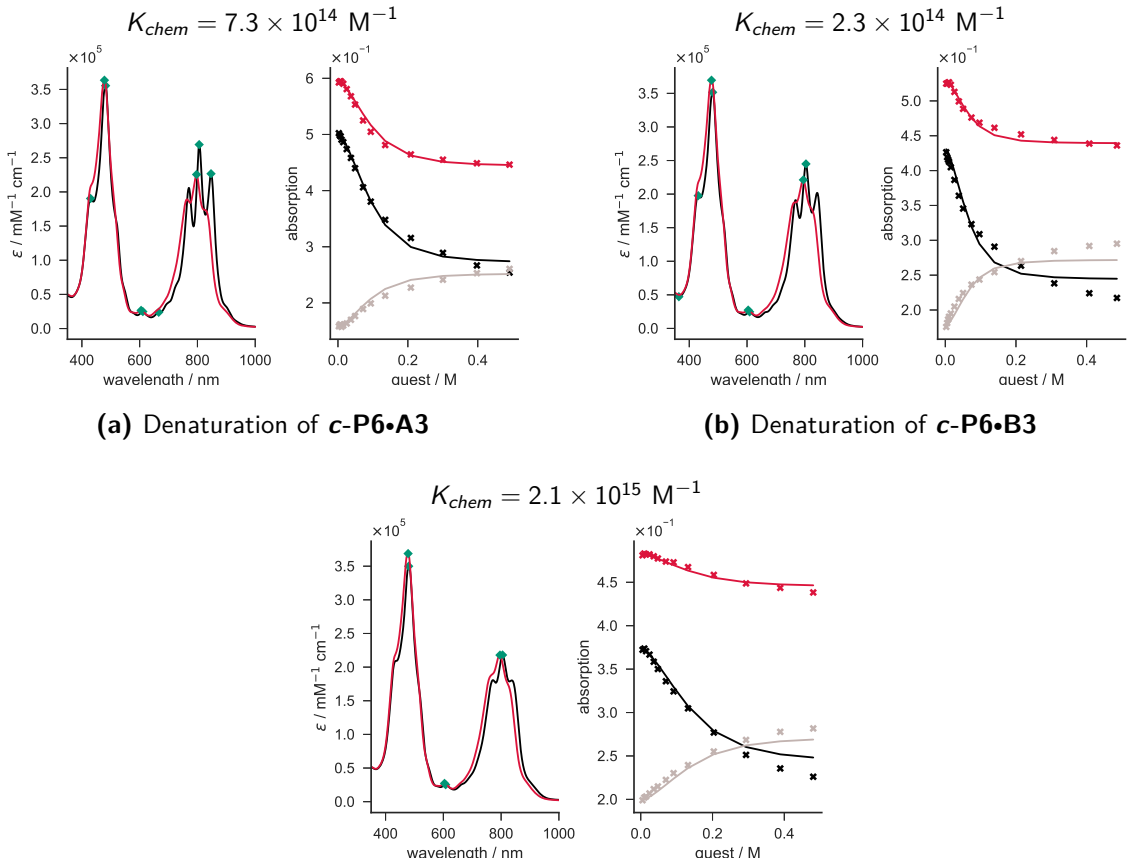

(a) Denaturation of ***c*-P6•A3**

(b) Denaturation of ***c*-P6•B3**

(c) Denaturation of ***c*-P6•C3**

Figure 3.17: Multivariant global fit results for the 'effective binding sites' model. Presented are the determined single components of the absorption spectra host-guest complex in black, denaturated complex in red, and the experimental point and the fitted binding isotherm of three characteristic wavelengths (735 nm in grey, 807 nm in red, 847 nm in black), respectively. Characteristic points of the spectra were used to validate the concentration of the individual measurements (green diamonds). (toluene, 298 K, [***c*-P6**] = 1.11 µM).

denaturation constant for a pyridine concentration below 0.2 M, the denaturation constant is underestimated for a higher pyridine concentration.

The 'independent optimisation' model improves the fit significantly. The results are shown in Figure 3.18. Using this model increases the number of variables, so an improvement of the fit is expected. The obtained binding constants are in good agreement for both methods, indicating that the determined statistical factors are correct. However, the model shows the same systematic errors as the 'Effective binding site' model, as the single wavelength binding isotherms indicate. This systematic error is an indication that the used model might be not sufficient as there are two processes with different binding constants involved.

If the binding constants are significantly different for the first and the second guest, the 'independent optimisation' model is expected to drastically improve the fit. The results are

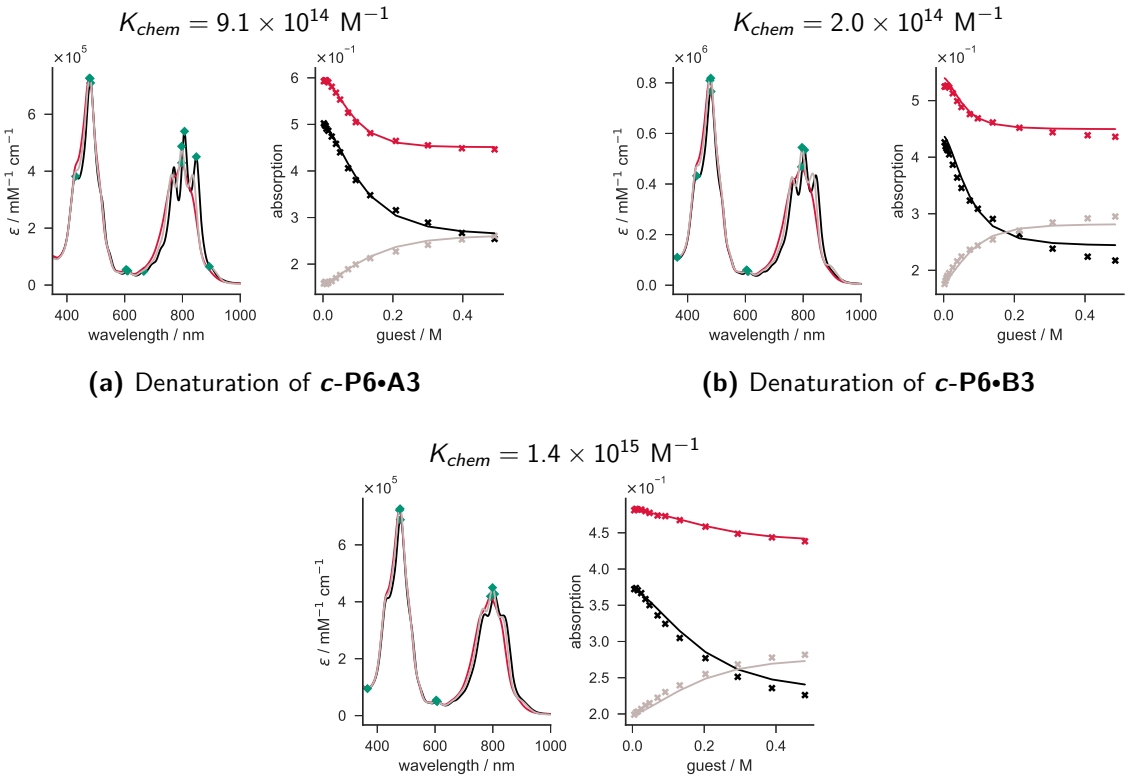

(a) Denaturation of ***c*-P6•A3**

(b) Denaturation of ***c*-P6•B3**

(c) Denaturation of ***c*-P6•C3**

Figure 3.18: Multivariant global fit results for the 'independent optimisation' model. Presented are the determined single components of the absorption spectra ***c*-P6•X3$_2$** in black, partially denaturated ***c*-P6•X3py$_3$** in grey, and fully denaturated ***c*-P6•py$_6$** in red. The fit accuracy is shown as experimental point compared to the fitted binding isotherm of three characteristic wavelengths (735 nm in grey, 807 nm in red, 847 nm in black), respectively. Characteristic points of the spectra were used to validate the concentration of the individual measurements (green diamonds). (toluene, 298 K, [***c*-P6**] = 1.11 µM).

shown in Figure 3.19. As expected, the fitted binding isotherms reproduce the experimental results well. The extracted individual binding constants for the first and the second guest ($K_{chem,1}$ and $K_{chem,2}$) are an order of magnitude different for **A3** and **B3**, whereas the two binding constants for **C3** are identical within the error limits of the fit. This result indicates that, in case of **A3** and **B3**, the steric hindrance between the first and the second guest binding inside the ***c*-P6** nanoring is significant and hence reduces the binding constant for the second guest. For all three guests, the average between $K_{chem,1}$ and $K_{chem,2}$ is identical to K_{chem} obtained by the previous models.

To verify the calculated statistical factors, the 'independent optimisation' model was tested, in which the first and the second denaturation constant are determined without any restrictions (Fig. 3.20). Only the fits for ***c*-P6•A3** and ***c*-P6•B3** converged, but resulted in the same binding constants as those found using the 'independent optimisation' model.

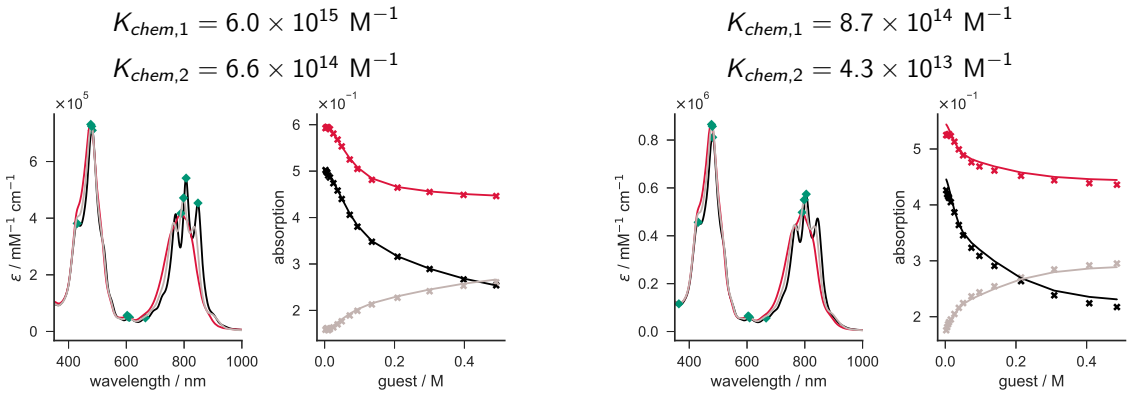

(a) Denaturation of ***c*-P6•A3**

(b) Denaturation of ***c*-P6•B3**

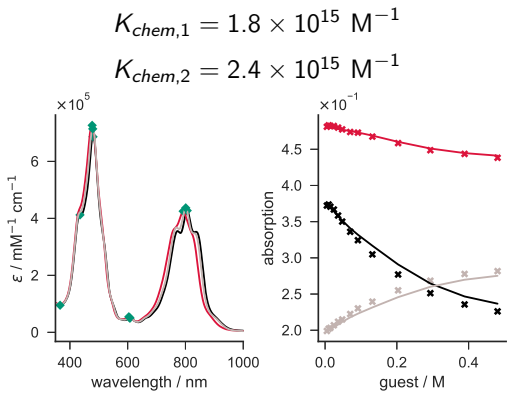

(c) Denaturation of ***c*-P6•C3**

Figure 3.19: Multivariant global fit results for the 'sterically hindered' model. Presented are the determined single components of the absorption spectra ***c*-P6•X3$_2$** in black, partially denaturated ***c*-P6•X3py$_3$** in grey, and fully denaturated ***c*-P6•py$_6$** in red. The fit accuracy is shown as experimental point compared to the fitted binding isotherm of three characteristic wavelengths (735 nm in grey, 807 nm in red, 847 nm in black), respectively. Characteristic points of the spectra were used to validate the concentration of the individual measurements (green diamonds). (toluene, 298 K, [***c*-P6**] = 1.11 µM).

3.7.2.2 Statistical Evaluation of Binding Models

To determine if the improvement is statistically significant or if the model overfits the provided data, the statistical significance of the change in the goodness of fit was verified.

The individual models use a different numbers of variables. All of the models are nested, meaning the 'statistically equivalent' model is a special case of the 'sterically hindered' model. Increasing the number of variables gives a higher flexibility for the fit function, so the fit will almost always show a lower sum-of-squares (indicating a better fit) than the model with less variables. To compare these models, the extra sum-of-squares F test[125] was used, which compares the difference in sum-of-squares between the two models with respect to the data points and the number of variables used to fit the model. Generally, the simpler

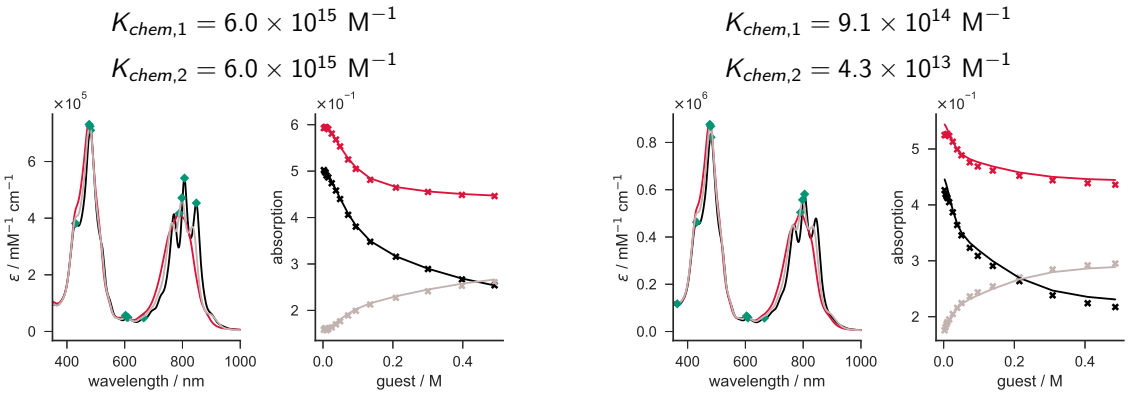

(a) Denaturation of ***c*-P6•A3** **(b)** Denaturation of ***c*-P6•B3**

Figure 3.20: Multivariant global fit results for the 'independent optimisation' model. Presented are the determined single components of the absorption spectra ***c*-P6•X3$_2$** in black, partially denaturated ***c*-P6•X3py$_3$** in grey, and fully denaturated ***c*-P6•py$_6$** in red. The fit accuracy is shown as experimental point compared to the fitted binding isotherm of three characteristic wavelengths (735 nm in grey, 807 nm in red, 847 nm in black), respectively. Characteristic points of the spectra were used to validate the concentration of the individual measurements (green diamonds). (toluene, 298 K, [***c*-P6**] = 1.11 µM).

model is used as a null hypothesis, that can only be rejected if a more complex model gives a significant improvement. The more complex model is assigned as the alternative hypothesis. The data are fitted to each model and the goodness-of-fit is estimated as the sum-of-squares of deviations (SSQ) from the data points to the model. The complexity of the model is quantified by the determination of the degrees of freedom. The degrees of freedom (DoF) is the number of data points minus the number of fitted parameters. The F ratio is calculated using equation 3.7. If the simple model represents the data sufficiently, the improvement of the sum-of-squares by the alternative, more complex model will be equal to to the relative increase in the degrees of freedom. This would result in an F value close to 1. The closer the ratio F is to 1, the more likely it is that the null hypothesis is correct and the improvement of the SSQ value is simply due to the higher flexibility of the fit. Therefore, the difference between both models will be statistically insignificant.

$$F = \frac{(\mathrm{SSQ_{null}} - \mathrm{SSQ_{alter}})/(\mathrm{DoF_{null}} - \mathrm{DoF_{alter}})}{\mathrm{SSQ_{alter}}/\mathrm{DoF_{alter}}} \tag{3.7}$$

To interpret the overall significance of the F-test results, its p-value (or probability value) has to be calculated. Starting with the most simple model, the 'effective binding sites' is assigned as null hypothesis and the 'statistically equivalent' model is the alternative hypothesis. The results are shown in Table 3.5. Expanding the model from 'effective binding

Table 3.5: Using the extra sum-of-squares F test to compare the 'effective binding sites' and the 'statistically equivalent' model (Number of data points is 31 per wavelength).

Model	***c*-P6•A3**		***c*-P6•B3**		***c*-P6•C3**	
	SSQ	DoF	SSQ	DoF	SSQ	DoF
null hypothesis	0.585	28	1.56	27	9.84	28
alter hypothesis	0.368	27	0.731	26	4.82	27
Difference	0.217	1	0.829	1	50.2	1
Ratio (F)	15.92		29.49		27.08	
p value	0.0005		$<$0.0001		$<$0.0001	

Table 3.6: Using the extra sum-of-squares F test to compare the 'statistically equivalent' and the 'sterically hindered' model (Number of data points is 31 per wavelength).

Model	***c*-P6•A3**		***c*-P6•B3**		***c*-P6•C3**	
	SSQ	DoF	SSQ	DoF	SSQ	DoF
null hypothesis	0.368	27	0.731	26	4.82	27
alter hypothesis	0.314	26	0.542	25	4.82	26
Difference	0.054	1	0.189	1	0	1
Ratio (F)	4.47		8.72		–	
p value	0.0442		0.0068		–	

sites' to 'statistically equivalent' and therefore allowing an independent optimisation for the ***c*-P6•X3py$_3$** spectrum results in a statistically significant improvement of the goodness-of-fit for all tridentate guests. With a p value far below the 5 % threshold, it is very unlikely that the improvement is a 'false-positive' result. Therefore, the 'statistically equivalent' model is assumed to be a better representation of the experimental data.

The next step is to compare the 'statistically equivalent' and the 'sterically hindered' model. The same procedure as described before was used and the results are shown on Table 3.6. However, the results are less clear as in the previous comparison. For ***c*-P6•C3**, there is no change in the SSQ. As there is no steric interaction between the first and the second guest in ***c*-P6**, the conclusion is that the 'sterically hindered' model is not statistically significant and not a true improvement of the binding model. This conclusion is supported by chemical intuition. For ***c*-P6•A3** and ***c*-P6•B3**, the decision to discard a hypothesis is more complicated.

To obtain a clearer conclusion, it was tested which one of the two fits is stronger supported by the data. Therefore, the AIC$_c$ method was used which is based on information

Table 3.7: Using the AIC_c method to compare the 'statistically equivalent' (SE, 4 variables) and the 'sterically hindered' (SH, 5 variables) model (Number of data points is 31 per wavelength).

Model	***c*-P6•A3**		***c*-P6•B3**		***c*-P6•C3**	
	SE	SH	SE	SH	SE	SH
Sum-of-squares	0.368	0.314	0.731	0.542	4.82	4.82
AIC_c	-125.04	-126.86	-98.94	-104.76	-45.30	-42.20
Difference in AIC_c	1.82		5.82		3.10	
Information ratio	2.48		18.38		4.71	

theory. For a given set of models, a likelihood function is defined which is based on an information criterion developed by Akaike.[126] Based on the reasonable assumption that the scatter of repeatedly measured data points is Gaussian distributed, the second order corrected AIC value (AIC_c) is defined by the following equation:

$$AIC_c = N \times \ln(\frac{SSQ}{N}) + 2 \times K + \frac{2K(K+1)}{N-K-1} \tag{3.8}$$

with N as the number of data points and K the number of variables. The AIC_c were calculated for both models. The model with the lower AIC_c is more likely to be correct. The results are shown in Table 3.7. Comparing the information ratio between the different AIC_c values of each system shows that the 'sterically hindered' model is 2.5 times for ***c*-P6•A3** and 18 times for ***c*-P6•B3** more likely to be correct than the 'statistically equivalent' one. However, it seems 4.7 times more likely that the 'statistically equivalent' model sufficiently describes the data for the ***c*-P6•C3** system. Therefore, the binding constants obtained by the 'sterically hindered' model are used for further analysis of the ***c*-P6•A3** and ***c*-P6•B3** systems, while the binding constants obtained by the 'statistically equivalent' model are used for ***c*-P6•C3**. This choice is supported by a naive comparison of the binding constants derived from the different models; while ***c*-P6•A3** and ***c*-P6•B3** show an order of magnitude difference in binding constants between the different models, the binding constant for ***c*-P6•C3** is nearly identical in all models.

3.7.3 Complexes involving Bidentate Guests

The same models were tested for the bidentate guests binding to ***c*-P6**. Since 1:1, 1:2, and 1:3 complexes are formed, a fully independent fit of all parameters would lead to overfitting.

While the number of variables for the 'effective binding sites' model is identical for the tridentate and the bidentate systems, the more complicated models suffer significantly from this effect. The 'statistically equivalent' model already requires five variables. For the 'sterically hindered' model, seven variables need to be optimised.

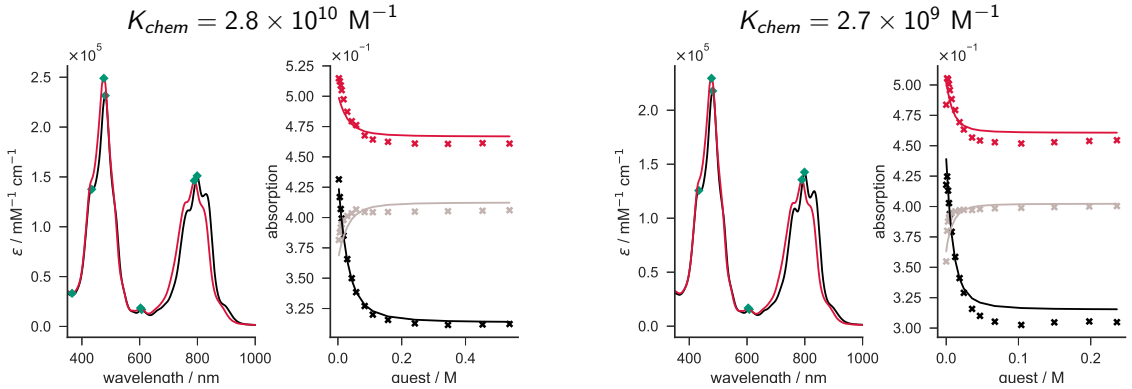

(a) Denaturation of ***c*-P6•A2**

(b) Denaturation of ***c*-P6•B2**

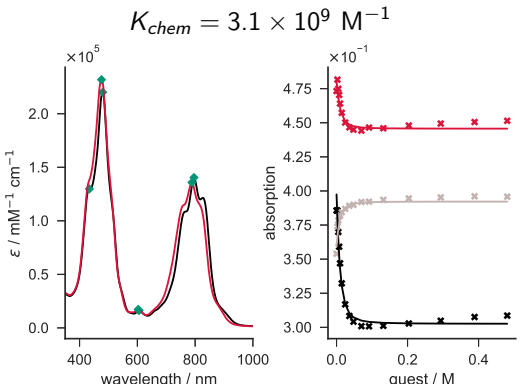

(c) Denaturation of ***c*-P6•C2**

Figure 3.21: Multivariant global fit results for the 'effective binding sites' model. Presented are the determined single components of the absorption spectra host-guest complex in black, denaturated complex in red, and the experimental point and the fitted binding isotherm of three characteristic wavelengths (757 nm in grey, 797 nm in black, 835 nm in red), respectively. Characteristic points of the spectra were used to validate the concentration of the individual measurements (green diamonds). (toluene, 298 K, [***c*-P6**] = 1.11 µM).

The results for the 'effective binding sites' model are shown in Figure 3.21. Similar to the tridentate ligands, a systematic error is observed, showing an overestimation of the denaturation process at low concentrations of pyridine, and an underestimation at higher pyridine concentrations. Overall, the binding model fits the experimental data poorly.

Expanding the model to the 'statistically equivalent' model improves the fit significantly. The results are shown in Figure 3.22. Here, all intermediate species have independent

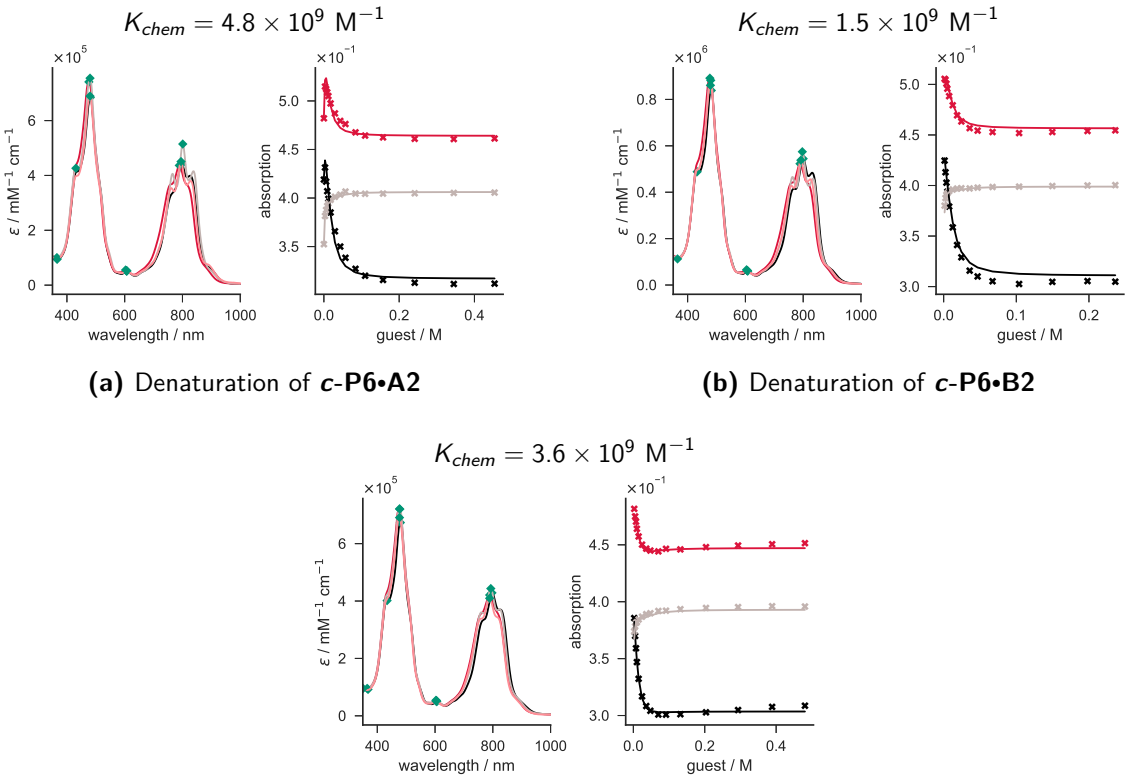

(a) Denaturation of ***c*-P6•A2**

(b) Denaturation of ***c*-P6•B2**

(c) Denaturation of ***c*-P6•C2**

Figure 3.22: Multivariant global fit results for the 'statistically equivalent' model. Presented are the determined single components of the absorption spectra ***c*-P6•X2$_3$** in black, partially denaturated ***c*-P6•X2$_2$py$_2$** in grey and ***c*-P6•X2py$_4$** in pink, and fully denaturated ***c*-P6•py$_6$** in red. The fit accuracy is shown as experimental point compared to the fitted binding isotherm of three characteristic wavelengths (757 nm in grey, 797 nm in black, 835 nm in red), respectively. Characteristic points of the spectra were used to validate the concentration of the individual measurements (green diamonds). (toluene, 298 K, [***c*-P6**] = 1.11 µM).

absorption spectra. The comparison of both models shows for the F test as well as for the AIC$_c$ method a strong likelihood, that the more complex model is a more accurate representation of the experimental system.

While the 'statistically equivalent' model delivers a satisfying fit, more complex models could not be tested due to convergence issues and overfitting. As an example, the 'sterically hindered' model is shown in Figure 3.23. When convergence is reached, the fit slightly improved compared to the previous model, but the number of parameters that need to be optimised to fully describe the model is so high as to lead to overfitting. This problem is illustrated by the fit for ***c*-P6•C2** (Fig. 3.23b). The small guest shows no steric interaction, but still the optimised binding constants for the first, second and third binding event differ by several orders of magnitude. Due to error compensation, the fit leads to a smaller sum-of-squares ratio. As the absence of allosteric effects is known for these systems and

Table 3.8: Using the extra sum-of-squares *F* test to compare the 'effective binding sites' and the 'statistically equivalent' model (Number of data points is 31 per wavelength).

Model	***c*-P6•A2**		***c*-P6•B2**		***c*-P6•C2**	
	SSQ	DoF	SSQ	DoF	SSQ	DoF
null hypothesis	1.653	44	0.370	45	0.161	26
alter hypothesis	0.997	42	0.133	43	5.03	24
Difference	0.657	2	0.237	2	–	2
Ratio (F)	13.84		38.31		–	
p value	<0.0001		<0.0001		–	

Table 3.9: Using the AIC_c method to compare the 'effective binding sites' (Conc, 3 variables) and the 'statistically equivalent' (SE, 5 variables) model (Number of data points is 47 per wavelength).

Model	***c*-P6•A2**		***c*-P6•B2**		***c*-P6•C2**	
	Conc	SE	Conc	SE	Conc	SE
Sum-of-squares	1.653	0.997	0.370	0.133	0.161	0.503
AIC_c	-148.36	-167.00	-224.61	-268.60	-140.95	31.79
Difference in AIC_c	18.64		43.99		3.10	
Information ratio	11162.05		18.38		172.74	

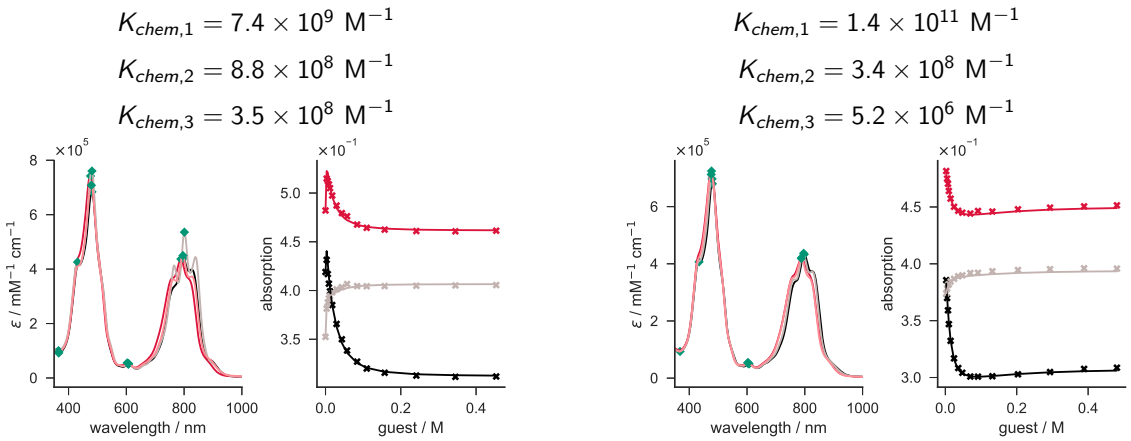

(a) Denaturation of ***c*-P6•A2** **(b)** Denaturation of ***c*-P6•C2**

Figure 3.23: Multivariant global fit results for the 'sterically hindered' model. Presented are the determined single components of the absorption spectra ***c*-P6•X2$_3$** in black, partially denaturated ***c*-P6•X2$_2$py$_2$** in grey and ***c*-P6•X2py$_4$** in pink, and fully denaturated ***c*-P6•py$_6$** in red. The fit accuracy is shown as experimental point compared to the fitted binding isotherm of three characteristic wavelengths (757 nm in grey, 797 nm in black, 835 nm in red), respectively. Characteristic points of the spectra were used to validate the concentration of the individual measurements (green diamonds). (toluene, 298 K, [***c*-P6**] = 1.11 µM).

molecular modelling allowed us to exclude any steric reasons, a difference in binding constants seems to be unreasonable and the model can be rejected based on chemical intuition. In conclusion, the binding constants obtained by the 'statistically equivalent' model were used for all three bidentate guests.

3.8 Effective Molarities

Chelate cooperativity is an intramolecular effect which arises from connecting binding sites in the host or in the guest, respectively. To quantify the chelate cooperativity of the individual ligands, the introduction of effective molarities (EM) is necessary.[7] The *EM* reflects the difference in binding efficiency for formation of a single-site complex and a chelate complex, and determines the threshold concentration below which a multivalent complex begins to open and/or forms oligomers. The mathematical definition of *EM* is the ratio between the intramolecular and the intermolecular binding constant:

$$EM = \frac{K_{\text{intra}}}{K_{\text{inter}}} \tag{3.9}$$

In a multi-step binding event, every binding interaction except the first one leads to an individual *EM*. The geometric mean $\overline{EM}$ for the *n*-site binding event is calculated using the following equation:

$$\overline{EM} = \sqrt[n-1]{\frac{K_{\text{chem}}}{K_1^n}} \tag{3.10}$$

where K_{chem} is the statistically corrected formation constant of the complex and K_1 is the statistically-corrected single-site association constant between a porphyrin unit and a monodentate ligand model for the corresponding complex.

The geometric average $\overline{EM}$ is related to the individual, stepwise EMs (EM_i) via the following equation:

$$\overline{EM} = \sqrt[n-1]{\prod_{i=2}^{i=n} EM_i} \tag{3.11}$$

An overview of all determined formation constants, the titration mode (direct or competition experiment), the binding model, the statistically corrected binding constants, $\overline{EM}$, and the stepwise EMs (EM_i, whereby i is equal to the number of intramolecular

Table 3.10: Overview of the determined formation constants (K_f), titration mode (TM), binding model (SH = 'sterically hindered'; SE = 'statistically equivalent'; EBS = 'effective binding sites'), statistically corrected binding constants(K_{chem}), geometric average ($\overline{EM}$), and stepwise effective molarities (EM_i, with $i = 1$ for bidentate and $i = 2$ for the tridentate guests).

Complex	TM	Model	K_f / M^{-1}	K_σ	K_{chem} / M^{-1}	$\overline{EM}$ / M	EM_i / M
***l*-P1•py**	direct	1:1	$(2.7 \pm 0.2) \times 10^4$	2	1.3×10^4	–	–
***l*-P1•A1**	direct	1:1	$(5.3 \pm 0.5) \times 10^4$	2	2.7×10^4	–	–
***l*-P1•C1**	direct	1:1	$(2.2 \pm 0.2) \times 10^4$	2	1.1×10^4	–	–
***c*-P6•py**	direct	EBS	$(3.0 \pm 0.3) \times 10^4$	2	1.5×10^4	–	–
***c*-P6•A1**	direct	EBS	$(7.3 \pm 0.7) \times 10^4$	2	3.7×10^4	–	–
***c*-P6•C1**	direct	EBS	$(3.8 \pm 0.4) \times 10^4$	2	1.9×10^4	–	–
***l*-P2•A2**	direct	1:1	$(7.9 \pm 0.1) \times 10^7$	8	9.9×10^6	(0.014±0.007)	(0.014±0.007)
***l*-P2•B2**	direct	1:1	$(1.8 \pm 0.2) \times 10^7$	8	1.4×10^6	(0.0019±0.0004)	(0.0019±0.0004)
***l*-P2•C2**	direct	1:1	$(1.7 \pm 0.2) \times 10^7$	8	2.1×10^6	(0.018±0.004)	(0.018±0.004)
***l*-P3•A3**	denat	1:1	$(2.0 \pm 0.2) \times 10^{11}$	16	1.3×10^{10}	(0.026±0.005)	(0.048±0.008)
***l*-P3•B3**	denat	1:1	$(1.5 \pm 0.2) \times 10^{10}$	16	9.1×10^8	(0.007±0.001)	(0.025±0.006)
***l*-P3•C3**	denat	1:1	$(9.4 \pm 0.9) \times 10^9$	16	5.9×10^8	(0.021±0.004)	(0.026±0.006)
***c*-P6•A2**	denat	SE	$(1.7 \pm 0.2) \times 10^{11}$	48	3.6×10^9	(2.7±0.8)	(2.7±0.8)
***c*-P6•B2**	denat	SE	$(7.3 \pm 0.9) \times 10^{10}$	48	1.5×10^9	(1.1±0.3)	(1.1±0.3)
***c*-P6•C2**	denat	SE	$(2.3 \pm 0.6) \times 10^{11}$	48	4.8×10^9	(13±4)	(13±4)
***c*-P6•A3**	denat	SH	$(6 \pm 1) \times 10^{17}$	96	6×10^{15}	(11±2)	(46±13)
***c*-P6•B3**	denat	SH	$(8 \pm 1) \times 10^{16}$	96	9×10^{14}	(4.2±0.8)	(16±5)
***c*-P6•C3**	denat	SE	$(1 \pm 0.5) \times 10^{17}$	96	1×10^{15}	(12±3)	(15±5)

bond formations) are shown in Table 3.10. The errors for binding constants determined via direct titration were calculated from the standard deviation of several independent experiments. The calculation of binding constants from competition experiments, or of the values for the effective molarities, involves several variables. Hence, the errors are determined by error propagation without covariance.[127]

3.9 Results and Discussion

The overall trend in the binding constants of the individual complexes is in good agreement. Regarding design principles, the most radical difference of the host-guest library is illustrated by the two different types of hosts: the preorganised cyclic ***c*-P6** nanoring *vs.* the flexible linear oligomers. The cyclic preorganised host ***c*-P6** leads for all guests to binding constants that are several orders of magnitude larger than those for the linear oligomers. The reduced binding affinity of the flexible systems originates from the bending of the butadiyne-linkers, supporting shape-complementary as an important design principle. However, the induced fit of the flexible hosts is quite large in these systems.

Analysing the different guest series allows a more subtle evaluation of preorganisation, flexibility, and rotational restrictions. Based on the molecular structure, all three guest series are shape-complementary. Guest series **A** is highly preorganised and shows the smallest loss of internal rotational degrees of freedom. The two remaining series, **B** and **C**, are not preorganised and show a similar reduction of internal rotations upon complexation. However, **B** is more flexible increasing the ability to adjust to the binding pocket. Contrary to this, **C** is very rigid and requires all binding sites in the host to be linearly aligned.

For both host systems, the binding constants of the guests in series **A** is an order of magnitude larger than the guests in series **B**, respectively. The most significant difference between these systems is presumably the change in the number of rotations frozen by complex formation. Comparing guest **A2** and **B2**, **B2** loses one additional rotational degree of freedom. Similarly, **B3** results in two frozen rotations more than **A3**.

The experimental values for freezing a rotation measured in literature are 5 to 6 kJ mol^{-1} in covalent complexes and 0.5 to 5 kJ mol^{-1} in non-covalent complexes.[33,91,128–130] If freezing rotations was the major source of differences between the complexes of series **A** and **B**, the energy difference between these complexes would be expected to scale linearly with the number of binding sites. Comparing the difference in Gibbs energy for ***c*-P6•A2** and ***c*-P6•B2**, the guest **A2** binds 2.2 kJ mol^{-1} more favourably than guest **B2**. The complex ***c*-P6•A3** is, by a difference in Gibbs energy of 4.8 kJ mol^{-1}, more favourable than ***c*-P6•B3**, which shows in fact that the energy difference doubled. Moreover, the values are within the expected Gibbs energy range for a frozen rotation found in the literature.

However, this systematic trend is not observed for the linear oligomers. The difference in Gibbs energies between ***l*-P2•A2** and ***l*-P2•B2** an between ***l*-P3•A3** and ***l*-P3•B3** is 5.0 kJ mol^{-1} and 6.1 kJ mol^{-1}, respectively. The same trend is observed in the stepwise effective molarities for the individual complexes (EM_i). As the effective molarity accounts for the single-site binding strength, all of the guest series can be directly compared. The linear oligomer ***l*-P3** shows a stepwise EM_i value within the same order of magnitude for all of the tridentate guests, indicating that the loss of a rotational degree of freedom is less dominant in the flexible hosts with more than two binding interactions. The EM_i for **A2** is an order of magnitude higher than that of **B2** guest binding to the divalent host ***l*-P2**, indicating the significance of rigidity for cooperativity.

The non-linear trend between the number of frozen-rotations and the loss of Gibbs energy indicates that the difference in flexibility is more significant than expected. This conclusion is supported by guest series **C**, which loses identical degrees of freedom as series **B**, but shows a higher rigidity. Nonetheless, the effective molarities for series **A** and **C** with the linear oligomers are identical within error tolerances, supporting that the loss of rotational degrees of freedom is less forceful then expected. In complexes with the cyclic ***c*-P6** host, **C2** shows with 13 M a significantly higher effective molarity than **A2** (EM_i =2.7 M), supporting rigidity as an important design principle. Going from the bidentate to the tridentate guests, the stepwise effective molarity of ***c*-P6•C3** is identical to that of ***c*-P6•C2**, showing a linear dependency of number of binding sites and cooperativity. The reduced chelate cooperativity may arise from the complex geometry or solvation effects. DFT calculations have shown a small shape-mismatch of the host and the guest in ***c*-P6•C3**, which requires a slight induced fit of the host molecule. Alternatively, solvation could impact chelate cooperativity. A strong effect of solvation on the absolute binding energy is well known (since binding constants are an orders of magnitude smaller in chloroform) but this effect may be strongly dependent on the individual system. Interestingly, a significant increase of EM_i is observed for ***c*-P6•A3** between the second and the third binding interaction. This stepwise EM_i is 46 M, which is an increase by a factor of 25. In case of the linear oligomers, an increase in EM_i by a factor of 3 is observed, which qualifies the impact of rigidity in flexible hosts.

Overall, the analysis of effective molarities is not sufficient to develop a model that predicts chelate cooperativity. Trends indicate that the loss of degrees of freedom might be a less significant impact than expected, while the effect of rigidity might have been underestimated. It appears that a prediction of chelate cooperativity based on molecular structure is challenging and additional information are required.

3.10 Conclusion

The relationship between chelate cooperativity and molecular structure was studied in this chapter. Systematic modifications to hosts and guests allowed us to probe whether the cooperativity strength can be related to simple structural parameters. A series of different hosts and guests were analysed with varying shape-complementarity, flexibility, preorganisation, and loss of degrees of freedom upon complex formation. The binding constants and effective molarities for the host-guest series were determined via UV-vis-NIR titrations.

3. Titration Experiments and Exploration of Binding Models

The analysis of the linear porphyrin oligomers gave satisfying results by using a simple binding models. The analysis of the cyclic host ***c*-P6** involved a different methodology. Due to the large variety of different species formed during the titration, several binding models were tested and their ability to represent the experimental data was compared using a statistical approach (extra sum-of-squares *F* test)[125] and the Akaike information criterion.[126] For the tridentate guests, four models were tested: 'effective binding sites'; 'statistically equivalent'; 'sterically hindered'; and 'independent optimisation'. The results showed that the complex formation process for ***c*-P6•X3** cannot be described by a simple fully independent 1:1 model. For the smallest ligand **C3**, the experimental difference between the apparent binding constants for ***c*-P6•C3** and ***c*-P6•C3$_2$** arises from statistical factors. This behaviour is expected, as the ligands show no significant steric interaction. For ***c*-P6•A3** and ***c*-P6•B3**, the first guest clearly influences the binding strength of the second. This results in a binding constant which is an order or magnitude lower for the second guest in comparison to the first one. The analysis of the bidentate ligands is limited to the simple 'statistically equivalent' model as the increased number of species leads to too many variables in the more elaborate model. Therefore, the determined binding constants might represent an average of the complexes ***c*-P6•X1**, ***c*-P6•X1$_2$**, and ***c*-P6•X1$_3$**. The difference between these statistically corrected binding constants is expected to be insignificant as the ***c*-P6** host provides enough flexibility to adapt and accommodate three bidentate guests, a control of the obtained results is not possible.

The obtained effective molarities cannot be related to a simple structural analysis. The trend for the cyclic ***c*-P6** host binding to the guest series **A** and **B** showed the expected correlation between loss of degrees of freedom and reduction of binding affinity. Generally, the results indicate a correlation between an increase in rigidity and chelate cooperativity strength. This conclusion is supported by the surprising results of the guest series **C**. Despite a stronger decrease of degrees of freedom in comparison to the guest series **A**, the highly rigid guest series **C** shows a surprisingly high chelate cooperativity. However, no quantitative relationship was found between molecular structure and the chelate cooperativity. As such, Chapter 4 will discuss the analysis of entropic and enthalpic contributions and investigates a dissection of thermodynamic origins of chelate cooperativity.

3.11 Appendix: Experimental Data for UV-vis-NIR titrations

The raw experimental data for the UV-vis-NIR titration spectra including experiment number for each individual measurement can be found here. Shown is an overlay of the individual spectra (**a**), the absorbance profile of a single (characteristic) wavelength in dependency of the guest concentration for the formation titrations, and in dependency of the pyridine concentration for the denaturation titrations (**b**). All titrations were performed in toluene at 298 K, with constant host concentration.

For a preliminary analysis, the formation titrations were fitted to a 1:1 binding isotherm assuming 'all-or-nothing' behaviour using the equation:

$$\frac{A - A_{initial}}{A_{\infty} - A_{initial}} = \left(\frac{(K_a\,(c\,[L] + [P]_0) + 1) - \sqrt{(K_a\,(c\,[L] + [P]_0) + 1)^2 - 4K_a^2[P]_0 c\,[L]}}{2K_a[P]_0} \right)$$

where A is the observed absorption at a specific wavelength or the difference of absorbance between two wavelengths; $A_{initial}$ is the starting absorption at this wavelength; A_{∞} is the asymptotic final absorption at this wavelength; K_a is the association constant between ligand and porphyrin host; [L] is the concentration of ligand; $[P]_0$ is the concentration of porphyrin host. For an accurate fit, the ligand concentration is multiplied by a scaling factor c which should compensate any errors occurring in the weighing process. The allowed tolerance range for scaling factor c is 15 %.

The denaturation titrations were analysed using the following equation as a first approximation:

$$\frac{A - A_{initial}}{A_{\infty} - A_{initial}} = \left(\frac{-K_{dn}[L]^2 + \sqrt{K_{dn}^2[L]^{2n} + 4K_{dn}[L]^n[P]_0}}{2[P]_0} \right)$$

where A is the observed absorption at a specific wavelength or difference of absorption between two wavelengths; $A_{initial}$ is the starting absorption at a specific wavelength or difference between absorption in two wavelengths; A_{∞} is the terminal absorption at a specific wavelength or difference of absorption in two wavelengths; K_{dn} is the dissociation constant

between ligand and porphyrin oligomer complex, [L] is the concentration of ligand; $[P]_0$ is the concentration of porphyrin oligomer complex, *n* is the number of binding sites in the complex.

Reference titrations with *l*-P1 host

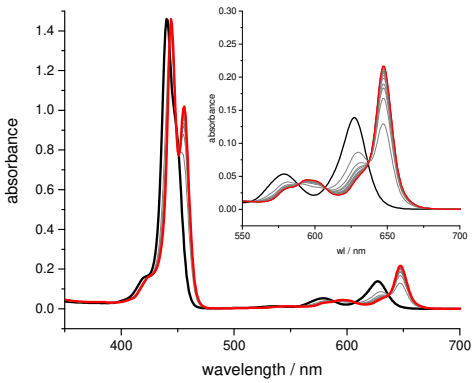

(a) Spectra

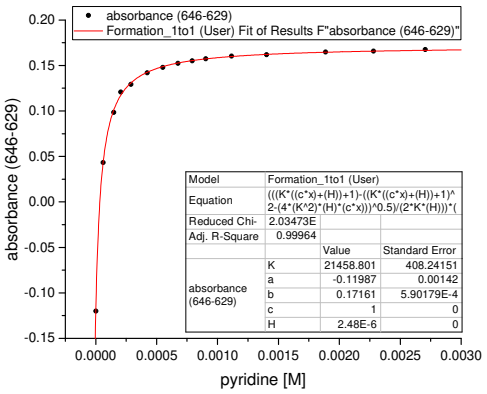

(b) Single wavelength concentration profile

Figure 3.24: UV-Vis titration of **py**and ***l*-P1**. Run 1, toluene, 298 K, [***l*-P1**] = 2.48E-06 M (IG-1-059).

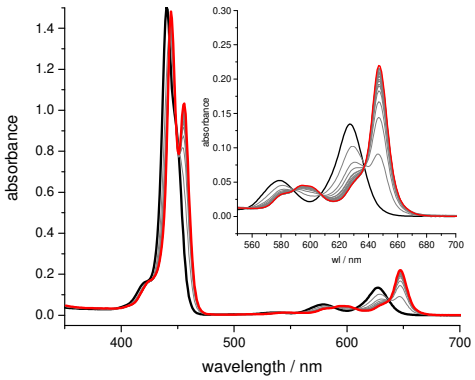

(a) Spectra

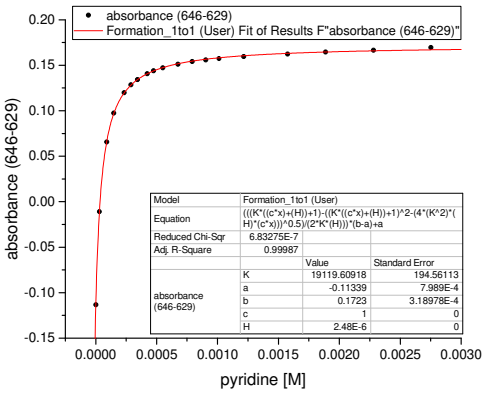

(b) Single wavelength concentration profile

Figure 3.25: UV-Vis titration of **py**and ***l*-P1**. Run 2, toluene, 298 K, [***l*-P1**] = 2.48E-06 M (IG-1-060).

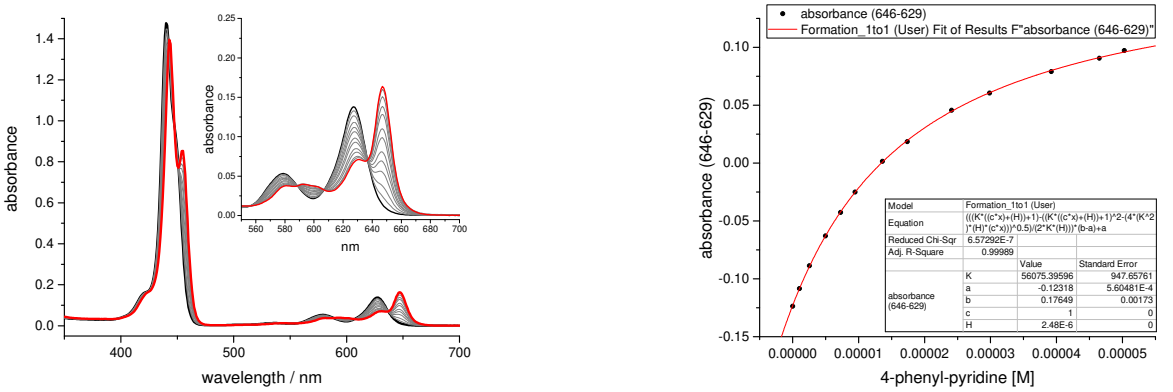

(a) Spectra **(b)** Single wavelength concentration profile

Figure 3.26: UV-Vis titration of **A1** and ***I*-P1**. Run 1, toluene, 298 K, [***I*-P1**] = 2.48E-06 M (IG-1-079).

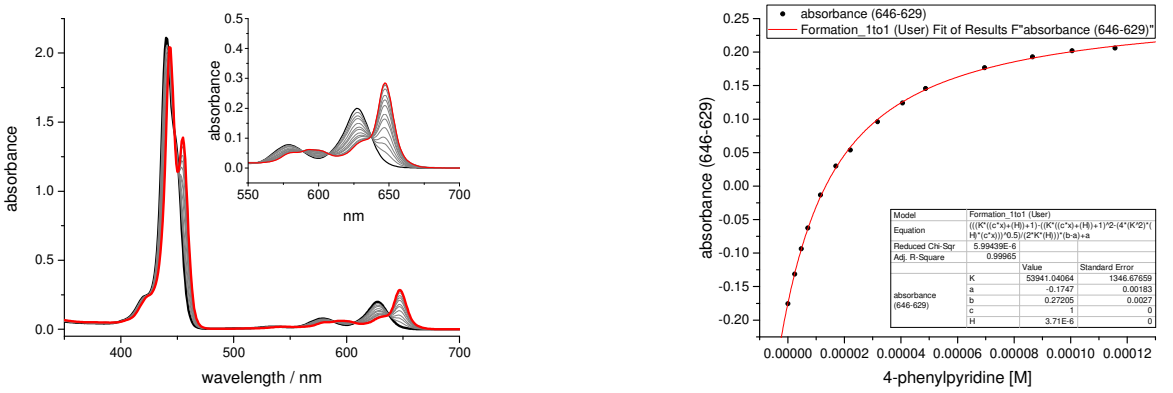

(a) Spectra **(b)** Single wavelength concentration profile

Figure 3.27: UV-Vis titration of **A1** and ***I*-P1**. Run 2, toluene, 298 K, [***I*-P1**] = 3.71E-06 M (IG-1-080).

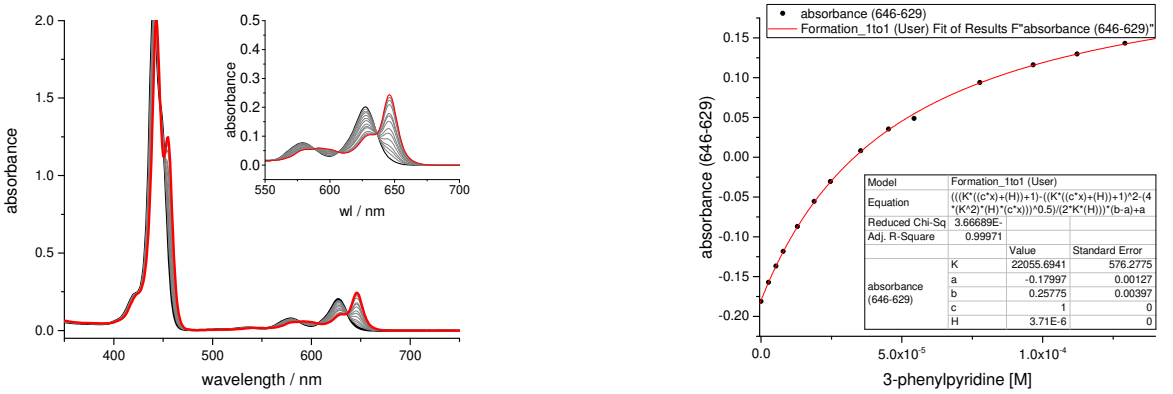

(a) Spectra **(b)** Single wavelength concentration profile

Figure 3.28: UV-Vis titration of **C1** and ***I*-P1**. Run 1, toluene, 298 K, [***I*-P1**] = 3.71E-06 M (IG-1-085).

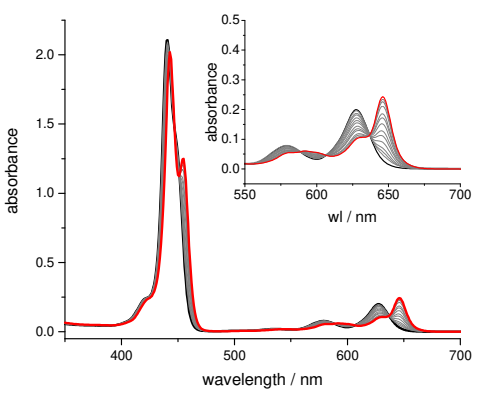

(a) Spectra

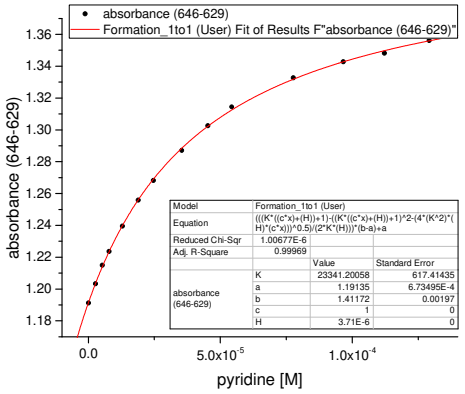

(b) Single wavelength concentration profile

Figure 3.29: UV-Vis titration of **C1** and ***l*-P1**. Run 2, toluene, 298 K, [***l*-P1**] = 3.71E-06 M (IG-1-086).

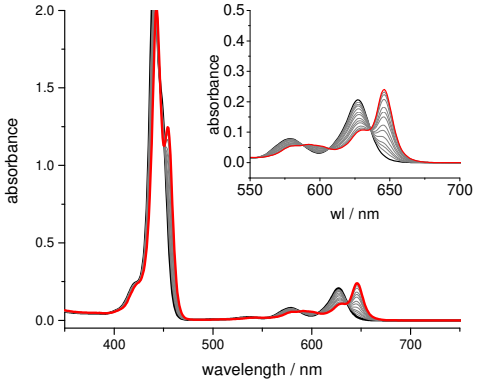

(a) Spectra

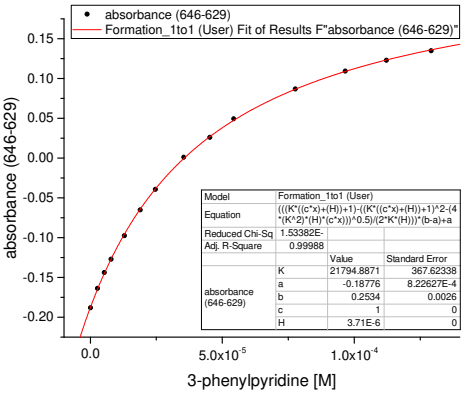

(b) Single wavelength concentration profile

Figure 3.30: UV-Vis titration of **C1** and ***l*-P1**. Run 3, toluene, 298 K, [***l*-P1**] = 3.71E-06 M (IG-1-087).

Titrations with *l*-P2 host

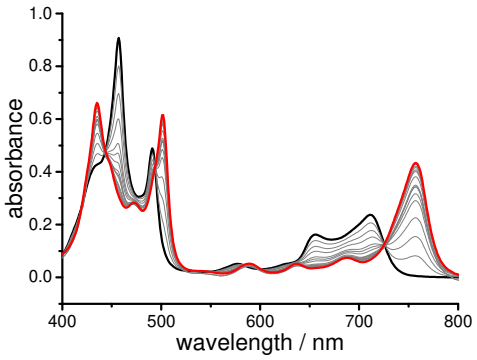

(a) Spectra

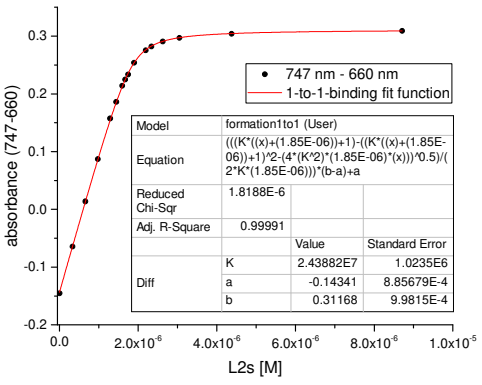

(b) Single wavelength concentration profile

Figure 3.31: UV-Vis titration of **C2** and ***l*-P2**. Run 1, toluene, 298 K, [***l*-P2**] = 1.85E-06 M (IG-1-049).

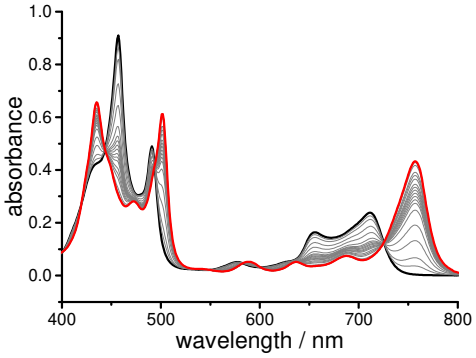

(a) Spectra

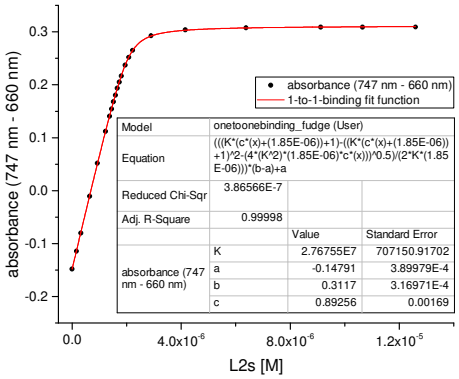

(b) Single wavelength concentration profile

Figure 3.32: UV-Vis titration of **C2** and ***I*-P2**. Run 2, toluene, 298 K, [***I*-P2**] = 1.85E-06 M (IG-1-051).

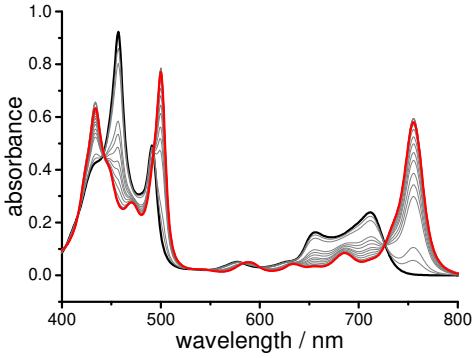

(a) Spectra

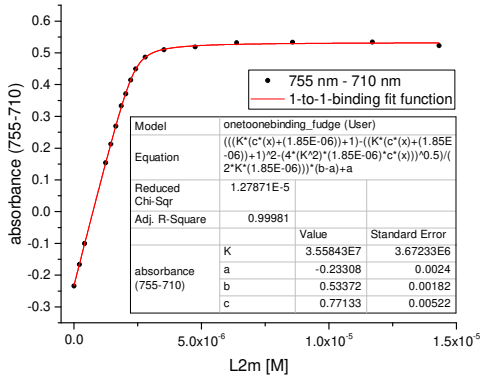

(b) Single wavelength concentration profile

Figure 3.33: UV-Vis titration of **B2** and ***I*-P2**. Run 1, toluene, 298 K, [***I*-P2**] = 1.85E-06 M (IG-1-052).

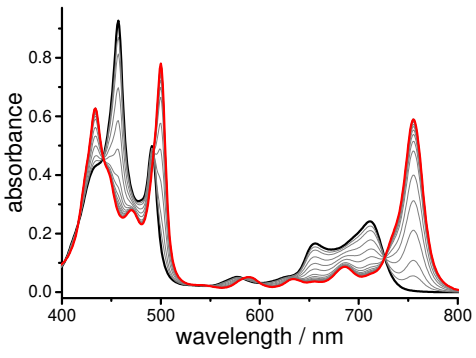

(a) Spectra

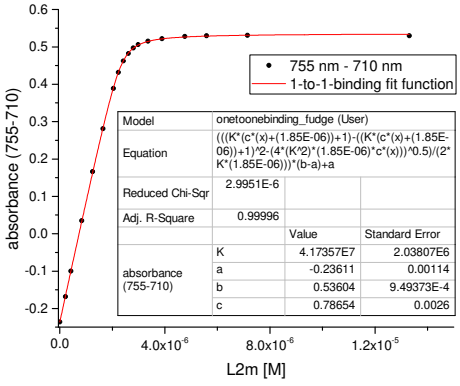

(b) Single wavelength concentration profile

Figure 3.34: UV-Vis titration of **B2** and ***I*-P2**. Run 2, toluene, 298 K, [***I*-P2**] = 1.85E-06 M (IG-1-053).

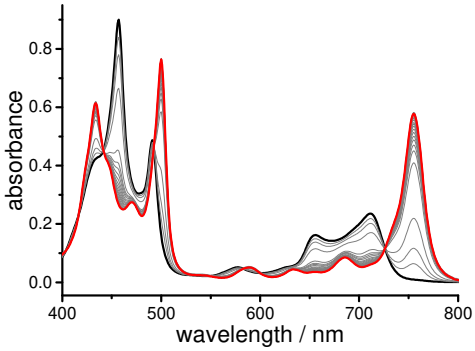

(a) Spectra

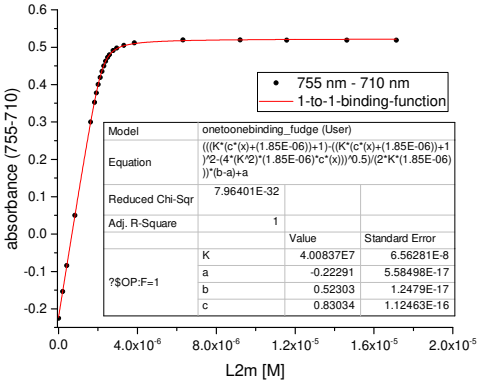

(b) Single wavelength concentration profile

Figure 3.35: UV-Vis titration of **B2** and ***I*-P2**. Run 3, toluene, 298 K, [***I*-P2**] = 1.85E-06 M (IG-1-055).

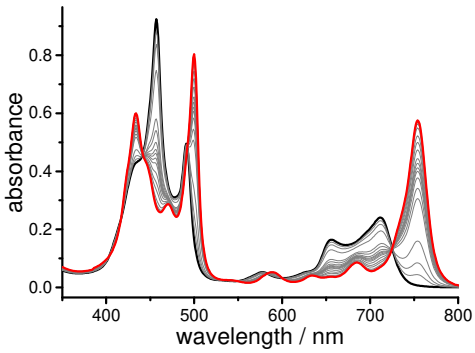

(a) Spectra

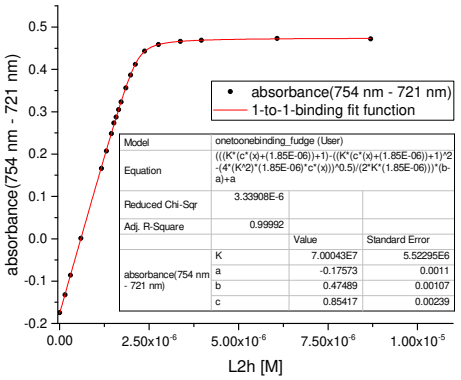

(b) Single wavelength concentration profile

Figure 3.36: UV-Vis titration of **A2** and ***I*-P2**. Run 1, toluene, 298 K, [***I*-P2**] = 1.85E-06 M (IG-1-054).

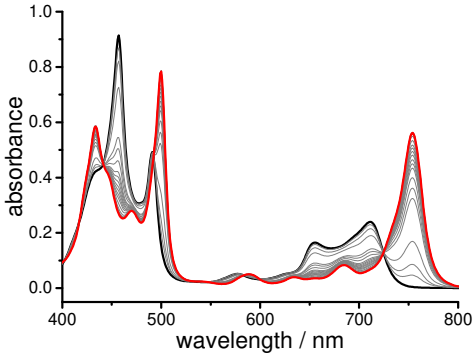

(a) Spectra

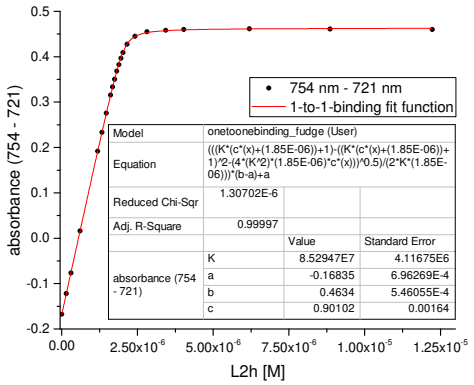

(b) Single wavelength concentration profile

Figure 3.37: UV-Vis titration of **A2** and ***I*-P2**. Run 2, toluene, 298 K, [***I*-P2**] = 1.85E-06 M (IG-1-056).

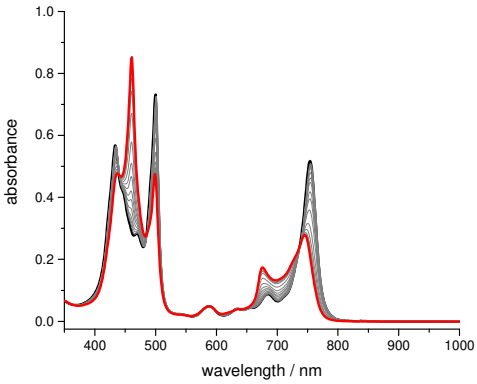

(a) Spectra

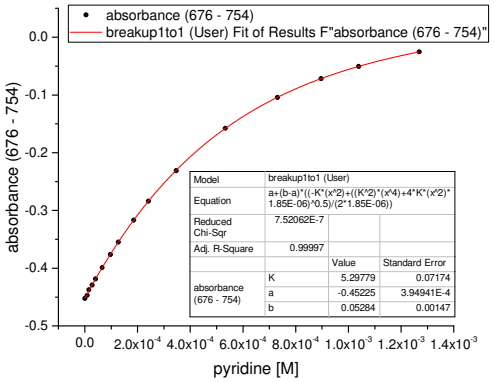

(b) Single wavelength concentration profile

Figure 3.38: UV-Vis breakup titration of **A2** and ***l*-P2**. Run 1, toluene, 298 K, [***l*-P2**] = 1.85E-06 M (IG-1-061).

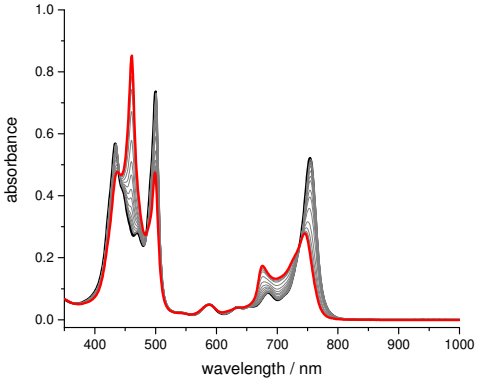

(a) Spectra

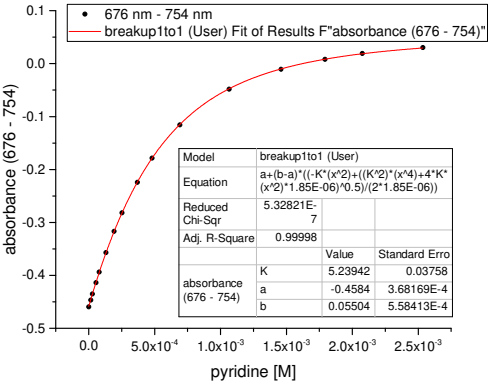

(b) Single wavelength concentration profile

Figure 3.39: UV-Vis breakup titration of **A2** and ***l*-P2**. Run 2, toluene, 298 K, [***l*-P2**] = 1.85E-06 M (IG-1-062).

Titrations with *l*-P3 host

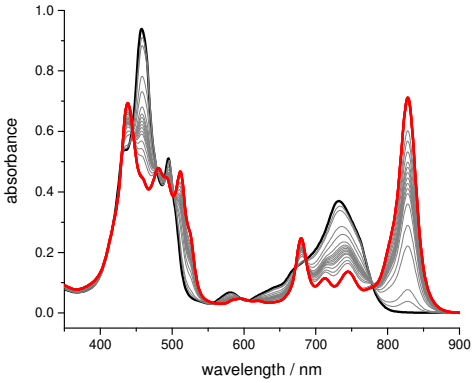

(a) Spectra

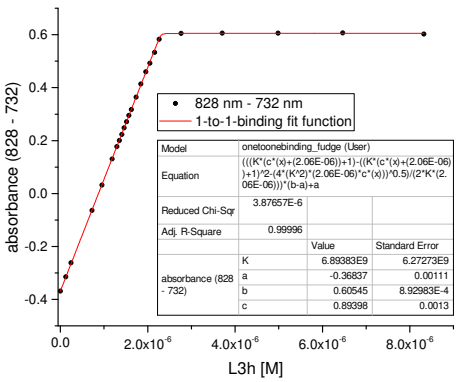

(b) Single wavelength concentration profile

Figure 3.40: UV-Vis titration of **A3** and ***l*-P3**. Run 1, toluene, 298 K, [***l*-P3**] = 2.06E-06 M (IG-1-063).

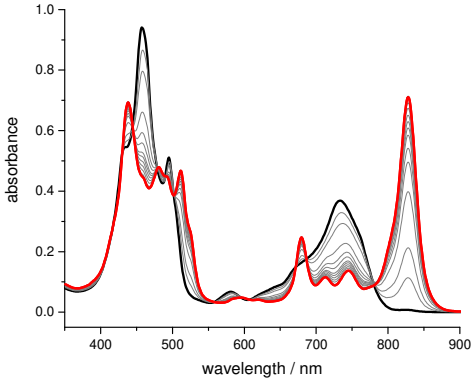

(a) Spectra

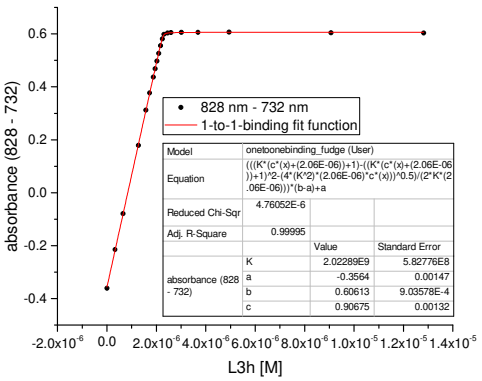

(b) Single wavelength concentration profile

Figure 3.41: UV-Vis titration of **A3** and ***l*-P3**. Run 2, toluene, 298 K, [***l*-P3**] = 2.06E-06 M (IG-1-064).

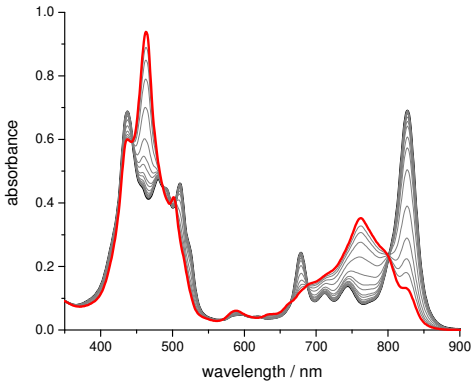

(a) Spectra

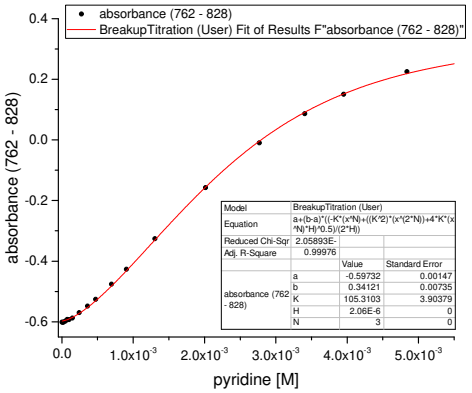

(b) Single wavelength concentration profile

Figure 3.42: UV-Vis breakup titration of the **A3** and ***l*-P3** complex with pyridine. Run 1, toluene, 298 K, [***l*-P3**] = 2.06E-06 M (IG-1-065)

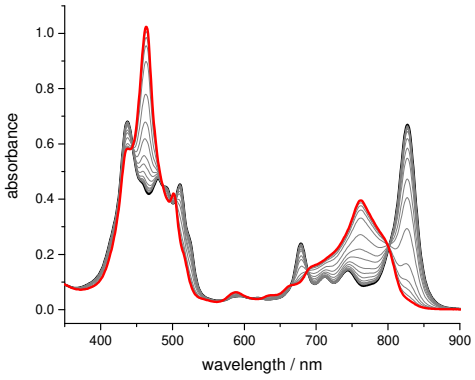

(a) Spectra

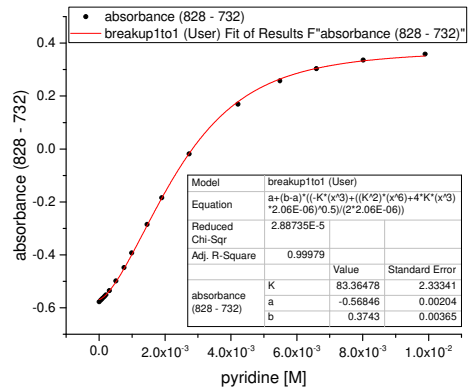

(b) Single wavelength concentration profile

Figure 3.43: UV-Vis breakup titration of the **A3** and ***l*-P3** complex with pyridine. Run 2, toluene, 298 K, [***l*-P3**] = 2.06E-06 M (IG-1-066)

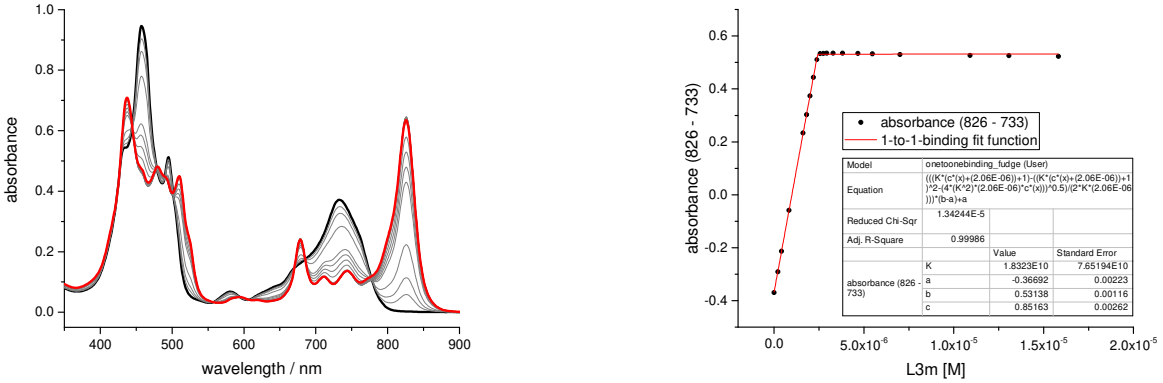

(a) Spectra **(b)** Single wavelength concentration profile

Figure 3.44: UV-Vis titration of the **B3** and ***I*-P3**. Run 1, toluene, 298 K, [***I*-P3**] = 2.06E-06 M (IG-1-068).

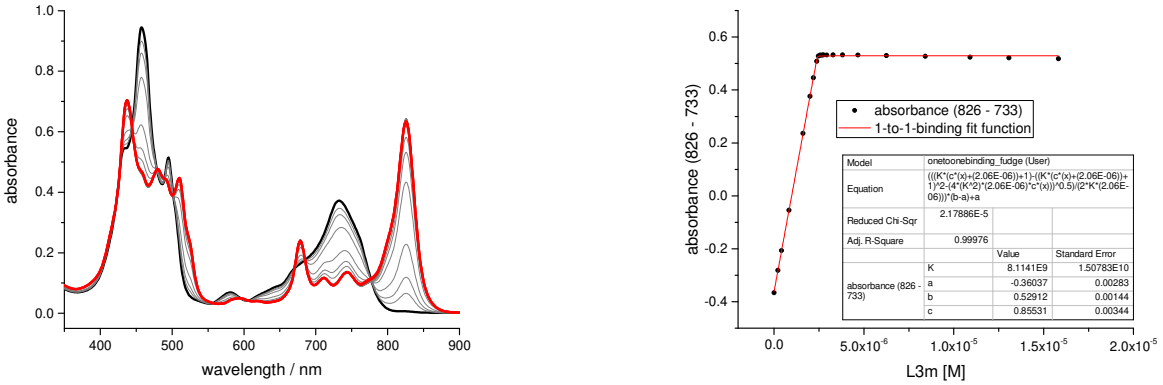

(a) Spectra **(b)** Single wavelength concentration profile

Figure 3.45: UV-Vis titration of the **B3** and ***I*-P3**. Run 2, toluene, 298 K, [***I*-P3**] = 2.06E-06 M (IG-1-069).

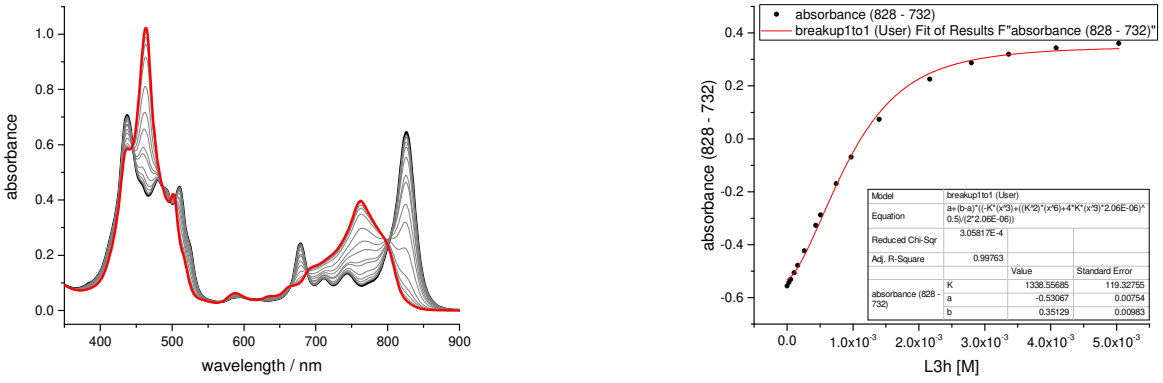

(a) Spectra **(b)** Single wavelength concentration profile

Figure 3.46: UV-Vis breakup titration of the **B3** and ***I*-P3** complex with pyridine. Run 1, toluene, 298 K, [***I*-P3**] = 2.06E-06 M (IG-1-070).

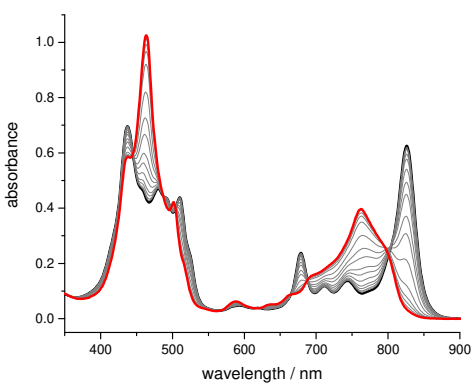

(a) Spectra

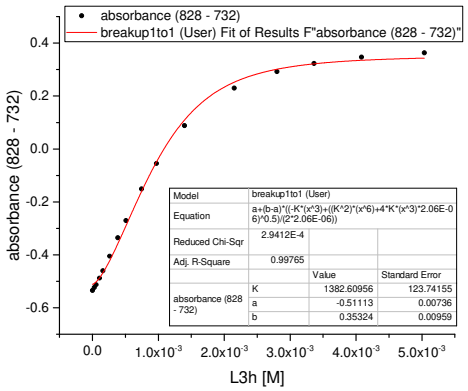

(b) Single wavelength concentration profile

Figure 3.47: UV-Vis breakup titration of the **B3** and ***I*-P3** complex with pyridine. Run 2, toluene, 298 K, [***I*-P3**] = 2.06E-06 M (IG-1-071).

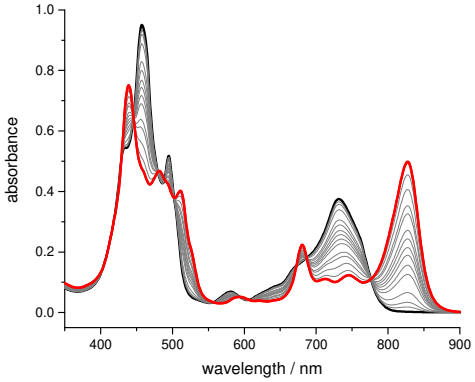

(a) Spectra

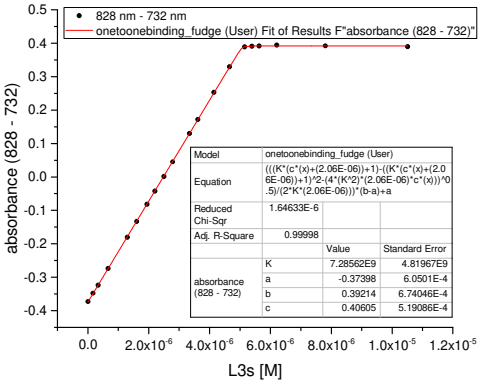

(b) Single wavelength concentration profile

Figure 3.48: UV-Vis titration of the **C3** and ***I*-P3**. Run 1, toluene, 298 K, [***I*-P3**] = 2.06E-06 M (IG-1-072).

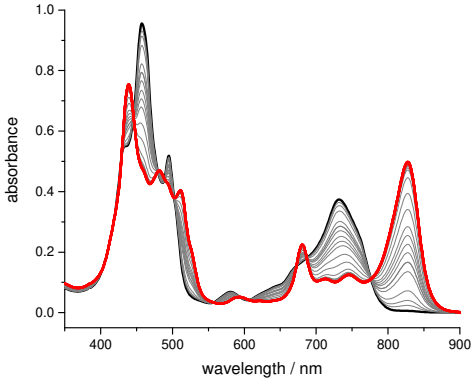

(a) Spectra

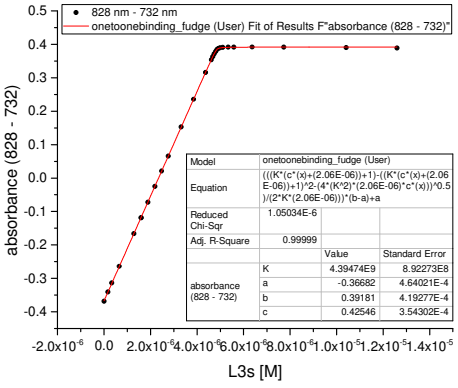

(b) Single wavelength concentration profile

Figure 3.49: UV-Vis titration of the **C3** and ***I*-P3**. Run 2, toluene, 298 K, [***I*-P3**] = 2.06E-06 M (IG-1-073).

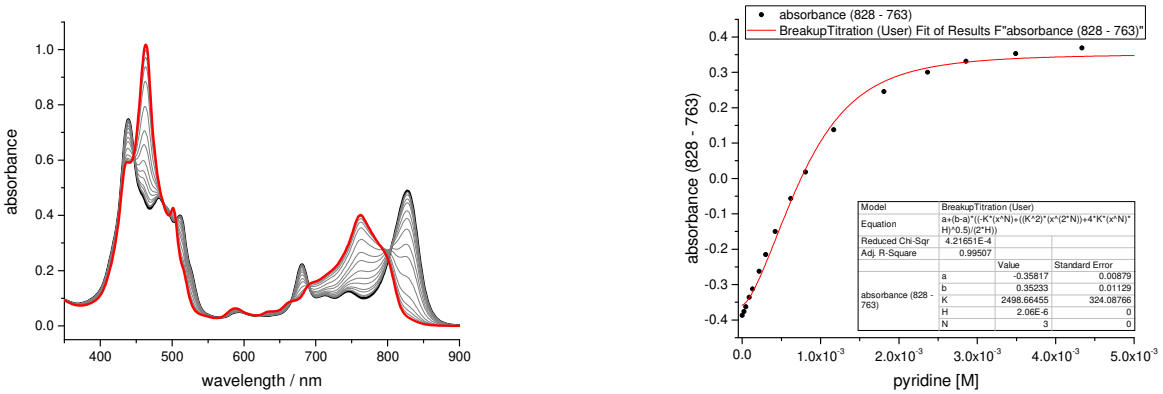

(a) Spectra **(b)** Single wavelength concentration profile

Figure 3.50: UV-Vis break-up titration of the **C3** and ***I*-P3**. Run 1, toluene, 298 K, [***I*-P3**] = 2.06E-06 M (IG-1-075).

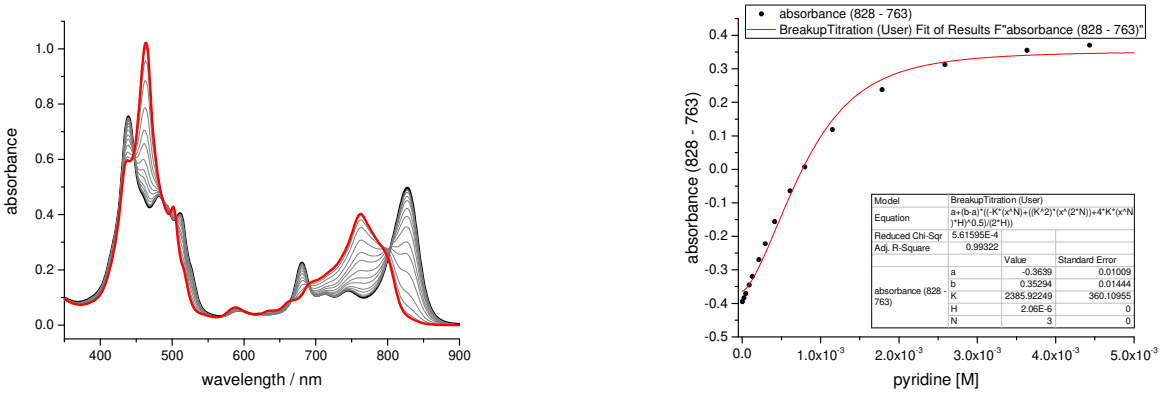

(a) Spectra **(b)** Single wavelength concentration profile

Figure 3.51: UV-Vis break-up titration of the **C3** and ***I*-P3**. Run 2, toluene, 298 K, [***I*-P3**] = 2.06E-06 M (IG-1-078).

Reference titrations with *c*-P6 host

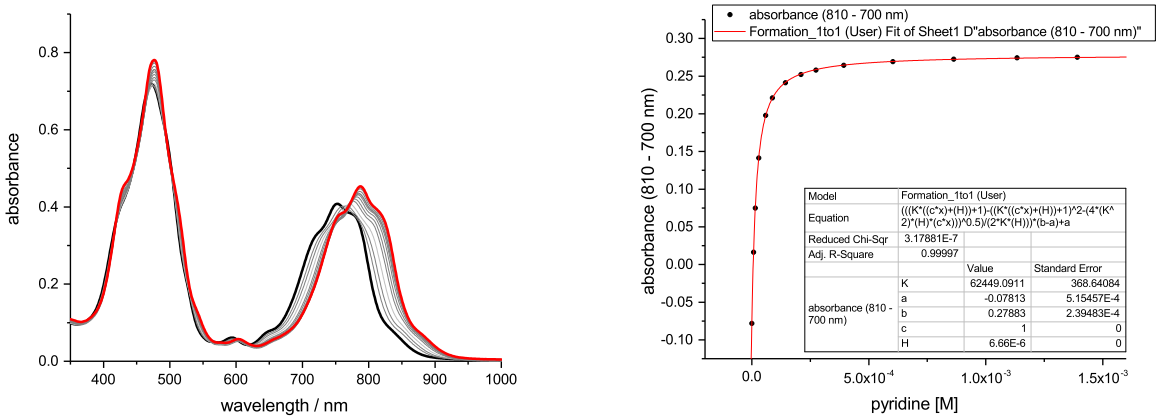

(a) Spectra **(b)** Single wavelength concentration profile

Figure 3.52: UV-Vis titration of **py**and ***c*-P6**. Run 1, toluene, 298 K, [***c*-P6**] = 1.22E-06 M (IG-2-79).

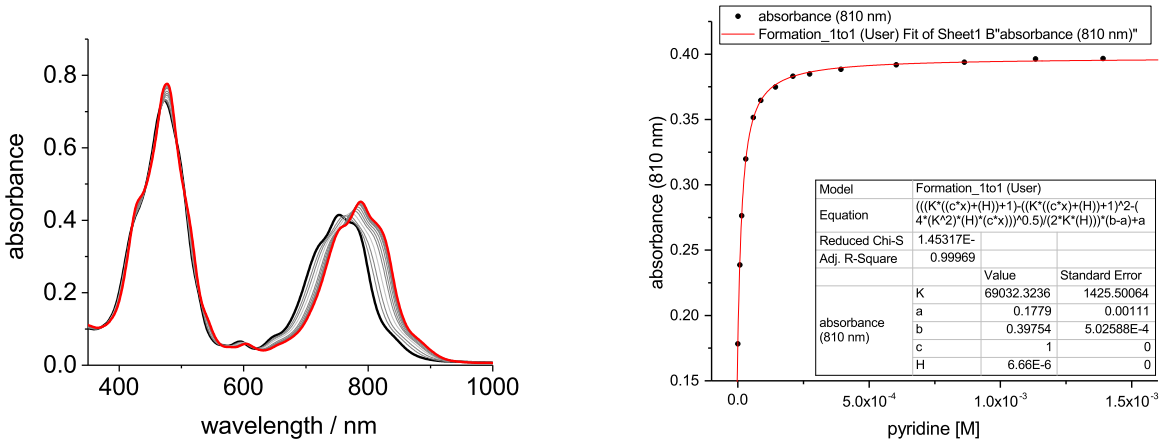

(a) Spectra **(b)** Single wavelength concentration profile

Figure 3.53: UV-Vis titration of **py**and ***c*-P6**. Run 1, toluene, 298 K, [***c*-P6**] = 1.22E-06 M (IG-2-86).

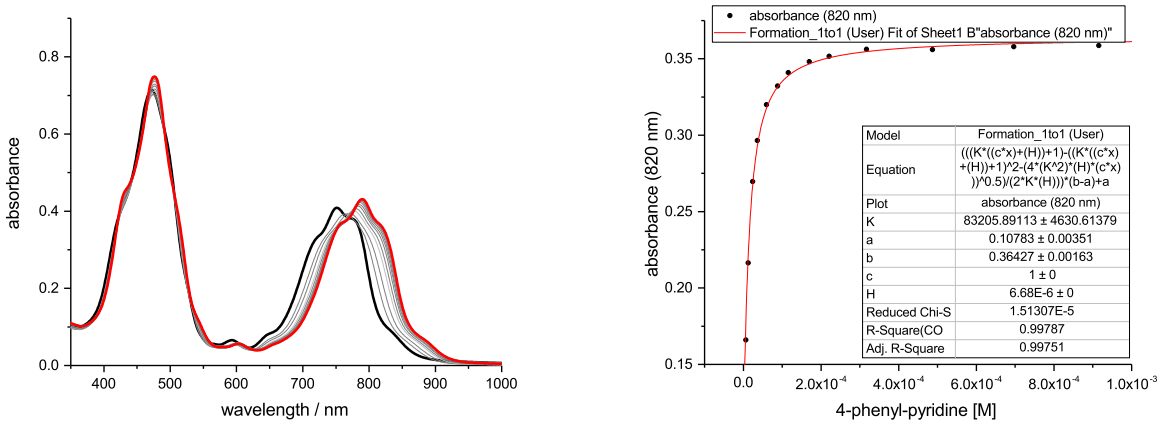

(a) Spectra **(b)** Single wavelength concentration profile

Figure 3.54: UV-Vis titration of **A1** and ***c*-P6**. Run 1, toluene, 298 K, [***c*-P6**] = 1.22E-06 M (IG-2-89).

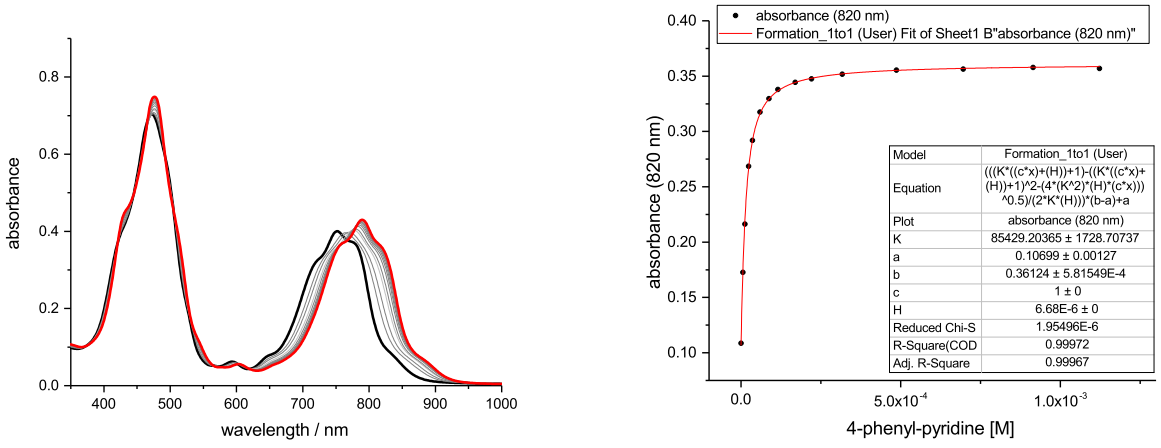

(a) Spectra **(b)** Single wavelength concentration profile

Figure 3.55: UV-Vis titration of **A1** and ***c*-P6**. Run 1, toluene, 298 K, [***c*-P6**] = 1.22E-06 M (IG-2-89).

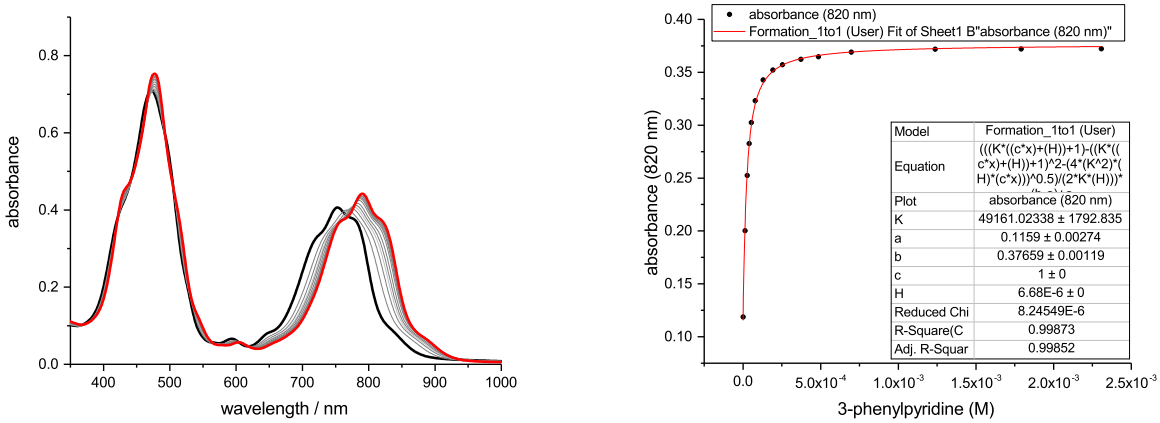

(a) Spectra **(b)** Single wavelength concentration profile

Figure 3.56: UV-Vis titration of **C1** and ***c*-P6**. Run 1, toluene, 298 K, [***c*-P6**] = 1.22E-06 M (IG-2-91).

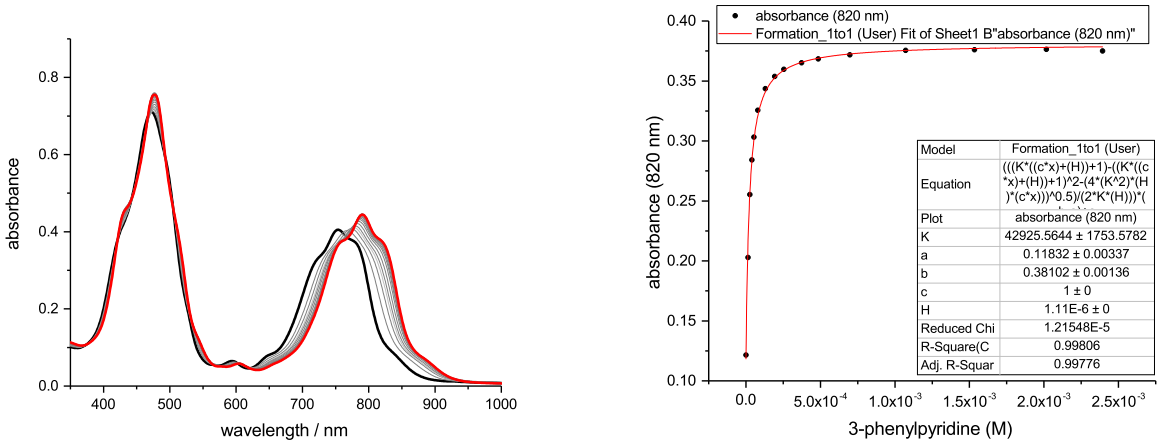

(a) Spectra **(b)** Single wavelength concentration profile

Figure 3.57: UV-Vis titration of **C1** and ***c*-P6**. Run 1, toluene, 298 K, [***c*-P6**] = 1.22E-06 M (IG-2-91).

Titrations with *c*-P6 host

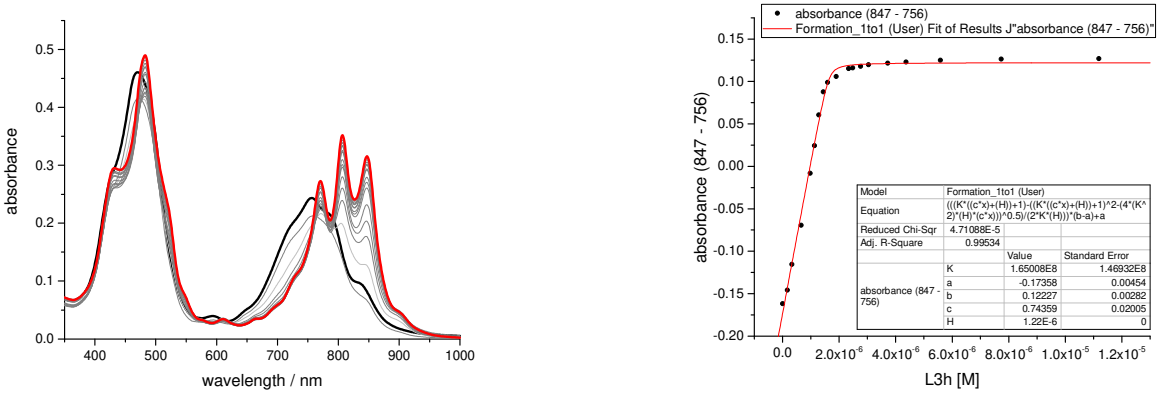

(a) Spectra **(b)** Single wavelength concentration profile

Figure 3.58: UV-Vis titration of **A3** and ***c*-P6**. Run 1, toluene, 298 K, [***c*-P6**] = 1.22E-06 M (IG-2-49).

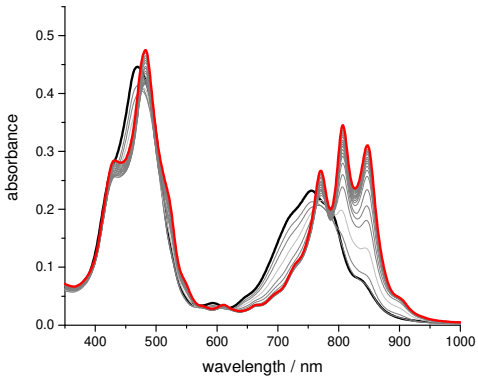

(a) Spectra

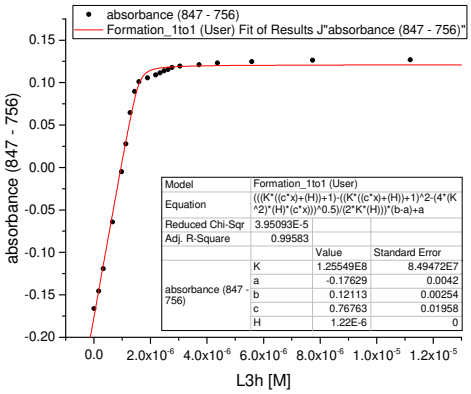

(b) Single wavelength concentration profile

Figure 3.59: UV-Vis titration of **A3** and ***c*-P6**. Run 2, toluene, 298 K, [***c*-P6**] = 1.22E-06 M (IG-2-52).

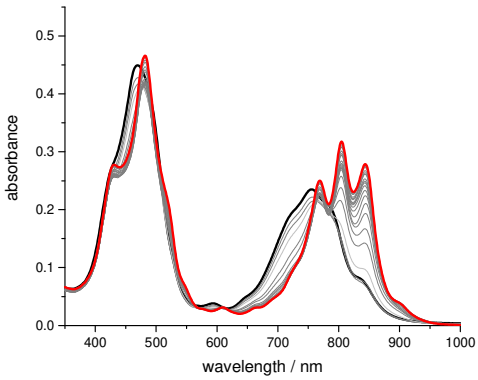

(a) Spectra

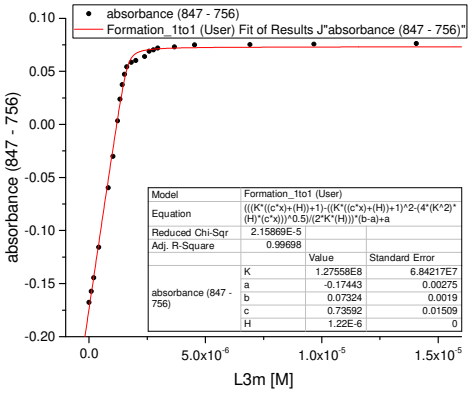

(b) Single wavelength concentration profile

Figure 3.60: UV-Vis titration of **B3** and ***c*-P6**. Run 1, toluene, 298 K, [***c*-P6**] = 1.22E-06 M (IG-2-51).

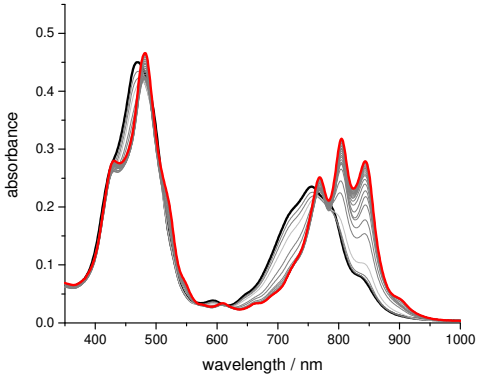

(a) Spectra

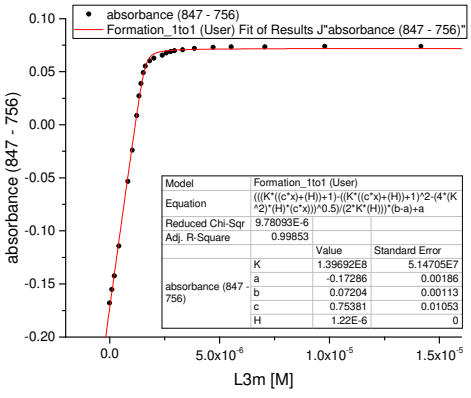

(b) Single wavelength concentration profile

Figure 3.61: UV-Vis titration of **B3** and ***c*-P6**. Run 2, toluene, 298 K, [***c*-P6**] = 1.22E-06 M (IG-2-54).

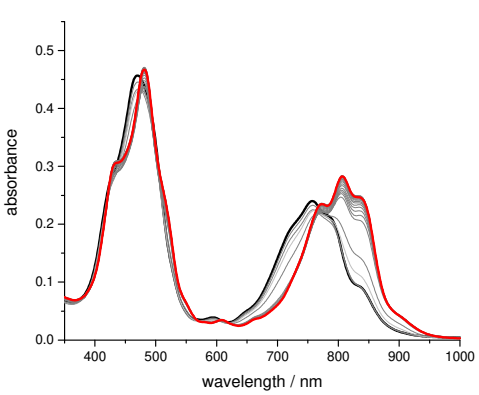

(a) Spectra

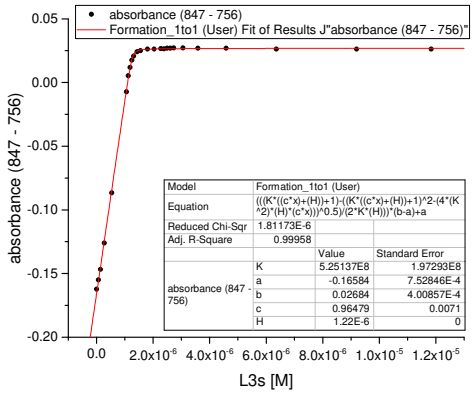

(b) Single wavelength concentration profile

Figure 3.62: UV-Vis titration of **C3** and ***c*-P6**. Run 1, toluene, 298 K, [***c*-P6**] = 1.22E-06 M (IG-2-56).

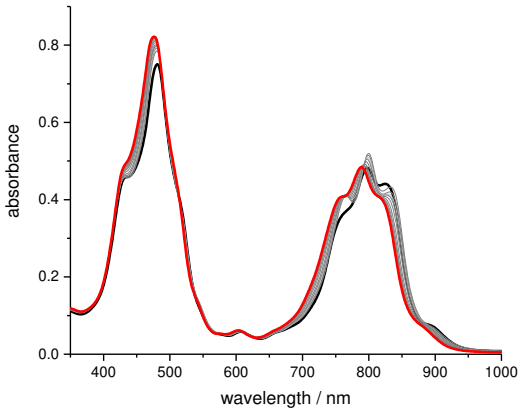

(a) Spectra

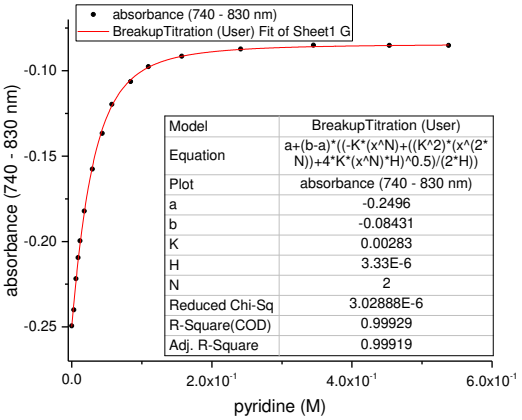

(b) Single wavelength concentration profile

Figure 3.63: V-Vis titration of pyridine and ***c*-P6•A2**. Run 1, toluene, 298 K, [***c*-P6**] = 1.11E-07 M (IG-2-82).

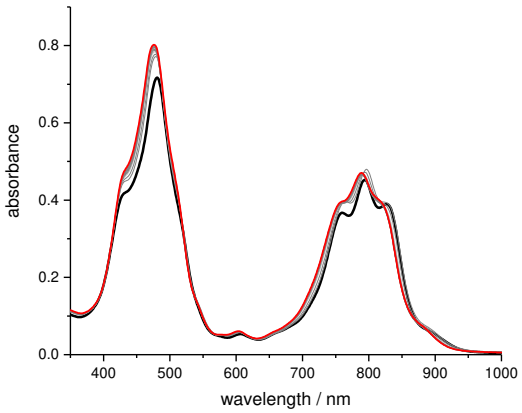

(a) Spectra

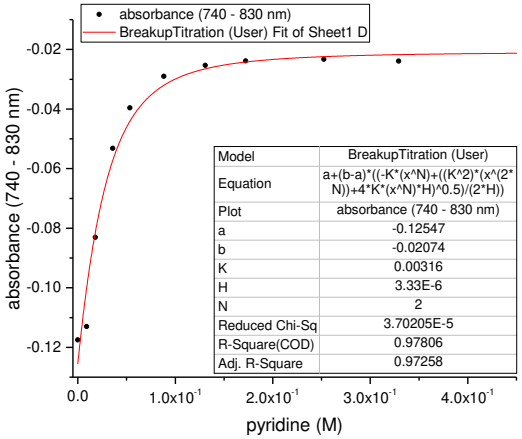

(b) Single wavelength concentration profile

Figure 3.64: UV-Vis titration of pyridine and ***c*-P6•A2**. Run 2, toluene, 298 K, [***c*-P6**] = 1.11E-07 M (IG-2-82).

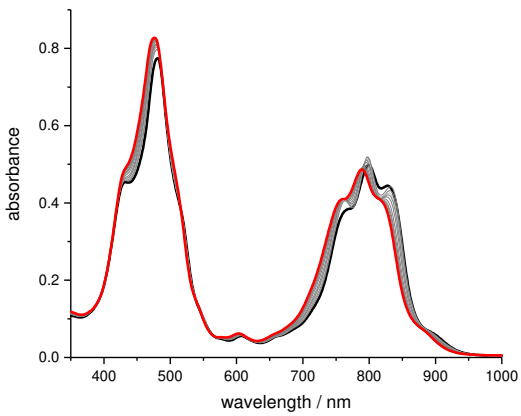

(a) Spectra

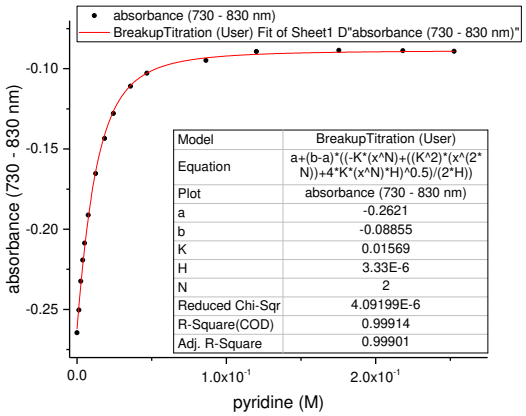

(b) Single wavelength concentration profile

Figure 3.65: UV-Vis titration of pyridine and ***c*-P6•B2**. Run 1, toluene, 298 K, [***c*-P6**] = 1.11E-07 M (IG-2-84).

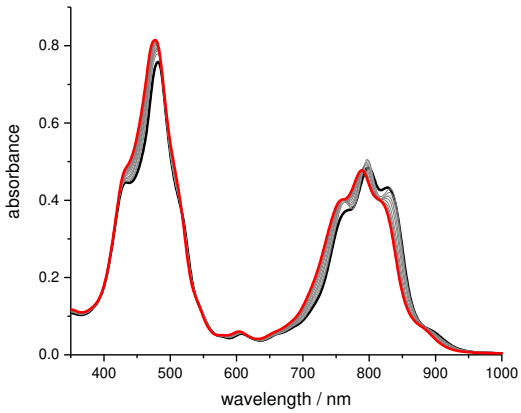

(a) Spectra

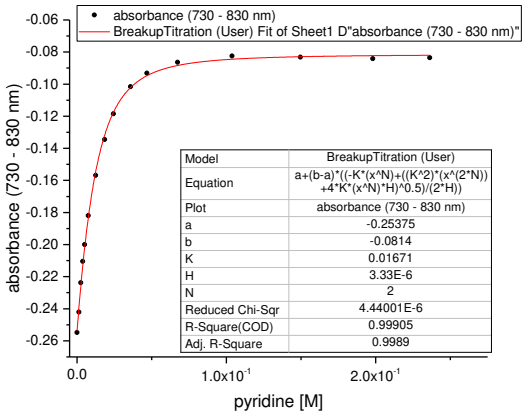

(b) Single wavelength concentration profile

Figure 3.66: UV-Vis titration of pyridine and ***c*-P6•B2**. Run 2, toluene, 298 K, [***c*-P6**] = 1.11E-07 M (IG-2-84).

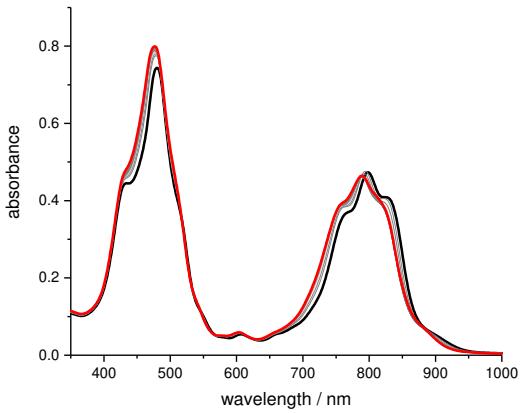

(a) Spectra

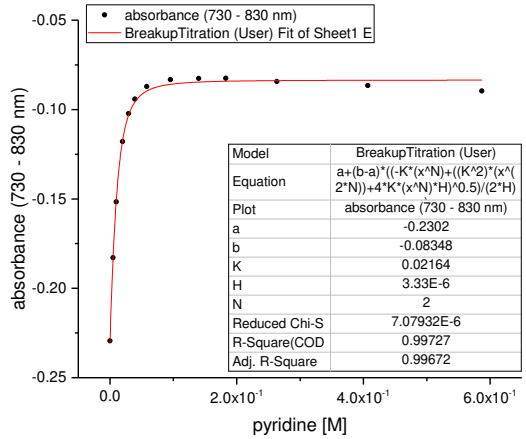

(b) Single wavelength concentration profile

Figure 3.67: UV-Vis titration of pyridine and ***c*-P6•C2**. Run 1, toluene, 298 K, [***c*-P6**] = 1.11E-07 M (IG-2-83).

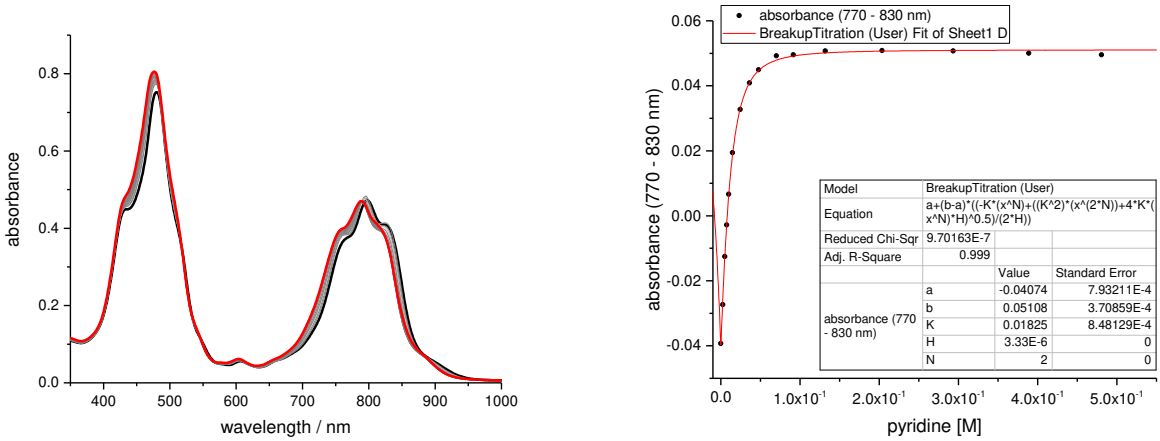

(a) Spectra **(b)** Single wavelength concentration profile

Figure 3.68: UV-Vis titration of pyridine and ***c*-P6•C2**. Run 2, toluene, 298 K, [***c*-P6**] = 1.11E-07 M (IG-2-83).

4

Analysis of the Contributions of Enthalpy and Entropy to Cooperativity

Contents

4.1 Abstract

In this chapter, the influence of enthalpy and entropy on chelate cooperativity was studied. Binding constants were determined via UV-vis-NIR titrations and translated into Gibbs energy.

The chapter introduction describes enthalpy and entropy from a statistical thermodynamics perspective and presents methods to determine enthalpy directly. Within this study, enthalpy was determined directly via ITC and van't Hoff experiments, while entropy was calculated from Gibbs energy and enthalpy.

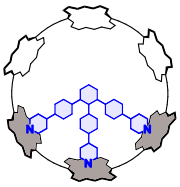

(a) *c*-P6•A3

$\Delta G^*_{coop} = -15.0\,\mathrm{kJ\,mol^{-1}}$
$\Delta H_{coop} = 11\,\mathrm{kJ\,mol^{-1}}$
$-T\Delta S^*_{coop} = -26\,\mathrm{kJ\,mol^{-1}}$

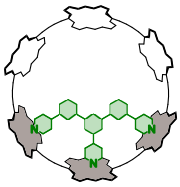

(b) *c*-P6•B3

$\Delta G^*_{coop} = -9.6\,\mathrm{kJ\,mol^{-1}}$
$\Delta H_{coop} = 33\,\mathrm{kJ\,mol^{-1}}$
$-T\Delta S^*_{coop} = -43\,\mathrm{kJ\,mol^{-1}}$

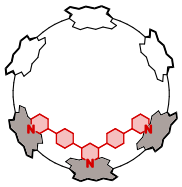

(c) *c*-P6•C3

$\Delta G^*_{coop} = -22.9\,\mathrm{kJ\,mol^{-1}}$
$\Delta H_{coop} = -11\,\mathrm{kJ\,mol^{-1}}$
$-T\Delta S^*_{coop} = -11\,\mathrm{kJ\,mol^{-1}}$

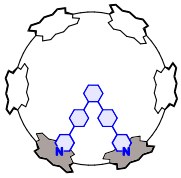

(d) *c*-P6•A2

$\Delta G^*_{coop} = -2.4\,\mathrm{kJ\,mol^{-1}}$
$\Delta H_{coop} = 7\,\mathrm{kJ\,mol^{-1}}$
$-T\Delta S^*_{coop} = -9\,\mathrm{kJ\,mol^{-1}}$

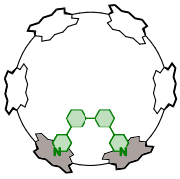

(e) *c*-P6•B2

$\Delta G^*_{coop} = -0.5\,\mathrm{kJ\,mol^{-1}}$
$\Delta H_{coop} = 13\,\mathrm{kJ\,mol^{-1}}$
$-T\Delta S^*_{coop} = -14\,\mathrm{kJ\,mol^{-1}}$

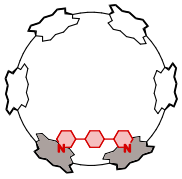

(f) *c*-P6•C2

$\Delta G^*_{coop} = -6.4\,\mathrm{kJ\,mol^{-1}}$
$\Delta H_{coop} = -16\,\mathrm{kJ\,mol^{-1}}$
$-T\Delta S^*_{coop} = 10\,\mathrm{kJ\,mol^{-1}}$

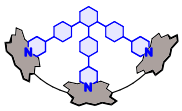

(g) *l*-P3•A3

$\Delta G^*_{coop} = 20.5\,\mathrm{kJ\,mol^{-1}}$
$\Delta H_{coop} = 57\,\mathrm{kJ\,mol^{-1}}$
$-T\Delta S^*_{coop} = -37\,\mathrm{kJ\,mol^{-1}}$

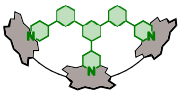

(h) *l*-P3•B3

$\Delta G^*_{coop} = 25.6\,\mathrm{kJ\,mol^{-1}}$
$\Delta H_{coop} = 61\,\mathrm{kJ\,mol^{-1}}$
$-T\Delta S^*_{coop} = -35\,\mathrm{kJ\,mol^{-1}}$

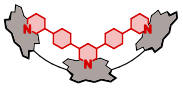

(i) *l*-P3•C3

$\Delta G^*_{coop} = 19.7\,\mathrm{kJ\,mol^{-1}}$
$\Delta H_{coop} = 29\,\mathrm{kJ\,mol^{-1}}$
$-T\Delta S^*_{coop} = -9\,\mathrm{kJ\,mol^{-1}}$

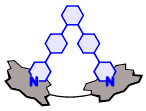

(j) *l*-P2•A2

$\Delta G^*_{coop} = 10.2\,\mathrm{kJ\,mol^{-1}}$
$\Delta H_{coop} = 20\,\mathrm{kJ\,mol^{-1}}$
$-T\Delta S^*_{coop} = -10\,\mathrm{kJ\,mol^{-1}}$

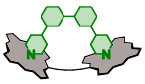

(k) *l*-P2•B2

$\Delta G^*_{coop} = 14.8\,\mathrm{kJ\,mol^{-1}}$
$\Delta H_{coop} = 46.0\,\mathrm{kJ\,mol^{-1}}$
$-T\Delta S^*_{coop} = -31\,\mathrm{kJ\,mol^{-1}}$

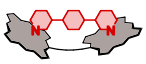

(l) *l*-P2•C2

$\Delta G^*_{coop} = 5.2\,\mathrm{kJ\,mol^{-1}}$
$\Delta H_{coop} = 5.2\,\mathrm{kJ\,mol^{-1}}$
$-T\Delta S^*_{coop} = 0\,\mathrm{kJ\,mol^{-1}}$

Figure 4.1: Comparison of experimental Gibbs energy of chelation (ΔG^*_{coop}), and their separation in enthalpic (ΔH_{coop}) and entropic ($-T\Delta S^*_{coop}$) contributions. (298 K, toluene, Ar=3,5-bis(trihexylsilyl)phenyl as solubilising group)

Comparing the chelation enthalpy (ΔH_{coop}) and entropy ($-T\Delta S^*_{coop}$), the difference in energy between the intra- and the intermolecular system, shows that the gain in entropy is

the driving force for (almost) all intramolecular processes (Fig. 4.1). This gain comes with a cost; overall, the chelation enthalpy becomes less favourable. By linking two binding sites in the guest together, flexibility is lost to reach the perfect host-guest binding geometry. Interestingly, the flexible systems (guest series **B**) did not exhibit the expected loss in entropy, but exhibit entropy-enthalpy compensation. The thermodynamic driving force for chelate cooperativity in guest series **C** strongly depends on the host molecule, indicating that additional effects such as solvation effects dominate the chelation energy.

4.2 Introduction

The strength of chelate cooperativity is influenced by various factors. The binding strength can be increased by favourable enthalpic and entropic contributions. However, as is the case of most chemical reactions, a balance between a strong enthalpic bond and a loss in degrees of freedom has to be found. If the unbound shape of the host and the guest are significantly different to the complexed form, strain energy is induced. For small-molecule complexes, the induced strain energy can reduce the association constant by several orders of magnitude.[131] Using molecular modelling is helpful to design a efficiently binding host-guest system. Recent findings confirm that, for an optimal affinity, the enthalpic advantage of an induced fit with more flexible host components can out-weigh the disadvantage of (entropic) conformational restriction in the host.[132] Enthalpic contributions are straight forward to measure, are temperature independent and additive. However, entropic contributions are difficult to partition, as ΔS values depend on the choice of the standard concentration and since entropy determination is indirect, measurement uncertainties are in general higher. Due to these issues in separating entropic and enthalpic contributions, there is a general confusion about entropy-enthalpy compensation reported in literature.

We will address the definition of binding energy from a statistical thermodynamics point of view and continue to explore the decomposition of enthalpy and entropy for inter- and intramolecular interactions.

4.2.1 Free Energy of Binding in Statistical Thermodynamics

In order to understand the effect of entropy and enthalpy on the studied host-guest systems, we will repeat their definitions in statistical thermodynamics. This section provides

background information to understand the theory of non-covalent binding. The free energy F can be seen as a quantitative measure of the stability at thermal equilibrium. On a microscopic level, a negative free energy relates to a higher stability. As a result the partition function, a statistical weight to describe the probability of state occupancy, increases with decreasing free energy. Therefore, the free energy can be expressed as a function of the partition function (Q):

$$F = -k_\mathrm{B} T \ln(Q) \tag{4.1}$$

For a quantised system with discrete energy values, the partition function corresponds to the canonical ensemble and can be written as the sum over all microstates (j):

$$Q = \sum_j e^{-k_\mathrm{B} T E_j} \tag{4.2}$$

The relationship between the free energy and the Gibbs free energy G is given by:

$$G = F + pV \tag{4.3}$$

with p as pressure and V as volume. Under constant pressure and volume (typical approximated experimental conditions), the Gibbs energy is proportional to the free energy.

Considering a reaction in which two molecules A and B form the complex C with the concentrations C_R, respectively: If the microstates can be partitioned in three non-overlapping macrostates A, B, and C, the partition function can be written as the sum of the macrostate functions. The probability of each macrostate is proportional to the ratio of the partition function of the macrostate to the overall partition function. Assuming the only significant interaction occurs between the two binding molecules A and B (and therefore treat the solvent implicitly) the Gibbs energy for this process is defined as:

$$\Delta G_b = \mu_\mathrm{C} - (\mu_\mathrm{A} + \mu_\mathrm{B}) = -k_\mathrm{B} T \ln\left(\frac{C_\mathrm{A} C_\mathrm{B}}{C_\mathrm{C}} K_\mathrm{a}\right) \tag{4.4}$$

where μ_R is the chemical potential of molecule R and K_a is the binding constant defined as the ratio of the reaction products to the starting components.[133] Dividing the macroscopic partition function for each component by the volume allows the binding constant to be expressed in terms of the equilibrium concentrations of the individual species.

$$K_a \equiv \left(\frac{Q_C/V}{(Q_A/V)(Q_B/V)}\right) = \left(\frac{(C_C)_{eq}}{(C_A)_{eq}(C_B)_{eq}}\right) \tag{4.5}$$

Once the composition reaches thermal equilibrium (where the binding free energy is equal to 0), the binding constant K_a determines the concentrations at which the three species exist in solution.

Even though the values are provided on different scales, the Gibbs free energy and the binding constant are equally able to describe the binding affinity of a system. Both are expressed in reference to the concentration of all species. In general, the Gibbs energy for a binding process is given at standard state conditions (concentration is 1 M in chemistry and $10^{-}7$ M in biology, temperature is 298 K, and pressure is 1 atm)[134] while the binding constant is given in the order 1 M without prefix and its actual dimension depends on the explicit system.[135]

4.2.1.1 Enthalpy-Entropy Segregation of Binding Free Energy

The entropy component of the binding free energy is given as the derivative of the Gibbs energy in relation to temperature:

$$\Delta S_b = \left(\frac{\partial \Delta G_b}{\partial T}\right)_{P,N_A} = k_B \ln\left(\frac{C_A C_B}{C_C} K_a\right) + k_B T \left(\frac{\partial \ln K_a}{\partial T}\right)_P + k_B T \left(\frac{\partial}{\partial T} \ln \frac{C_A C_B}{C_C}\right)_{P,N_A} \tag{4.6}$$

Under constant pressure and number of molecules, the concentration is a function of temperature due to volume changes, leading to the last term in the expression for entropy. This can be transferred to the thermal expansion factor, which is generally insignificant for solutions and will be neglected. This leads to the description of binding entropy as:

$$\Delta S_b = k_B \ln\left(\frac{C_A C_B}{C_C} K_a\right) + k_B T \left(\frac{\partial \ln K_a}{\partial T}\right)_P \tag{4.7}$$

The first term illustrates entropy's concentration dependence. As a result, the value of ΔS_b depends on the choice of (the standard) concentration. The conventional value of 1 M does not bear any physical significance and is historical in nature. The Gibbs free energy, enthalpy and entropy are related via the Gibbs function,

$$\Delta H_b = \Delta G_b - T \Delta S_b \tag{4.8}$$

which leads to the expression for the concentration-independent binding enthalpy as:

$$\Delta H_b = -k_B T^2 \left(\frac{\partial \ln K_a}{\partial T}\right)_P \tag{4.9}$$

Thus, changing the arbitrarily selected value of the standard concentration shifts both the standard free energy and the standard entropy of binding, but does not affect the enthalpy change. The concentration dependence of entropy should not be confused with the later discussed entropy-enthalpy compensation, as a change in concentration shifts the entropy of all involved species by a constant value, without influencing any possible correlation between ΔS_b and ΔH_b.

4.2.1.2 Changes in Entropy upon Binding

Although entropy is a property of a whole system, it can be useful to divide the change in binding entropy into two components: the configurational entropy, which is related to the components actively involved in the binding process (A,B, and C in our example) and the solvent entropy, which summarises changes in solvent motion introduced by the binding reaction. Both can be determined by analysing the change in degrees of freedom.

The configurational entropy relates to the change in degrees of freedom between the bound host-guest complex and the unbound host and guest. Different theoretical approaches exist for the experimental evaluation of configurational entropy and its theoretical partition into translational, rotational, and internal parts. Plenty of theoretical approaches exist to determine translational entropy changes, since the change in translation and overall rotations (which is to be distinguished from internal rotations in a complex molecule) upon the combination of two components are likely to dominate the overall changes in entropy. Partitioning the configurational entropy into contributions of different regions of configurational space allows vibrational and conformational entropies to be defined.

Two famous approaches are the flexible molecule (FM) approach[135] and the rigid rotor harmonic oscillator (RRHO) approach.[133,136] The latter relies (as the name indicates) on the rigid rotor approximation, whereby all internal motions of the system's components are treated as vibrations. The relative translational motions are not treated differently from other internal motions, and as a consequence the formed complex translates only as a whole without any translation of subunits. In contrast to this, the FM approach relies on

classical statistical mechanics, whereby the formed complex is described by an internal coordination system and is therefore better suited for flexible molecules. The change of translational entropy is then related to the effectively accessible volume in the bound state relative to the standard volume. The disadvantage of this approach is that the choice of the internal coordination system can be crucial for the estimation of entropy and increases in complexity quickly with the size of the system.

4.2.1.3 Entropy in Intramolecular Binding

While these approaches allow a reasonable estimate for intermolecular reactions, intramolecular binding breaks certain approximations within these approaches. Considering the case of a bivalent guest A binding to bivalent host B. The first intermolecular bond formation proceeds as discussed above. The binding affinity of the second binding event, an intramolecular process, has a significantly different entropy. Interestingly, in contrast to the intermolecular binding step, the concentration of the guest binding intramolecular is determined by the strength of the precursor complex: the guest and the host are already connected with the first (intermolecular) interaction. Therefore, the intramolecular step appears to be independent of the concentration of unbound host and guest, but determined by the proximity of the intramolecular binding sites.[135] This probability can be expressed as effective concentration. For an ideal system, the intramolecular binding step can be deconvoluted into two different contributions; the (more simple) enthalpic part, which relates to the bond formation and is concentration independent, and a complicated part which relates to the conformational changes in entropy and free energy upon binding. Due to the generally additive behaviour of enthalpy, partitioning it into additive contributions from individual chemical groups seems justified. An equivalent approach for binding entropies is highly problematic because of the dependence on standard concentration and on correlated motions (e.g., overall translation).[135] However, as the intramolecular binding entropy is related to effective (and not the standard) concentration, a further analysis could help understand the effects of chelate cooperativity.

From an experimental point of view, a comparison between the probability of an intramolecular step to a competing intermolecular step is more interesting and easier to quantify. Therefore, an empirical experimental parameter *EM*, termed the (thermodynamic)

effective molarity (*EM*) has been used, defined as the ratio between the intramolecular and intermolecular binding constant (Eq. 4.10).

$$EM = \frac{K_{\text{intra}}}{K_{\text{inter}}} \tag{4.10}$$

Equivalent to binding constants, the relationship between *EM* and the Gibbs energy is:

$$-RT\ln(EM) = -RT\ln(K_{intra}) + RT\ln(K_{intra}) = \Delta G_{intra} - \Delta G_{inter} \tag{4.11}$$

These terms can be separated again into enthalpic and entropic components (Eq. 4.12). For a host-guest system, whereby the intramolecular interactions occur in absence of strain, the intramolecular and intermolecular binding enthalpy are identical and cancel each other. As presented in Chapter 3, even host-guest systems with apparently ideal shape-complementary can show enthalpic effects upon binding.

$$-RT\ln(EM) = \Delta H_{intra} - \Delta H_{inter} - T(\Delta S_{intra} - \Delta S_{inter}) \tag{4.12}$$

Another important point to emphasize here, is that the intramolecular and intermolecular systems not only differ in the change of translation, rotation, vibration and solvation, but also in the difference in symmetry which has an effect on the entropic part of the *EM* value. Considering the case of a symmetric host binding an unsymmetric guest, the host loses its symmetry and construct a variety of conformationally identical, but statistically different species. Comparing this situation with an unsymmetric host, a statistical difference is observed between those to host-guest complexes. However, this behaviour is not related to the individual binding strength, but by the the degeneracy of bound states which is different for a symmetric system than for an unsymmetric one. Therefore, it is useful to separate the entropic part into the symmetry corrected standard entropy and the the corresponding statistical factor:[137]

$$\Delta S_{intra} - \Delta S_{inter} = \Delta\Delta S = \Delta\Delta S^{*} - RT\ln(K_{\sigma}) \tag{4.13}$$

Therefore, it is crucial to specify whether the apparent or the symmetry corrected (indicated with a * throughout the chapter) entropy or Gibbs energy are refereed to. The determination has been extensively discussed in Chapter 3.

4.2.2 Experimental Methods to Determine Binding Entropy

The most famous experiment to determine the total change in entropy is the determination of K_a at various temperatures (van't Hoff experiment). An alternative is isothermal titration calorimetry (ITC), a very convenient method for measuring the heat release of a binding reaction. As a calorimetric technique, ITC measures the heat change occurring during the complex formation directly and non-invasively. Both methods will be used within this study and will be discussed in detail.

However, both approaches only access the overall change in entropy and cannot partition into the different contributions. More exotic experiments, like neutron-scattering methods, have shown promising results in the determination of the vibrational density of states. In inelastic neutron scattering spectroscopy, the change of energy in radiation is measured to reflect the excitation of the material. Conceptually similar to Raman spectroscopy, whereby photons are inelastically scattered, neutron scattering benefits from the interaction between the neutron and the nucleus. Generally, scattering by hydrogen is considerably stronger than by any other nucleus and therefore enables the application to a broad range of organic molecules, which has been demonstrated by the investigation of atomic motion in hydrated myoglobin.[138] Another example is the investigation of a protein (dihydrofolate reductase) binding methotrexate as a guest. By determining the the vibrational density of the bound and unbound protein, the change in configurational entropy could be estimated as 4 kcal mol^{-1}.[139] Another interesting technique is NMR, which can be used to gain information about specific structural areas. For example, NMR relaxation data are able to provide structurally correlated information about the configurational entropy change upon binding.[135,140–142]

4.2.2.1 Isothermal Titration Calorimetry

In general, an ITC experiment exceeds any other technique in terms of information density as it delivers information about the association stoichiometry n, the formation constant K_f, the Gibbs free formation energy ΔG, the formation enthalpy ΔH, and the formation entropy ΔS of the system in a single experiment.[21] Due to the simplicity of the binding experiment, ITC is increasingly used in the determination of stoichiometry for multiple binding events, such as the formation of multiprotein complexes[22] or the binding of multivalent ligands.[23,24]

The general experiment involves titrating two reactants, with the extent of binding determined via direct measurement of heat exchange with the environment. The host is

generally placed in the calorimeter cell which is filled to the effective volume V_0, while a syringe adds small aliquots to the reaction cell. With each injection volume v, a volume equivalent to the injection will be pushed out of the cell. Hence, the macromolecule concentration decreases as the titration proceeds, which needs to be corrected in the data analysis. The concentration of the guest, $[X]_t$, and the host, $[M]_t$, in the cell is dependent on the number of injections (i) and is given by:[24]

$$[X]_{t,i} = [X]_0\Big(1 - (1 - \frac{v}{V_0})^i\Big), \qquad [M]_{t,i} = [M]_0\Big(1 - \frac{v}{V_0}\Big)^i \tag{4.14}$$

with $[X]_0$ and $[M]_0$ as the initial guest and host concentrations, respectively. In the case of binding, a new species emerges during the titration process. For a simple 1:1 system, the corresponding complex concentration is given with $[MX]$. The binding process initiates heat release. To maintain constant temperature, the instrument requires energy to counteract the temperature change. This energy use is measured as a function of the titration progress and, by integrating the area under each peak corresponding to an injection, a heat profile in dependence of total guest aliquots is obtained. The result is a well-known sigmoidal-shaped binding curve, with the total heat content of the solution in the cell, Q, as:

$$Q = [M]_t V_0 n \Delta H \Theta \tag{4.15}$$

with V_0 as the effective cell volume, n the number of binding sites, ΔH is the binding enthalpy and Θ the fraction of occupied binding sites.[24]

The simplest binding process (a 1:1 system) can be fitted using a simple one-site model based on the Wiseman isotherm:[143]

$$Q = \frac{n[M]_t V_0 \Delta H}{2}\Big[1 + \frac{[X]_t}{n[M]_t} + \frac{1}{nK_a[M]_t} - \sqrt{\Big(1 + \frac{[X]_t}{n[M]_t} + \frac{1}{nK_a[M]_t}\Big)^2 - \frac{4[X]_t}{n[M]_t 4}}\Big] \tag{4.16}$$

where K_a is the association constant. The data analysis of ITC experiments is limited by the c value, which is defined as:

$$c = nK_a[M]_t \tag{4.17}$$

A reliable analysis of binding constant and stoichiometry requires values of c between 1 and 1000.[143] However, the binding enthalpy is independent of this limit. For very strong

binding processes ($K_f > 10^9$ M^{-1}),[144,145] the enthalpy can be measured directly if the binding stoichiometry is known (from other experiments).

In the last decade, ITC moved beyond simple 1:1 models. Impressive binding models were designed, allowing the analysis of complex host-guest interactions.[146] This powerful tool experienced high popularity, as indicated by over 1180 reported ITC measurements of binding thermodynamics in the BindingDB database.[147]

4.2.2.2 Van't Hoff Experiments

Despite all these benefits, ITC remains a structure-insensitive method. An alternative procedure to obtain binding enthalpies is the determination of binding constants at various temperatures: the commonly used van't Hoff experiment. The equation relates the change in the equilibrium constant to the change in temperature, T, via the standard enthalpy change as expressed in Equation 4.18.

$$\frac{\partial(\ln K)}{\partial T} = -\frac{1}{R}\frac{\partial}{\partial T}\left(\frac{\Delta G^\circ}{T}\right) = \frac{\Delta H^\circ}{RT^2} \tag{4.18}$$

Measuring the equilibrium constant at two temperatures (T_1 and T_2) allows us to integrate over these values:

$$\int_{\ln K_1}^{\ln K_2} \partial(\ln K) = \int_{T_1}^{T_2} \frac{\Delta H^\circ}{RT^2}\,\partial T \tag{4.19}$$

The result is the definite integral:

$$\ln\left(\frac{K_2}{K_1}\right) = -\frac{\Delta H^\circ}{R}\left[\frac{1}{T_2} - \frac{1}{T_1}\right] \tag{4.20}$$

Measuring the equilibrium constant at several temperatures allows us to plot a graph $\ln(K)$ against $1/T$. For a simple 1:1 binding model, where ΔH is independent of the used temperature range, the data are expected to show a linear relationship. A significant disadvantage of the van't Hoff analysis is the time consuming requirement of multiple measurements across a wide range of temperatures. Moreover, the data analysis and error evaluation can be technically challenging.[148]

4.3 Methods

The porphyrin compounds were prepared as described in Chapter 2. All porphyrin compounds in this chapter contain trihexylsilyl (THS) solubilising groups on the *meso*-aryls. Experiments were performed under high dilution conditions (10^{-6} M). The UV-vis-NIR titration experiments were conducted using a constant total host concentration, benefiting from the presence of isosbestic points - wavelengths at which different species exhibit identical absorption coefficients. These points indicate that very few species are involved in the titration process as the probability of observing an isosbestic point decreases drastically as the number of species increases. All experiments use toluene as solvent. The spectra were recorded using a Perkin-Elmer Lambda 20 spectrometer with a 1 cm quartz cuvette. To determine the EMs, titration experiments were performed at 298 K.

ITC experiments were performed on a VP-ITC calorimeter and analysed using the Microcal ITC Data Analysis module. The experiments were done in a direct titration mode, where the guest is placed in the syringe to avoid using high concentration of the porphyrin oligomers that would result in aggregation. A typical titration schedule included addition of small aliquots (2 µL per injection) of titrant with 20 injections spaced for at least 3 min intervals. The titration syringe was continuously stirred, and the cells were kept at 298 K. For the first injection only, 0.5 µL of titrant was added, and the corresponding data point was deleted from the analysis. Reference titrations were carried out by injecting each titrant into toluene alone in the calorimetric cell, and heat of dilution was subtracted from the host-guest titration data. The host concentration (C_{host}) was estimated using the dissociation constant (K_D, previously determined via UV-Vis titrations) according to the following equation:

$$C_{host} = 10 \text{ to } 50 \times K_D \tag{4.21}$$

The guest concentration (C_{guest}) was chosen in accordance to the host concentration via the following equation:

$$C_{guest} = 7 \text{ to } 10 \times n \times K_D \tag{4.22}$$

with n as the number of binding sites. Due to solubility issues, the ITC titrations for guest **C3** could not be done. To exclude experimental errors and analyse the accuracy of the

ITC technique, reference formation titrations were done using ***I*-P1** monomer binding to **py**, **A1**, and **C1** which are presented in Table 4.1. The ITC measurements were analysed with the MicroCal software developed by Malvern[149] and the AFFINImeter software.[150] Both gave identical results. The formation constants showed good agreement with those determined by UV-vis-NIR titrations.

Table 4.1: Overview of K_f, ΔH, and ΔS determined via ITC experiments for Reference.

Parameter		***I*-P1•A1**	***I*-P1•C1**	***I*-P1•py**
K_f (M^{-1})	*ITC*	$(3.2 \pm 0.1) \times 10^4$	$(1.0 \pm 0.1) \times 10^4$	$(1.6 \pm 0.2) \times 10^4$
K_f (M^{-1})	*UV-Vis-NIR*	$(3.18 \pm 0.16) \times 10^4$	$(1.08 \pm 0.16) \times 10^4$	$(1.39 \pm 0.16) \times 10^4$
ΔH ($kJ\,mol^{-1}$)		-51.5 ± 0.5	-41.8 ± 0.5	-42.6 ± 0.5
ΔS ($cal\,mol^{-1}\,K^{-1}$)		-21.3 ± 0.5	-15.1 ± 0.1	-15.3 ± 0.1

Despite the ability to determine binding constants, the systems studied in this thesis exceed the upper range of formation constants ($K_f > 10^9\ M^{-1}$) that can be determined directly.[144,145] A competition experiment similar to the UV-vis-NIR denaturation titrations would be possible to determine the formation constants via ITC. However, the change in enthalpy by replacing the multivalent guest with monovalent guests at the host-guest complex is rather small and would require very high concentrations, resulting in aggregation. Therefore, the ITC experiments were only used to measure the enthalpy contributions to Gibbs energy obtained by the binding constants.

However, the gained information relates to the overall occurring processes and can therefore not be directly related to the causes of the heat changes at the molecular level. Hence, the ITC experiments were combined with van't Hoff plots from variational temperature UV-vis-NIR titration experiments. The UV-vis-NIR titrations were repeated over a temperature range of 40 K, and fit to Equation 4.20. The experimental error analysis and error propagation followed literature procedures.[148]

4.4 Determination of Binding Constants and EMs

In this section, the binding constants and effective molarities are determined for the hosts with THS groups. The ITC experiments require a higher concentration range which could potentially show a significant amount of aggregation affecting the determined binding enthalpy. Therefore, (3,5-bis(trihexylsilyl))phenyl (THS) solubilising groups were used

throughout this chapter. While these solubilising groups guarantee the absence of any aggregation, the flexible and large THS groups can both sterically interact with guest molecules but also change the solvation environment and can therefore highly influence the binding energy. Electronic influences on the binding strength are rather weak; for the the ground state geometry of a porphyrin with aryls in the *meso* position, the phenyl groups show a torsion angle to the porphyrin plane around 40° which reduces any electronic conjugation between the aryls and the porphyrin.

The lower binding constant for THS side chain is observed by the UV-vis-NIR and ITC titrations of ***I*-P1** binding to all monodentate ligands (Table 4.1). Entropic changes cannot be determined directly, but need to be calculated as a difference between Gibbs energy and enthalpy. While the single-site binding strength does not affect the effective molarities, the Gibbs energy and enthalpy are affected by the reduced axial binding strength. Therefore, the binding constants for all complexes were determined for the oligoporphyrins containing trihexylsilyl solubilising groups. The models were used as described in Chapter 3. The effective molarities for the complexes were determined as well to probe the innocence of the single-site binding strength.

4.4.1 Reference Binding Constant

In order to quantify chelate cooperativity, the binding strength of an intermolecular reference system has to be determined. Therefore, binding constants for the non-cooperative reference system were determined with a porphyrin monomer (***I*-P1**) combination with the monodentate guests **A1**, **C1**, and pyridine and the results are shown in Figure 4.2. Comparing the THS and the tBu porphyrins, the axial binding strength is reduced by a factor of two for all three monovalent guests. The ratios between the individual binding constants are identical within experimental error tolerance. This observation is rather surprising. The silicon atom has a weak inductive effect, increasing the electron density in the phenyl ring, and an electron-withdrawing mesomeric effect, which mostly influences the *ortho* and *para* positions in the phenyl ring.[151] Therefore, no electronic difference between the tBu and the THS porphyrins is expected and the observed differences in binding constants are most likely caused by the difference in solvation (changing the chemical environment around the axial coordination).

Due to the large solubilising groups, the experimental preparation of fully dry, pyridine-free samples of the oligomeric hosts is relatively demanding and therefore accurate determination

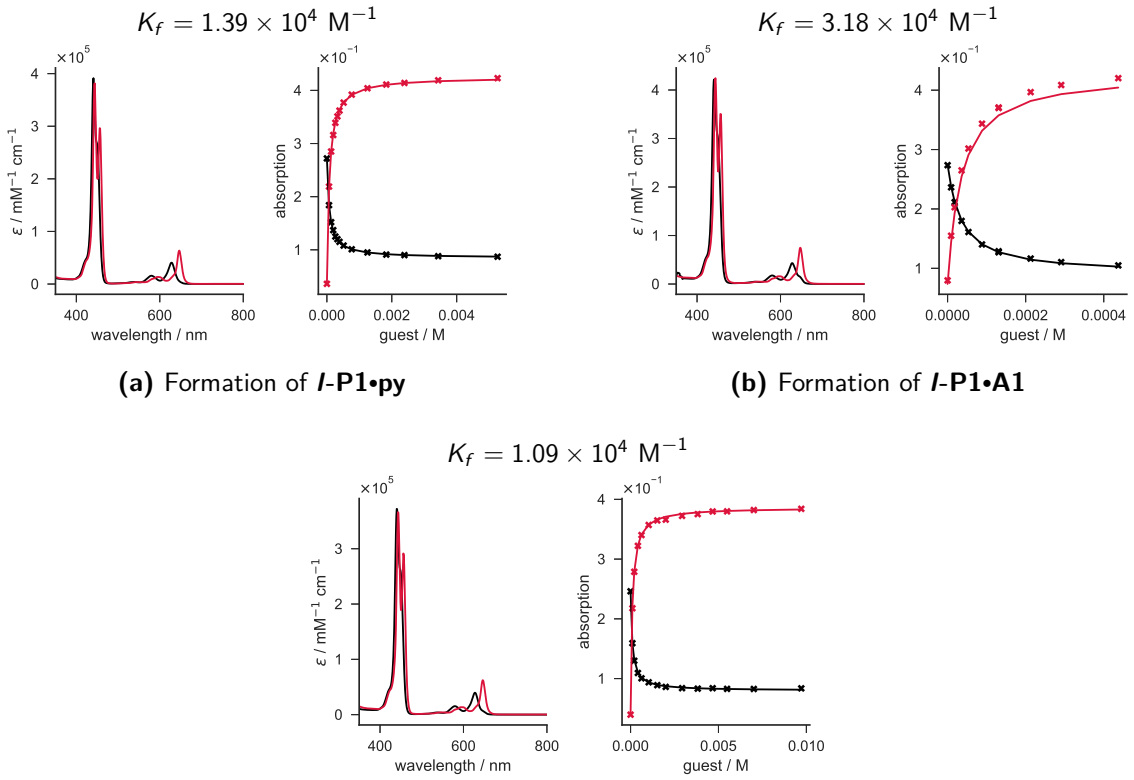

(a) Formation of ***l*-P1•py**

(b) Formation of ***l*-P1•A1**

(c) Formation of ***l*-P1•C1**

Figure 4.2: Multivariant global fit results of multiple UV-vis-NIR titration experiment showing the single components of the absorption spectra (unbound host in black, host-guest complex in red) and the experimental point and the fitted binding isotherm of two characteristic wavelengths (629 nm in black, 646 nm in red), respectively. (toluene, 298 K, [***l*-P1**] = 4.57 µM).

of extinction coefficients and a reference monovalent binding constant is challenging. Deviations between the cyclic and the linear hosts binding to a monomeric guest are reported in literature.[39] However, it is very likely that these are based on solvent impurities. As shown in Chapter 3, the cyclic host ***c*-P6** exhibits a very similar binding strength to pyridine as the monomeric ***l*-P1** host. It seems possible that the binding constant of the cyclic host to pyridine is affected by the bending of the acetylene linkers and the resulting strain on the individual porphyrin centres. To test this hypothesis, the binding constant of pyridine binding to the **Zn_2-P6** was determined (Fig. 4.3). The **Zn_2-P6** is composed of 6 porphyrin centres, whereby only two neighbouring porphyrins carry a zinc atom, the remaining four porphyrins are free-base. The dizinc nanoring was synthesised by Pernille Bols following the Shadow Mask template method.[152] By coordinating an oligopyridine ligand to the nanoring, the coordinated porphyrins are protected against demetallation and therefore, a site-specific demetallation is enabled.

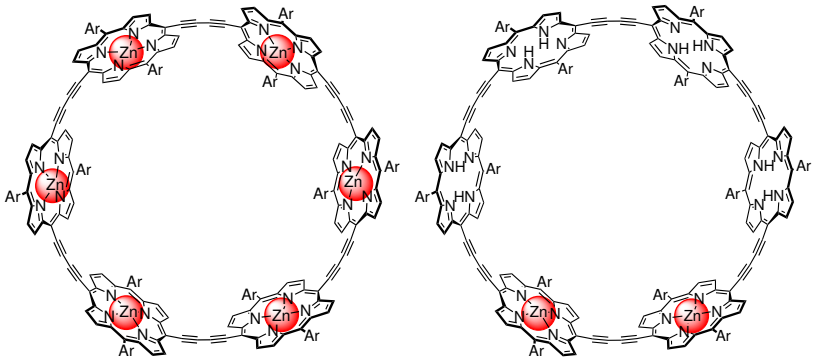

Figure 4.3: Comparison of regulat ***c*-P6** and **Zn_2-P6**. Ar = (3,5-bis(trihexylsilyl))phenyl.

Using a porphyrin ring with only two zinc centres allows the determination of each binding constant individually, similar to the measurements of ***I*-P2**.[20] The UV-vis-NIR titration of **Zn_2-P6** binding the monovalent ligand pyridine shows no isosbestic points, and therefore provides enough information to separate the first and second binding constant. The experimental data were fitted to the 'effective binding sites' (EBS, Fig. 4.4a) and the 'independent optimisation' (IO, Fig. 4.4b) model.

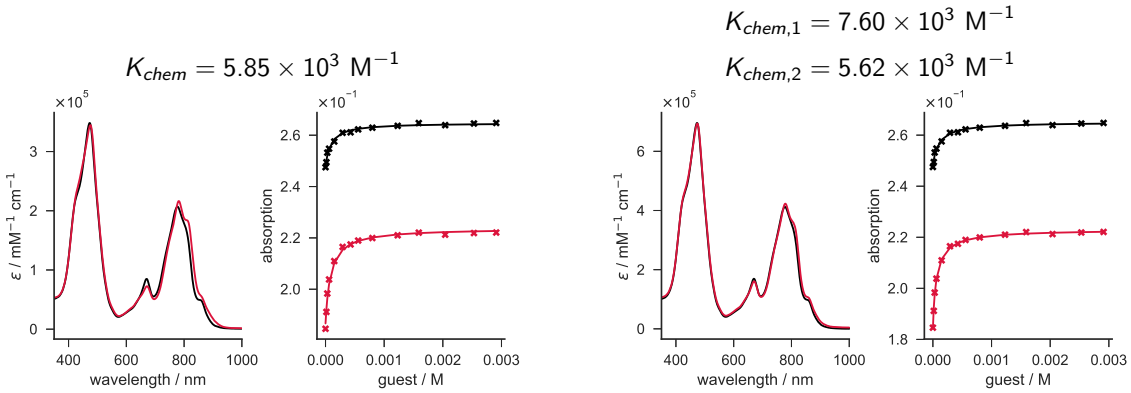

(a) EBS model **(b)** IO model

Figure 4.4: Multivariant global fit results of multiple UV-vis-NIR titration experiment of **Zn_2-P6** binding **py**. The single components of the absorption spectra (unbound host in black, fully bound host-guest complex in red) and the experimental point and the fitted binding isotherm of two characteristic wavelengths (784 nm in black, 814 nm in red) are shown, respectively. (toluene, 298 K, [**Zn_2-P6**] = 0.65 µM).

Within error tolerances, both models result in identical binding constants. The statistically corrected binding constants for the first and the second pyridine binding differ by a factor of 1.3 ($K_{chem,1} = 7.60 \times 10^3$ M^{-1} and $K_{chem} = 5.62 \times 10^3$ M^{-1}), which can be assumed as identical within error tolerances. Moreover, the average statistically corrected binding constant for **Zn_2-P6** binding one pyridine ($K_{chem} = 6.61 \times 10^3$ M^{-1}) is identical with the geometric average binding constant for the hexazinc porphyrin nanoring ***c*-P6**

(K_{chem} = 5.92 × 10^3 M^{-1}) and the linear porphyrin monomer ***I*-P1** binding pyridine (K_{chem} = 6.97 × 10^3 M^{-1}). This result shows that bending the oligoporphyrin has no significant effect on the binding strength to pyridine. Therefore, the ***I*-P1** reference constant was used for all further data analysis.

4.4.2 Determination of Multivalent Binding Constants

The formation constants for the bidentate guests binding to ***I*-P2** were determined in direct titration mode and using a 1:1 binding model (Fig. 4.7a - 4.7c). Generally, the divalent systems with THS solubilising groups show lower binding constants than the systems with tBu side chains, but follow the trend observed with the monovalent reference binding constants. The slightly weaker formation constants allowed a reliable determination via direct formation titration.

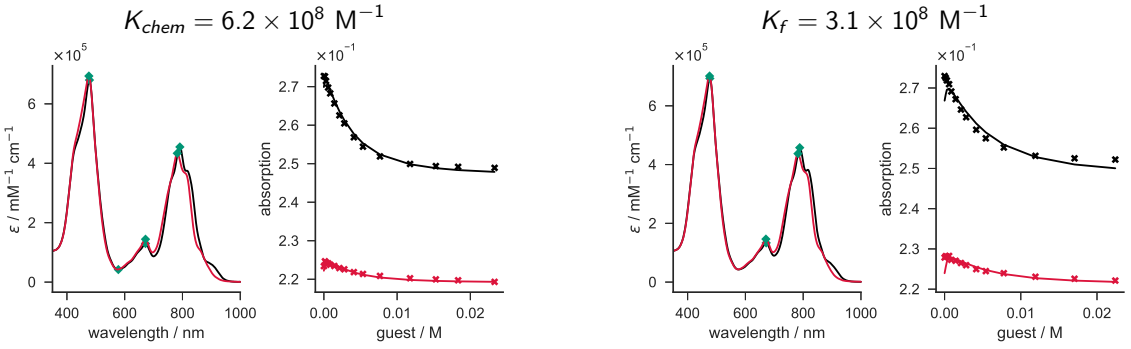

(a) Denaturation of **Zn_2-P6•A2**

(b) Denaturation of **Zn_2-P6•B2**

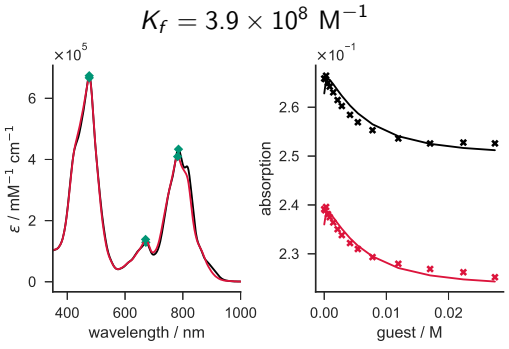

(c) Deanturation of **Zn_2-P6•C2**

Figure 4.5: Multivariant global fit results of multiple UV-vis-NIR titration experiment showing the single components of the absorption spectra (host-guest complex in black, pyridine bound host in red) and the experimental point and the fitted binding isotherm of two characteristic wavelengths (791 nm in black, 813 nm in red), respectively. Characteristic points of the spectra were used to validate the concentration of the individual measurements (green diamonds). Experimental conditions were 298 K, toluene as a solvent, [**Zn_2-P6**] = 0.67 µM.

The formation constants for the tridentate guests binding to ***l*-P3** were determined in competition experiments by using pyridine as a competing monovalent guest. The data were analysed using an 'all-or-nothing' binding model, that allows to limit the number of species to two, the fully bound ***l*-P3•X3** and the fully denaturated ***l*-P3•py$_3$** (Fig. 4.7d - 4.7f). Again, the overall trend of the binding constants is in good agreement with the tBu systems. The goodness-of-fit is identical for both systems, indicating that the used binding model is sufficient to describe the data.

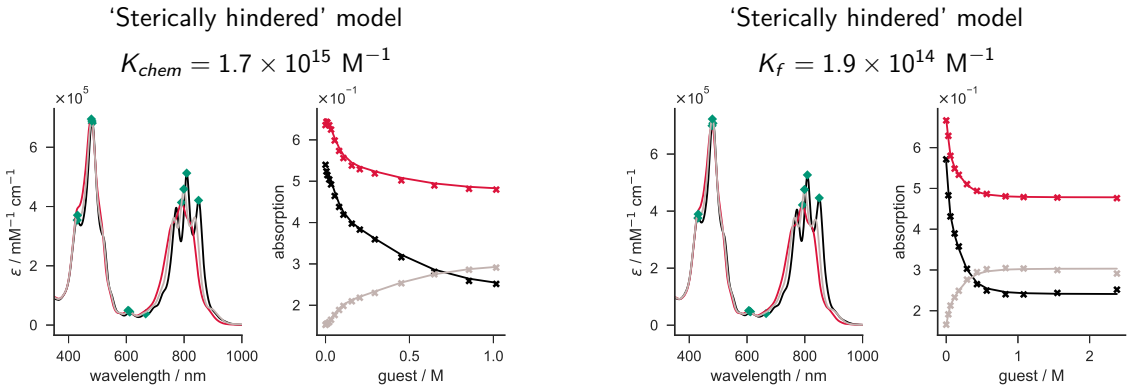

(a) Denaturation of ***c*-P6•A3**

(b) Denaturation of ***c*-P6•B3**

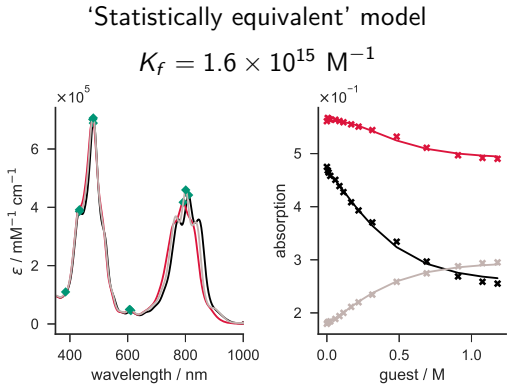

(c) Denaturation of ***c*-P6•C3**

Figure 4.6: Multivariant global fit results of multiple UV-vis-NIR titration experiment of ***c*-P6** and the tridentate guests. Presented are the determined single components of the absorption spectra ***c*-P6•X3$_2$** in black, partially denaturated ***c*-P6•X3py$_3$** in grey, and fully denaturated ***c*-P6•py$_6$** in red. The fit accuracy is shown as experimental point compared to the fitted binding isotherm of three characteristic wavelengths (735 nm in grey, 807 nm in red, 847 nm in black), respectively. Characteristic points of the spectra were used to validate the concentration of the individual measurements (green diamonds). (toluene, 298 K, [***c*-P6**] = 1.29 µM).

The formation constants of the bidentate guests binding to the cyclic host were determined using the **Zn$_2$-P6** nanoring. The regular ***c*-P6** nanoring can bind up to three bidentate guests, leading to 1:1, 1:2, and 1:3 complexes. Due to the high number of species

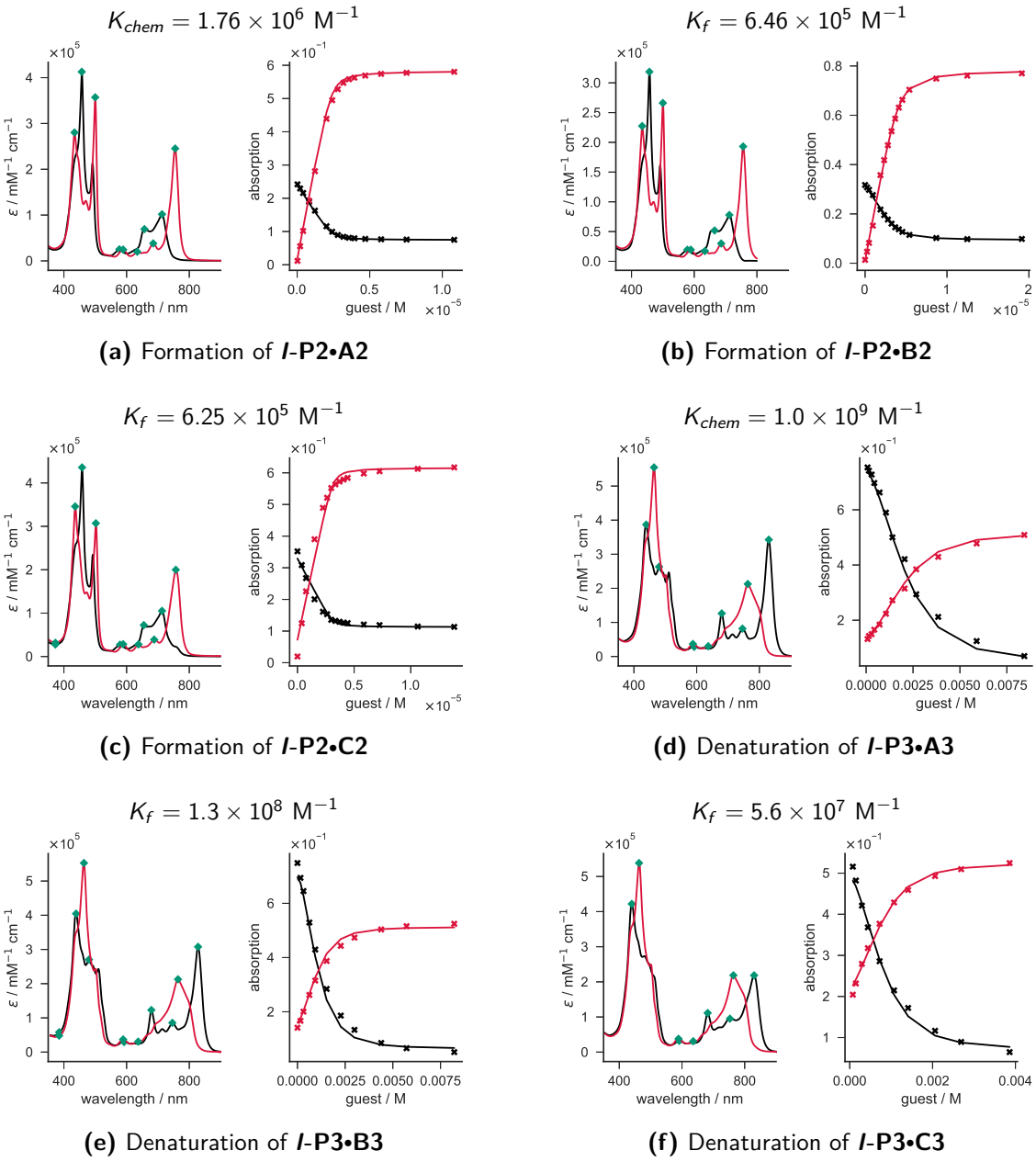

(a) Formation of ***l*-P2•A2**

(b) Formation of ***l*-P2•B2**

(c) Formation of ***l*-P2•C2**

(d) Denaturation of ***l*-P3•A3**

(e) Denaturation of ***l*-P3•B3**

(f) Denaturation of ***l*-P3•C3**

Figure 4.7: Multivariant global fit results of multiple UV-vis-NIR titration experiment showing the single components of the absorption spectra and the experimental point, characteristic points comparing total absorbance for several experiments (green diamonds), and the fitted binding isotherm of two characteristic wavelengths. (Formation: unbound host in black, complex in red, wavelengths are 712 nm in black, 755 nm in red, [***l*-P2**] = 1.85 µM; Denaturation: host-guest complex in black, pyridine bound host in red, wavelengths are 824 nm in black, 762 nm in red, [***l*-P3**] = 2.42 µM). Toluene, 298 K.

involved in both, the formation and the denaturation process, a fully independent fit of all parameters led to overfitting. Using the **Zn_2-P6** nanoring only allows the formation of 1:1 complexes, and reduces the number of species to two. Again, an 'all-or-nothing' behaviour is assumed. The results are shown in Figure 4.5.

For the tridentate guests, the regular ***c*-P6** nanoring was used. The denaturation

titrations were analysed as described previously (Chap. 3.7). For the ***c*-P6•A3** and ***c*-P6•B3** systems, the binding constants were determined using the 'sterically hindered' model, which determines two independent binding constants for the 1:1 and the 1:2 complex. For the smaller, sterically non-interacting ***c*-P6•C3** host-guest system, the 'statistically equivalent' model is used, which assumes identical, statistically corrected binding constants.

4.4.3 Overview of Binding Constants and EMs

An overview of all determined formation constants (K_f), the titration mode (direct or competition experiment), the binding model, the statistically corrected binding constants (K_{chem}), $\overline{EM}$, and the stepwise EMs are shown in Table 4.2. The errors for binding constants determined via direct titration were calculated from the standard deviation at 95 % confidence interval of several independent experiments. The calculation of binding constants from competition experiments, or of the values for the effective molarities, involves several variables. Hence, the errors are determined by error propagation without covariance.[127]

Table 4.2: Overview of the determined formation constants (K_f), titration mode (TM), binding model (SH = 'sterically hindered'; SE = 'statistically equivalent'; EBS = 'effective binding sites'),statistical factor (K_σ), statistically corrected binding constants(K_{chem}), geometric average ($\overline{EM}$), and stepwise effective molarities (EM_i).

Complex	TM	Model	K_f / M^{-1}	K_σ	K_{chem} / M^{-1}	$\overline{EM}$ / M	EM_i / M
***I*-P1•py**	direct	1:1	$(1.39 \pm 0.16) \times 10^4$	2	7.0×10^3	–	–
***I*-P1•A1**	direct	1:1	$(3.18 \pm 0.16) \times 10^4$	2	1.6×10^4	–	–
***I*-P1•C1**	direct	1:1	$(1.08 \pm 0.16) \times 10^4$	2	5.4×10^3	–	–
***I*-P2•A2**	direct	1:1	$(3.18 \pm 0.31) \times 10^7$	8	4.2×10^6	(0.017±0.005)	(0.017±0.005)
***I*-P2•B2**	direct	1:1	$(5.9 \pm 1.5) \times 10^6$	8	7.4×10^5	(0.0026±0.0008)	(0.0026±0.0008)
***I*-P2•C2**	direct	1:1	$(5.2 \pm 1.3) \times 10^6$	8	6.5×10^5	(0.021±0.006)	(0.021±0.006)
***I*-P3•A3**	denat	1:1	$(1.66 \pm 0.31) \times 10^{10}$	16	1.0×10^{10}	(0.016±0.003)	(0.015±0.006)
***I*-P3•B3**	denat	1:1	$(2.14 \pm 0.4) \times 10^9$	16	1.3×10^8	(0.0058±0.0012)	(0.013±0.004)
***I*-P3•C3**	denat	1:1	$(8.94 \pm 1.7) \times 10^8$	16	5.6×10^7	(0.019±0.004)	(0.0029±0.0011)
Zn_2-P6•A2	denat	1:1	$(5.3 \pm 1.7) \times 10^9$	8	6.6×10^8	(2.6±0.7)	(2.6±0.7)
Zn_2-P6•B2	denat	1:1	$(2.5 \pm 0.6) \times 10^9$	8	3.1×10^8	(1.2±0.3)	(1.2±0.3)
Zn_2-P6•C2	denat	1:1	$(3.1 \pm 0.5) \times 10^9$	8	3.8×10^8	(13±4)	(13±4)
***c*-P6•A3**	denat	SH	$(1.6 \pm 0.5) \times 10^{17}$	96	1.7×10^{15}	(20±4)	(160±60)
***c*-P6•B3**	denat	SH	$(1.9 \pm 0.6) \times 10^{16}$	96	1.9×10^{14}	(6.9±1.5)	(40±15)
***c*-P6•C3**	denat	SE	$(1.6 \pm 0.5) \times 10^{17}$	96	1.6×10^{15}	(102±22)	(780±200)

Comparing the binding constants between the tBu and the THS oligo porphyrin hosts (Tab. 3.10 and 4.2), all determined binding constants are lower for the THS porphyrins. If single-site binding strength is not a factor affecting cooperativity, it would be expected

to obtain identical values for $\overline{EM}$ and EM_i. Generally, this behaviour is observed, except for ***l*-P2•C2** and ***c*-P6•C3**, where the EM values are significantly increased with the stronger solubilising groups. The results were confirmed with the repetition of independent experiments. Interestingly, the other host-guest complexes involving series **C** guests are not affected, indicating that cooperativity strength is indeed independent of the single-site binding strength. A possible explanation for this behaviour could be the change in the chemical environment. Due to the large, flexible solubilising groups, the solvent around the complex is partially replaced and the large THS groups might behave like as solvent in itself. This hypothesis is further analysed and tested in Chapter 5.

4.5 Determination of Binding Enthalpy

Binding enthalpies were determined via ITC titration experiments. As a method insensitive to structural changes on the molecular level, the ITC experiments were complimented with van't Hoff experiments when necessary.

Table 4.3: Overview of the apparent (ΔG) and the statistically corrected Gibbs energies (ΔG*), and binding enthalpies determined via ITC (ΔH_{ITC}) and van't Hoff plots($\Delta H_{\text{vantHoff}}$).

Structure	K_{f} (M^{-1})	K_{chem} (M^{-1})	ΔG (kJ mol^{-1})	ΔG* (kJ mol^{-1})	ΔH_{ITC} (kJ mol^{-1})	$\Delta H_{\text{vantHoff}}$ (kJ mol^{-1})
***l*-P1•A1**	3.18×10^4	1.59×10^4	-25.7	-24.0	-51.5	
***l*-P1•C1**	1.08×10^4	5.55×10^3	-23.0	-21.4	-41.7	
***l*-P1•py**	1.39×10^4	6.97×10^3	-23.6	-21.9	-42.6	
***l*-P2•A2**	3.36×10^7	4.20×10^6	-42.9	-37.8	-82.5	-81.6
***l*-P2•B2**	5.17×10^6	6.46×10^5	-38.3	-33.1	-71.2	-56.9
***l*-P2•C2**	2.86×10^7	3.57×10^6	-42.5	-37.4	-78.2	-76.0
***l*-P3•A3**	1.66×10^{10}	1.03×10^9	-58.3	-51.4	-96.9	
***l*-P3•B3**	2.14×10^9	1.34×10^8	-53.2	-46.4	-93.5	
***l*-P3•C3**	8.94×10^8	5.59×10^7	-51.1	-44.2		-95.90
Zn_2-P6•A2	5.30×10^9	6.62×10^8	-55.5	-50.3	-96.2	-95.4
Zn_2-P6•B2	2.45×10^9	3.07×10^8	-53.6	-48.4	-89.5	-86.1
Zn_2-P6•C2	3.11×10^9	3.89×10^8	-54.2	-49.0	-99.7	-87.9
***c*-P6•A3**	(K_1) 1.62×10^{17}	1.69×10^{15}	-98.2	-86.9	-131.0	-143.2
	(K_2) 1.44×10^{16}	1.50×10^{14}	-92.2	-80.9	-131.0	-135.0
***c*-P6•B3**	(K_1) 1.85×10^{16}	1.93×10^{14}	-92.8	-81.5	-118.0	-121.1
	(K_2) 1.89×10^{15}	1.97×10^{13}	-87.2	-75.8	-118.0	-112.20
***c*-P6•C3**	1.57×10^{17}	1.64×10^{15}	-98.1	-86.8		-136.5

An overview of all determined values is shown in Table 4.3. Both methods are generally in agreement and deliver identical results, and any differences are explained in Section 4.5.1 and 4.5.2. In the absence of conflict, enthalpy values obtained via ITC are used. Otherwise, van't Hoff values are used for the data analysis in Section 4.6.

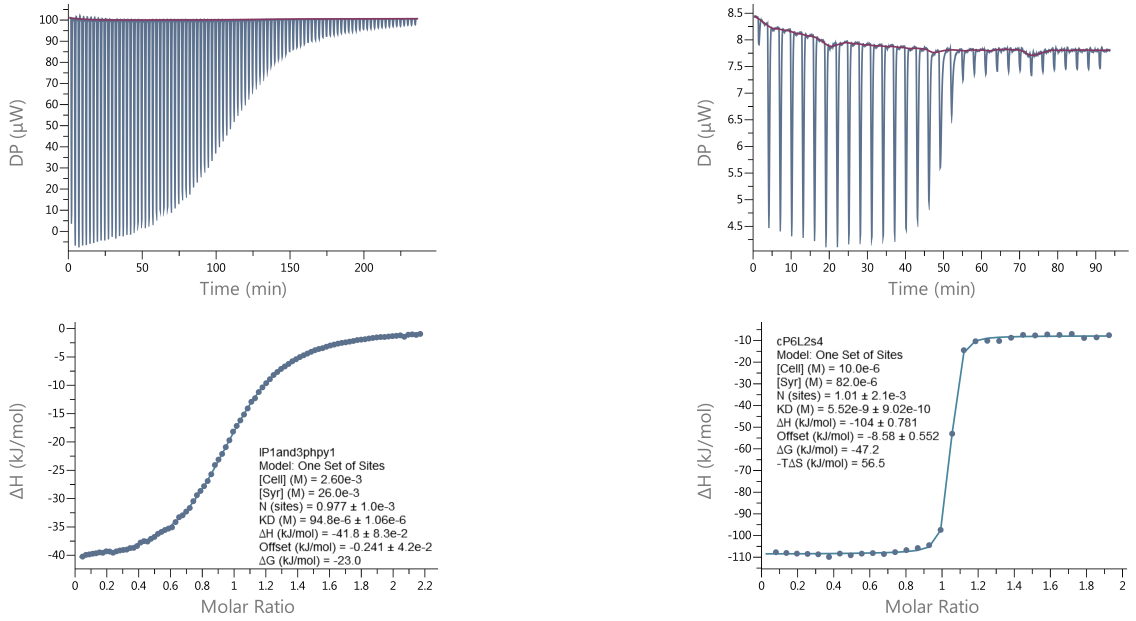

(a) *I*-P1•C1 **(b) Zn_2-P6•C2**

Figure 4.8: Representative ITC titration example for a weak (a) and a strong (b) binding process of a 1:1 system.

Figure 4.8 shows two representative examples for the measurements performed in this study. For weak binding processes, as in the case of the linear porphyrin monomer (***I*-P1**) binding to the guest **C1** (Fig. 4.8a), a high concentration (mM range) is required to obtain a reliable sigmoidal curve. The top figure shows the raw, unprocessed data. The red line indicates the baseline, which is subtracted from the data to obtain the binding enthalpy. The baseline is determined via a dilution experiment of neat toluene titrated into a cell containing the desired host concentration, and a dilution experiment of the guest, whereby the guest is diluted into a cell containing neat toluene. Both dilution experiments yielded a low heat of dilution compared to the heat release obtained by the binding experiment.

The preorganised hosts bind very exothermically, as the example of **Zn_2-P6** binding **C2** illustrates (Fig. 4.8b). Due to the strong heat release upon complex formation ($-104\,\mathrm{kJ\,mol^{-1}}$), very dilute concentrations could be used to determine ΔH. The example also displays the strong binding constant; the sigmoidal curve shows a steep slope around

1 equivalent. Again, the baseline was determined via dilution experiments. Small baseline corrections were added manually to compensate minor fluctuations. If bigger corrections were required, the experimental data were discarded.

4.5.1 Cyclic Hosts

As shown in Chapter 3, the tridentate guests can form 1:2 complexes with the multivalent ***c*-P6** guest. In general, different models can be used to fit the data. Due to the very strong association constants and the high cooperativity effect, an 'all-or-nothing' behaviour is observed, resulting in a steep slope around the point of inflection. Due to this rapid transition, separation of the binding enthalpy for the first and the second guest is not possible. Therefore, all ITC experiments were analysed using a simple 1:1 binding model to determine the enthalpy.

However, the UV-vis-NIR titrations have shown that the first and the second binding constant are not identical. The same behaviour was observed for the ITC titrations. The comparison of ***c*-P6•A3** (a), ***c*-P6•A2** (b),and **Zn_2-P6•A2** (Fig. 4.9) illustrates this. The **Zn_2-P6•A2** follows the expected behaviour of a simple, strong binding 1:1 complex and the experimental data points are well reproduced with the calculated binding isotherm (Fig. 4.9 c). The fitted binding isotherm 1:1 for ***c*-P6•A3** (Fig. 4.9 a) shows high deviations from the experimental data. The experimental points differ from the expected point symmetry centred in the point of inflection. This difference suggests multiple overlaying binding processes with different binding enthalpies. This hypothesis is supported by the ITC formation titration of ***c*-P6•A3** (Fig. 4.9 a), which shows higher deviations.

Therefore, UV-vis-NIR titrations experiments were done at various temperatures. All binding constants exceed $K_f > 5 \times 10^7$ M^{-1}. Hence, competition experiments are required and were conducted as described in Section 4.4. If the number of species is very limited and the absorption spectra of the components are either known at each temperature or are temperature-independent, a entire titration experiment is not necessary for the

Table 4.4: Overview ΔH determined via ITC experiments for ***c*-P6•A3**, ***c*-P6•B3** and ***c*-P6•C3**.

ΔH ($kJ\,mol^{-1}$)	***c*-P6•A3**	***c*-P6•B3**	***c*-P6•C3**
ITC	-131 ± 6	-118 ± 6	–
van't Hoff (K_1)	-143 ± 6	-121 ± 6	-136 ± 6
van't Hoff (K_2)	-135 ± 6	-112 ± 6	–

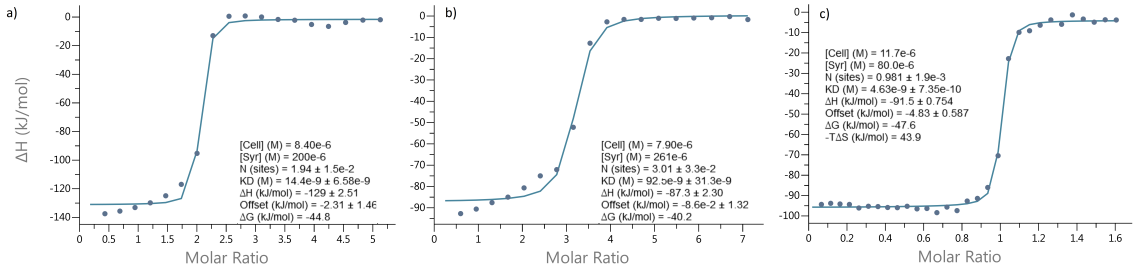

Figure 4.9: ITC titrations for ***c*-P6•A3** (a), ***c*-P6•A2** (b), and **Zn_2-P6•A2** (c).

determination of the binding constant at each temperature. However, experiments with our host-guest system have shown that the spectra show significant shift and broadening. Therefore, the uncertainty of the binding enthalpy would be very high and a complete titration at each temperature was necessary. The binding constant of pyridine binding to ***l*-P1** was calculated based on the binding enthalpy determined via ITC. The fitted titration experiments and the corresponding binding constants for ***c*-P6•A3** and ***c*-P6•B3** are shown in Figure 4.10. ***c*-P6•C3** is shown in Figure 4.11.

The determined binding constants were plotted following equation 4.20. Within the temperature range 298–333 K, the van't Hoff plots (4.12) of the extracted equilibrium constants show excellent straight-line fits for all three host-guest systems. The cyclic host can form a 1:1 and a 1:2 complex. While the binding strength for the first and the second guest is identical for ***c*-P6•C3**, the first and the second binding event for **A3** and **B3** shows different binding strengths. For ***c*-P6•A3** and ***c*-P6•B3**, both binding constants were plotted to determine each binding enthalpy. The binding of the second guest is less exothermic in both cases. The average between the first and second binding enthalpy is in good agreement with the ITC data. The host-guest system ***c*-P6•C3** could not be measured via ITC due to the poor solubility of **C3**. Due to the issues of solubility and the lack of information for the binding differences of the first and second guest in the ITC experiments, the enthalpy values determined via van't Hoff are used for further data analysis.

Table 4.5: Overview ΔH determined via ITC experiments for **Zn_2-P6•A2**, **Zn_2-P6•B2**, and **Zn_2-P6•C2**.

ΔH (kJ mol^{-1})	**Zn_2-P6•A2**	**Zn_2-P6•B2**	**Zn_2-P6•C2**
ITC	-96.2 ± 5	-89.5 ± 5	-99.7 ± 5
van't Hoff	-95.9 ± 5	-86.1 ± 5	-87.9 ± 5

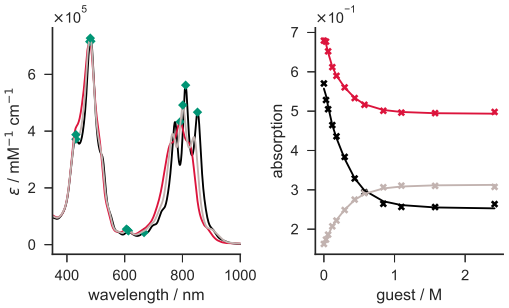

(a) ***c*-P6•A3**, 298 K, $K_{chem,1} = 7.5 \times 10^{14}$ M^{-1}

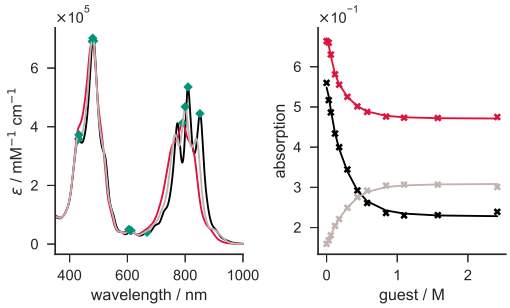

(b) ***c*-P6•A3**, 308 K, $K_{chem,1} = 1.2 \times 10^{14}$ M^{-1}

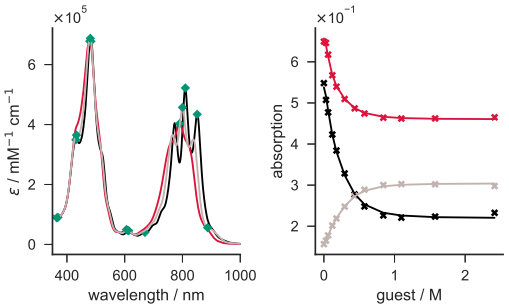

(c) ***c*-P6•A3**, 318 K, $K_{chem,1} = 2.2 \times 10^{13}$ M^{-1}

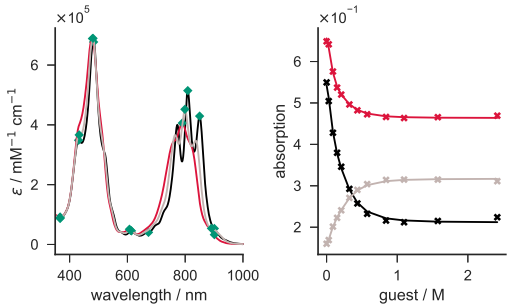

(d) ***c*-P6•A3**, 328 K, $K_{chem,1} = 3.7 \times 10^{12}$ M^{-1}

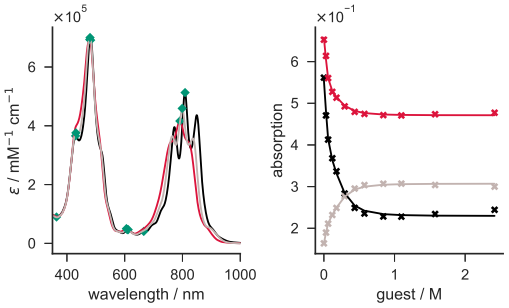

(e) ***c*-P6•B3**, 298 K, $K_{chem,1} = 1.9 \times 10^{14}$ M^{-1}

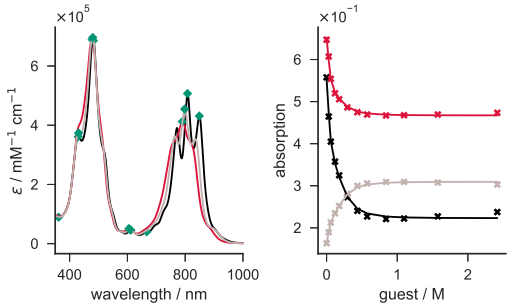

(f) ***c*-P6•B3**, 303 K, $K_{chem,1} = 8.5 \times 10^{13}$ M^{-1}

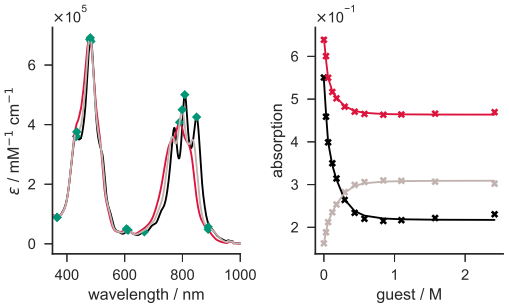

(g) ***c*-P6•B3**, 318 K, $K_{chem,1} = 6.2 \times 10^{12}$ M^{-1}

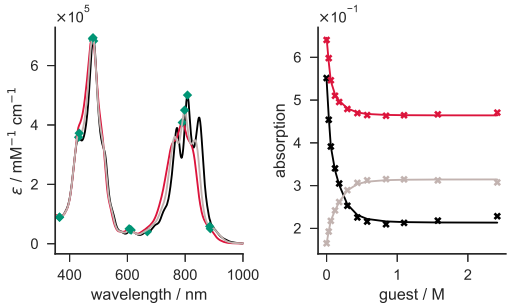

(h) ***c*-P6•B3**, 323 K, $K_{chem,1} = 5.4 \times 10^{12}$ M^{-1}

Figure 4.10: TD UV-vis-NIR denaturation titration experiment of ***c*-P6•X3**. Presented are the determined single components of the absorption spectra ***c*-P6•X3$_2$** in black, partially denaturated ***c*-P6•X3py$_3$** in grey, and fully denaturated ***c*-P6•py$_6$** in red. The fitted binding isotherm of three characteristic wavelengths (735 nm in grey, 807 nm in red, 847 nm in black) are shown, respectively. Characteristic points of the spectra were used to validate the concentration of the individual measurements (green diamonds). (toluene, [***c*-P6**] = 1.29 µM).

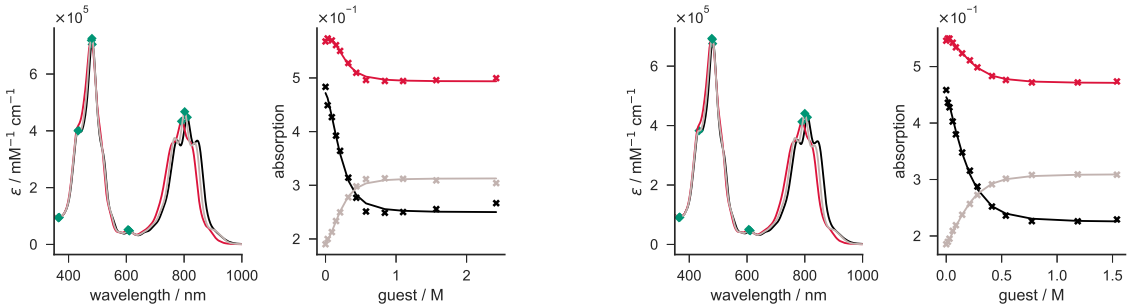

(a) 298 K, $K_{chem} = 2.4 \times 10^{14}$ M^{-1} **(b)** 308 K, $K_{chem} = 4.3 \times 10^{13}$ M^{-1}

(c) 318 K, $K_{chem} = 7.8 \times 10^{12}$ M^{-1} **(d)** 328 K, $K_{chem} = 1.6 \times 10^{12}$ M^{-1}

Figure 4.11: TD UV-vis-NIR denaturation titration experiment of ***c*-P6•C3**. Presented are the determined single components of the absorption spectra ***c*-P6•C3$_2$** in black, partially denaturated ***c*-P6•C3py$_3$** in grey, and fully denaturated ***c*-P6•py$_6$** in red. The fit accuracy is shown as experimental point compared to the fitted binding isotherm of three characteristic wavelengths (735 nm in grey, 807 nm in red, 847 nm in black), respectively. Characteristic points of the spectra were used to validate the concentration of the individual measurements (green diamonds). (toluene, [***c*-P6**] = 1.29 µM).

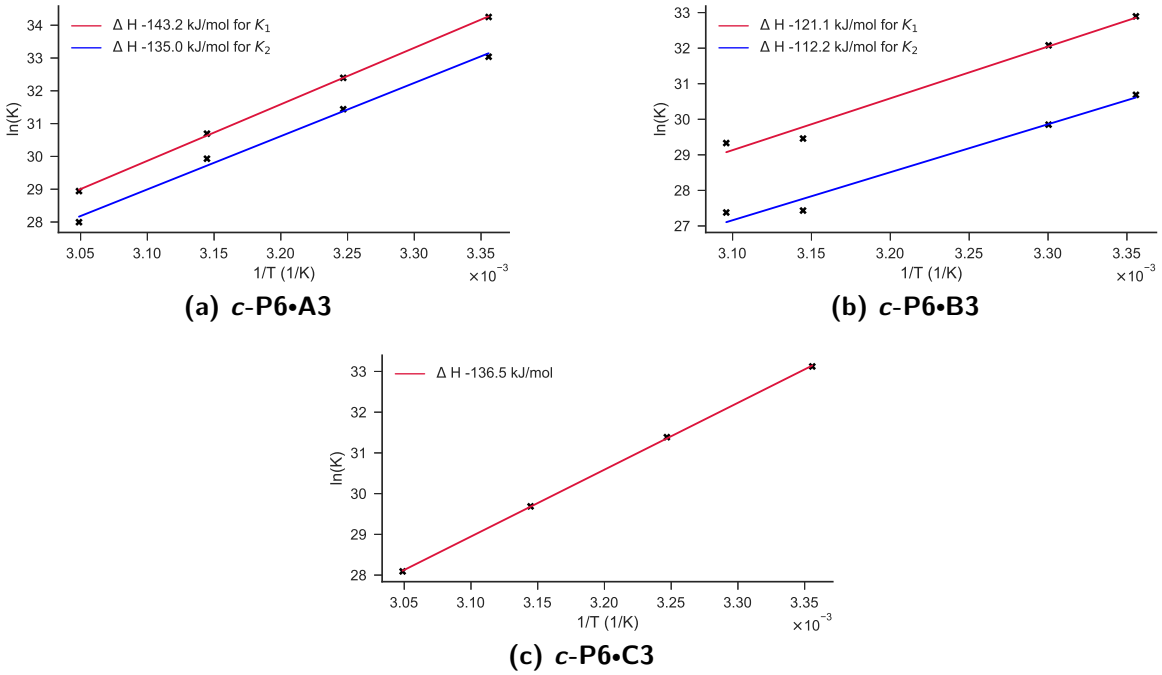

(a) ***c*-P6•A3** **(b)** ***c*-P6•B3**

(c) ***c*-P6•C3**

Figure 4.12: Van't Hoff plot and fit line for VT experiments (toluene, [***c*-P6**] = 1.29 µM).

4. Analysis of the Contributions of Enthalpy and Entropy to Cooperativity

Multiple very strong binding processes with independent binding enthalpies made the analysis of ***c*-P6** and the bidentate ligands very complicated. Therefore, the ITC experiments were done with the cyclic porphyrin nanoring **Zn_2-P6**, which has only two zinc centres and forms only 1:1 complexes. The ITC experiments show an excellent fit for all three bidentate guests. As a comparison, van't Hoff plots were done for all three bidentate guests (Fig. 4.13). Similar to the tridentate guests, the equilibrium constant at each temperature was determined via competition titration experiments for each host-guest system (Fig. 4.14).

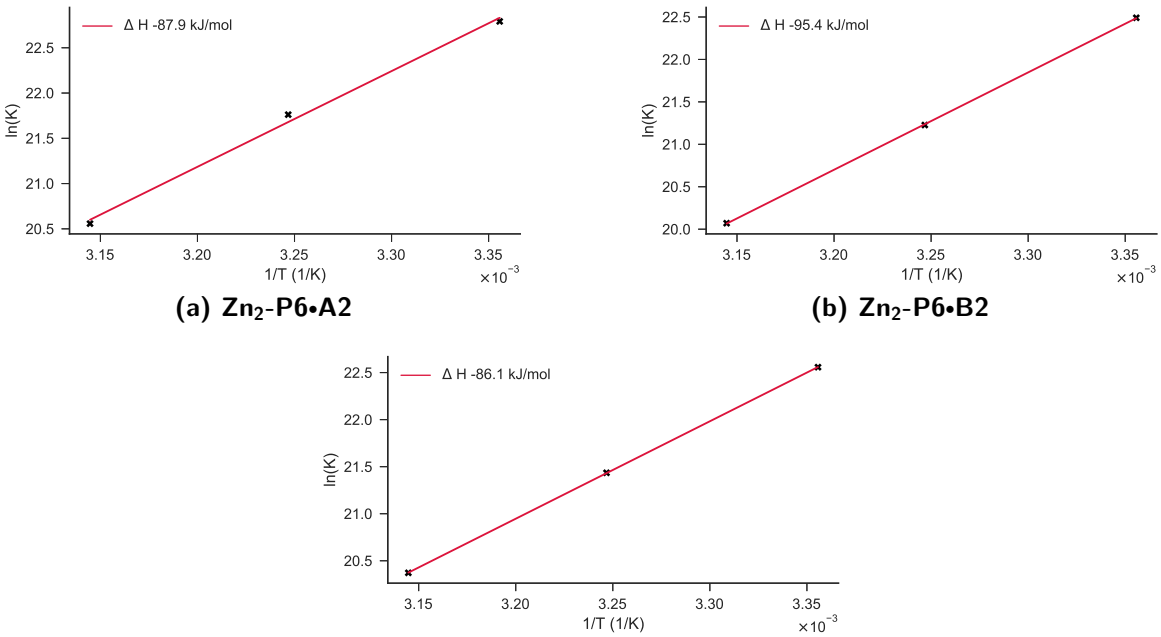

(a) Zn_2-P6•A2 **(b) Zn_2-P6•B2**

(c) Zn_2-P6•C2

Figure 4.13: Van't Hoff plot and fit line for VT experiments (toluene, [**Zn_2-P6**] = 0.67 µM).

An overview of the values is shown in Table 4.5. Both methods are in excellent agreement for **Zn_2-P6•A2** and **Zn_2-P6•B2**. For **Zn_2-P6•C2**, the methods give a different mean average between multiple repetitions. However, the values are within error of standard deviation. The comparison proves that both methods deliver valid binding enthalpies for these host-guest systems. For any further data analysis, the values obtained via ITC are used for the **Zn_2-P6** host. In the case of the tridentate guests, the binding enthalpies determined via van't Hoff appear more reliable since they can account for difference between 1:1 and 1:2 complexes.

It is notable that ITC experiments can be affected by both high experimental errors and overfitting of the experimental data. While we apply the most simple binding model

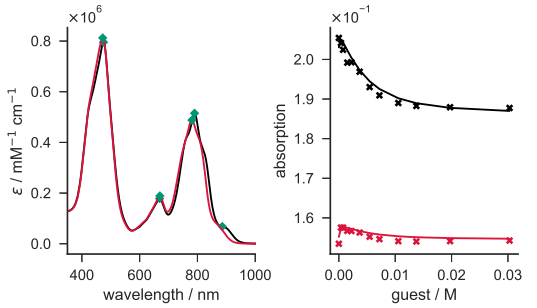

(a) Zn_2-P6•A2, 308 K, $K_{chem} = 1.7 \times 10^9$ M^{-1}

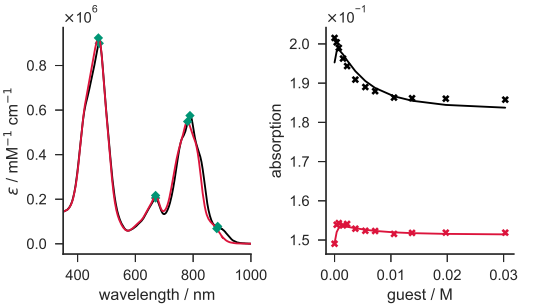

(b) Zn_2-P6•A2, 318 K, $K_{chem} = 5.2 \times 10^8$ M^{-1}

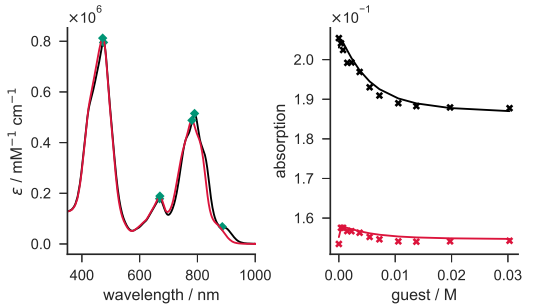

(c) Zn_2-P6•B2, 308 K, $K_{chem} = 2.0 \times 10^9$ M^{-1}

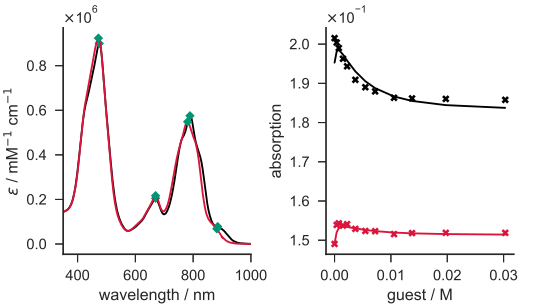

(d) Zn_2-P6•B2, 318 K, $K_{chem} = 7.0 \times 10^8$ M^{-1}

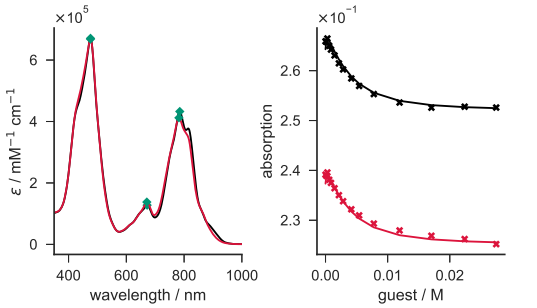

(e) Zn_2-P6•C2, 308 K, $K_{chem} = 2.8 \times 10^9$ M^{-1}

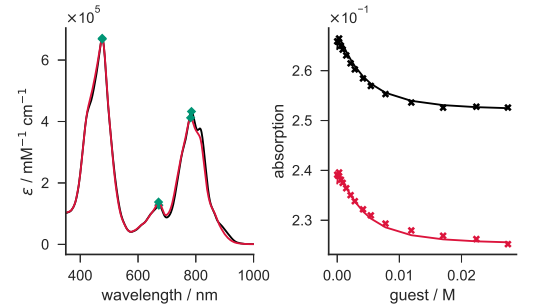

(f) Zn_2-P6•C2, 318 K, $K_{chem} = 8.5 \times 10^8$ M^{-1}

Figure 4.14: TD UV-vis-NIR denaturation titration experiment of **Zn_2-P6•X2**. Presented are the determined single components of the absorption spectra (host-guest complex in black, pyridine bound host in red) and the experimental point and the fitted binding isotherm of two characteristic wavelengths (791 nm in black, 813 nm in red), respectively. Characteristic points of the spectra were used to validate the concentration of the individual measurements (green diamonds) (toluene, [**Zn_2-P6**] = 0.67 µM).

(and therefore are likely to overfit the data), experimental errors are a significant error source. For carefully conducted ITC experiments, the experimental error can be reduced to 2 %. Without any further approximations or additional control experiments, the estimated average experimental error based on values reported in databases is around 20 %.[153] To minimise the errors in this experimental series, all ITC experiments were done with independent stock solutions. The concentration of the stock solutions was controlled via UV-vis-NIR experiments. Any experiments indicating air bubbles or other instabilities in the measurement were discarded. With this careful design, the overall experimental error

for the ITC experiments could be reduced to 5 %.

4.5.2 Linear Hosts

All complexes involving linear hosts only form 1:1 complexes, and can therefore be analysed via a simple 1:1 binding model. The binding constants for all complexes involving the linear trimer are sufficiently high to perform the ITC experiments at mM concentrations. The formation enthalpy for the tridentate guests binding to ***l*-P3** were determined via ITC experiments, with the exception of ***l*-P3•C3** due to solubility issues. The formation enthalpy for ***l*-P3•C3** was determined via van't Hoff experiments (Fig. 4.15). An overview of the values is shown in Table 4.6.

Table 4.6: Overview ΔH determined via ITC experiments for ***l*-P3•A3**, ***l*-P3•B3**, and ***l*-P3•C3**.

ΔH (kJ mol^{-1})	***l*-P3•A3**	***l*-P3•B3**	***l*-P3•C3**
ITC	-96.9 ± 5	-93.5 ± 5	–
van't Hoff	–	–	-95.9 ± 5

Compared to the cyclic hosts, the linear hosts show a lower binding enthalpy in general due to the induced bending on the acetylene linkers via complex formation. The formation enthalpies of complexes involving **A3**, **B3**, and **C3** are identical within experimental error.

The determination of binding enthalpy for the ***l*-P2** host was more challenging. Due to the low heat release, concentrations in the mM range were required. With an increase in concentration, a decrease in the determined binding constant was observed. For the lowest possible dimer concentration ([***l*-P2**] $= 5 \times 10^{-5}$ M), the binding constants are an order of magnitude lower than those obtained by UV-Vis-NIR titrations (see Appendix). Therefore, van't Hoff plots were done for all the bidentate guests binding to ***l*-P2**.

For the complexes ***l*-P2•A2** and ***l*-P2•C2**, both methods result in identical values within experimental error tolerances (Table 4.7).

Table 4.7: Overview ΔH determined via ITC experiments for ***l*-P2•A2**, ***l*-P2•B2**, and ***l*-P2•C2**.

ΔH (kJ mol^{-1})	***l*-P2•A2**	***l*-P2•B2**	***l*-P2•C2**
ITC	-82.5 ± 5	-71.2 ± 4	-78.2 ± 5
van't Hoff	-85.6 ± 5	-56.9 ± 3	-76.0 ± 4

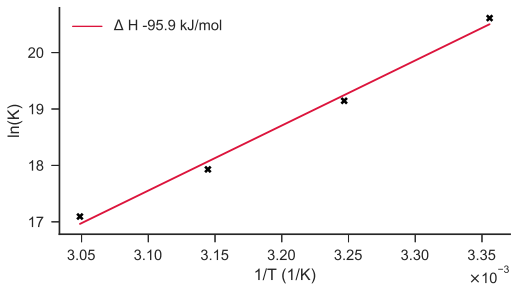

(a) Van't Hoff plot and fit line for VT experiments

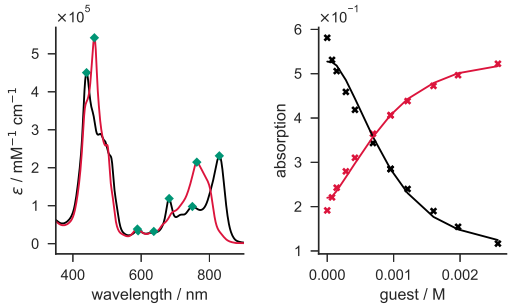

(b) 308 K, $K_{chem} = 2.1 \times 10^8$ M^{-1}

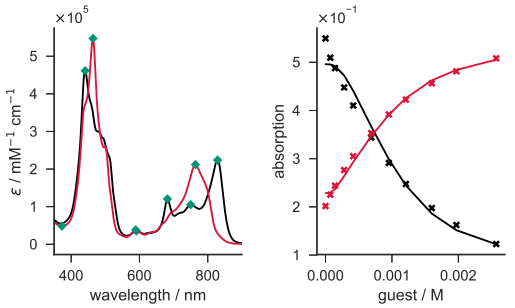

(c) 318 K, $K_{chem} = 6.1 \times 10^7$ M^{-1}

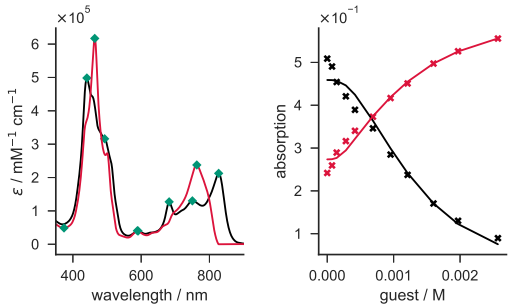

(d) 328 K, $K_{chem} = 2.7 \times 10^7$ M^{-1}

Figure 4.15: TD UV-vis-NIR denaturation titration experiment of ***c*-P6•C3**. Presented are the determined the single components of the absorption spectra and the experimental point, characteristic points comparing total absorbance for several experiments (green diamonds), and the fitted binding isotherm of two characteristic wavelengths (toluene, host-guest complex in black, pyridine bound host in red, wavelengths are 824 nm in black, 762 nm in red, [***l*-P3**] = 2.42 µM).

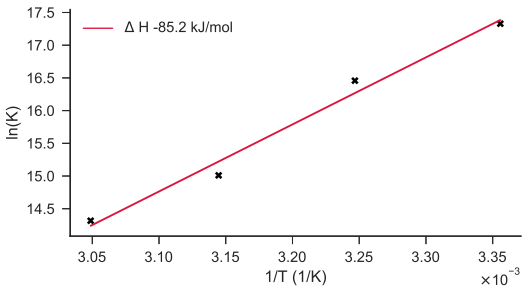

(a) ***l*-P2•A2**

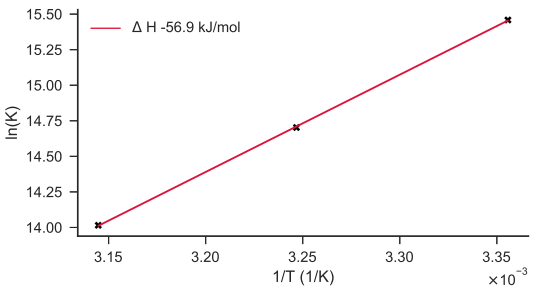

(b) ***l*-P2•B2**

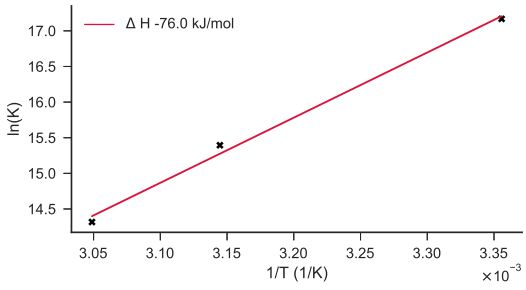

(c) ***l*-P2•C2**

Figure 4.16: Van't Hoff plot and fit line for VT experiments (toluene, [***l*-P2**] = 3.13 µM).

However, the complex ***l*-P2•B2** shows a high deviation between ITC and van't Hoff, as the binding enthalpy determined via van't Hoff experiment is 14 kJ mol^{-1} lower than the ITC value. The dependency of the binding constant with concentration in the ITC experiments in combination with the overestimation of binding enthalpy suggests that the presence of intermolecular complexes increases with higher concentrations.

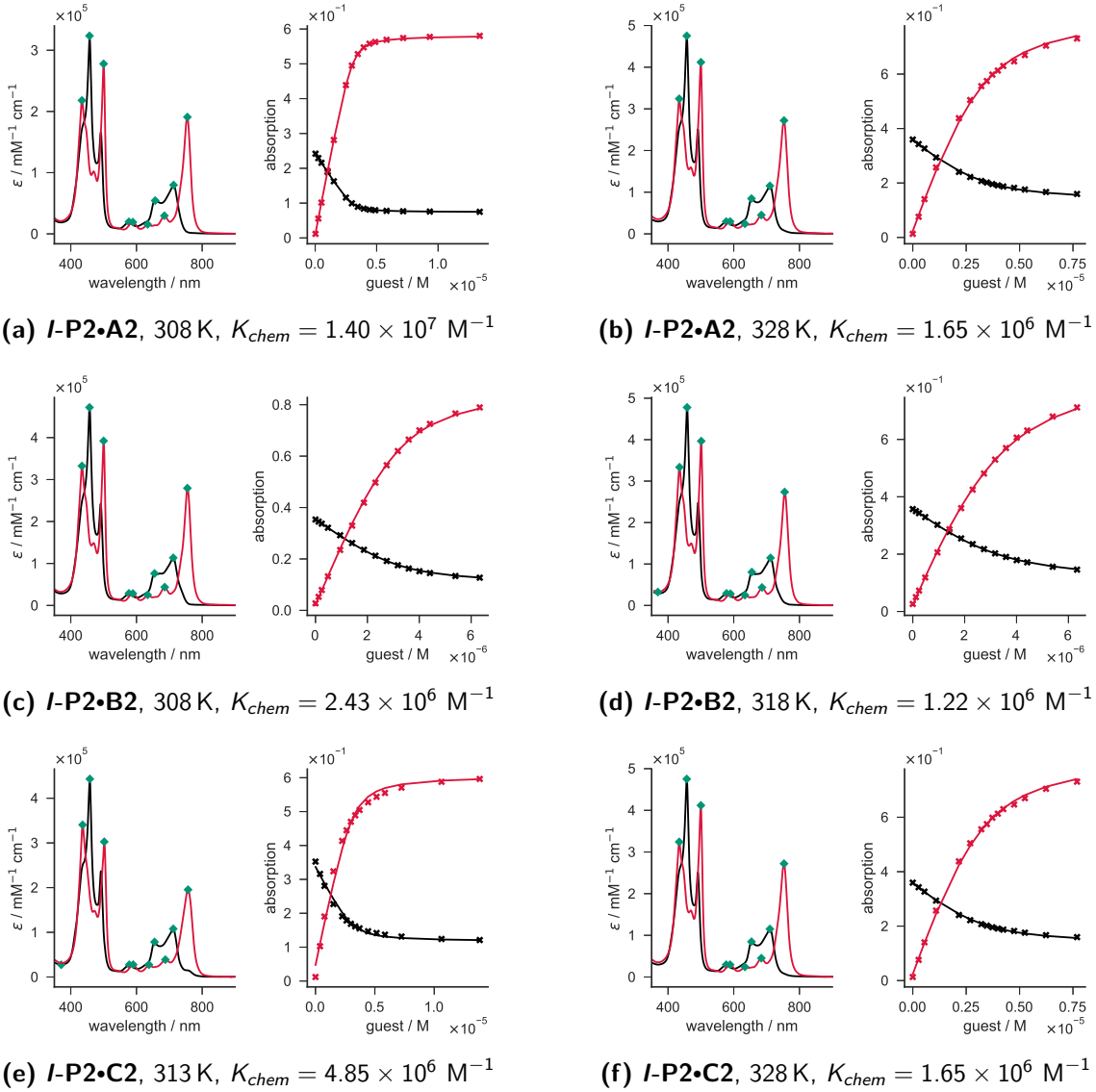

(a) ***l*-P2•A2**, 308 K, $K_{chem} = 1.40 \times 10^7$ M^{-1}

(b) ***l*-P2•A2**, 328 K, $K_{chem} = 1.65 \times 10^6$ M^{-1}

(c) ***l*-P2•B2**, 308 K, $K_{chem} = 2.43 \times 10^6$ M^{-1}

(d) ***l*-P2•B2**, 318 K, $K_{chem} = 1.22 \times 10^6$ M^{-1}

(e) ***l*-P2•C2**, 313 K, $K_{chem} = 4.85 \times 10^6$ M^{-1}

(f) ***l*-P2•C2**, 328 K, $K_{chem} = 1.65 \times 10^6$ M^{-1}

Figure 4.17: TD UV-vis-NIR denaturation titration experiment of ***l*-P2•X2**. Presented are the determined single components of the absorption spectra and the experimental point, characteristic points comparing total absorbance for several experiments (green diamonds), and the fitted binding isotherm of two characteristic wavelengths (bound host in black, complex in red, wavelengths are 712 nm in black, 755 nm in red, [***l*-P2**] = 1.85 µM). Characteristic points of the spectra were used to validate the concentration of the individual measurements (green diamonds) (toluene, [***l*-P2**] = 3.13 µM).

By opening the intramolecular complex, a significant amount of strain is released. Both ***l*-P2•A2** and ***l*-P2•C2** complexes have significantly higher EM values than ***l*-P2•B2**.

An intramolecular complex with a high EM value would be less affected by the total concentration. For ***I*-P2•B2** with an EM value of 0.0026 M, the ITC experiments reach the concentrations at which the open, intermolecular complex might start competing with the intramolecular one. Therefore, the results obtained by van't Hoff seem to be more reliable for the ***I*-P2** hosts and any further data analysis uses the enthalpy values determined via van't Hoff experiments for the ***I*-P2** hosts.

4.6 Results and Discussion

4.6.1 Calculation of Gibbs Energy of Chelation, Chelation Enthalpy, and Entropy

The statistically corrected binding constants can be transferred into statistically corrected Gibbs energy of binding ($\Delta G^*_{complex}$) via Equation 4.23. This Gibbs energy can be calculated for each complex. Since the enthalpy of binding ($\Delta H_{complex}$) was determined in independent experiments, the entropy of binding can be calculated by subtracting the enthalpy from the Gibbs energy (Eq. 4.24).

$$\Delta G^*_{complex} = -\mathrm{R}T \ln K_{\mathrm{chem}} \tag{4.23}$$

$$-T\Delta S^*_{complex} = \Delta G^*_{complex} - \Delta H_{complex} \tag{4.24}$$

To determine the Gibbs energy related to chelate cooperativity (ΔG^*_{coop}), the overall energetic changes upon binding can be separated into a cooperative and a non-cooperative part which relate to the singe site interaction. Therefore, we subtract the Gibbs energy related to the single-site interaction ($\Delta G^*_{single-site}$) multiplied by the number of binding interactions in the cooperative complex (N) from $\Delta G^*_{complex}$ (Eq. 4.25). The Gibbs energy ΔG^*_{coop} will be referred to as the Gibbs energy of chelation.

$$\Delta G^*_{coop} = \Delta G^*_{complex} - N \times \Delta G^*_{single-site} \tag{4.25}$$

As described in the chapter introduction, a Gibbs energy of $\Delta G^*_{coop} = 0$ relates to standard state conditions, for which $EM = 1\mathrm{M}$. However, there is no significant cooperativity related to $\Delta G^*_{coop} = 0$. In an analogous manner, we are able to determine the entropic and enthalpic contributions to chelate cooperativity. The cooperative enthalpic contributions

(ΔH_{coop}, Eq. 4.26) will be referred to as chelation enthalpy and is determined by subtracting the reference single-site interaction ($\Delta H_{single-site}$) multiplied with the number of binding interactions in the cooperative complex (N) from the binding enthalpy of the multivalent complex formation ($\Delta H_{complex}$). For the entropic contributions, all binding entropies are statistically corrected, to factor out symmetry differences between the intra- and the intermolecular system and make the changes in entropy easier to relate to molecular properties. Similar to the calculation of the enthalpic part of the cooperative energy of binding, the cooperative, temperature-corrected entropic contribution ($-T\Delta S^*_{coop}$) is calculated by subtracting N times the temperature-corrected binding entropy of the reference single-site interaction ($-T\Delta S^*_{single-site}$) from the temperature-corrected binding entropy of the multivalent complex formation ($-T\Delta S^*_{complex}$). We will refer to $-T\Delta S^*_{coop}$ as chelation entropy (Eq. 4.27).

$$\Delta H_{coop} = \Delta H_{complex} - N \times \Delta H_{single-site} \tag{4.26}$$

$$-T\Delta S^*_{coop} = -T\Delta S^*_{complex} + N \times (-T\Delta S^*_{single-site}) \tag{4.27}$$

4.6.2 Discussion of Chelation Energies

An overview of all determined values is shown in Table 4.8 and illustrated in Figure 4.18. Careful analysis of the data reveals four major conclusions which we will explain in this section.

Conclusion 1: The gain in chelation entropy is favourable, but does not scale linearly based on molecular rotors.

All entropies of complex formation ($-T\Delta S^*_{complex}$) are unfavourable due to the restriction in degrees of freedom by combining independent molecules. The complexation is driven by the very exothermic binding enthalpies ($\Delta H_{complex}$), which compensate the entropic changes. Despite these trends, comparing the chelation energies reveals the opposite trend. The entropic difference between the intramolecular and the equivalent intermolecular reaction step (quantified as chelation entropy $-T\Delta S^*_{coop}$) is favourable for all intramolecular complexes over the intermolecular ones (with exception of ***c*-P6•C2**, see Conclusion 4). The entropic gain of the intramolecular complex formation can be seen as favourable energetic driving force, which is in agreement with literature.[7]

Table 4.8: Overview of the geometric average effective molarity ($\overline{EM}$ in M) the experimentally determined, symmetry corrected Gibbs energy for complex formation $\Delta G^*_{complex}$, the experimental determined binding enthalpy $\Delta H_{complex}$, and the calculated, temperature and symmetry binding entropy $-T\Delta S^*_{complex}$ as well as the calculated cooperative contributions (ΔG^*_{coop}, ΔH_{coop}, $-T\Delta S^*_{coop}$) (all in kJ mol^{-1}).

Complex	$\Delta G^*_{complex}$	$\Delta H_{complex}$	$-T\Delta S^*_{complex}$	$\overline{EM}$	ΔG^*_{coop}	ΔH_{coop}	$-T\Delta S^*_{coop}$
***l*-P1•A1**	−23.97±0.25	−51.5±1.5	27.5±1.6	0	0	0	0
***l*-P2•A2**	−37.8±0.5	−82.5±2.5	44.7±2.5	0.017±0.005	10.2±0.7	20±4	−10±4
***l*-P3•A3**	−51.4±0.7	−96.9±2.9	45.5±3.0	0.0160±0.0034	20.5±1.1	57±5	−37±6
***l*-P1•B1**	−23.97±0.25	−51.5±1.5	27.5±1.6	0	0	0	0
***l*-P2•B2**	−33.1±0.5	−56.9±1.7	23.8±1.8	0.0026±0.0007	14.8±0.7	46.0±3.5	−31±4
***l*-P3•B3**	−46.4±0.7	−93.5±2.8	47.1±2.9	0.0058±0.0012	25.6±1.1	61±5	−35±6
***l*-P1•C1**	−21.30±0.25	−41.7±1.3	20.4±1.3	0	0	0	0
***l*-P2•C2**	−37.4±0.5	−78.2±2.3	40.8±2.4	0.122±0.035	5.2±0.7	5.2±3.4	0.0±3.5
***l*-P3•C3**	−44.2±0.7	−95.9±2.9	51.7±3.0	0.019±0.004	19.7±1.1	29±5	−9±5
***l*-P1•A1**	−23.97±0.25	−51.5±1.5	27.5±1.6	0	0		0
***c*-P6•A2**	−50.3±0.5	−96.2±2.9	45.8±2.9	2.6±0.7	−2.4±0.7	7±4	−9±4
***c*-P6•A3**	−86.9±0.7	−143±4	56±4	20±4	−15.0±1.1	11±6	−26±6
***l*-P1•B1**	−23.97±0.25	−51.5±1.5	27.5±1.6	0	0	0	0
***c*-P6•B2**	−48.4±0.5	−89.5±2.7	41.1±2.7	1.21±0.34	−0.5±0.7	13±4	−14±4
***c*-P6•B3**	−81.5±0.7	−121±4	40±4	6.9±1.5	−9.6±1.1	33±6	−43±6
***l*-P1•C1**	−21.30±0.25	−41.7±1.3	20.4±1.3	0	0	0	0
***c*-P6•C2**	−49.0±0.5	−99.7±3.0	50.7±3.0	13±4	−6.4±0.7	−16±4	10±4
***c*-P6•C3**	−86.8±0.7	−136±4	50±4	102±22	−22.9±1.1	−11±6	−11 ±6

Despite the importance of chelation entropy onto chelate cooperativity strength, the differences in chelation entropy between the different guest series are minor. The guest series were designed, so that **A** should show the most favourable chelation entropy, while both, **B** and **C**, have additional molecular rotors (but identical in the total number), which are frozen upon complexation. Therefore, a systematic energetic difference in chelation entropy was expected, but not observed (see Conclusion 3).

Conclusion 2: Chelate binding in the rings is much more favourable than to the linear oligomers, due to lower enthalpy penalty.

The difference in chelation entropy does not fully explain the experimental EM values. The second component influencing the stability of the intramolecular complex is the chelation enthalpy. The chelation enthalpy is endothermic for all complexes except ***c*-P6•C2** and ***c*-P6•C3** (see Conclusion 4). A favourable chelation enthalpy relates to an intramolecular process, in which the reaction heat is higher than in the corresponding intermolecular one. A possible source would be an allosteric effect, *e.g.* electronic changes influencing the attraction between the nitrogen in the guest and the zinc in the host molecule. However,

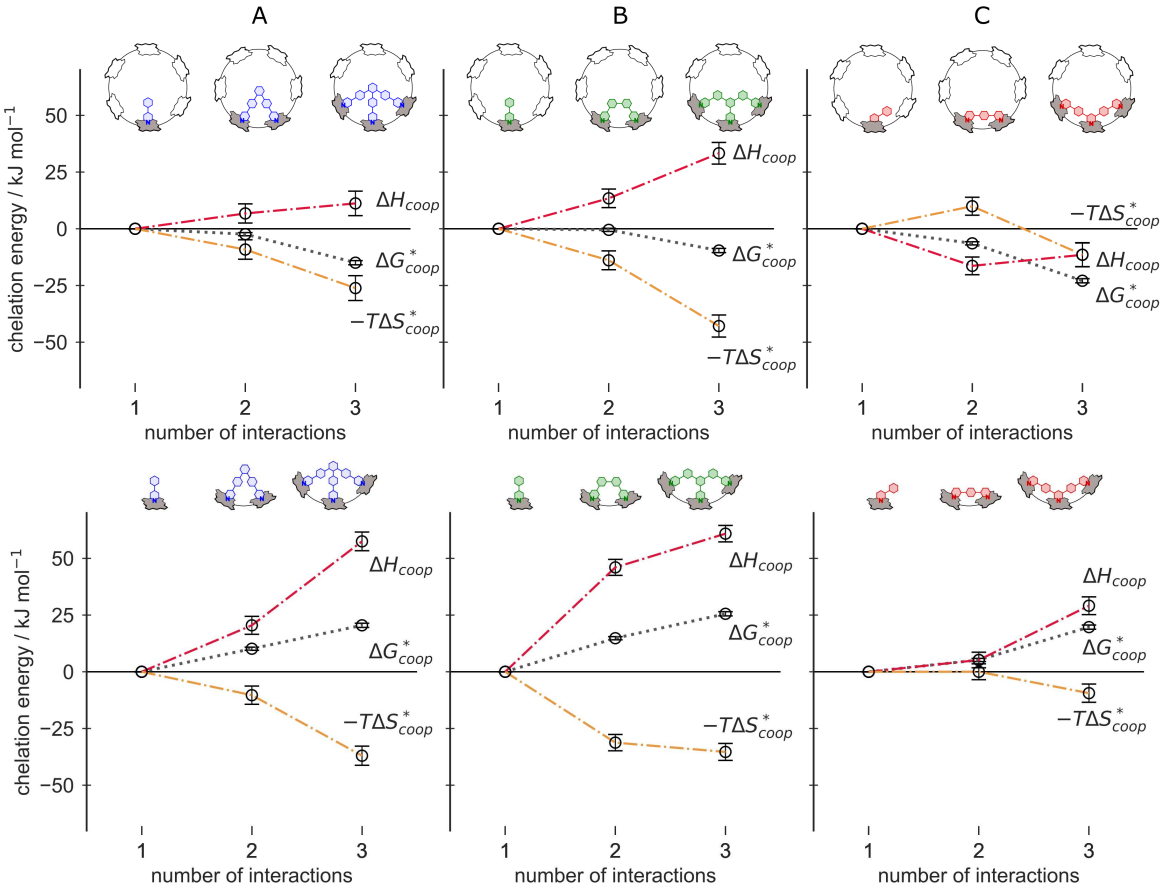

Figure 4.18: Plot of chelation enthalpy $\Delta H_{complex}$, chelation entropy $-T\Delta S^*_{coop}$, and Gibbs energy of chelation $\Delta G^*_{complex}$ in dependence of the number of interactions (in kJ mol^{-1}).

we eliminated allosteric effects as a source of changes in enthalpy within the guest design; there are no electronic changes induced by binding one site of a multivalent guest (see Chapter 2). Comparing the two different types of hosts illustrates that the linear hosts (***l*-P2** and ***l*-P3**) pay a higher cost in chelation enthalpy compared to the cyclic, rigid, shape-complementary one (***c*-P6**). This endothermic effect is based on the strain induced on the system by bending the acetylene linkers. As a result, the observed difference in $\overline{EM}$ and chelation energy between the linear and cyclic hosts are based on chelation enthalpy not entropy, which is nicely illustrated in Figure 4.18. Comparing the stepwise change in chelation energies, the chelation enthalpy (shown in red) is less unfavourable for the cyclic than the linear hosts within each guest series.

Conclusion 3: Entropy and enthalpy are antagonists.

Comparison of the chelation enthalpy for the three guest series within the linear hosts illustrates different profiles for the induced strain. Explicitly, the experimental determined chelation enthalpy shows only moderate strain for ***l*-P2•C2** and ***l*-P3•C3** and a harsh strain

in case of ***l*-P2•B2** and ***l*-P3•B3**. Controversially, DFT calculations have shown that the amount of bending (and hence the amount of induced strain energy) does not support the trend (compare Figure 4.19). This is qualitatively illustrated by the comparison of the calculated Zn–Zn distances. In the absence of strain, the Zn–Zn distance is 13.585 Å in the linear ***l*-P2** (B3LYP/6-31G*). By binding any of the bidentate guests, the complexation introduces strain. Therefore, the Zn–Zn distances decrease. The shortest Zn–Zn distances was found in the ***l*-P2•C2** complex (12.311 Å), which has the most favourable chelation enthalpy (Fig. 4.19).

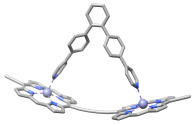

Zn–Zn: 13.018 Å

$\Delta H_{coop} = 20\,\mathrm{kJ\,mol^{-1}}$

(a) *l*-P2•A2

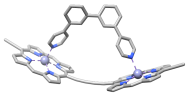

Zn–Zn: 12.786 Å

$\Delta H_{coop} = 46\,\mathrm{kJ\,mol^{-1}}$

(b) *l*-P2•B2

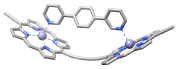

Zn–Zn: 12.311 Å

$\Delta H_{coop} = 5.2\,\mathrm{kJ\,mol^{-1}}$

(c) *l*-P2•C2

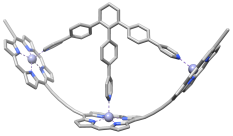

Zn–Zn: 12.570 Å

$\Delta H_{coop} = 57\,\mathrm{kJ\,mol^{-1}}$

(d) *l*-P3•A3

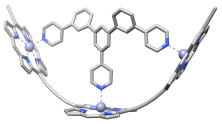

Zn–Zn: 12.384 Å

$\Delta H_{coop} = 61\,\mathrm{kJ\,mol^{-1}}$

(e) *l*-P3•B3

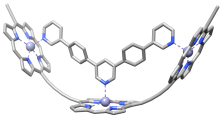

Zn–Zn: 12.275 Å

$\Delta H_{coop} = 29\,\mathrm{kJ\,mol^{-1}}$

(f) *l*-P3•C3

Figure 4.19: Optimised molecular geometries of the host-guest complexes on B3LYP/6-31G* level. Given values describe the zinc–nitrogen axial coordination bond length (Zn–N for the divalent systems, Zn–N_1 for the central and Zn–N_2 for the outer axial coordination for the trivalent systems), the distance between the nitrogens in the guests (N_1–N_2 gives the distance between the central and an outer nitrogen in the trivalent systems).

The trimer complexes follow this trend; the differences between the Zn–Zn distances become smaller for the complexes ***l*-P3•A3**, ***l*-P3•B3**, and ***l*-P3•C3**. While the chelation enthalpy is similar for ***l*-P3•A3** and ***l*-P3•B3**, ***l*-P3•C3** shows again the most favourable experimental chelation enthalpy for all three systems despite the highest amount of strain (based on the calculations). Based on the guest series **A** and **B**, the average strain energy required to bend one acetylene linker is $30\,\mathrm{kJ\,mol^{-1}}$.

Interestingly, series **B** shows unfavourable enthalpic properties, in both linear and cyclic cases. The guest series **B** shows a typical example of enthalpy-entropy-compensation (Fig.

4.18). It should be clarified at this point that we use the term enthalpy-entropy-compensation as a counter-play: strong attraction restricts degrees of freedom but conversely weakly interacting complexes retain higher degrees of freedom. The enthalpy-entropy-compensation is supported by theoretical and experimental evidence. The chelation enthalpy for ***l*-P2•B2** is with 46 kJ mol^{-1} by a factor of two more unfavourable than ***l*-P2•A2** (20 kJ mol^{-1}). This trend is reflected by theoretical calculations (on B3LYP/6-31G* level). Those have shown that the Zn-N bond length in ***l*-P2•B2** (2.184 Å) deviates 5 times more the from the ideal optimised bond value (2.164 Å) than ***l*-P2•A2** (2.173 Å) (see Chapter 2, Figure 2.15 on page 28). For the cyclic systems, the chelation enthalpy is identical for ***c*-P6•A2** and ***c*-P6•B2**. The same behaviour is observed in the theoretical calculations, where the Zn-N bond length is 2.171 Å in both cases. For the tridentate guests **A3** and **B3**, relating the chelation enthalpy to the Zn-N bond length is not sensible since the complex formation requires a planarisation of the phenly groups for guest **B3** which will influence the binding enthalpy and hence the chelation enthalpy.

Conclusion 4: Other factors need consideration; no unique relationship was found between chelation enthalpy and entropy and molecular structure.

Regarding Conclusion 3, it is apparent that relating chelation enthalpy and entropy and molecular structure is not sufficient to understand chelate cooperativity. This is demonstrated by the investigation of guest series **C**. Considering that the complex formation for the linear series shows more favourable chelation enthalpies than expected, it seems likely that an additional influence is compensating the strain energy. This hypothesis is supported by the exothermic chelation enthalpy of the cyclic complexes ***c*-P6•C2** and ***c*-P6•C3**, which experience no strain upon complex formation. An exothermic chelation enthalpy seems counterintuitive as it suggests that the (spatially restricted) intramolecular bond formation is more favourable than the intermolecular one, which has perfect flexibility to adjust to the binding geometry and reaches the ideal axial nitrogen zinc bond distance. This favourable chelation enthalpy is reflected in the effective molarity. The EM value is significantly increased for ***c*-P6•C2** and ***c*-P6•C3**. In terms of chelation entropy, the intramolecular process seems to be less favourable or equally unfavourable compared to the respective intermolecular process. A low EM value and hence a weak cooperative effect was expected due to the frozen rotations. Nevertheless, it was assumed that the unfavourable

effect on the chelation entropy would be the similar to guest series **B**. The experiments revealed a surprisingly favourable chelation entropy for guest series **B** (see Conclusion 3), while guest series **C** shows a chelation entropy identical or worse to the competing intermolecular interaction. Therefore, the chelate cooperativity effect observed in guest series **C** is not driven by a favourable chelation entropy.

An explanation for the surprisingly high chelation enthalpy and less favourable chelation entropy could be a strong interaction with solvent molecules. A strong interaction between solvent molecules and the formed complex could restrict the degrees of freedom of the solvent molecules and hence reduces the entropic gain for the complexation process. Consequently, a strong electrostatic interactions would result in a favourable enthalpy. However, the experimental determination of solvent effects is complicated. A solvent screening study on similar systems has revealed a strong dependency of *EM* values with different solvents.[154] However, the correlation between *EM* and the solvent properties is not understood and requires further analysis. This will be discussed in detail in Chapter 5.

4.7 Conclusion

In this chapter, we experimentally determined the entropic and enthalpic energies related to the complex formation of the host-guest library. The overall changes in enthalpy and entropy were separated into an intermolecular and an intramolecular part. The intramolecular part includes any energetic changes related to chelate cooperativity in the multivalent system. Exploring the chelation energies and its components revealed four overall insights. First, a favourable entropic effect is observed in nearly all intramolecular systems. Second, lesser distortion of the hosts and the guest leads to a more favourable chelation enthalpy, demonstrated by the rings which bind much more favourably than to the linear oligomers. However, the loss in chelation enthalpy is surprisingly high for a host-guest system optimised to the intermolecular bond lengths; the chelation enthalpy ranges between 7 and 46 $\mathrm{kJ\,mol^{-1}}$.

Interestingly, the expected trend in chelation entropy based on the number of frozen rotations was not found, leading to the third insight: enthalpy-entropy-compensation complicates the definition of a relationship between molecular structure and chelate cooperativity. This counter-play was observed in multiple systems: strong, tight binding on several binding sites reduces the degrees of freedom and equally a weaker chelation

enthalpy lets the complex maintain higher flexibility leading to a surprisingly favourable chelation entropy. Based on these compensation effect, the chelation entropy and enthalpy could not be directly related to molecular structures. The rigid hosts enable a more straightforward approach of linking cooperativity strength to molecular geometries, while the flexible oligomers are influenced by several competing factors.

The last insight is the challenges of molecular design based on individual entropic and enthalpic effects due to entropy-enthalpy compensation. The investigation of the host-guest library has shown that the prediction of chelate cooperativity will require consideration of additional factors such as solvation. While trends in chelation enthalpy could be related to individual molecular parts, entropy was better understood as a property of the overall system and hard to partition. Therefore, Chapter 5 will explore the potential of quantum mechanical calculations to predict chelate cooperativity based on Gibbs energy and the estimation of solvation effects.

4.8 Appendix: UV-vis-NIR and ITC Titration Data

The raw experimental data for the UV-vis-NIR titration spectra including experiment number for each individual measurement can be found here. Shown is an overlay of the individual spectra (**a**), the absorbance profile of a single (characteristic) wavelength in dependency of the guest concentration for the formation titrations, and in dependency of the pyridine concentration for the denaturation titrations (**b**). All titrations were performed in toluene at 298 K, with constant host concentration.

For a preliminary analysis, the formation titrations were fitted to a 1:1 binding isotherm assuming 'all-or-nothing' behaviour using the equation:

$$\frac{A - A_{initial}}{A_{\infty} - A_{initial}} = \left(\frac{(K_a\,(c\,[L] + [P]_0) + 1) - \sqrt{(K_a\,(c\,[L] + [P]_0) + 1)^2 - 4K_a^2[P]_0 c\,[L]}}{2K_a[P]_0} \right)$$

where A is the observed absorption at a specific wavelength or the difference of absorbance between two wavelengths; $A_{initial}$ is the starting absorption at this wavelength; A_{∞} is the asymptotic final absorption at this wavelength; K_a is the association constant between ligand and porphyrin host; [L] is the concentration of ligand; $[P]_0$ is the concentration of porphyrin host. For an accurate fit, the ligand concentration is multiplied by a scaling factor c which should compensate any errors occurring in the weighing process. The allowed tolerance range for scaling factor c is 15 %.

The denaturation titrations were analysed using the following equation as a first approximation:

$$\frac{A - A_{initial}}{A_{\infty} - A_{initial}} = \left(\frac{-K_{dn}[L]^2 + \sqrt{K_{dn}^2[L]^{2n} + 4K_{dn}[L]^n[P]_0}}{2[P]_0} \right)$$

where A is the observed absorption at a specific wavelength or difference of absorption between two wavelengths; $A_{initial}$ is the starting absorption at a specific wavelength or difference between absorption in two wavelengths; A_{∞} is the terminal absorption at a specific wavelength or difference of absorption in two wavelengths; K_{dn} is the dissociation constant between ligand and porphyrin oligomer complex, [L] is the concentration of ligand; $[P]_0$ is the concentration of porphyrin oligomer complex, n is the number of binding sites in the complex.

Titrations of Monodentate Ligands and *l*-P1, *c*-P6, Zn_2-P6

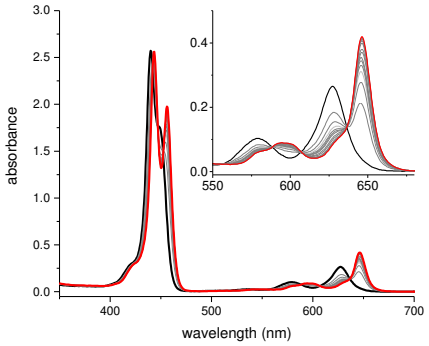

(a) Spectra

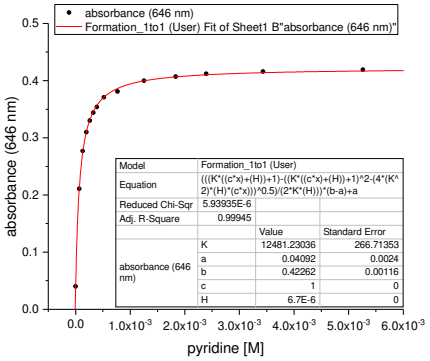

(b) Single wavelength concentration profile

Figure 4.20: UV-vis-NIR formation titration of **pyridine** and ***l*-P1**. Toluene, 298 K, [***l*-P1**] = 6.70×10^{-6} M, $K_a = 1.36 \times 10^4$ M^{-1}.

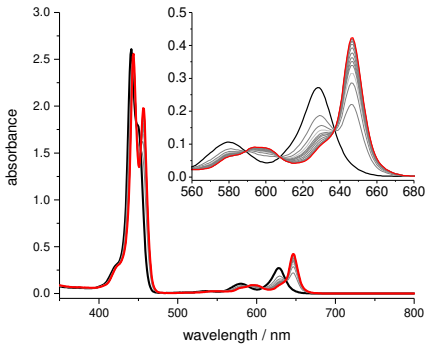

(a) Spectra

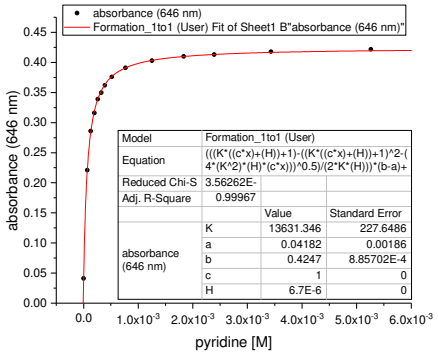

(b) Single wavelength concentration profile

Figure 4.21: UV-vis-NIR formation titration of **pyridine** and ***l*-P1**. Toluene, 298 K, [***l*-P1**] = 6.70×10^{-6} M, $K_a = 1.36 \times 10^4$ M^{-1}.

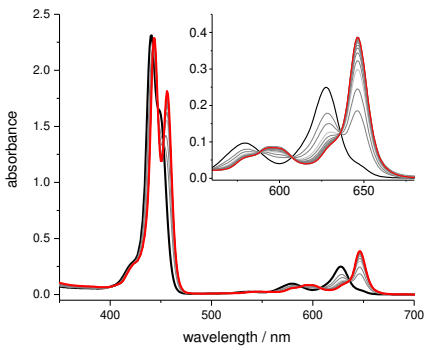

(a) Spectra

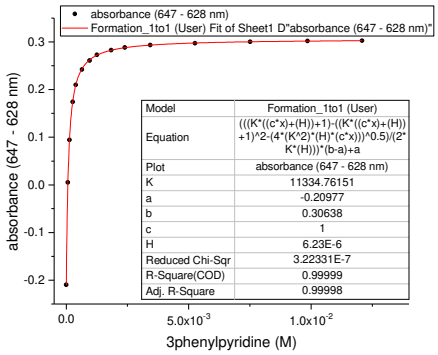

(b) Single wavelength concentration profile

Figure 4.22: UV-vis-NIR formation titration of **3-phenylpyridine** and ***l*-P1**. Toluene, 298 K, [***l*-P1**] = 6.23×10^{-6} M, $K_a = 1.13 \times 10^4$ M^{-1}.

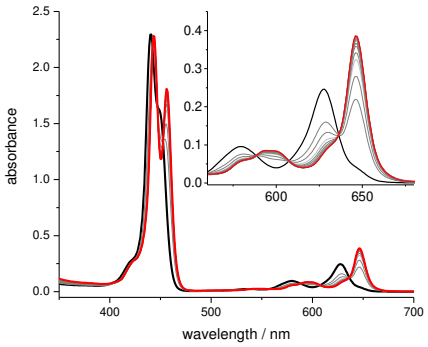

(a) Spectra

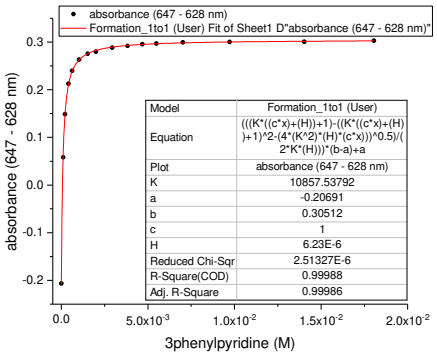

(b) Single wavelength concentration profile

Figure 4.23: UV-vis-NIR formation titration of **3-phenylpyridine** and ***l*-P1**. Toluene, 298 K, [***l*-P1**] = 6.23×10^{-6} M, $K_a = 1.09 \times 10^4$ M^{-1}.

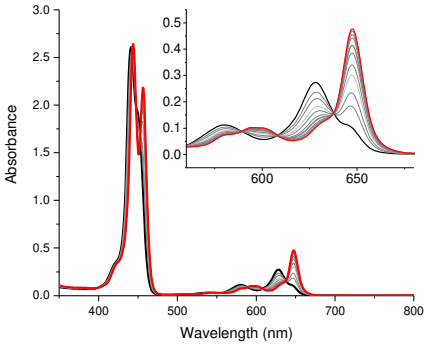

(a) Spectra

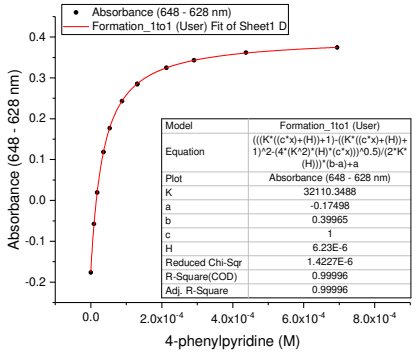

(b) Single wavelength concentration profile

Figure 4.24: UV-vis-NIR formation titration of **4-phenylpyridine** and ***l*-P1**. Toluene, 298 K, [***l*-P1**] = 6.23×10^{-6} M, $K_a = 3.21 \times 10^4$ M^{-1}.

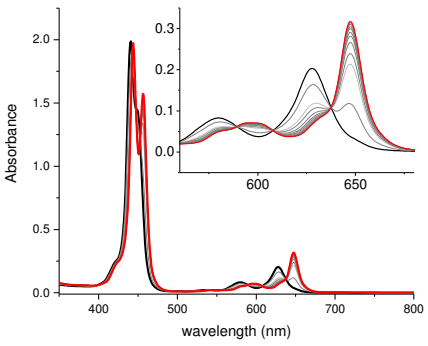

(a) Spectra

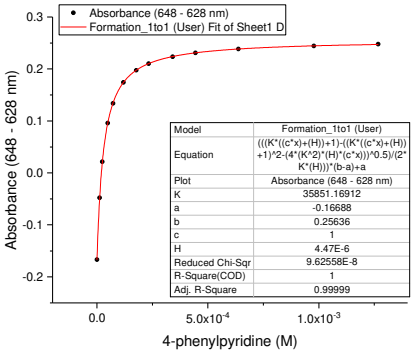

(b) Single wavelength concentration profile

Figure 4.25: UV-vis-NIR formation titration of **3-phenylpyridine** and ***l*-P1**. Toluene, 298 K, [***l*-P1**] = 4.47×10^{-6} M, $K_a = 3.39 \times 10^4$ M^{-1}.

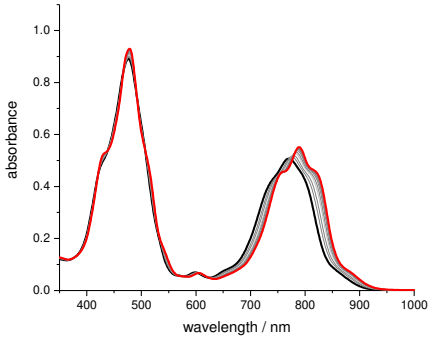

(a) Spectra, Run1, $K_a = 1.30 \times 10^4$ M^{-1}.

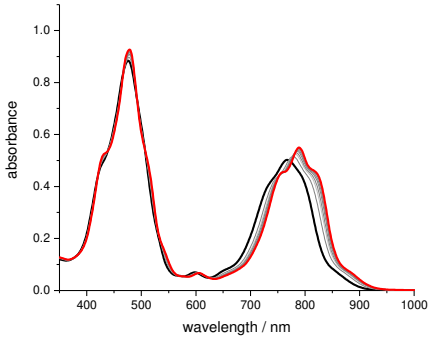

(b) Spectra, Run2, $K_a = 1.26 \times 10^4$ M^{-1}.

Figure 4.26: UV-vis-NIR formation titration of **pyridine** and ***c*-P6**. Toluene, 298 K, [***c*-P6**] = 1.29 × 10^{-6} M.

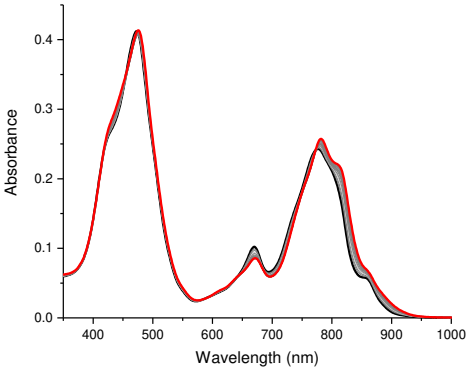

(a) Spectra, Run1, , $K_a = 1.20 \times 10^4$ M^{-1}.

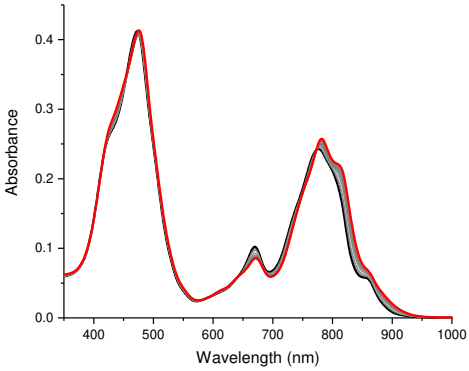

(b) Spectra, Run2, $K_a = 1.17 \times 10^4$ M^{-1}.

Figure 4.27: UV-vis-NIR formation titration of **pyridine** and **Zn_2-P6**. Toluene, 298 K, [**Zn_2-P6**] = 1.23 × 10^{-6} M.

Formation Titrations of Bidentate Ligands and *I*-P2

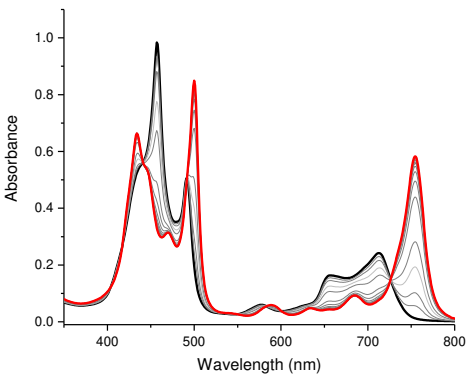

(a) Spectra

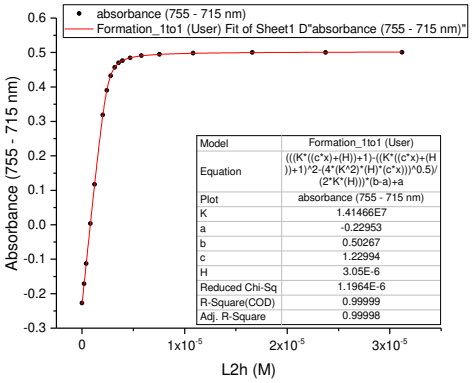

(b) Single wavelength concentration profile

Figure 4.28: UV-Vis titration of ***I*-P2** with **A2**. Run 1, toluene, 298 K, [***I*-P2**] = 3.05E-06 M (IG-3-04).

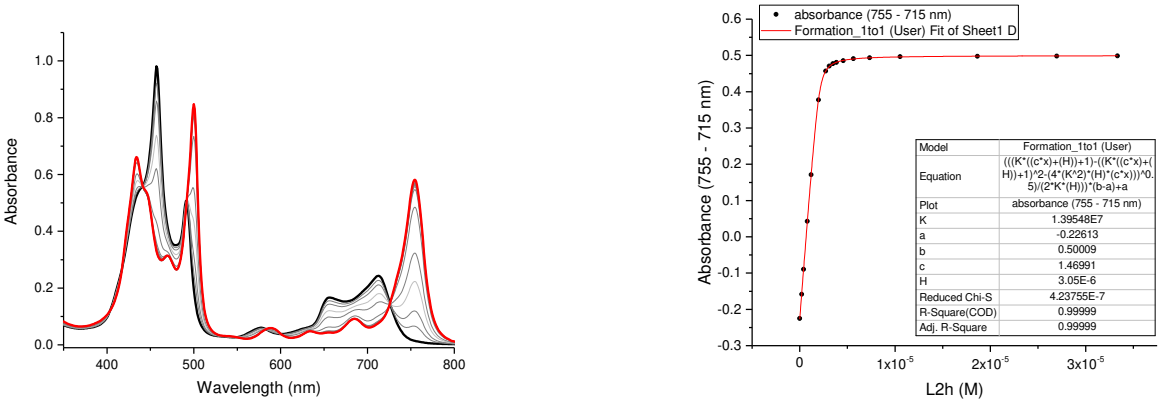

(a) Spectra **(b)** Single wavelength concentration profile

Figure 4.29: UV-Vis titration of ***I*-P2** with **A2**. Run 2, toluene, 298 K, [***I*-P2**] = 3.05E-06 M (IG-3-05).

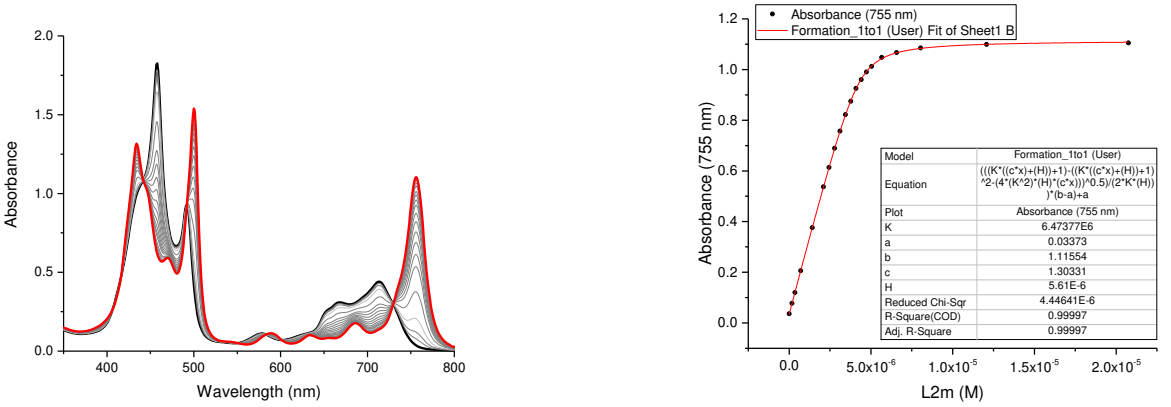

(a) Spectra **(b)** Single wavelength concentration profile

Figure 4.30: UV-Vis titration of ***I*-P2** with **B2**. Run 1, toluene, 298 K, [***I*-P2**] = 5.61E-06 M (IG-3-35).

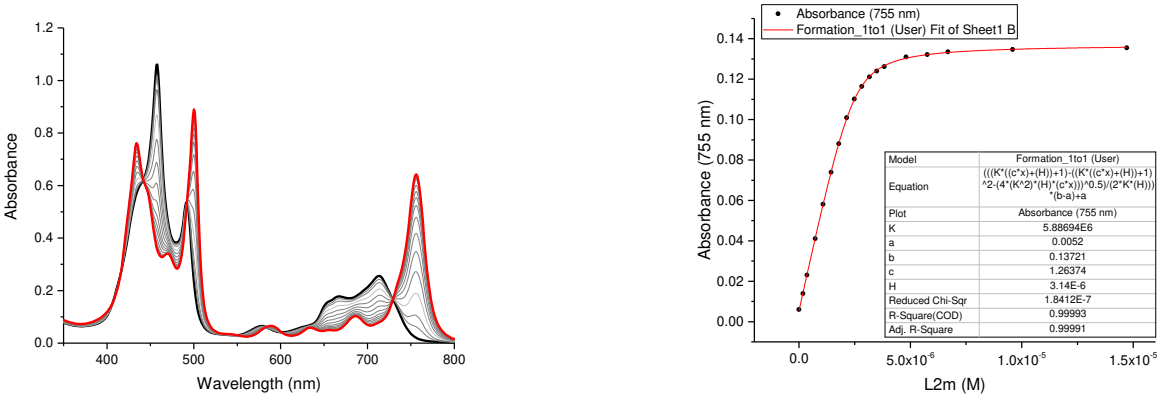

(a) Spectra **(b)** Single wavelength concentration profile

Figure 4.31: UV-Vis titration of ***I*-P2** with **B2**. Run 2, toluene, 298 K, [***I*-P2**] = 3.14E-06 M (IG-3-35).

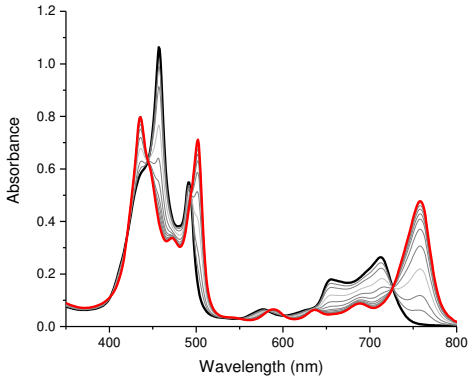

(a) Spectra

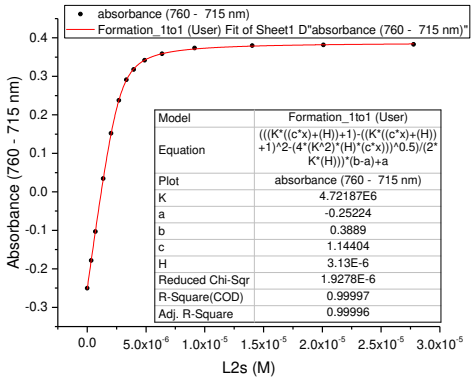

(b) Single wavelength concentration profile

Figure 4.32: UV-Vis titration of ***I*-P2** with **C2**. Run 1, toluene, 298 K, [***I*-P2**] = 3.13E-06 M (IG-3-01).

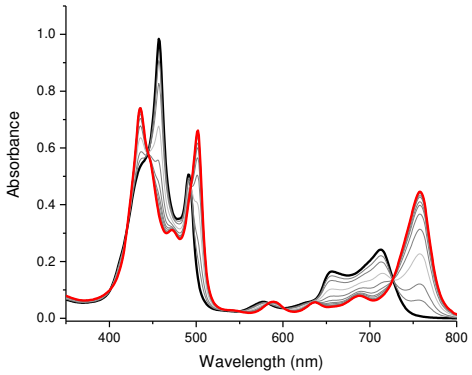

(a) Spectra

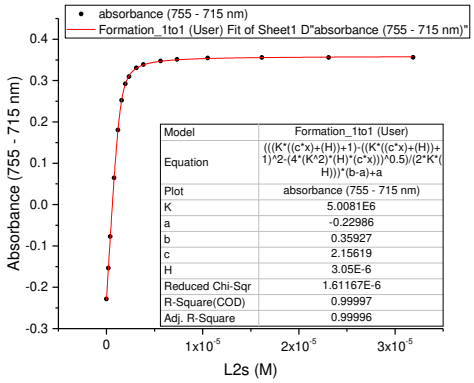

(b) Single wavelength concentration profile

Figure 4.33: UV-Vis titration of ***I*-P2** with **C2**. Run 2, toluene, 298 K, [***I*-P2**] = 3.05E-06 M (IG-3-03).

Formation and Denaturation Titrations of Tridentate Ligands and *I*-P3

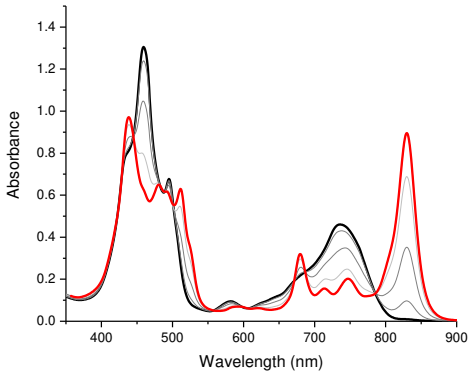

(a) Spectra

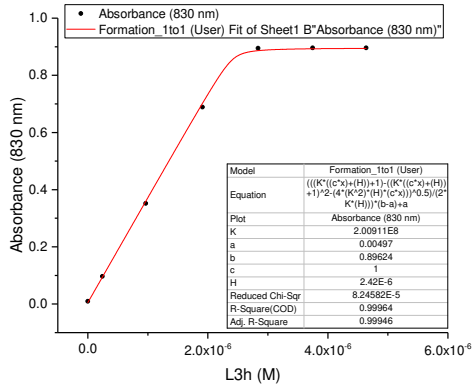

(b) Single wavelength concentration profile

Figure 4.34: UV-Vis titration of ***I*-P3** with **B3**. Run 1, toluene, 298 K, [***I*-P3**] = 2.42E-06 M (IG-3-35).

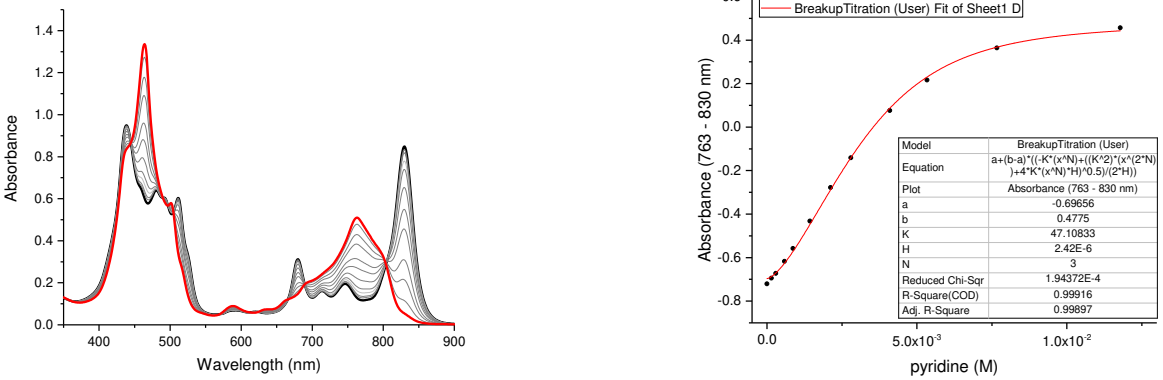

(a) Spectra **(b)** Single wavelength concentration profile

Figure 4.35: UV-Vis breakup titration of ***I*-P3•A3** with **pyridine**. Run 1, toluene, 298 K, [***I*-P3**] = 2.42E-06 M (IG-3-35).

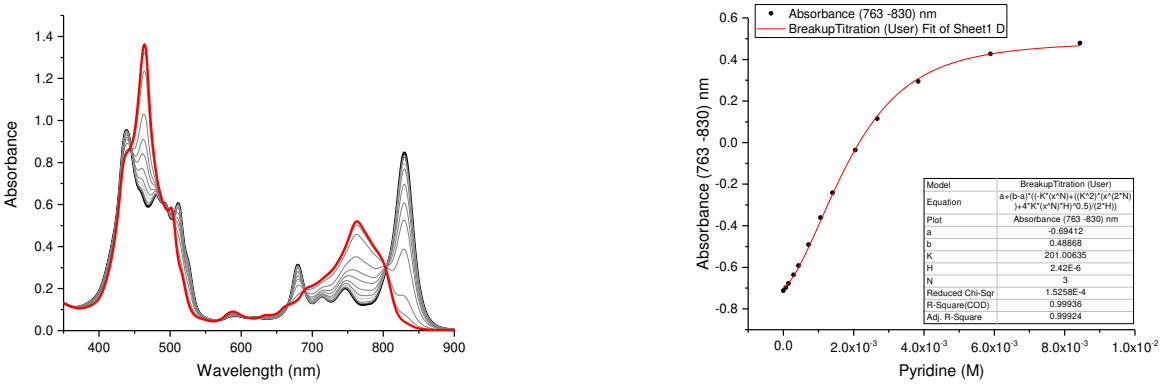

(a) Spectra **(b)** Single wavelength concentration profile

Figure 4.36: UV-Vis breakup titration of ***I*-P3•A3** with **pyridine**. Run 2, toluene, 298 K, [***I*-P3**] = 2.42E-06 M (IG-3-35).

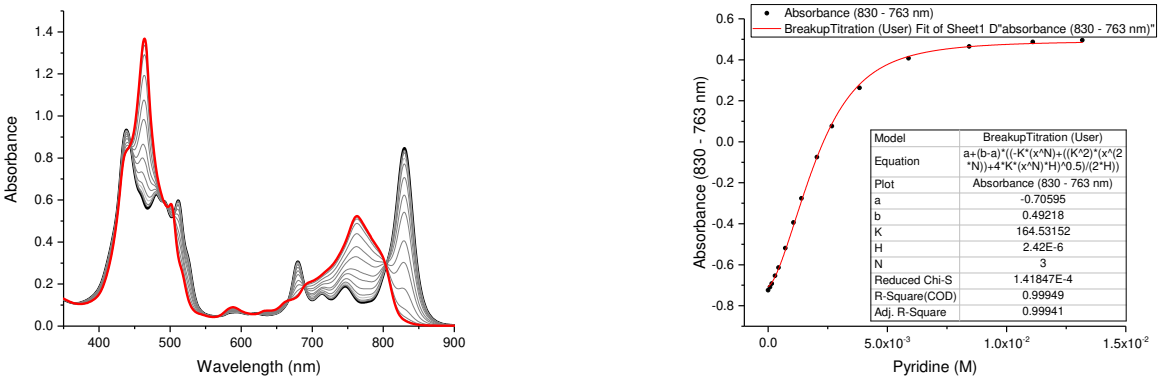

(a) Spectra **(b)** Single wavelength concentration profile

Figure 4.37: UV-Vis breakup titration of ***I*-P3•A3** with **pyridine**. Run 3, toluene, 298 K, [***I*-P3**] = 2.42E-06 M (IG-3-35).

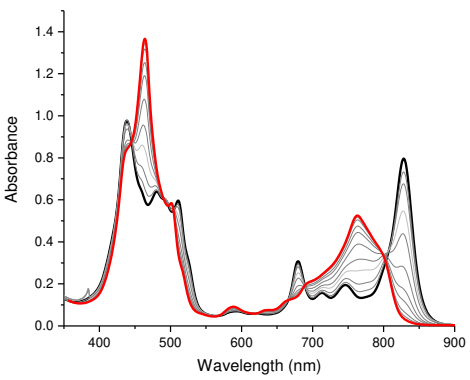

(a) Spectra

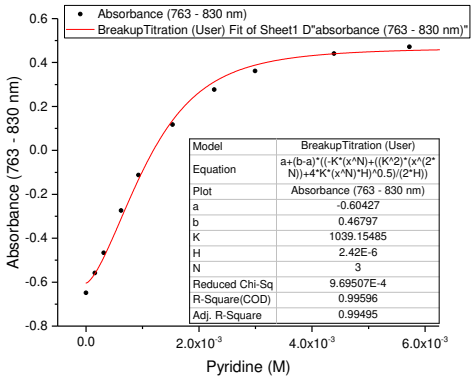

(b) Single wavelength concentration profile

Figure 4.38: UV-Vis breakup titration of ***l*-P3•B3** with **pyridine**. Run 1, toluene, 298 K, [***l*-P3**] = 2.42E-06 M (IG-3-35).

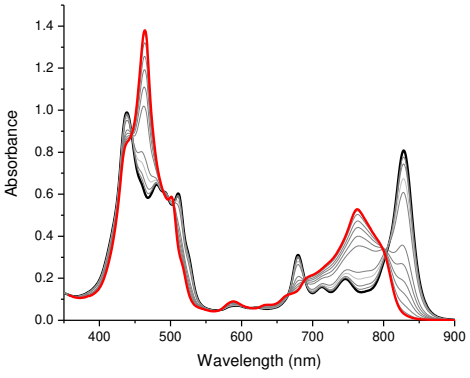

(a) Spectra

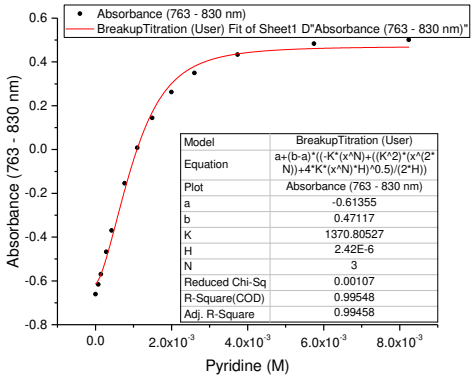

(b) Single wavelength concentration profile

Figure 4.39: UV-Vis breakup titration of ***l*-P3•B3** with **pyridine**. Run 2, toluene, 298 K, [***l*-P3**] = 2.42E-06 M (IG-3-35).

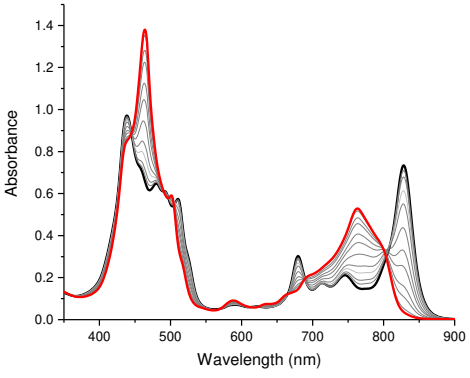

(a) Spectra

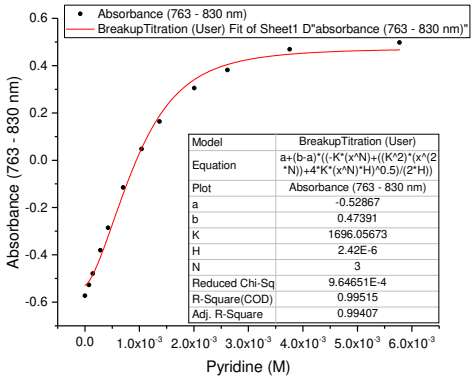

(b) Single wavelength concentration profile

Figure 4.40: UV-Vis breakup titration of ***l*-P3•B3** with **pyridine**. Run 3, toluene, 298 K, [***l*-P3**] = 2.42E-06 M (IG-3-35).

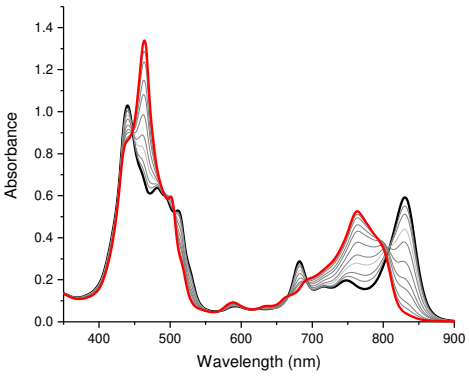

(a) Spectra

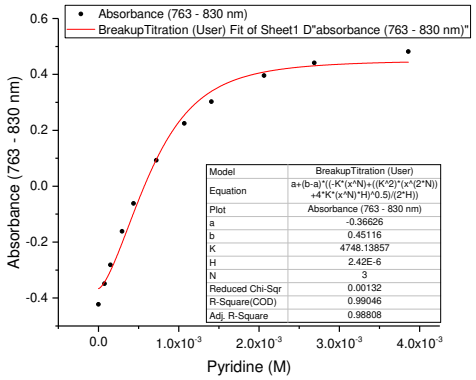

(b) Single wavelength concentration profile

Figure 4.41: UV-Vis breakup titration of ***I*-P3•C3** with **pyridine**. Run 1, toluene, 298 K, [***I*-P3**] = 2.42E-06 M (IG-3-35).

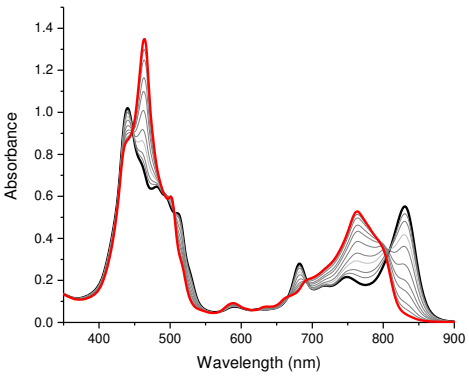

(a) Spectra

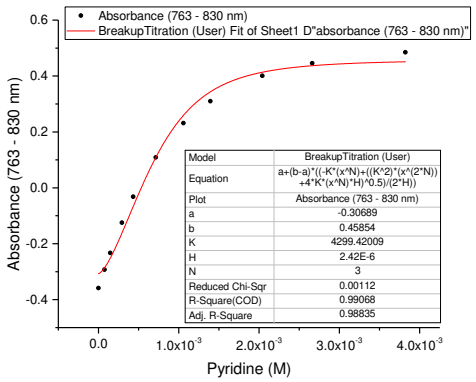

(b) Single wavelength concentration profile

Figure 4.42: UV-Vis breakup titration of ***I*-P3•C3** with **pyridine**. Run 2, toluene, 298 K, [***I*-P3**] = 2.42E-06 M (IG-3-35).

Denaturation Titrations of Bidentate Ligands and Zn_2-P6

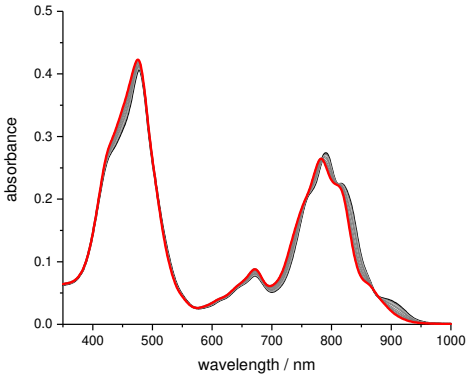

(a) Spectra

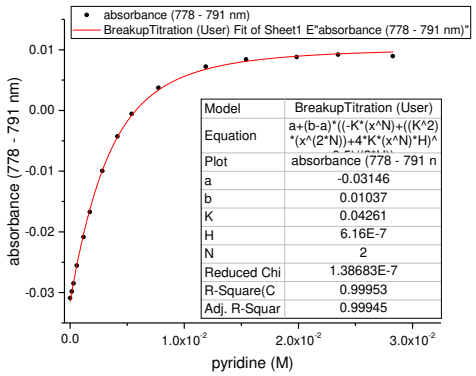

(b) Single wavelength concentration profile

Figure 4.43: UV-Vis titration of **pyridine** and **Zn_2-P6•A2**. Run 1, toluene, 298 K, [**Zn_2-P6**] = 6.16E-07 M (IG-3-16).

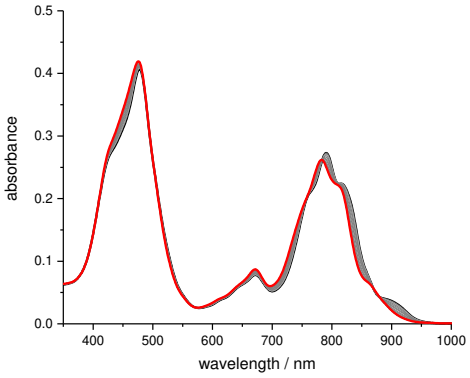

(a) Spectra

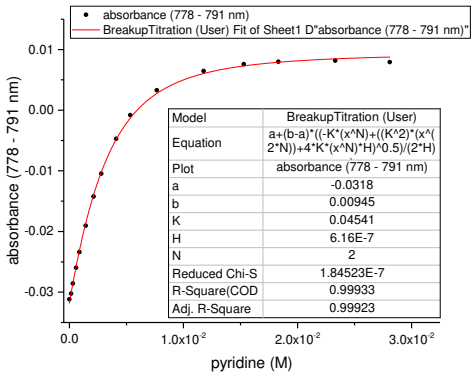

(b) Single wavelength concentration profile

Figure 4.44: UV-Vis titration of **pyridine** and **Zn_2-P6•A2**. Run 2, toluene, 298 K, [**Zn_2-P6**] = 6.16E-07 M (IG-3-16).

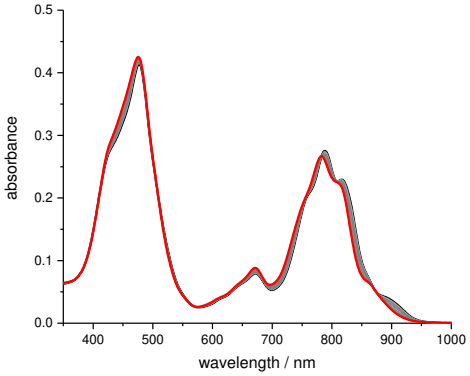

(a) Spectra

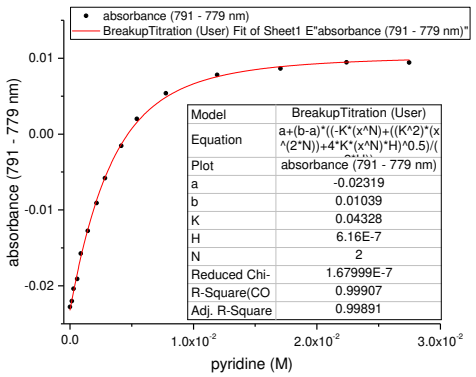

(b) Single wavelength concentration profile

Figure 4.45: UV-Vis titration of **pyridine** and **Zn_2-P6•B2**. Run 1, toluene, 298 K, [**Zn_2-P6**] = 6.16E-07 M (IG-3-18).

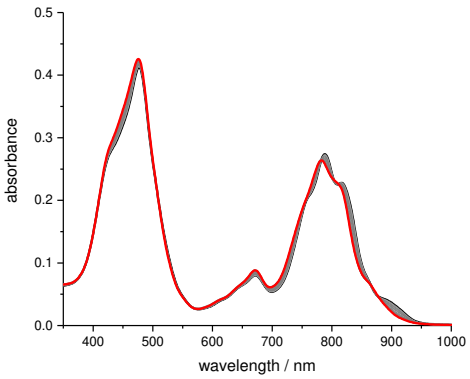

(a) Spectra

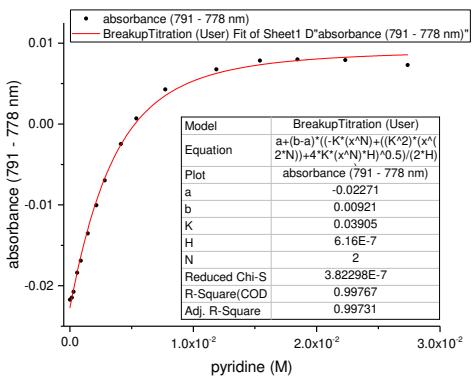

(b) Single wavelength concentration profile

Figure 4.46: UV-Vis titration of **pyridine** and **Zn_2-P6•B2**. Run 2, toluene, 298 K, [**Zn_2-P6**] = 6.16E-07 M (IG-3-18).

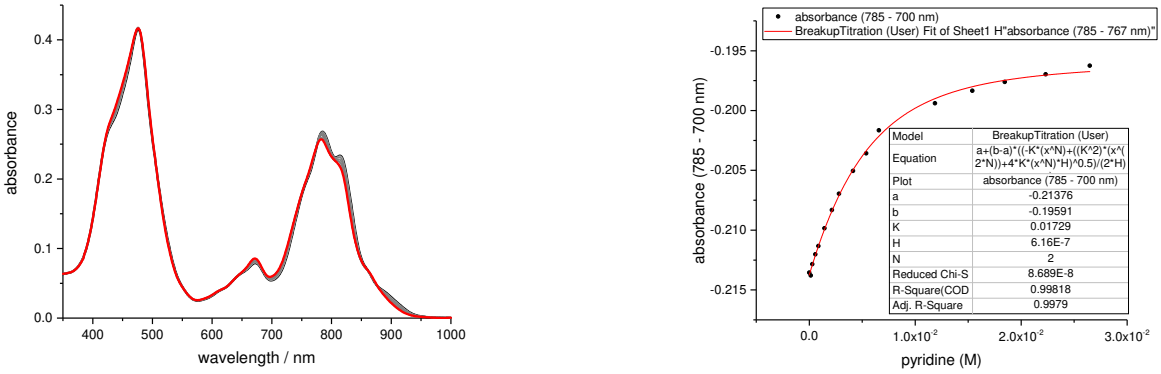

(a) Spectra **(b)** Single wavelength concentration profile

Figure 4.47: UV-Vis titration of **pyridine** and **Zn_2-P6•C2**. Run 1, toluene, 298 K, [**Zn_2-P6**] = 6.16E-07 M (IG-3-19).

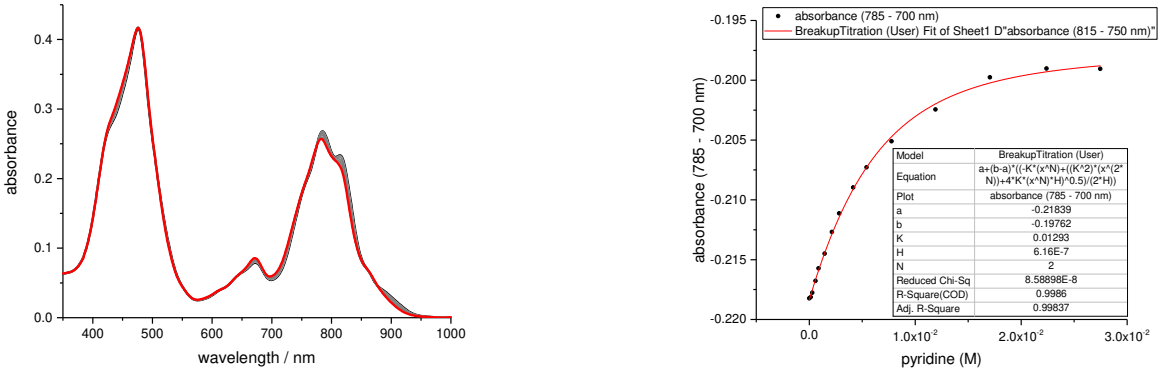

(a) Spectra **(b)** Single wavelength concentration profile

Figure 4.48: UV-Vis titration of **pyridine** and **Zn_2-P6•C2**. Run 2, toluene, 298 K, [**Zn_2-P6**] = 6.16E-07 M (IG-3-19).

Formation and Denaturation Titrations of Tridentate Ligands and *c*-P6

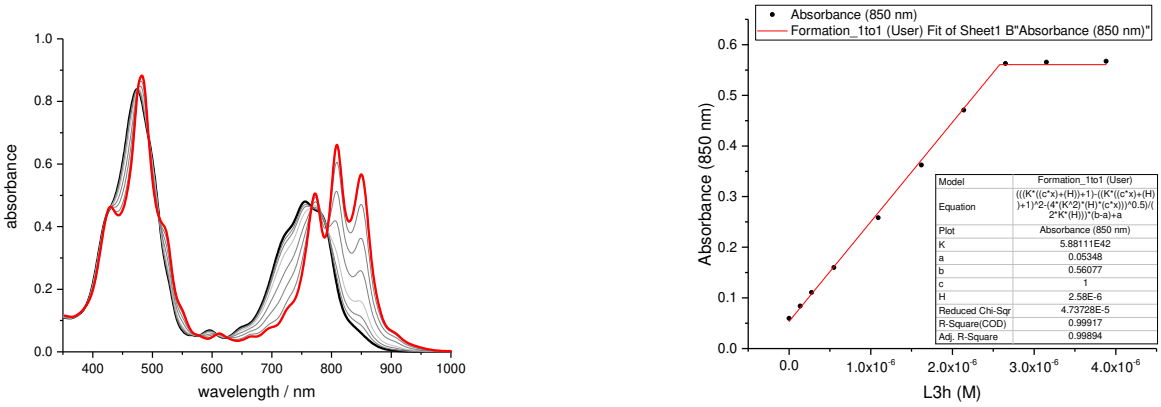

(a) Spectra **(b)** Single wavelength concentration profile

Figure 4.49: UV-Vis titration of ***c*-P6** with **A3**. Run 1, toluene, 298 K, [***c*-P6**] = 1.29E-06 M (IG-3-34).

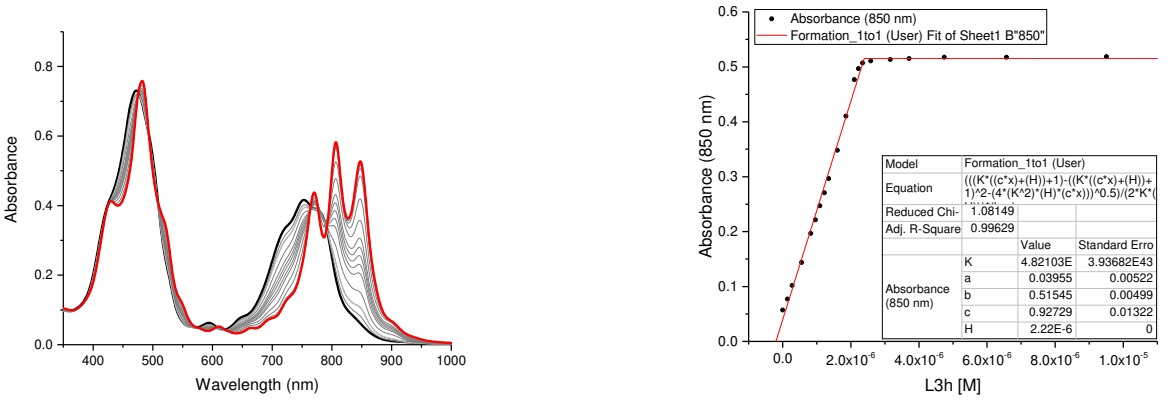

(a) Spectra **(b)** Single wavelength concentration profile

Figure 4.50: UV-Vis titration of ***c*-P6** with **A3**. Run 2, toluene, 298 K, [***c*-P6**] = 1.11E-06 M (IG-2-80).

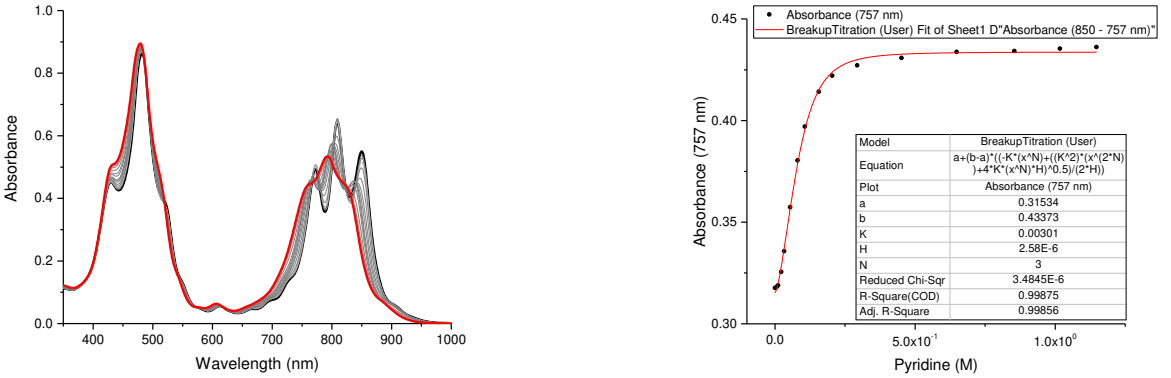

(a) Spectra **(b)** Single wavelength concentration profile

Figure 4.51: UV-Vis breakup titration of ***c*-P6•A3** with **pyridine**. Run 1, toluene, 298 K, [***c*-P6**] = 1.29E -06 M (IG-3-34).

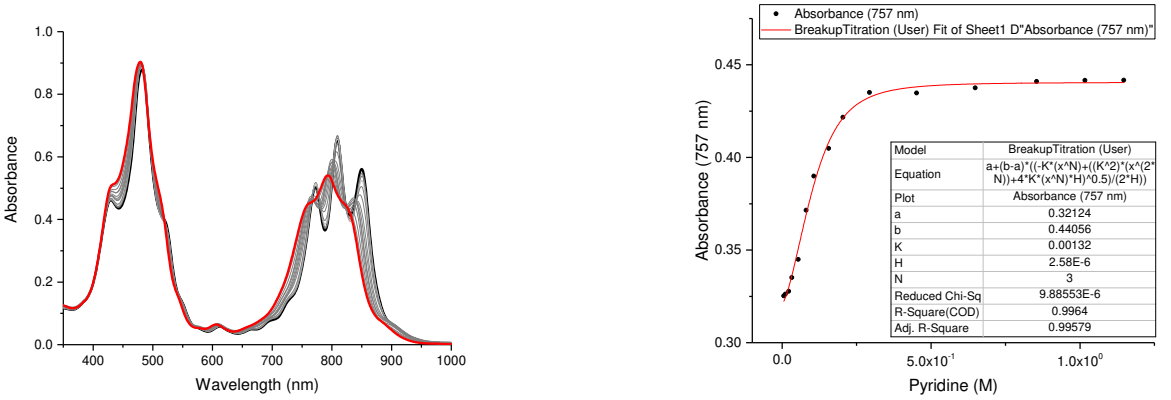

(a) Spectra **(b)** Single wavelength concentration profile

Figure 4.52: UV-Vis breakup titration of ***c*-P6•A3** with **pyridine**. Run 2, toluene, 298 K, [***c*-P6**] = 1.29E -06 M (IG-3-34).

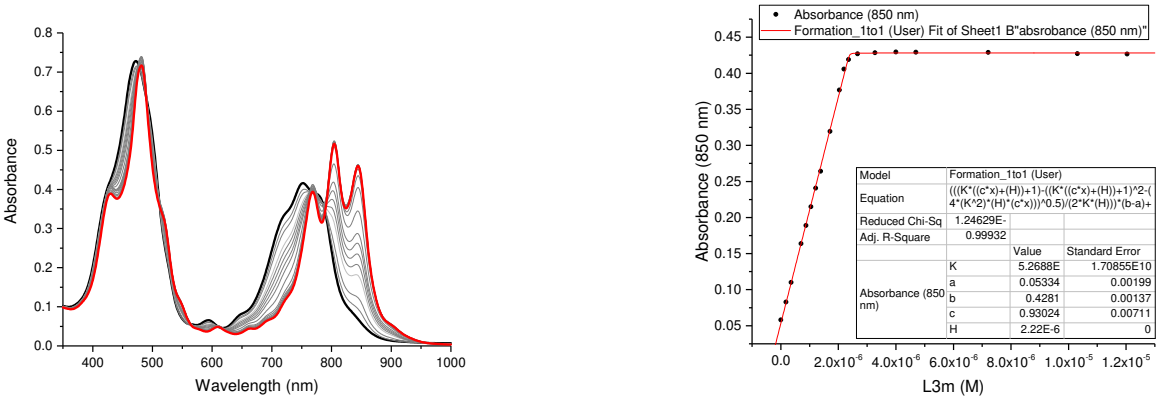

(a) Spectra **(b)** Single wavelength concentration profile

Figure 4.53: UV-Vis titration of ***c*-P6** with **B3**. Run 1, toluene, 298 K, [***c*-P6**] = 1.11E-06 M (IG-2-81).

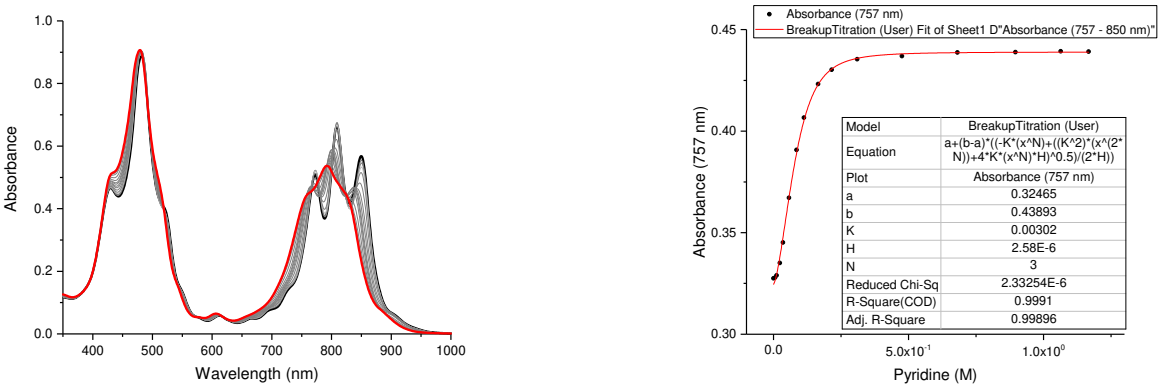

(a) Spectra **(b)** Single wavelength concentration profile

Figure 4.54: UV-Vis breakup titration of ***c*-P6•B3** with **pyridine**. Run 1, toluene, 298 K, [***c*-P6**] = 1.29E -06 M (IG-3-34).

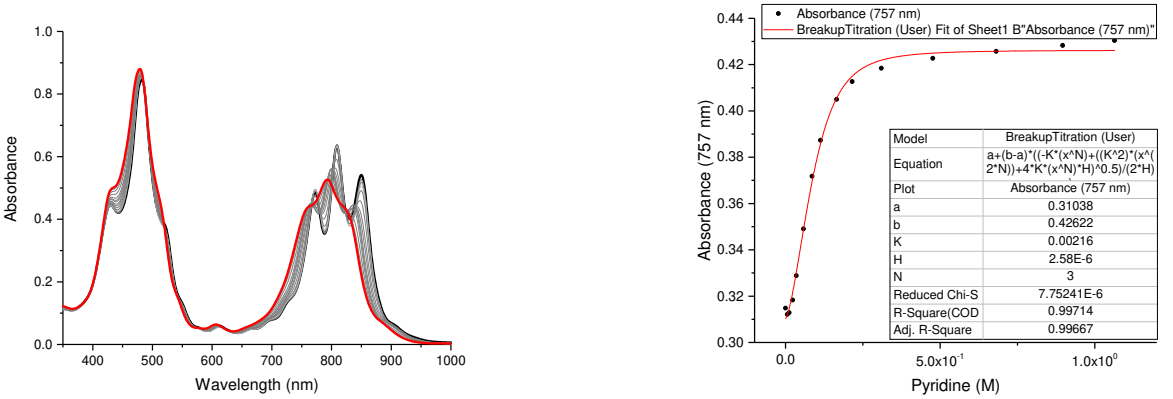

(a) Spectra **(b)** Single wavelength concentration profile

Figure 4.55: UV-Vis breakup titration of ***c*-P6•B3** with **pyridine**. Run 2, toluene, 298 K, [***c*-P6**] = 1.29E -06 M (IG-3-34).

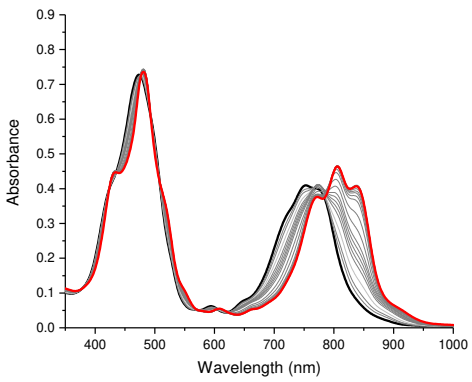

(a) Spectra

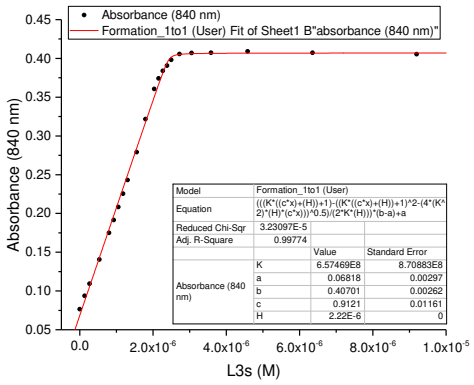

(b) Single wavelength concentration profile

Figure 4.56: UV-Vis titration of ***c*-P6** with **C3**. Run 1, toluene, 298 K, [***c*-P6**] = 1.11E-06 M (IG-2-81).

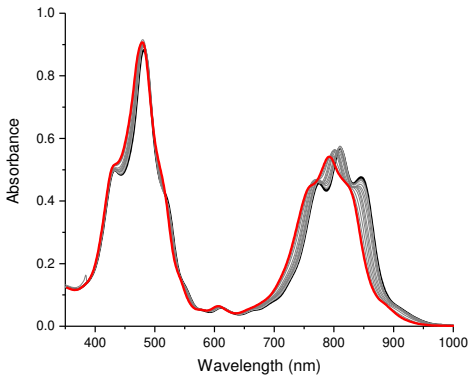

(a) Spectra

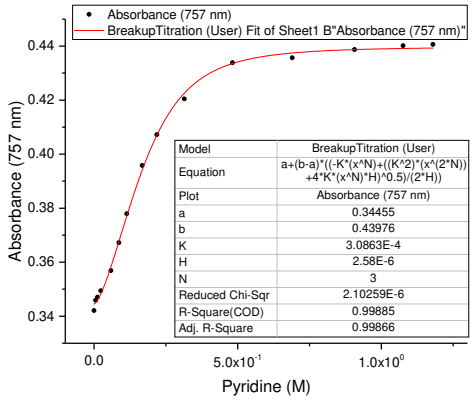

(b) Single wavelength concentration profile

Figure 4.57: UV-Vis breakup titration of ***c*-P6•C3** with **pyridine**. Run 1, toluene, 298 K, [***c*-P6**] = 1.29E -06 M (IG-3-34).

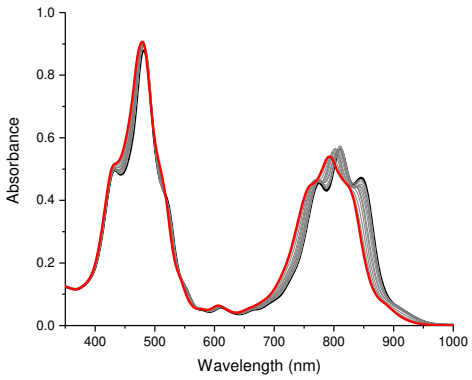

(a) Spectra

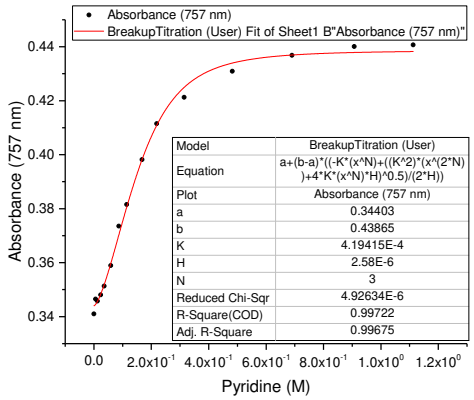

(b) Single wavelength concentration profile

Figure 4.58: UV-Vis breakup titration of ***c*-P6•C3** with **pyridine**. Run 2, toluene, 298 K, [***c*-P6**] = 1.29E -06 M (IG-3-34).

Temperature-dependent UV-vis-NIR Titrations

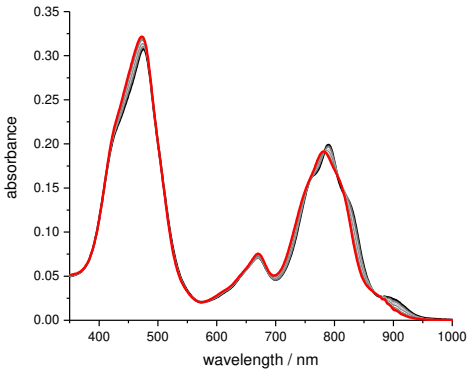

(a) Spectra

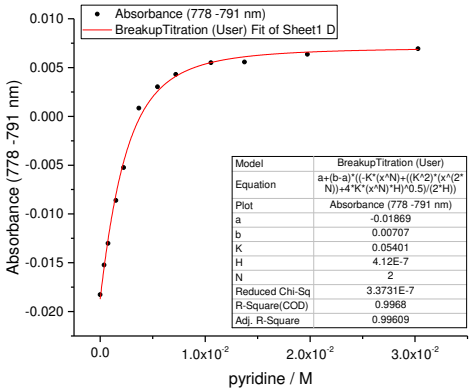

(b) Single wavelength concentration profile

Figure 4.59: UV-Vis denaturation titration of **Zn_2-P6•A2** with **pyridine**. Run 1, toluene, 318 K, [**Zn_2-P6**] = 4.12E-07 M (IG-3-40).

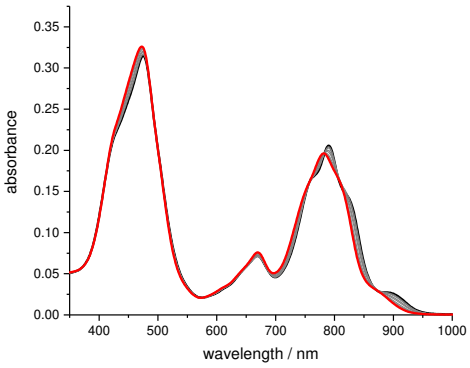

(a) Spectra

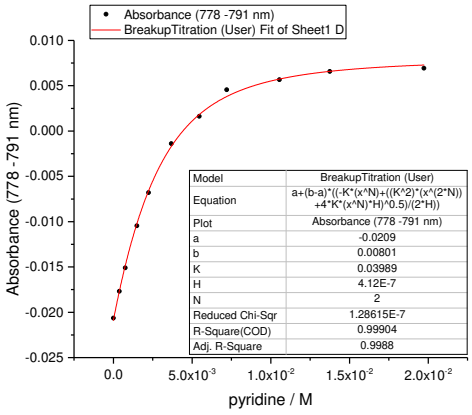

(b) Single wavelength concentration profile

Figure 4.60: UV-Vis denaturation titration of **Zn_2-P6•A2** with **pyridine**. Run 1, toluene, 308 K, [**Zn_2-P6**] = 4.12E-07 M (IG-3-40).

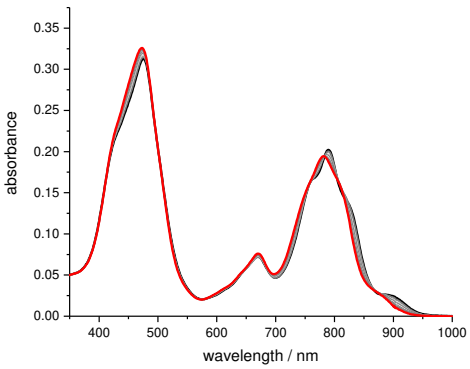

(a) Spectra

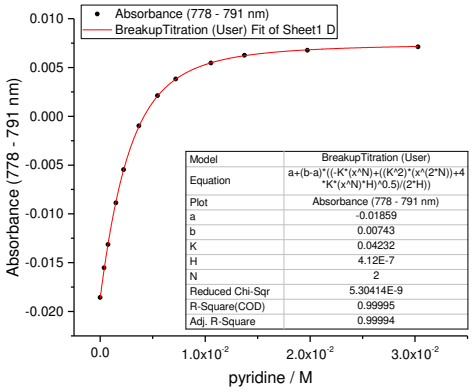

(b) Single wavelength concentration profile

Figure 4.61: UV-Vis denaturation titration of **Zn_2-P6•A2** with **pyridine**. Run 2, toluene, 318 K, [**Zn_2-P6**] = 4.12E-07 M (IG-3-40).

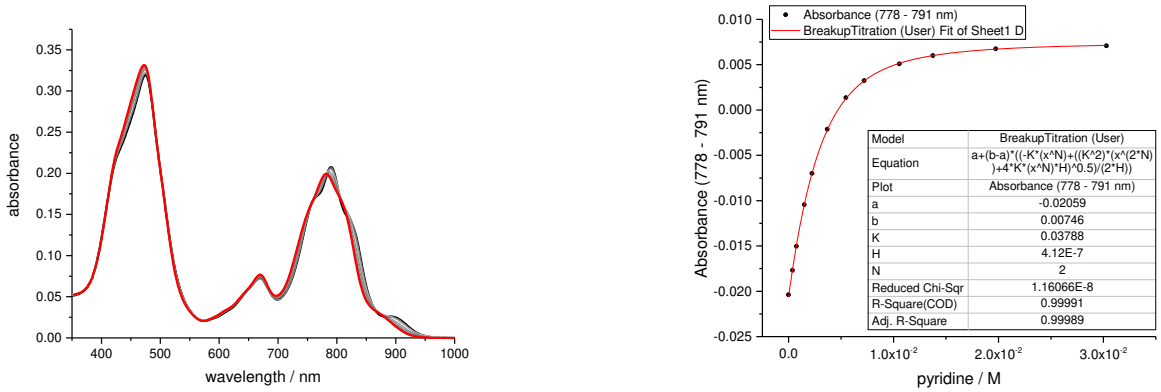

(a) Spectra **(b)** Single wavelength concentration profile

Figure 4.62: UV-Vis denaturation titration of **Zn_2-P6•B2** with **pyridine**. Run 1, toluene, 308 K, [**Zn_2-P6**] = 4.12E-07 M (IG-3-40).

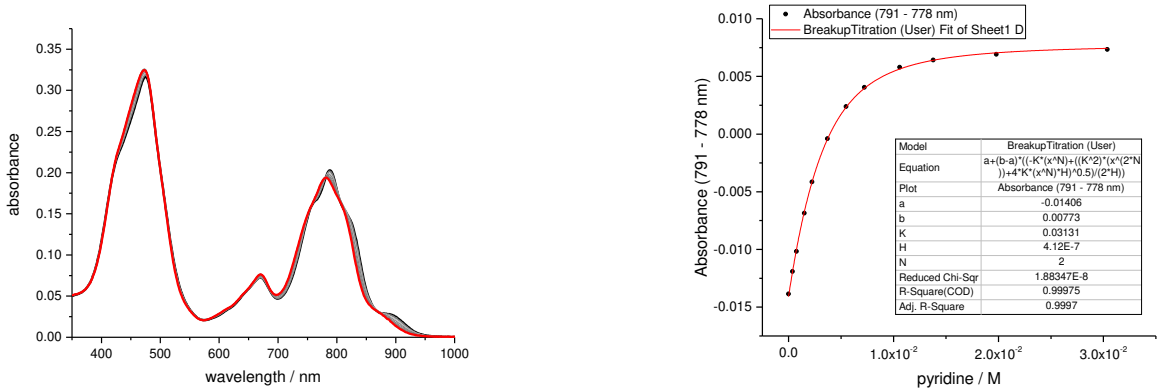

(a) Spectra **(b)** Single wavelength concentration profile

Figure 4.63: UV-Vis denaturation titration of **Zn_2-P6•B2** with **pyridine**. Run 1, toluene, 318 K, [**Zn_2-P6**] = 4.12E-07 M (IG-3-40).

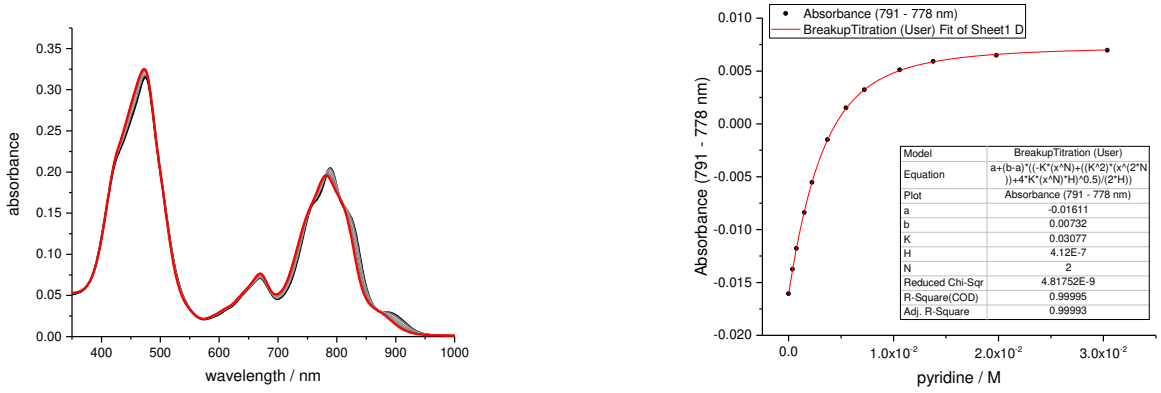

(a) Spectra **(b)** Single wavelength concentration profile

Figure 4.64: UV-Vis denaturation titration of **Zn_2-P6•C2** with **pyridine**. Run 1, toluene, 318 K, [**Zn_2-P6**] = 4.12E-07 M (IG-3-40).

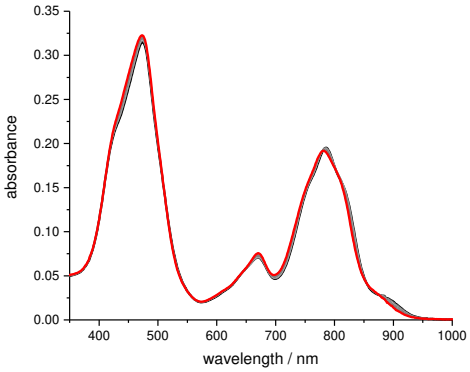

(a) Spectra

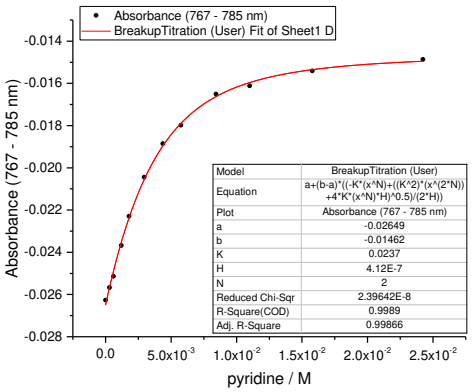

(b) Single wavelength concentration profile

Figure 4.65: UV-Vis denaturation titration of **Zn_2-P6•C2** with **pyridine**. Run 1, toluene, 308 K, [**Zn_2-P6**] = 4.12E-07 M (IG-3-40).

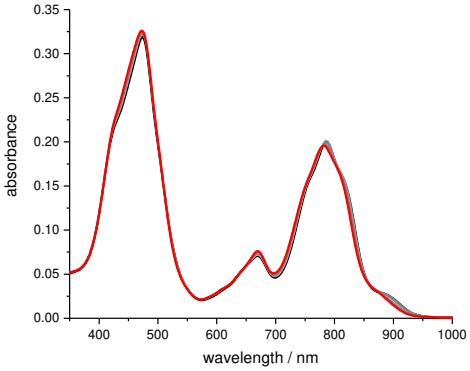

(a) Spectra

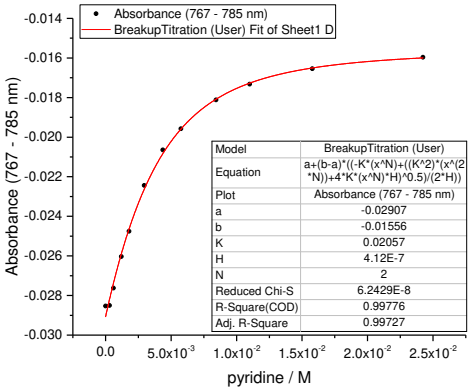

(b) Single wavelength concentration profile

Figure 4.66: UV-Vis denaturation titration of **Zn_2-P6•C2** with **pyridine**. Run 2, toluene, 318 K, [**Zn_2-P6**] = 4.12E-07 M (IG-3-40).

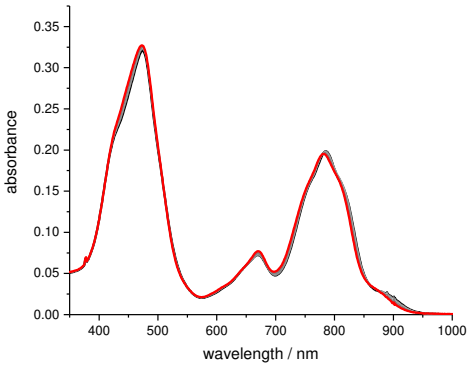

(a) Spectra

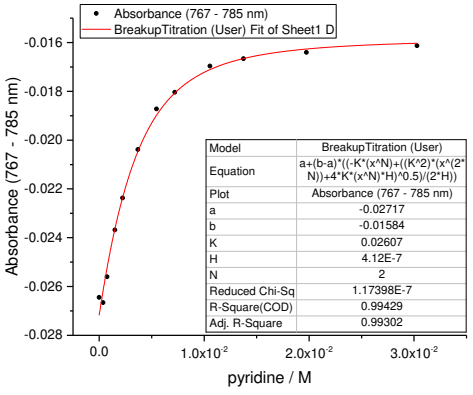

(b) Single wavelength concentration profile

Figure 4.67: UV-Vis denaturation titration of **Zn_2-P6•C2** with **pyridine**. Run 2, toluene, 308 K, [**Zn_2-P6**] = 4.12E-07 M (IG-3-40).

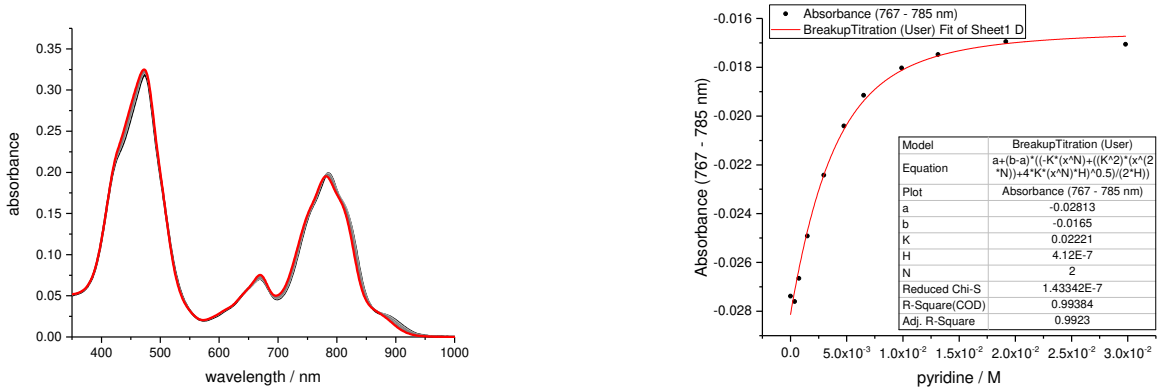

(a) Spectra **(b)** Single wavelength concentration profile

Figure 4.68: UV-Vis titration of ***I*-P2•A2**. Run 1, toluene, 318 K, [***I*-P2**] = 3.14E-06 M (IG-3-35).

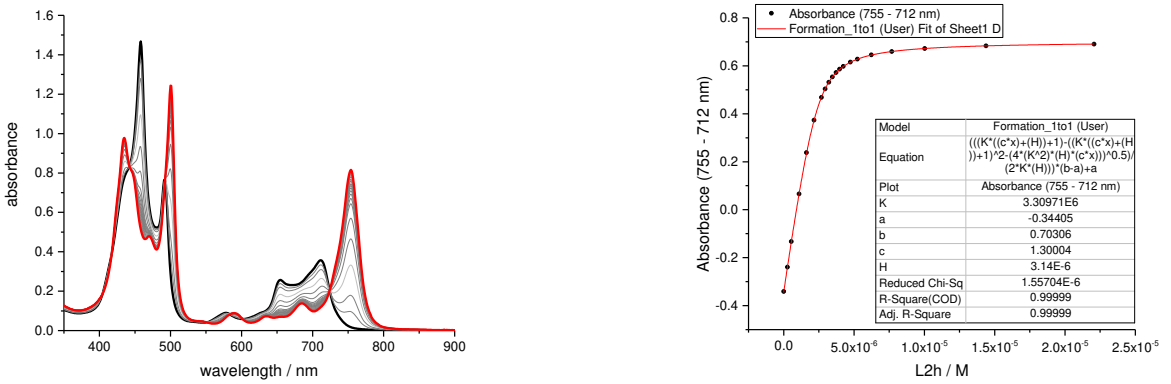

(a) Spectra **(b)** Single wavelength concentration profile

Figure 4.69: UV-Vis titration of ***I*-P2•A2**. Run 1, toluene, 308 K, [***I*-P2**] = 3.14E-06 M (IG-3-35).

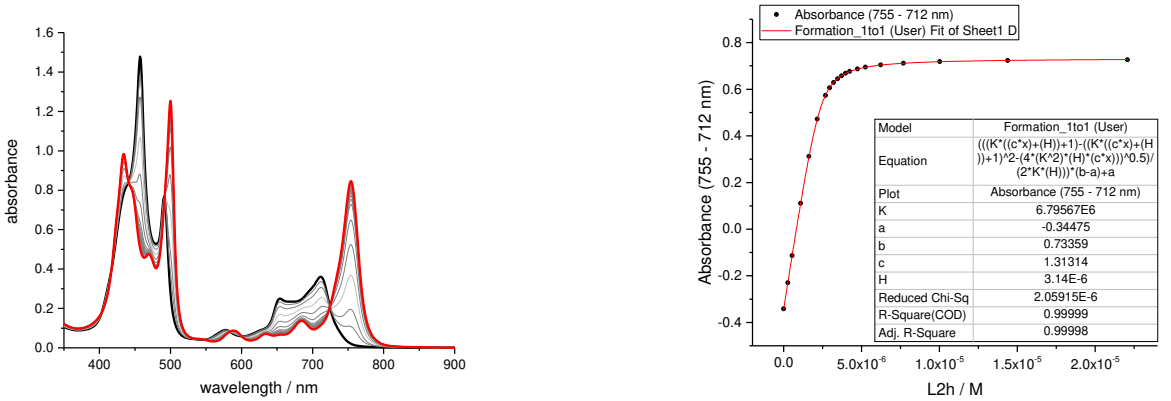

(a) Spectra **(b)** Single wavelength concentration profile

Figure 4.70: UV-Vis titration of ***I*-P2•B2**. Run 1, toluene, 318 K, [***I*-P2**] = 3.14E-06 M (IG-3-35).

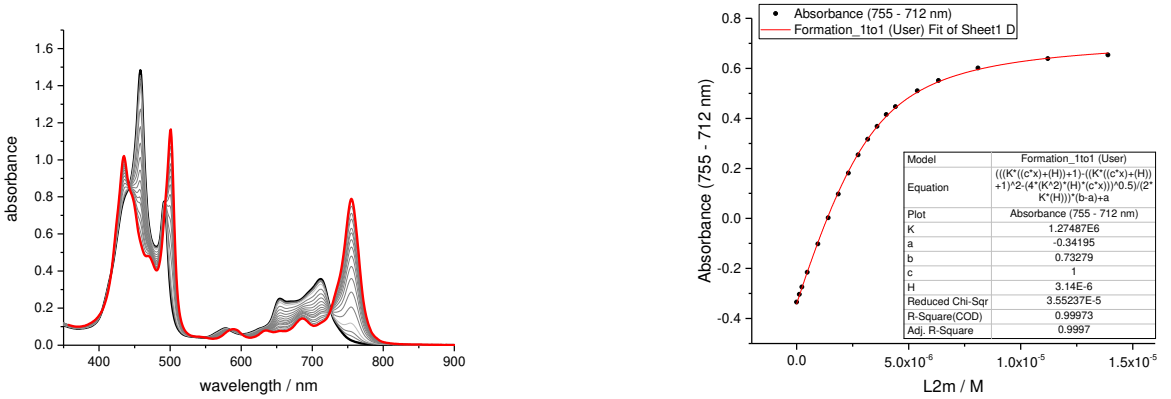

(a) Spectra **(b)** Single wavelength concentration profile

Figure 4.71: UV-Vis titration of ***I*-P2•B2**. Run 1, toluene, 308 K, [***I*-P2**] = 3.14E-06 M (IG-3-35).

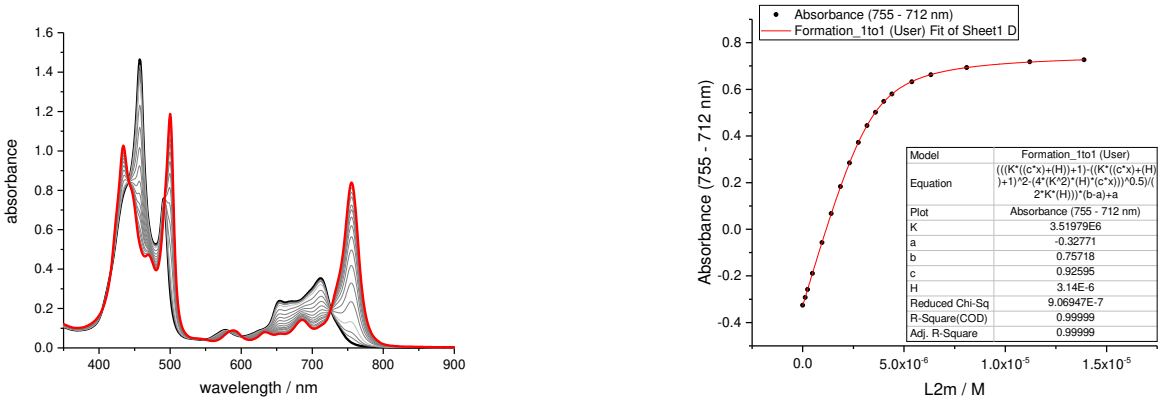

(a) Spectra **(b)** Single wavelength concentration profile

Figure 4.72: UV-Vis titration of ***I*-P2•C2**. Run 1, toluene, 318 K, [***I*-P2**] = 3.14E-06 M (IG-3-35).

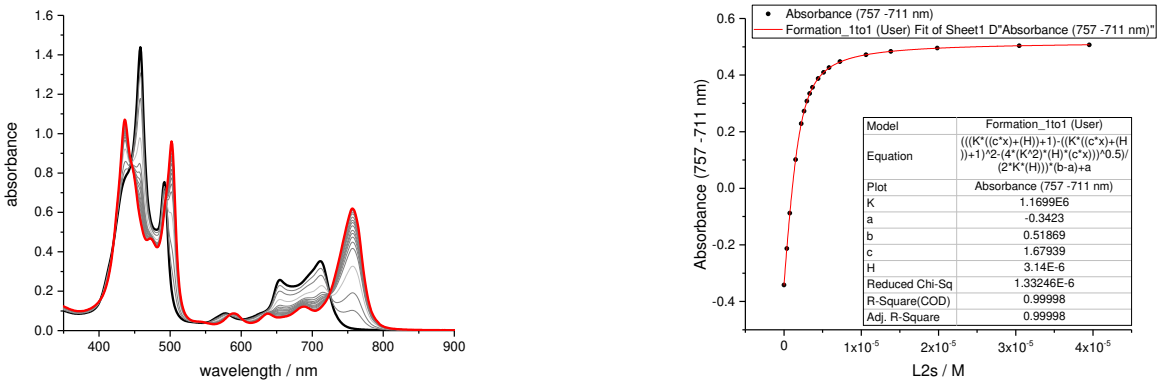

(a) Spectra **(b)** Single wavelength concentration profile

Figure 4.73: UV-Vis titration of ***I*-P2•C2**. Run 1, toluene, 308 K, [***I*-P2**] = 3.14E-06 M (IG-3-35).

ITC - Reference Titrations

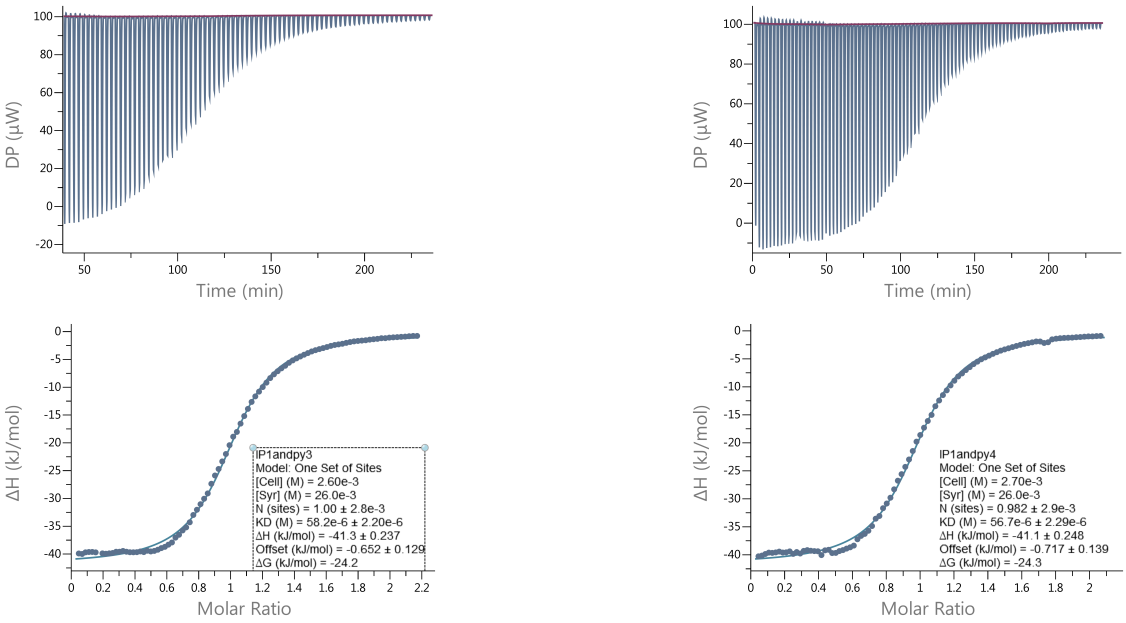

(a) Run 1 **(b)** Run 2

Figure 4.74: ITC measurement of **pyridine** with ***I*-P1**. Toluene, 298 K, [***I*-P1**] = 2.61×10-3 M.

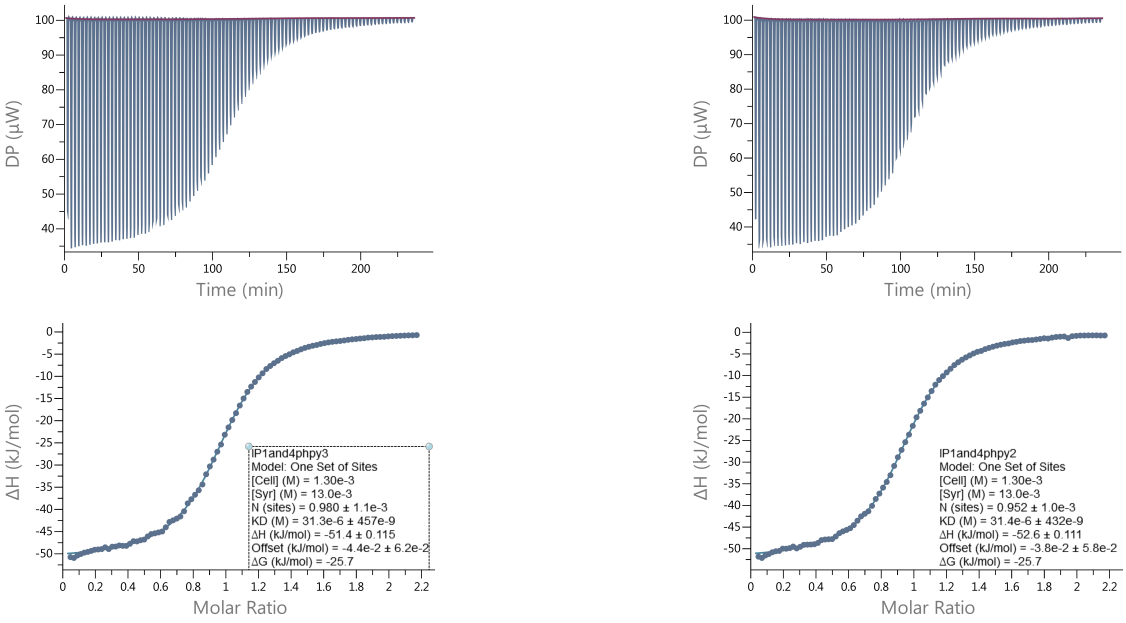

(a) Run 1 **(b)** Run 2

Figure 4.75: ITC measurement of **A1** with ***I*-P1**. Toluene, 298 K, [***I*-P1**] = 2.62×10-3 M.

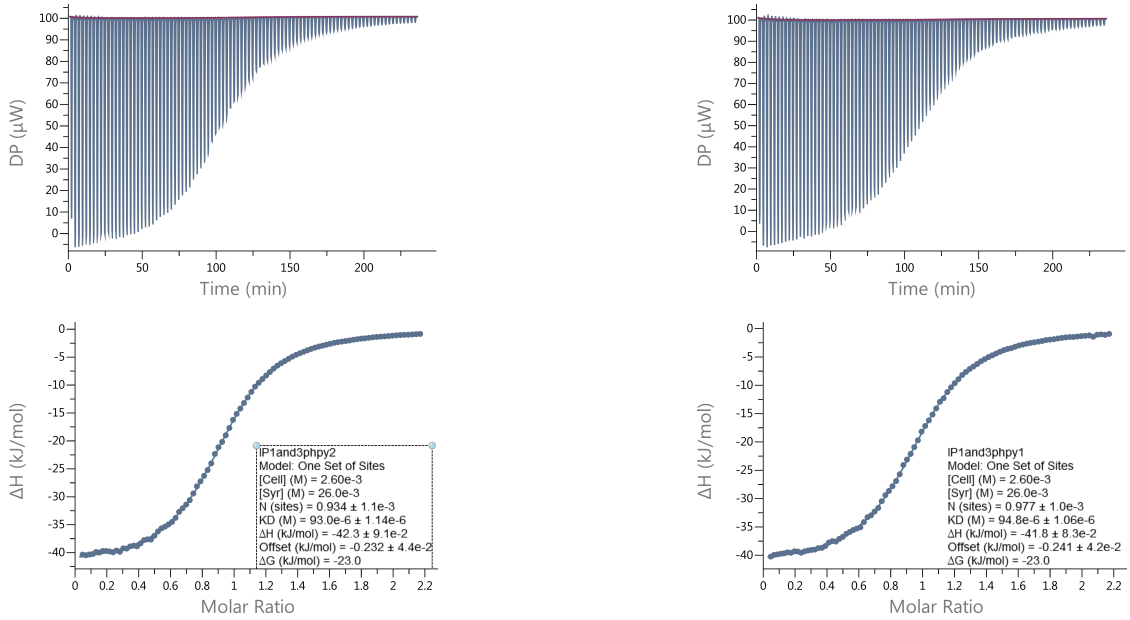

(a) Run 1 **(b)** Run 2

Figure 4.76: ITC measurement of **C1** with ***I*-P1**. Toluene, 298 K, [***I*-P1**] = 2.62×10-3 M.

ITC - Dimer Titrations

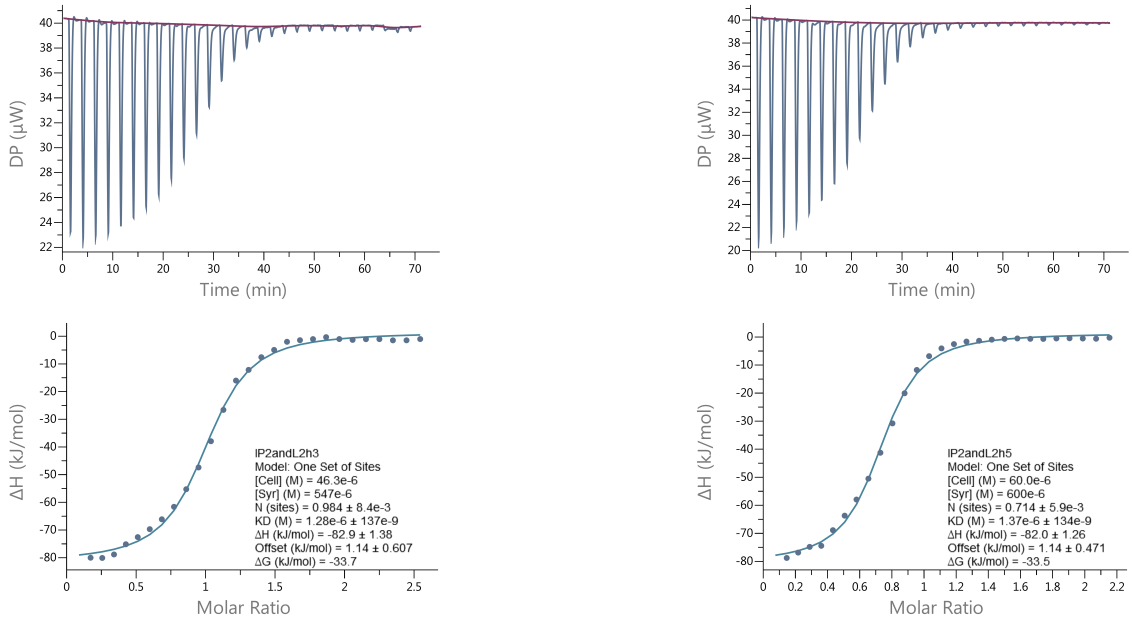

(a) Run 1 **(b)** Run 2

Figure 4.77: ITC measurement of **A2** with ***I*-P2**. Toluene, 298 K, [***I*-P2**] = 4.63×10-5 M.

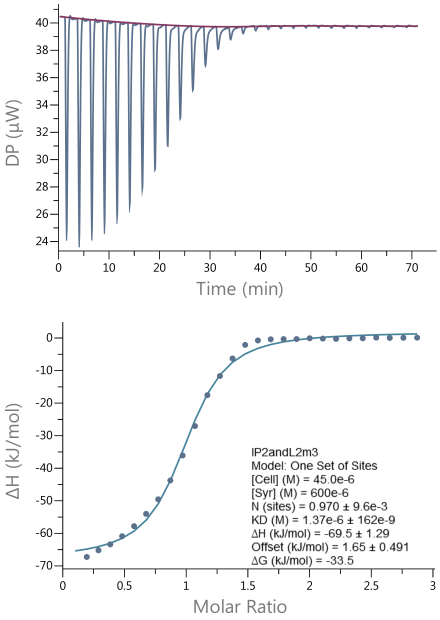

(a) Run 1

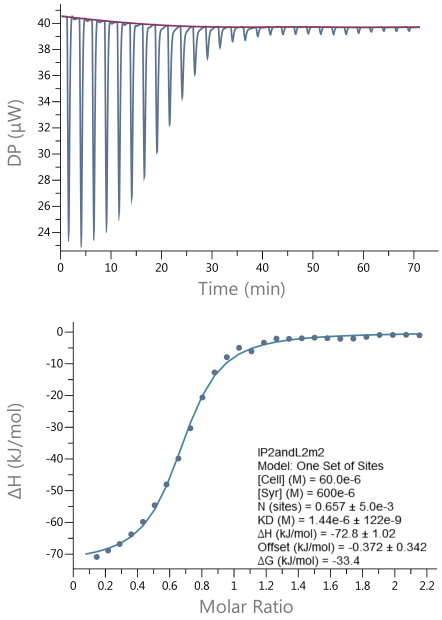

(b) Run 2

Figure 4.78: ITC measurement of **B2** with ***I*-P2**. Run 1, toluene, 298 K, [***I*-P2**] = 4.63×10-5 M.

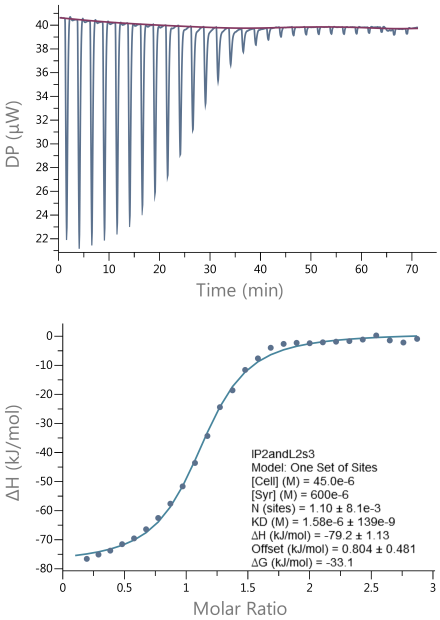

(a) Run 1

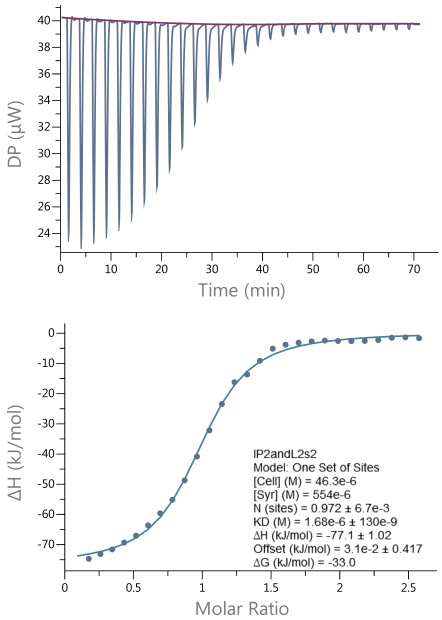

(b) Run 2

Figure 4.79: ITC measurement of **C2** with ***I*-P2**. Toluene, 298 K, [***I*-P2**] = 4.63×10-5 M.

ITC - Trimer Titrations

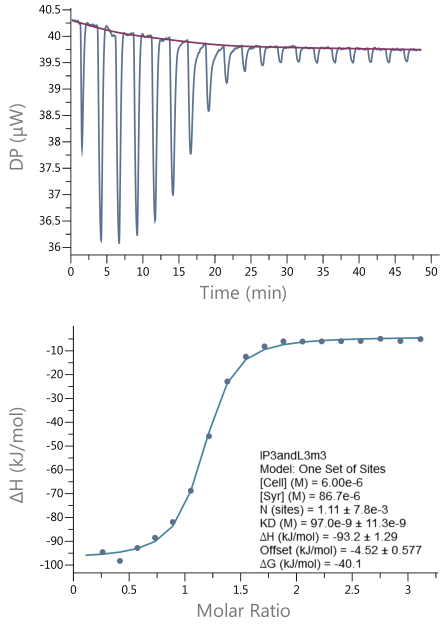

(a) Run 1

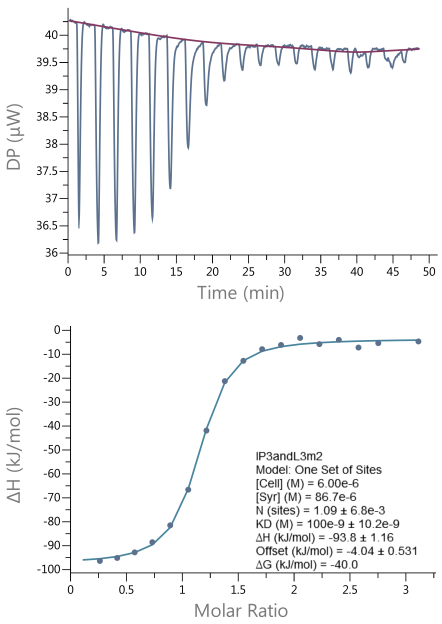

(b) Run 2

Figure 4.80: ITC measurement of **A3** with ***I*-P3**. Toluene, 298 K, [***I*-P3**] = 6.05×10-6 M.

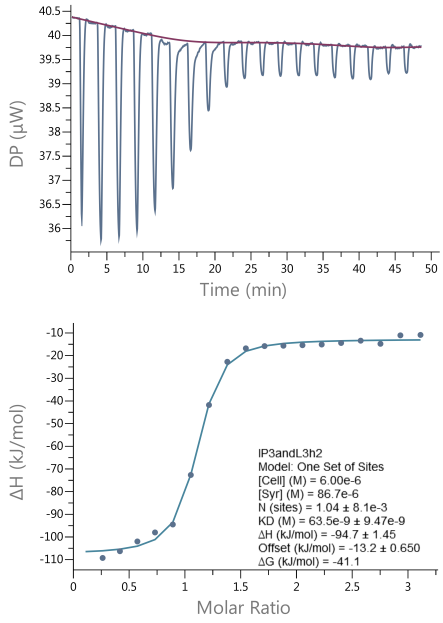

(a) Run 1

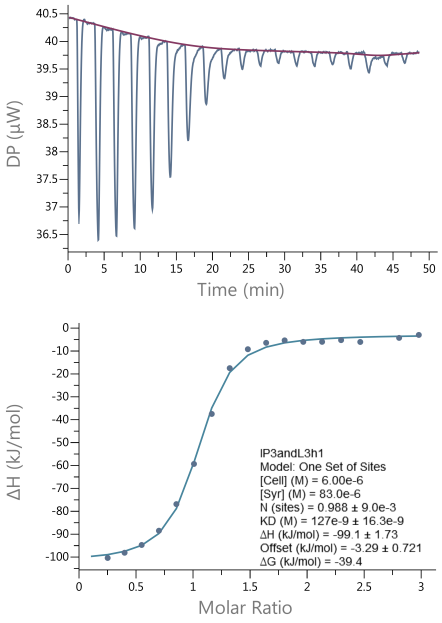

(b) Run 2

Figure 4.81: ITC measurement of **B3** with ***I*-P3**. Toluene, 298 K, [***I*-P3**] = 6.05×10-6 M.

ITC - Zn_2-P6 Titrations

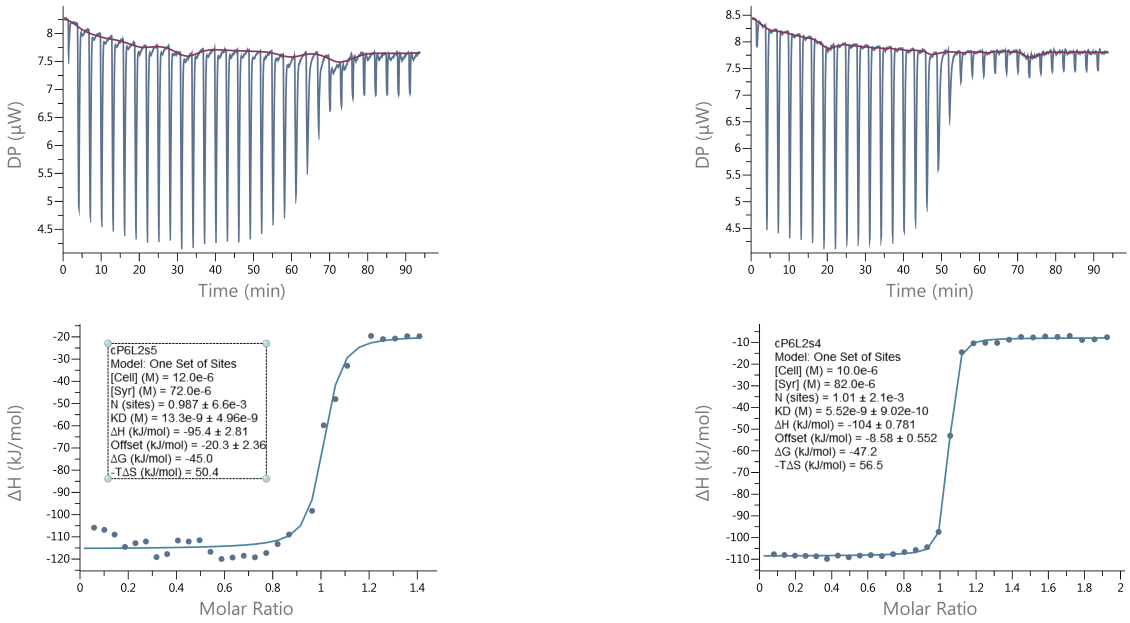

(a) Run 1 **(b)** Run 2

Figure 4.82: ITC measurement of **A2** with **Zn_2-P6**. Run 1, toluene, 298 K, [**Zn_2-P6**] = 5.58×10-6 M

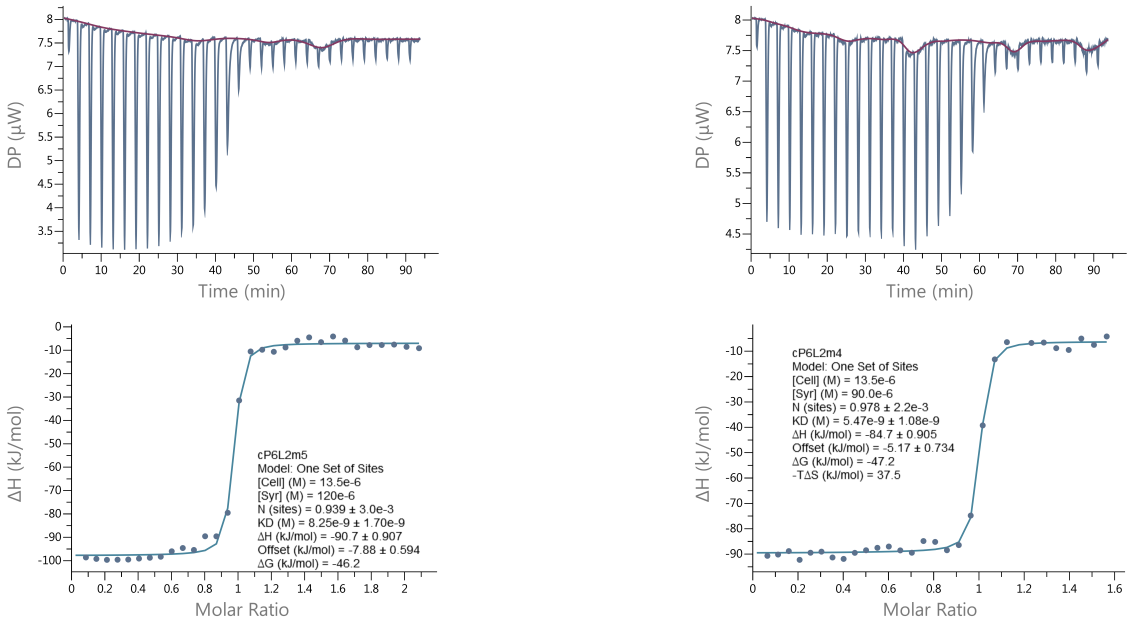

(a) Run 1 **(b)** Run 2

Figure 4.83: ITC measurement of **B2** with **Zn_2-P6**. Toluene, 298 K, [**Zn_2-P6**] = 0.90×10-5 M.

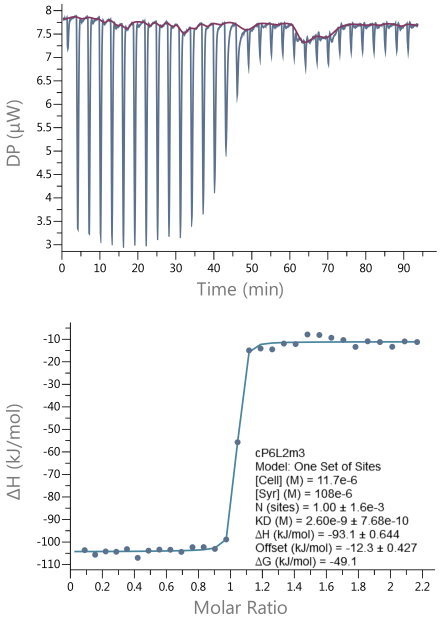

(a) Run 1

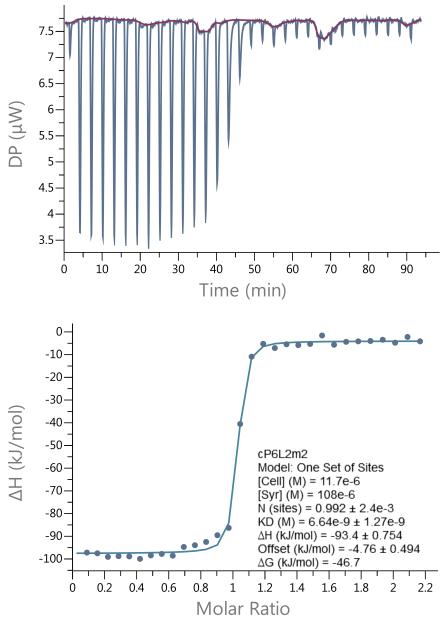

(b) Run 2

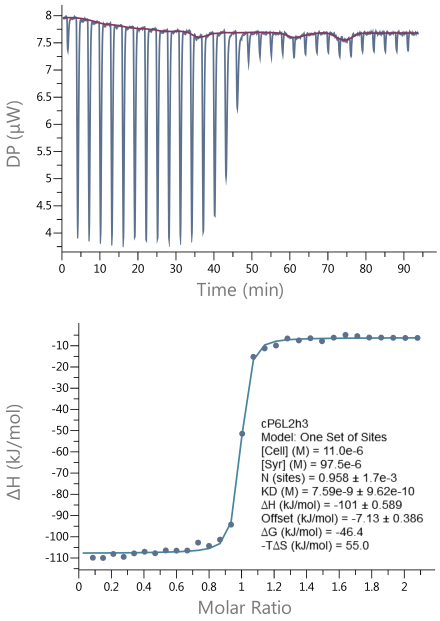

(a) Run 1

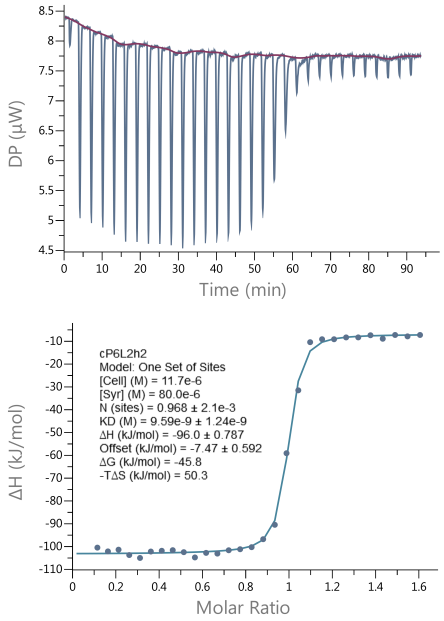

(b) Run 2

Figure 4.84: ITC measurement of **C2** with **Zn_2-P6**. Toluene, 298 K, [**Zn_2-P6**] = 1.30×10-5 M.

ITC - *c*-P6 Titrations

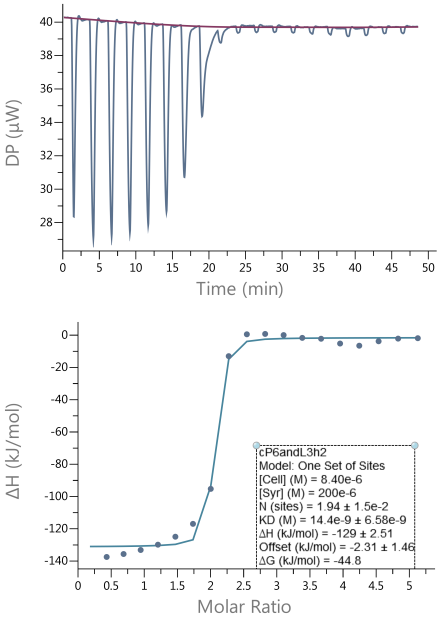

(a) Run 1

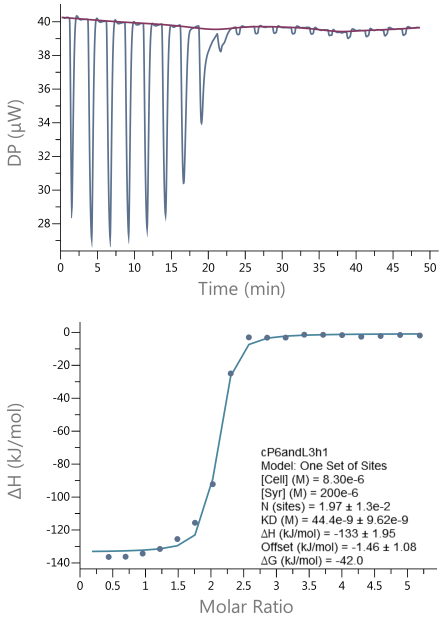

(b) Run 2

Figure 4.85: ITC measurement of **A3** with ***c*-P6**. Toluene, 298 K, [***c*-P6**] = 7.90×10-6 M.

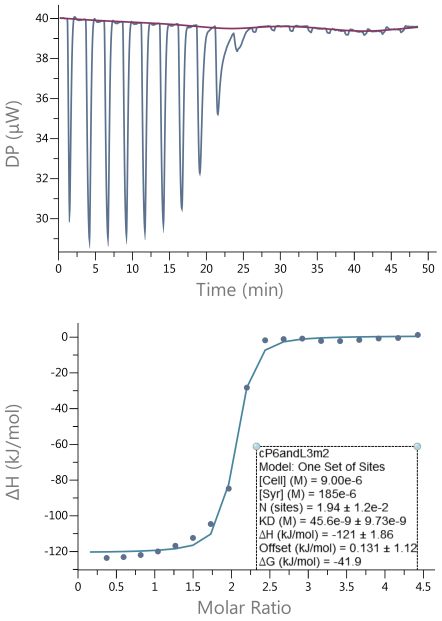

(a) Run 1

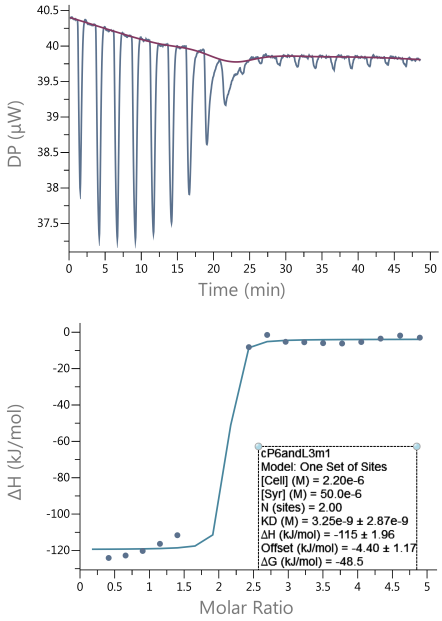

(b) Run 2

Figure 4.86: ITC measurement of **B3** with ***c*-P6**. Toluene, 298 K, [***c*-P6**] = 2.11×10-6 M.

5

Computational Studies of Cooperativity

Contents

5.1 Abstract

This chapter explores the use of quantum mechanical calculations to predict chelate cooperativity. A benchmark was constructed to test the performance of nine DFT functionals in combination with three different basis sets, in the absence or presence of a continuum solvation model, to predict Gibbs energies of binding. Two combinations were most promising in the prediction of binding energies for a monovalent model system: M05-2X/6-

31G*/LANL2DZ in combination with the SMD solvent model and B3LYP/6-31G* without a solvation model. The performance of both methods was tested against a multivalent host-guest library, resulting in an excellent accuracy for Gibbs energy predictions (mean absolute deviation (MAD) is 3.1 kJ mol^{-1} and 2 kJ mol^{-1}, respectively). The B3LYP functional proved to be particularly successful in the prediction of *EM* values. Even though the exact, quantitative value cannot be predicted, a strong correlation between experimental and calculated values suggest the possibility of systematic improvement of this method.

Since B3LYP does not account for any solvation effect, the COSMO-RS method was used to explore the impact of solvation on chelate cooperativity. The computational results were compared to the experimental result for the ***I*-P2•A2** complex, for which *EM* values have been determined in various solvents. For rigid solvents, an excellent correlation between experimental and calculated values was observed. However, the COSMO-RS approach collapses for flexible solvents that can adapt to the binding pocket. The application of COSMO-RS also qualitatively supports the hypothesis in Chapter 4, that the *EM* values in the host-guest library exhibit significant solvation effects, but further investigations are required to quantify this effect.

5.2 Introduction

The benefits and opportunities offered by computer modelling at the quantum mechanical level are well-known, such techniques are helpful in understanding chemical processes. The theoretical landscape is wide and there is not a universal approach to describe any system. For small chemical molecules or molecular complexes, high-level *ab initio* calculations deliver results of 'chemical accuracy' quality.[155,156] Unfortunately, the computational costs scales dramatically with the system size for such *ab initio* methods. The most simplistic applicable *ab initio* method is Hartree-Fock theory, which neglects any correlation effects and scales with N^4, where N is the number of electrons in the system. For scientifically useful structures or binding energies, a correction of correlation effects is required. Even simple approaches that can deliver virtually exact results, like Configuration Interaction, scale exponentially with the number of electrons.[157,158] Therefore, applying high level *ab initio* methods to large molecular systems always requires a trade-off between the accuracy of the method and its computational cost.

5.2.1 Molecular Mechanics

Simpler methods are needed for larger molecules. Molecular Mechanics only considers molecular structure via Newtonian motion and classical mechanics. Molecular bonds are modelled as springs between atoms, with an equilibrium distance resembling the actual bond length and a stiffness of the bond spring representing the ease of deformations.[159] Under certain conditions, covalent bond length and other properties can remain largely unaffected by its surroundings.[160,161] Therefore, any modulations in their strength caused by neighbouring (covalent bonds) can be small compared to its absolute value.[32]

On the contrary, non-covalent interactions are heavily influenced by their surroundings. This is illustrated by the example of water molecules connected via hydrogen bonds. The bond length observed in a water dimer in vacuum is significantly longer than that in highly ordered structures like ice.[162] This is also reflected in the hydrogen bond strength ranges, which vary from very weak to a strength comparable with a weak covalent bond.[163] Expanding this idea to a larger molecular system found in biology or supramolecular chemistry, where multiple non-covalent interactions operate simultaneously, illustrates the significance of the proper treatment of these interactions. This non-additive, environment-dependent behaviour often makes the electron-independent treatment applied by molecular mechanics unsuitable for non-covalent bonds. Therefore, molecular mechanics is not suitable for our study and will not discussed further.

5.2.2 Semi-Empirical Methods

Including some exact treatment of electronic effects significantly improves the theoretical description of non-covalent interactions. This approach is the foundation for most semi-empirical methods, in which only valence electrons are treated explicitly. To reduce computational cost, core electrons are approximated by simple core functions. The formalism for electrons is generally based on the Hartree-Fock theory, but many approximations are made and empirically determined parameters are used to find solutions for the exact Hamiltonian. Due to its excellent scalability, semi-empirical methods have been shown to deliver good results for supramolecular complexes, biomolecules, and more.[164]

A variety of semi-empirical methods exists, and the applicability of a certain method highly depends on the parameterisation. The accuracy of known parameter sets such as

MINDO, AM1, and the PM*X* family has been tested and documented for various types calculations.[164–166] Compared to the previous version, PM6, PM7 is not only a more robust method but also outperforms most semi-empirical methods in the description of geometry and the determination of heats of formation for non-covalently bound large organic molecules.[167]

A crucial improvement of the scaling formed the implementation of MOZYME[168] in MOPAC,[169] which allows faster evaluation of absolute heats of formation of large molecules without a significant loss in accuracy. Therefore, MOZYME is used for all semi-empirical calculations in this chapter.

5.2.3 Quantum mechanical approaches

Most of the quantum chemical approaches are based on finding the solution of the time-independent, non-relativistic Schrödinger equation (Eq. 5.1).[170–173]

$$\widehat{\mathrm{H}}\Psi_i(\vec{x}_1, \vec{x}_2, ..., \vec{x}_N, \vec{R}_1, \vec{R}_2, ..., \vec{R}_M) = E_i\Psi_i(\vec{x}_1, \vec{x}_2, ..., \vec{x}_N, \vec{R}_1, \vec{R}_2, ..., \vec{R}_M) \tag{5.1}$$

$\widehat{\mathrm{H}}$ represents the Hamiltonian, a differential operator representing the total energy (Eq. 5.2), and Ψ_i the wave function, in the i'th state, for a system containing N electrons and M nuclei.

$$\widehat{\mathrm{H}} = \underbrace{-\frac{1}{2}\sum_{i=1}^{N}\nabla_i^2}_{T_\mathrm{e}} \underbrace{-\frac{1}{2}\sum_{A=1}^{M}\frac{1}{M_A}\nabla_A^2}_{T_\mathrm{N}} \underbrace{-\sum_{i=1}^{N}\sum_{A=1}^{M}\frac{Z_A}{r_{iA}}}_{V_\mathrm{eN}} + \underbrace{\sum_{i=1}^{N}\sum_{j>i}^{N}\frac{1}{r_{ij}}}_{V_\mathrm{ee}} + \underbrace{\sum_{A=1}^{M}\sum_{B>A}^{M}\frac{Z_A Z_B}{R_{AB}}}_{V_\mathrm{NN}} \tag{5.2}$$

∇^2 is the Laplacian operator. The first two terms represents the kinetic energy of the electrons and nuclei (with charge Z), while the remaining three terms describe the potential energy of the system including all attractive interactions (between electrons and nuclei) as well as all repulsive interactions (electron-electron and nucleus-nucleus).

The motion of nuclei and electrons occurs on very different time scales due to the significant difference in mass. This forms the basis for the Born-Oppenheimer[174] approximation, which allows the nuclei to be treated as fixed in space on the time-scale of electron motion (eliminating nuclear kinetic energy and reducing the potential energy between nuclei to a constant). This approximation simplifies the Hamiltonian to the electronic Hamiltonian (Eq. 5.3).

$$\widehat{H}_{el} = -\frac{1}{2}\sum_{i=1}^{N}\nabla_i^2 - \sum_{i=1}^{N}\sum_{A=1}^{M}\frac{Z_A}{r_{iA}} + \sum_{i=1}^{N}\sum_{j>i}^{N}\frac{1}{r_{ij}} = \widehat{T} + \widehat{V}_{Ne} + \widehat{V}_{ee} \tag{5.3}$$

The remaining terms in the electronic Hamiltonian are the kinetic energy of the electrons ($\widehat{T}$), the attractive interaction between electrons and nuclei ($\widehat{V}_{Ne}$) and the repulsive electron-electron interactions ($\widehat{V}_{ee}$). The crucial step to solve the Schrödinger equation with the electronic Hamiltonian, as it is given in Eq. 5.3, is to determine the exact wave function, which yields the lowest possible energy for the system. The most common way to determine the wave function is the variational principle. Therefore an initial trial wave function, as a linear combination of other (basis) functions which represent electrons, is chosen to determine the energy of the system. The trial function is varied with the goal of attaining lower energies, until a convergence limit is reached, resulting in the minimum energy of the system. As the exact ground state wave function determines the lowest possible ground state energy, every other trial wave function will result in higher energies.

Physically relevant solutions of the Schrödinger equation can be obtained with the Hartree-Fock method or with density functional theory. Due to its scalability, density functional theory is more applicable to our current problem.

5.2.4 Density Functional Theory

The foundation for density functional theory (DFT) is based on the landmark paper by Hohenberg and Kohn[175] in 1964, which proves that the ground state energy is a function of the electron density ($\rho(\vec{r})$) (first Hohenberg-Kohn theorem). Using the density instead of the wavefunction reduces the number of variables significantly as the density at a point in space only depends on 3 spatial coordinates instead of $4N$ variables (three spatial coordinates and one spin coordinate for each particle).

5.2.4.1 The First and Second Hohenberg-Kohn Theorem

The first Hohenberg-Kohn theorem proves, based on *reductio ad absurdum*, that an external potential V_{ext} is an unique functional of the electron density $\rho(\vec{r})$. The same external potential also determines the Hamilton operator, therefore the ground state energy of a system is a function of the electron density. Consequently every component of the ground state energy can be written as a functional of its electron density. Isolating system

dependent from independent components leads to the system independent Hohenberg-Kohn functional F_{HK} (Eq. 5.4).

$$E_0(\rho) = \underbrace{\int \rho_0(\vec{r}) V_{ext}\ d\vec{r}}_{\text{system independent}} + \underbrace{T(\rho_0) + V_{ee}(\rho_0)}_{\text{system dependent}} = \int \rho_0(\vec{r}) V_{ext}\ d\vec{r} + F_{HK}(\rho_0) \tag{5.4}$$

The electron-electron interaction V_{ee} includes the assessable classical Coulomb part $J(\rho)$ as well as the non-classical parts, comprising correlation, exchange- and self-interaction, which were combined to the non-classical energy $E_{xc}(\rho)$. The exact form of the functional density $E_{nc}(\rho)$ and the kinetic energy of the electrons $T(\rho)$ are not known.

The second Hohenberg-Kohn theorem proves that ground state density can therefore be determined in a variational way, as F_{HK} delivers the ground state energy only for the exact electron density. Every other density results in a higher energy, allowing the variational principle with the exact functional to be used.

5.2.4.2 Kohn-Sham Approach

Following the theorems by Hohenberg and Kohn, Kohn and Sham[176] proposed a method determining the unknown Hohenberg-Kohn functional. This approach constructs a non-interacting N particle system, which reflects the exact electron density of the interacting system. The ground state energy can be calculated via Equation 5.5.

$$E_0 = T(\rho) + J(\rho) + E_{nc}(\rho) + \int \rho(\vec{r}) V_{ext}\ d\vec{r} \tag{5.5}$$

The only known part is the Coulomb term $J(\rho)$. Attempts by Thomas and Fermi to determine the kinetic energy of interacting electrons were unsuccessful.[156] However, since the kinetic energy of non interacting fermions (e.g. electrons) is exactly known in the framework of Hartee-Fock theory, a reference system with N non-interacting particles based on orbitals can be described. Similar to Hartee-Fock, the difference in the kinetic energy is called *effective potential* (V_{eff}) and leads to an effective Hamilton operator (Eq. 5.6).

$$\widehat{H}_{eff} = -\frac{1}{2}\sum_i^N \nabla_i^2 + \sum_i^N V_{eff}(\vec{r}_i) \tag{5.6}$$

This effective Hamilton operator (Eq. 5.7) is constructed by the sum of Kohn-Sham one-electron operators.

$$\widehat{f}^{KS} = -\frac{1}{2}\nabla^2 + V_{eff}(\vec{r}) \tag{5.7}$$

The exact solution of the Schrödinger equation with this effective Hamilton operator is feasible with a Kohn-Sham Slater determinant Θ_S, leading to Kohn-Sham spin orbitals $\vartheta_i(\vec{x}_i)$ (Eq. 5.8).

$$\Theta_S = \frac{1}{\sqrt{N!}} |\vartheta_1(\vec{x}_1)\vartheta_2(\vec{x}_2)...\vartheta_N(\vec{x}_N)| \tag{5.8}$$

By choosing the correct effective potential, the electron density will reflect the exact electron density of the interacting system. The Hohenberg-Kohn functional is separated as Kohn-Sham suggested (Eq. 5.9). This separation divides the exact known solutions of the kinetic energy and electron-electron interactions from the unknown parts, summarized into the *exchange-correlation* functional ($E_{XC}(\rho)$).

$$F_{HK}(\rho) = T_S(\rho) + J(\rho) + E_{XC}(\rho) \tag{5.9}$$

In order to calculate the energy of a real interaction system, the attractive (and known) electron-nucleus interaction is included ($E_{Ne}(\rho)$). The only remaining unknown part in calculating the exact ground state energy is $E_{XC}(\rho)$ (Eq. 5.10), and its determination is the "holy grail" in DFT. Different approximations to this functional are described in subsection 5.2.5.

$$E(\rho(\vec{r})) = \underbrace{T_S(\rho) + J(\rho) + E_{Ne}(\rho)}_{\text{known}} + \underbrace{E_{XC}(\rho)}_{\text{unknown}} \tag{5.10}$$

Again, to minimize the energy expression, the variational principle is used in the Kohn-Sham approach.

The implementation of the Kohn-Sham method (KS)[176] in combination with the the emergence of efficient computers has lead to broad application of computational

chemistry to molecular systems.[177] The DFT label covers a range of different methods, based on first-principles or involving empirical parameters. Generally, the current DFT methods lead to a higher accuracy than Hartree-Fock methods and with significant practical benefits concerning the 'price-to-performance' ratio.[178] Nowadays, computer modelling of large systems comprising thousands of atoms is possible,[179] allowing the applications of DFT on proteins, membranes, nucleic acids, supramolecular complexes, large organometallic complexes, etc.[180]

5.2.5 The 'Functional Zoo'

Within the thirty years of DFT in computational chemistry, a large number of approximations have been proposed to describe the unknown exchange–correlation. While this offers a custom-tailored solution for specific niche problems, the downside is usually weak generalisation. A method working for one example might fail for a slightly modified system. Due to the conceptually different approaches, it is challenging to systematically improve methods.[181] These issues make it hard to find the right functional for a specific chemical problem, as calculations require an extensive benchmark to test their robustness in this explicit situation. To this day, no single functional is known that outperforms for all chemical applications. Hence, a careful choice based on the system under study needs to be made.

Since the exact form of the exchange–correlation is unknown, different formulations with varying levels of empiricism have been used to describe the exchange and correlation between electrons. These levels range from using simple quantum mechanical rules (LDA, PBE, and TPSS) to using numerous empirical parameters derived from experimental data (for example MN12-L with 48 fitted parameters).[182,183]

A helpful classification of functionals is their separation according to Perdew's 'Jacob's Ladder' into five rungs of density functional approximations (Fig. 5.1).[185] The first rung and hence the simplest formulation of the exchange-correlation function is the local density approximation (LDA), with determines the exchange-correlation energy simply by the electron density. LDA describes the exchange-correlation energy per electron as uniform electron gas (with uniform electron density). To account for the fact that a real system does not consist of a uniform electron density independent of space, the overall density is calculated based on infinitesimal volume elements, each expressed as a locally uniform

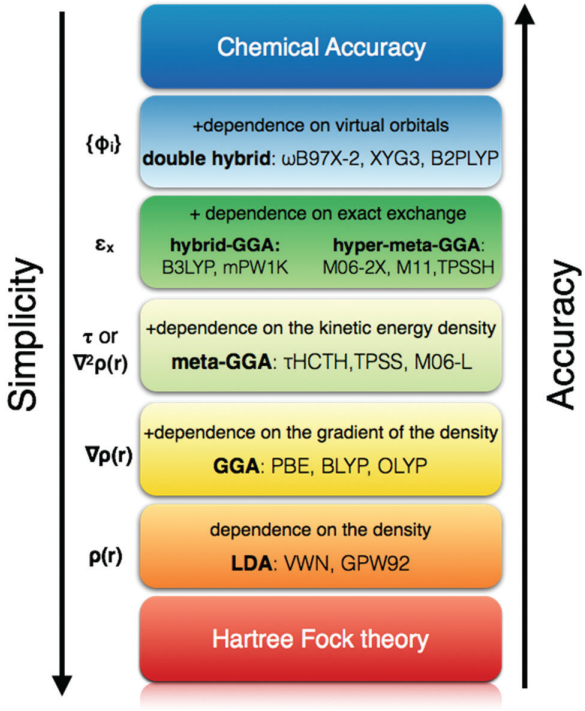

Figure 5.1: The hierarchy of exchange–correlation functionals is often represented by the rungs of Jacob's ladder, according to the number and kind of local ingredients. Reproduced Figure with permission from Reference [184].

electron gas. The required information about the uniform electron gas can be obtained by Monte Carlo computations, which is why the LDA approach does not require any fitted parameters and is therefore a non-empirical approximation. Equally, LDA delivers exact solutions for uniform densities.[186,187] LDA finds broad application in material science due to the accurate description of systems with small interatomic distances and metallic types of bonds. Molecules with strong electron density polarisation are poorly represented by LDA. Polarised molecules show a rapidly changing density, which would require an extremely fine and small grid to divide the actual density into uniform densities. As a consequence, LDA overbinds in chemical reactions. This has been shown in the calculation of atomisation energies (the energy required to break a material/molecule into atoms).[156,157,188]

The second rung uses the same local density approximation, but tackles the description of rapidly changing electron densities. Therefore, a second term is added to the local density approximation describing the gradient of the density. This approximation is called the generalized-gradient approximation (GGA). For most chemical problems, the GGA approach leads to equally good or (system dependent) improved results compared to LDA, which is not surprising; systems with weak gradients experience a small correction (and are therefore

almost equal to the LDA results) while regions with a strong gradient can benefit from significant corrections. The expressions for the gradient functional vary from systematic approaches (development of the gradient as a rational function of the reduced density)[189] to empirically optimised inhomogeneity parameters (as for the Becke88 exchange functional, where the reduced density gradient is fitted to examples of the exact exchange).[190] The most famous GGAs is the Perdew–Burke–Ernzerhof (PBE) approximation.[191] For a slowly varying density, PBE constructs an accurate second-order gradient expansion for correlation which is not satisfied by the LDA approach, while it is still able to reproduce the accurate linear response of LDA for a uniform density. With regard to accuracy in molecules, PBE still overbinds in most cases but substantially less than L(S)DA.[192]

The next rung adds another term, the orbital kinetic energy density, which means that additionally to the first derivative of the Laplacian (as in GGA), also the second derivative is included. Functionals including the orbital kinetic energy density are called meta-GGAs For a one-electron atom, the exchange energy can be calculated exactly. Similarly, a system consisting of a one-electron density shows no correlation effects (which is what you are aiming for). One of the most known meta-GGAs is the revTPSS23,[193] which applications are mainly limited to condensed-matter systems.[188,192]

Until this point, all of the functionals discussed have been semi-local and are therefore computationally very efficient. The fourth rungs are non-local functionals which improve the accuracy of calculations drastically but introduce a huge increase of computational cost. This rung is formed by the famous hybrid functionals,[191,194] which tackle one of the major error sources in KS-DFT: the self-interaction error. KS-DFT turns an intractable N-body problem into N coupled one-body problems similar to the Hartree-Fock approach which also uses a mean-field approximation. Describing the Coulomb interaction of each electron in a mean-field generated by all electrons causes one electron to interact with itself. This non-physical behaviour is known as the self-interaction error (SIE). In the case of Hartree-Fock (HF) theory, the Coulomb interaction is described explicitly and so the SIE is subtracted. Since DFT methods are based on the electron density, the mean-field approach leads to implicit expressions of exchange interactions. Precisely, the repulsion of one electron with itself in the Coulomb potential is not exactly cancelled by the approximated exchange potential (as it is done for Hartree-Fock). A significant deviation

is the asymptotic behaviour (described exponentially in LDA or GGA) in regions far from the nucleus (electron density should decay with $-1/r$), which is specifically problematic for weakly bound electrons. To reduce the SIE in search of the exact exchange-correlation functionals, hybrid functionals were developed which include an (HF-based) exact exchange component. The amount of exact HF exchange is functional-dependent and is applied as an empirical parameter. A typical portion is between 20% and 25%.[183] An common criticism of this hybridisation approach is that successful hybrid functionals often contain multiple (in some cases over 50) empirical parameters which makes systematic development and improvement difficult.[192] Even though this approach could be described as the opposite of *ab inito* development, the design principle can be rationalised[191] and the success of hybrid functionals is a tribute to their overall performance: the most popular (hybrid) DFT functional B3LYP is known as an 'all-rounder' in quantum chemistry.[195] The computational cost varies with the explicit hybrid functional. Generally, hybrid functionals are between a factor of 10 to 100 slower than GGA and meta-GGA functionals, depending on the amount of exact exchange included in the approximation.[196,197]

The last rung is formed by the random phase approximation (RPA).[198–200] RPA-like functionals use a many-body approximation that includes unoccupied Kohn–Sham orbitals (in addition to the first four rungs). While RPA can lead to an almost exact description of the long-range part of the exchange-correlation hole, the short-range part shows significant deviations. This leads to a large total error, which is $-0.5\,\text{eV}$ per electron in a typical system. Despite this significant error, as most chemical problems are interested in relative energies, the error cancels out for most systems.[199] However, the increased accuracy comes with a price; the RPA can easily be 100 times slower than GGA and meta-GGA approaches.[192]

5.2.6 Prediction of Binding Energies and EMs

Despite the exhaustive list of experimental studies, computational studies into the chelate effect or chelate cooperativity are rare. To predict effective molarities, an accurate determination of Gibbs energies is required and so computational techniques are currently limited to smaller systems. Studies have been reported which tackle the theoretical prediction of kinetic effective molarities.[201–203] Thermodynamic effective molarities for supramolecular host-guest systems are rare in literature.[204] The challenges lies in the combination of:

accurate description of weak interactions; the impacts of solvation, sometimes requiring explicit solvent molecules; and various non-linear scaling errors caused by comparison of an intramolecular supramolecular system with multiple bond formations to a (generally smaller) reference system with a single bond formation.[205]

One such weak interactions is dispersion. Dispersion, or London forces, describes the induction of a dipole–dipole interaction arising from an instantaneous dipole created by random motion of electrons. Therefore, dispersion is an effect which finds its origin in electron correlation, and so requires high level theoretical methods for accurate simulation.[206] A suitable treatment of dispersion varies from case to case. For DFT methods, dispersion correction can be added explicitly using Grimme's empirical dispersion correction D3, for example, or implicitly (as demonstrated by the Minnesota functional family). Plain HF methods fail in the description of dispersion due to the lack of correlation effects. This can be accounted for by post-HF methods. The SCS-MP2 method has demonstrated good performance in the description of dispersion and weak interactions but has a large increase in cost and is therefore unsuitable for our systems.[207] Therefore, the description of effective molarities related to supramolecular host-guest systems creates significant challenges for DFT approaches, including the description of weakly interacting molecules, delocalisation, and static strong correlation, to name a few.[204]

Nonetheless, several benchmarks have shown the utility of DFT methods to determine non-covalent binding energies and hence the prediction of *EM* values.[206,208,209] To find the ideal method for our systems, a benchmark is required to determine the most suitable method for the discussed host-guest systems. Based on the system size and the computational cost, a robust and fast method is required. Therefore a benchmark is conducted in two steps: first a model system is used to test a variety of different functionals and basis sets, and second the performance of the best method(s) is tested against the host-guest library. The second step is necessary, as a simple model system cannot represent all important factors. For example, testing the functionals by binding a porphyrin monomer (which is a suitable size for a benchmark) does not include the effect of strain introduced to the acetylene upon complex formation.

The nine most suitable functionals were determined by an extensive literature search. As mentioned above, the limiting factor in this benchmark is the system size. Hence, the

functionals are combined with moderate basis set sizes. These functionals were combined with two basis sets: the 6-31G* double-zeta Pople basis set for all atoms – or the combination of 6-31G* for the atoms C,H,N and the LANL2DZ basis set with an effective core potential[210] for zinc. The latter reduces the computational cost since it treats the Zn core electrons as an effective potential instead of calculating all of them explicitly.

B3LYP and CAM-B3LYP: Due to relatively low resource requirements and its satisfying (qualitative) determination of binding energies, B3LYP[190,194,211] is a heavily used functional in the literature. The hybrid functional uses 20 % HF exchange and has shown reasonably good results for porphyrin systems.[212–214] Due to the system size of the host-guest systems in this study and the importance of of dispersion in non-covalent systems, Grimme's D3 dispersion correction will be used.

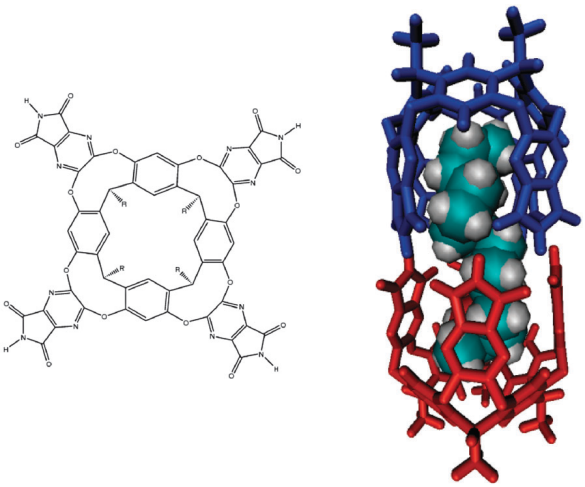

Figure 5.2: Resorcinarene schematic (left) and 3D figure (right) of two resorcinarene encapsulating a linear *n*-tetradecane (B97-D2/TZVP optimized geometry). Figure reprinted with permission from Reference [207].

Interestingly, B3LYP/6-31G* has shown a similar accuracy in the calculation of binding energies of non-covalent complexes as the dispersion corrected B3LYP-D2/TZVP. This was demonstrated by resorcinarene encapuslating linear alkanes (Fig. 5.2).[207] Error cancellation due to the missing dispersion correction and the small basis set seems to cause this surprising accuracy. However, this cancellation effect is quite unreliable as an extensive study of different host-guest complexes revealed.

For a broader analysis of effects, the long-range corrected CAM-B3LYP[215] was included. The space-dependent hybrid functional is a variation of the famous B3LYP functional

and uses a range separation. In this approach, the interelectronic Coulomb operator is separated into short range (SR) and long range (LR) parts which allows weakly bound electrons that are far away from the nucleus to be described differently. The rationale behind this approach is the correction of the self interaction error, which can become significant for weakly bound electrons. Hence, the HF exchange can be increased in the long range and correct for the incorrect asymptotic behaviour (which results in the self interaction error) while the short range can profit from the non-dynamic correlation description included in the DFT part of the exchange-correlation functional. In case of CAM-B3LYP, 19 % HF exchange is used in the short range and 65 % for the long range description.

PBE and PBE0: The other two functionals found in the literature, which are heavily used to describe porphyrin systems, are PBE[191,216,217] and PBE0[218,219] . The GGA-functional PBE is a fully local functional which is only dependent on the density gradient, resulting in robust and fast optimised structures. Even though it tends to overestimate binding energies (since the density gradient is not sufficient to counteract the underlying local density approximation), it has shown promising results in the prediction of supramolecular geometries, and could be used as a starting point for single-point optimisations with a more complex method. It has generally shown good performance for porphyrin structures.[213] The hybrid functional PBE0[218,219] mixes 25 % of HF exchange to the PBE-GGA exchange and uses full PBE correlation. The addition of HF exchange leads to significant improvement in the determination of binding energies (in comparison to PBE).[192] Similar observations have been made for porphyrins.[212]

M05-2X, M06-L, and M06: The Minnesota functional family is well-known for its overall good performance. A detailed benchmark by Mardirossian and Head-Gordon has shown the broad success of the different functionals.[182] In terms of binding energies for complexes involving transition metals the functionals M05-2X[220] and M06[221] have shown the best performance for the whole family. Both functionals are hybrid functionals. M05-2X uses 56 % HF exchange and includes 19 fitted parameters which control the performance of the functional. M06 uses 27 % HF exchange but is defined by 29 parameters. A benchmark conducted by Truhlar and co-workers has shown a

good performance of both functionals in calculating bond dissociation energies of zinc-ligand complexes.[222,223] The good performance of these functionals was also independently reported by Grimme and co-workers.[224]

M06-L[221] is a local meta-generalized gradient approximation (meta-GGA). Hence, the stand-alone functional is self-contained, has no HF exchange and is only dependent on the local spin densities, their gradients, and the local spin-specific kinetic energy densities. Due to its great computational efficiency, it found broad applicability in chemistry and physics.[221] Despite the high number of fitted parameters (34), M06-L shows a higher convergence stability (especially involving symmetry) in comparison to the other Minnesota functionals with a slightly higher error in the prediction of thermochemistry.

ωB97XD and mPW1PW91: The hybrid functional mPW1PW91[225] uses 25 % HF exchange and uses local (LDA) and non-local (Perdew-Wang91) correlation. The combination of local and non-local correlation in combination with the specifically designed exchange functional[217] leads to a reduction of self interaction error. While a similar effect can be accomplished with functionals using exclusively HF exchange (like HFLYP), the benefit of mPW1PW91 is that the remaining non-physical self interaction can be used to mimic the system-independent non-dynamic left-right correlation.

The range separated ωB97XD[226] functional uses 22 % HF exchange in the SR and 100 % in the LR. The functional is optimised to include explicit dispersion correction (Grimme's D2[227]). The successful combination of range separation and dispersion correction is well-suited to describe weak interactions. This has been demonstrated in an extensive benchmark investigating the description of non-covalent interactions, in particular for H-bond interactions.[208,228,229]

Moreover, the effect of solvent models was studied. Two different approaches were tested to calculate the free energy of the complexation reaction; on the one hand using the solvation model to optimise the structure and calculate vibrational frequencies within the solvation model (as suggested by Truhlar) and on the other hand calculating both in the gas phase and calculating the solvation energy as a single-point calculation (as suggested by Klamt).[230,231]

For the first approach the implicit continuum solvent models implemented in Gaussian09 were used to estimate solvation effects. In detail, these are the Polarizable Continuum Model (PCM) and the density-based Solvation Model (SMD). PCM is based on the idea of generating multiple overlapping spheres for each of the atoms within the calculated molecule inside of a dielectric continuum. Additionally, SMD includes a second term that adds effects such as dispersion arising from short-range interactions between the solute and the solvent molecules in the first solvation shell to the solvation energy. This contribution makes the SMD solvation model better parametrised for solvents with dispersive interaction and usually produces more accurate results. The second approach is tested by applying the COSMO-RS solvation model, which performs a single-point calculation to estimate the solvation energy. The advantage is a lower computational cost since the calculation is using BP86 (composition of the Becke 1988 exchange functional and the Perdew 86 correlation functional) in TURBOMOLE. Hence, it is possible to perform the calculation on any modern computer. Moreover, solvation models usually lead to flat potential energy surfaces, which can drastically complicate the optimisation procedure. The COSMO-RS solvation model has shown impressive performance in the description of non-covalent solvation energies.[208,209]

5.3 Prediction of Effective Molarities

The prediction of *EM* values requires accurate binding energies. In a first step, a benchmark was conducted to compare the performance of suitable DFT functionals based on a representative model system. The second step is to use the most suitable functional(s) to calculate Gibbs energies and *EM* values for the host-guest library.

5.3.1 Benchmark on a Model System

The aim of this benchmark is to find a robust method, allowing us the determination of accurate binding energies and ideally including solvent effects. As a test system, the association reaction of pyridine to zinc tetraphenyl porphyrin (**TPP**, **2**) was used (Fig. 5.3). The chosen model system is well-studied, free binding energies and enthalpies are reported in literature as well as crystal structures of the bound and the unbound molecule.[51,52] It is, therefore, an appropriate model system represents all changes occurring in the actual host-guest library. In our case, the model as well as the actual system involve an axial nitrogen zinc bond formation and the reduction of symmetry from C_4 (**TPP**) to C_2 (**31**) upon binding.

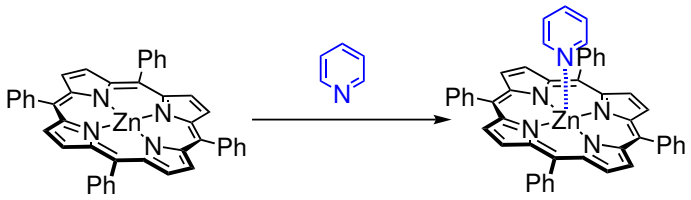

2 **31**

Figure 5.3: Pyridine binding to the monomeric tetraphenylporhpyrin ($\Delta G_{benzene} = -5.1 \pm 0.6$ kcal mol^{-1} and $\Delta G_{chloroform} = -3.8 \pm 0.8$ kcal mol^{-1}).[54]

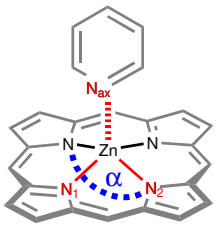

Figure 5.4: Bond length and angles used as evaluation criteria to compare experimental results from the crystal structure and the calculated DFT results.

Based on the molecular size, the dispersion interaction should be taken into account. Therefore, functionals without any dispersion correction (B3LYP, CAM-B3LYP, PBE, and PBE0) were used in combination with the Grimme D3[232] dispersion correction with the Becke-Johnson-damping function.[233] For the Minnesota functional family, implicit dispersion is already included in the definition of the functionals which is why M05-2X, M06, and M06L are used without Grimme's dispersion. Moreover, it has been reported that the combination of B3LYP with the small double zeta 6-31G* basis set results in non-systematic error cancellation effects (in contrast to the other methods), which is why B3LYP/6-31G* is also included without dispersion correction in the benchmark.[207] These functionals were combined with the 6-31G* and the 6-31G*/LANL2DZ basis set, were zinc is described by the LANL2DZ effective core potential. All functionals and basis set combinations were tested using gas phase conditions and two different types of continuum solvation model (PCM and SMD). The solvation energy was additionally determined with single-point calculations using the COSMO-RS approach.

All calculations were done using Gaussian09, Revision D.01.[234] Structural parameters were compared between the different calculation methods. Most interesting are the four nitrogen zinc bond length and the N–Zn–N angle, which is an indication of how out-of-plane the zinc atom is, and the axial nitrogen zinc bond length.[235]

Table 5.1: Overview of bond length and angles determined by different methods for the optimised gas phase structure (**31**).

Method	N_{ax}–Zn	N_1–Zn	N_2–Zn	$\alpha 1$	$\alpha 2$
B3LYP/LANL2DZ	2.293	2.101	2.103	160.5	162.1
B3LYP/6-31G*	2.180	2.084	2.086	159.3	159.2
M05-2X/LANL2DZ	2.212	2.083	2.084	163.7	163.8
M05-2X/6-31G*	2.136	2.074	2.075	160.8	161.1
M06/LANL2DZ	2.237	2.083	2.080	164.5	163.6
M06/6-31G*	2.142	2.066	2.065	161.3	160.3
M06-L/6-31G*	2.144	2.073	2.073	160.7	160.9
M06-L/LANL2DZ	2.243	2.089	2.089	164.0	164.1
PBE0-D3BJ/LANL2DZ	2.215	2.083	2.084	164.4	164.7
PBE0/6-31G*	2.118	2.066	2.067	161.6	161.9
Experimental[235]	2.143	2.067	2.079	161.4	2.143

Besides some minor deviations, all functionals are in agreement with the structural parameters. The bond lengths calculated with the LANL2DZ basis set are longer than the bond length using the plain 6-31G*. To illustrate the differences, an overview of the determined parameters in the gas phase is given in Table 5.1. A detailed summary of all bond lengths and angles can be found in the appendix. Besides B3LYP in combination with the LANL2DZ basis set, all nitrogen zinc bond lengths are within the 3σ standard deviation of the crystal structure (0.012 Å for the N_{ax} bond length). The same is valid for bond angles. M05-2X with the LANL2DZ basis set shows the values closest to the experimental value. This may suggest that this method could be useful for crystal structure prediction.

The effects of the SMD and PCM solvent models are rather small. Even though application of the solvent model shortens the bond length, the impact on the absolute value is rather small (for example: B3LYP shortening: 0.01 Å using 6-31G*). This is an important factor, since it may indicate that the geometry optimisation can be done without the solvent model. Hence, the solvation energy can be calculated as a single-point calculation.

The Gibbs energy of the complexation reaction was experimentally determined by UV/Vis titrations and is -5.1 ± 0.6 kcal mol^{-1} in benzene.[54] The results were reproduced with several titration experiments, giving a binding constant of $(3.73 \pm 0.01) \times 10^{-3}$ M^{-1}. Hence, the corresponding Gibbs energy has the value 5.1 ± 0.1 kcal mol^{-1} and is in agreement with the literature results. The calculated energies are shown in Table 5.2. The energies calculated

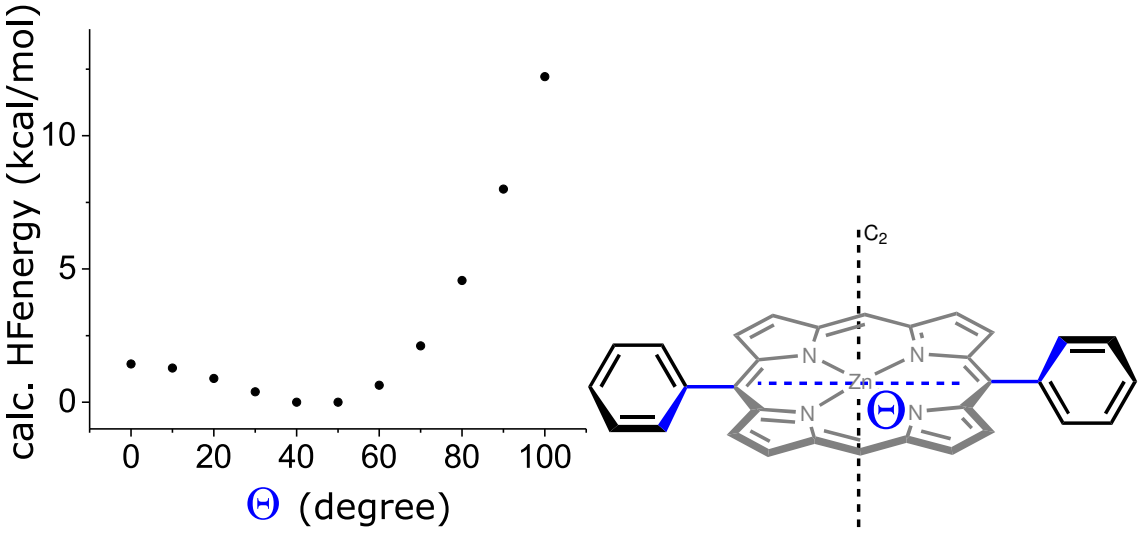

(a) electronic energy profile **(b)** electronic energy profile

Figure 5.5: Electronic energy in dependency of the torsional angle Θ from 0 to 100 degree (gas phase, B3LYP/6-31G).

with different basis sets are in agreement. The 6-31G* basis set tends to overestimate the Gibbs energy of binding. Reducing the size of basis set functions (with the 6-31G*/LANL2DZ basis set), reduces this effect and results in binding energies closer to the experimental value for most methods. As observed in the literature, B3LYP shows poor performance in combination with solvation models.[208] The performance for each member of the Minnesota functional family is very similar. All tend to overestimate the Gibbs energy in absence of a solvation model which was expected since their parameterisation is optimised for use with solvation.[182] All methods seem to overestimate the binding energy in the gas phase. Most likely, this is caused by the dispersion correction since the correction is not compensated for. Using a solvation model, the magnitude of the free energy values decreases. B3LYP/6-31G* in the gas phase and M05-2X/LANL2DZ using the SMD solvation model produce the values closest to the experimental binding energy. The B3LYP values calculated with the LANL2DZ basis set underestimate the binding energy; especially the PCM solvation model shows significant deviations with a positive Gibbs energy for the complex formation. Overall, the COSMO-RS approach showed rather small impacts and did not reproduce the experimental free energy values. Hence, COSMO-RS should not be used for the Gibbs energy calculation.

The energy difference between the two solvation models is rather small. Interestingly, no minimum structure in C_4 symmetry was found for **TPP** with the SMD model due to an unsymmetric torsion between the phenyl groups. However, the impact on the Gibbs energy

Table 5.2: Calculated binding energies of **31** in kcal/mol and each solvation model parametrised for benzene as solvent (C-RS = COSMO-RS). Missing energies are caused by complications in the optimisation process. *one of the structures is showing an imaginary frequency around 10 cm^{-1} wave numbers

Functional	Gp	PCM	SMD	C-RS	ΔGp	ΔPCM	ΔSMD	ΔC-RS
				6-31G*				
B3LYP	−4.7	−2.8			−0.3	−2.2	−5.0	
B3LYP-D3BJ	−15.6	−14.0	−14.0	−12.4	10.6	9.0	9.0	7.4
CAM-B3LYP-D3BJ		−13.6	−13.6	−12.8				7.8
M05-2X	−10.1	−12.2	−12.1	−9.7	5.1	7.2	7.1	4.7
M06	−8.7		−17.4	−10.7	3.7			5.7
M06-L								
mPW1PW91	−3.3		−3.9	−2.7	−1.8		−1.1	−2.4
PBE-D3BJ	−11.8		−12.3	−13.1	6.8		7.3	8.0
PBE0-D3BJ	−12.7	−12.3		−10.9	7.7	7.3		5.9
ωB97XD	−12.1			−11.1	7.0			6.1
				6-31G*/LANL2DZ				
B3LYP	−1.3	0.9			−3.8	−6.0		
B3LYP-D3BJ	−12.1*	−8.3*	−8.7*	−13.5*				
CAM-B3LYP-D3BJ	−12.8	−9.7		−14.4	7.7	4.6		9.3
M05-2X	−9.2	−7.0	−4.1	−10.9	4.1	1.9	−0.9	5.8
M06	−9.8		−6.1*	−11.4	4.7			6.3
M06-L	−9.2			−10.8				
mPW1PW91	−2.4	0.3	1.5	−3.9	−2.7	−5.4	−6.5	−1.2
PBE-D3BJ	−11.7	−8.7		−12.7	6.6	3.6		7.6
PBE0-D3BJ	−11.2	−8.8	−6.2*	−13.2	6.1			8.1
ωB97XD	−12.4	−9.2		−14.0	7.3	4.1		8.9
				Experimental Value: -5.1				

is insignificant since the potential energy surface is very flat along this torsional reaction coordinate. This is demonstrated by the torsional angle scan shown in Figure 5.5. Expanding the angle between the perpendicular phenyl groups while the porphyrin remains C_2 molecular symmetry reduces the torsion angle between the phenyl groups and the porphyrin plane (Fig. 5.5b). In the presented relaxed scan, the torsion angle varies between from 0° (both phenly groups are aligned and perpendicular to the porphyrin plane) to 100° in 10° steps illustrates that the minimum structure is around 50° and that the repulsion only becomes significant for the phenyl groups being in plane with the porphyrin. Nevertheless, the energy difference between 0° and 50° is around 1.7 kcal mol^{-1}. This value is of course different for the individual functionals but one can conclude that the energetic difference around 50°

are rather small and these effects can be neglected for the benchmark analysis.

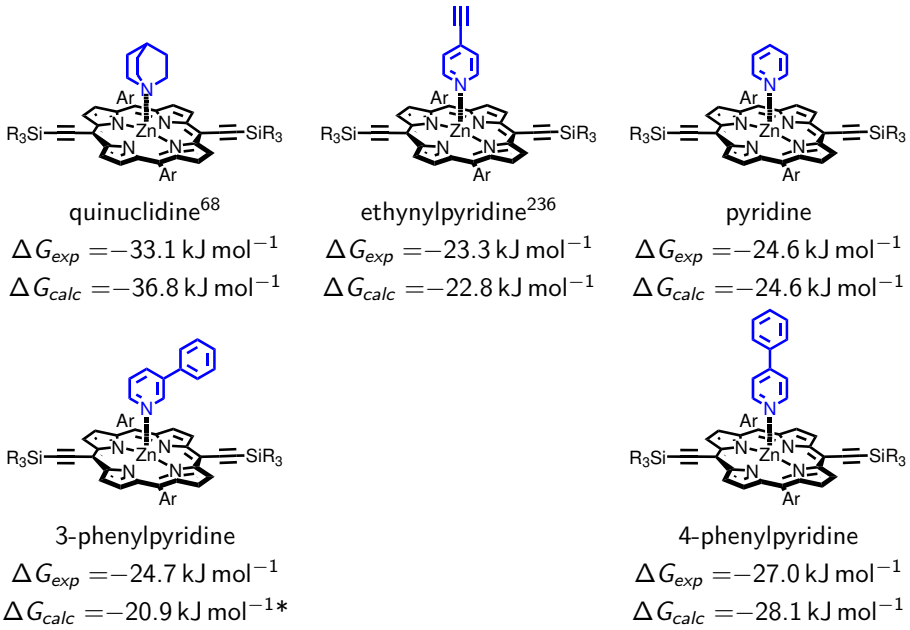

Figure 5.6: Comparison of experimental and calculated binding energies for the ***I*-P1** (tBu as solubilising groups) and different monovalent guest complexes. Experimental values are determined at 298 K in toluene, calculated values on M05-2X/6-31G*/LANL2DZ level using SMD(toluene); *small imaginary Frequency

In conclusion, B3LYP/6-31G* (gas phase) and M05-2X/6-31G*/LANL2DZ (SMD) showed the best results regarding the overall performance. All other methods showed significant deviations from the experimental Gibbs energies, are computationally expensive, or show convergence issues. The disadvantage of B3LYP is the lack of dispersion correction which might introduce issues in the prediction of larger systems and no option to include solvent effects. M05-2X performs remarkably well with an error of 1 kJ mol^{-1}. A comparison of monomer complexes with different amine-based ligands supports the same excellent agreement between the experimentally determined value and the one calculated at the M05-2X/6-31G*/LANL2DZ (SMD) level (Fig. 5.6). The disadvantage of M05-2X are convergence issues for structures in symmetry, which might make calculations quite expensive. Therefore, both methods were tested in the description of the host-guest library.

5.3.2 Performance Evaluation on Host-Guest-Library

The performance of M05-2X/6-31G*/LANL2DZ in combination with the SMD solvent model as well as B3LYP/6-31G*, was tested against the experimental results of complex formation. For the multivalent hosts, all phenyl solubilising groups were replaced by hydrogens (Fig. 5.7).

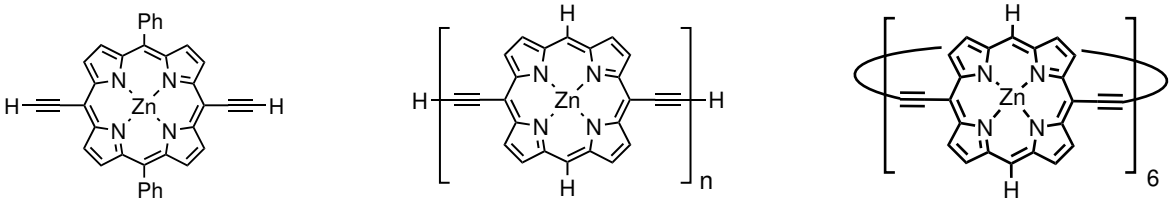

Figure 5.7: Molecular structures used for the DFT calculations.

The substitution effect was investigated by a comparison of the ***l*-P1** monomer with protons and phenyl groups showed that the influence on the axial coordination is rather weak. The difference in calculated Gibbs energy of binding for both derivatives of ***l*-P1** binding to pyridine show a difference of $2\,\mathrm{kJ\,mol^{-1}}$ for M05-2X/6-31G*/LANL2DZ and SMD and $1.5\,\mathrm{kJ\,mol^{-1}}$ for B3LYP/6-31G*. As a result, a substitution of the phenyl groups seem to be a sensible reduction of computational cost.

The results for the bi- and trivalent host-guest systems are shown in Figure 5.8. Generally, B3LYP accurately predicts the Gibbs energy of binding and outperforms M05-2X in terms of computational cost and prediction accuracy. The mean absolute deviation (MAD) for the calculations at the B3LYP/6-31G* level is $2.1\,\mathrm{kJ\,mol^{-1}}$.

The determination of Gibbs energies for the multivalent host-guest systems with M05-2X/6-31G*/LANL2DZ and SMD was challenging. The computational cost increased significantly and symmetry as well as convergence issues made it impractical to obtain values for the cyclic host. A better convergence could be obtained by optimising the molecular geometries in the gas phase. As seen in the benchmark, the deviations between gas phase optimised structures those optimised utilising a solvent model are minor. The potential energy surface is steeper in the gas phase which improves convergence.

In case of the linear guests, the determined Gibbs energies Gibbs energies for the multivalent host-guest complexes show high deviations to the experimental values with a MAD of $13.2\,\mathrm{kJ\,mol^{-1}}$. The divergence between the excellent performance for the smaller monovalent systems and the size-increasing multivalent systems indicates that the M05-2X method in combination with the small basis set suffers from a large basis set superposition error (BSSE).

An approach to overcome the BSSE is the application of counterpoise methods. Due to the system size, the geometrical counterpoise correction (gCP) was chosen which does not require any optimisation of the molecule and is simply added to the final energy.[195,237]

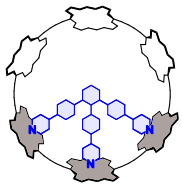

(a) *c*-P6•A3

$\Delta G_{exp} = -101.3\,\mathrm{kJ\,mol^{-1}}$

$\Delta G_{B3LYP} = -96.9\,\mathrm{kJ\,mol^{-1}}$

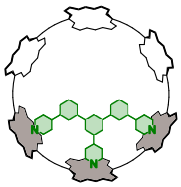

(b) *c*-P6•B3

$\Delta G_{exp} = -96.5\,\mathrm{kJ\,mol^{-1}}$

$\Delta G_{B3LYP} = -94.4\,\mathrm{kJ\,mol^{-1}}$

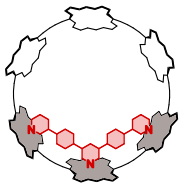

(c) *c*-P6•C3

$\Delta G_{exp} = -97.7\,\mathrm{kJ\,mol^{-1}}$

$\Delta G_{B3LYP} = -95.0\,\mathrm{kJ\,mol^{-1}}$

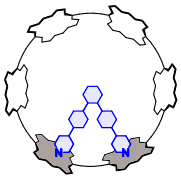

(d) *c*-P6•A2

$\Delta G_{exp} = -64.1\,\mathrm{kJ\,mol^{-1}}$

$\Delta G_{B3LYP} = -57.6\,\mathrm{kJ\,mol^{-1}}$

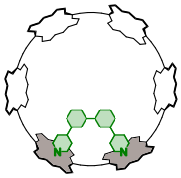

(e) *c*-P6•B2

$\Delta G_{exp} = -62.0\,\mathrm{kJ\,mol^{-1}}$

$\Delta G_{B3LYP} = -56.6\,\mathrm{kJ\,mol^{-1}}$

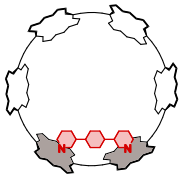

(f) *c*-P6•C2

$\Delta G_{exp} = -64.8\,\mathrm{kJ\,mol^{-1}}$

$\Delta G_{B3LYP} = -48.4\,\mathrm{kJ\,mol^{-1}}$

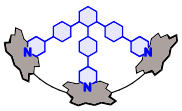

(g) *l*-P3•A3

$\Delta G_{exp} = -64.5\,\mathrm{kJ\,mol^{-1}}$

$\Delta G_{B3LYP} = -61.4\,\mathrm{kJ\,mol^{-1}}$

$\Delta G_{M05-2X} = -108.6\,\mathrm{kJ\,mol^{-1}}$

$\Delta G_{M05-2X,gcp} = -79.6\,\mathrm{kJ\,mol^{-1}}$

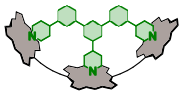

(h) *l*-P3•B3

$\Delta G_{exp} = -58.0\,\mathrm{kJ\,mol^{-1}}$

$\Delta G_{B3LYP} = -55.2\,\mathrm{kJ\,mol^{-1}}$

$\Delta G_{M05-2X} = -91.7\,\mathrm{kJ\,mol^{-1}}$

$\Delta G_{M05-2X,gcp} = -60.7\,\mathrm{kJ\,mol^{-1}}$

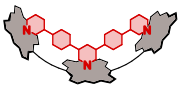

(i) *l*-P3•C3

$\Delta G_{exp} = -56.9\,\mathrm{kJ\,mol^{-1}}$

$\Delta G_{B3LYP} = -58.5\,\mathrm{kJ\,mol^{-1}}$

$\Delta G_{M05-2X} = -99.5\,\mathrm{kJ\,mol^{-1}}$

$\Delta G_{M05-2X,gcp} = -65.8\,\mathrm{kJ\,mol^{-1}}$

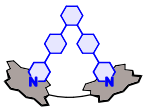

(j) *l*-P2•A2

$\Delta G_{exp} = -42.1\,\mathrm{kJ\,mol^{-1}}$

$\Delta G_{B3LYP} = -40.4\,\mathrm{kJ\,mol^{-1}}$

$\Delta G_{M05-2X} = -66.7\,\mathrm{kJ\,mol^{-1}}$

$\Delta G_{M05-2X,gcp} = -49.5\,\mathrm{kJ\,mol^{-1}}$

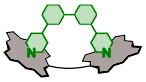

(k) *l*-P2•B2

$\Delta G_{exp} = -40.1\,\mathrm{kJ\,mol^{-1}}$

$\Delta G_{B3LYP} = -36.3\,\mathrm{kJ\,mol^{-1}}$

$\Delta G_{M05-2X} = -64.3\,\mathrm{kJ\,mol^{-1}}$

$\Delta G_{M05-2X,gcp} = -46.7\,\mathrm{kJ\,mol^{-1}}$

(l) *l*-P2•C2

$\Delta G_{exp} = -41.1\,\mathrm{kJ\,mol^{-1}}$

$\Delta G_{B3LYP} = -35.8\,\mathrm{kJ\,mol^{-1}}$

$\Delta G_{M05-2X} = -64.2\,\mathrm{kJ\,mol^{-1}}*$

$\Delta G_{M05-2X,gcp} = -44.5\,\mathrm{kJ\,mol^{-1}}*$

Figure 5.8: Comparison of experimental and calculated binding energies for the ***l*-P2**, ***l*-P3**, and ***c*-P6** complexes with the three series of guests. Experimental values (ΔG_{exp}) are determined at 298 K in toluene, tBu as solubilising group. ΔG_{B3LYP} is calculated on B3LYP/6-31G* level, ΔG_{M05-2X} on M05-2X/6-31G*/LANL2DZ level using SMD(toluene), and $\Delta G_{M05-2X,gcp}$ applies additionally Grimme's geometric counterpoise correction. *complex is showing an imaginary frequency around 10 $\mathrm{cm^{-1}}$ wave numbers.

The corrected Gibbs energies are shown in Figure 5.8 ($\Delta G_{M05-2X,gcp}$). The counterpoise correction reduces the MAD to 3.6 kJ mol^{-1}.

Regarding the overall benchmark, B3LYP/6-31G* delivered the best results from all tested method combinations. The lack of dispersive interactions is compensated by the moderate basis set size. Moreover, the absence of dispersion and a missing solvation model might mimic the experimental conditions, as continuum solvation models do not account for dispersive, cohesive interactions between solvent molecules.[238] Molecular geometries obtained by B3LYP show slightly longer bonds compared to the other methods and the experimental crystal structures. However, the determined Gibbs energies show very low MAD. The biggest disadvantage of the method is the poor performance in combination with solvation models. However, the Gibbs energies are in good agreement with the experimental values obtained using non-polar solvents like toluene or benzene. In conclusion B3LYP is our method of choice.

5.3.3 Theoretical predictions of EM

Based on the accurately predicted Gibbs energies of binding, we explored the theoretical determination of effective molarities. The *EM* values can be derived from the calculated Gibbs energies. Even though B3LYP is more suitable for determination of Gibbs energies, the comparison of an inter- and an intramolecular host-guest system might lead to error cancellation for the calculated *EM* values. Hence, M05-2X determined EM values are included in the comparison.

By subtracting the statistical correction for the molecular symmetry, the symmetry corrected Gibbs energy (ΔG^*_{B3LYP} and $\Delta G^*_{M05-2X,gcp}$) can be determined and used to determine the *EM* values. The calculated geometric average *EM* values were determined using B3LYP/6-31G* (EM_{B3LYP}) and M05-2X/6-31G*/LANL2DZ with SMD and the gCP correction ($EM_{M05-2X,gcp}$). Both methods show significant deviations from the experimental values. M05-2X fails to reproduce the experimental trend. Despite the difference in absolute values, a strong correlation is observed for the B3LYP and the experimental values. This is illustrated by the logarithmic plot of calculated against experimental *EM* values (Fig. 5.9a).

The calculation of *EM* benefits highly from error compensation; most systematic errors which originate from the formulation of the theoretical method are present in the monovalent as well as the multivalent system and are compensated by relating both to each other.

Table 5.3: Experimental *EM* values (geometric average, Ar=tBu, with ***l*-P1** used as intermolecular reference), *EM* values determined based on statistically corrected Gibbs energies calculated on B3LYP/6-31G* level, and *EM* values calculated on M05-2X/6-31G*/LANL2DZ with SMD and the gCP correction.

Complex	EM_{exp}	EM_{B3LYP}	$EM_{M05-2X,gcp}$
***l*-P2•A2**	0.026	2.445	0.034
***l*-P2•B2**	0.002	0.471	0.011
***l*-P2•C2**	0.018	0.970	3.920
***l*-P3•A3**	0.026	2.751	0.279
***l*-P3•B3**	0.007	0.786	0.006
***l*-P3•C3**	0.021	2.996	2.792
***c*-P6•A2**	5.174	418.989	–
***c*-P6•B2**	2.162	284.898	–
***c*-P6•C2**	40.282	–	–
***c*-P6•A3**	18.035	1437.645	–
***c*-P6•B3**	6.857	881.596	–
***c*-P6•C3**	32.854	1960.017	–

This is supported by the strong linear correlation of both values ($R^2 = 0.986$). A similar strong linear correlation is observed comparing the calculated Gibbs energies of binding to the experimental ones (Fig. 5.9b, $R^2 = 0.962$). With decreasing level of theory, the correlation is less strong for enthalpy based on the harmonic oscillator approximation (Fig. 5.9c, $R^2 = 0.820$) and worse for entropy, determined via statistical thermodynamics (Fig. 5.9d, $R^2 = 0.157$). However, combining entropy and enthalpy to Gibbs energy again profits from error compensation.

Most likely, deviations between the calculated and experimental results are caused by solvation effects. As a reminder, the Gibbs energy is determined in the gas phase at the B3LYP/6-31G* level. It was concluded in Chapter 4 that solvation must have a significant contribution to chelate cooperativity. Therefore, differences between the experimental and theoretical values is expected and the impact of solvation will be addressed in the next section.

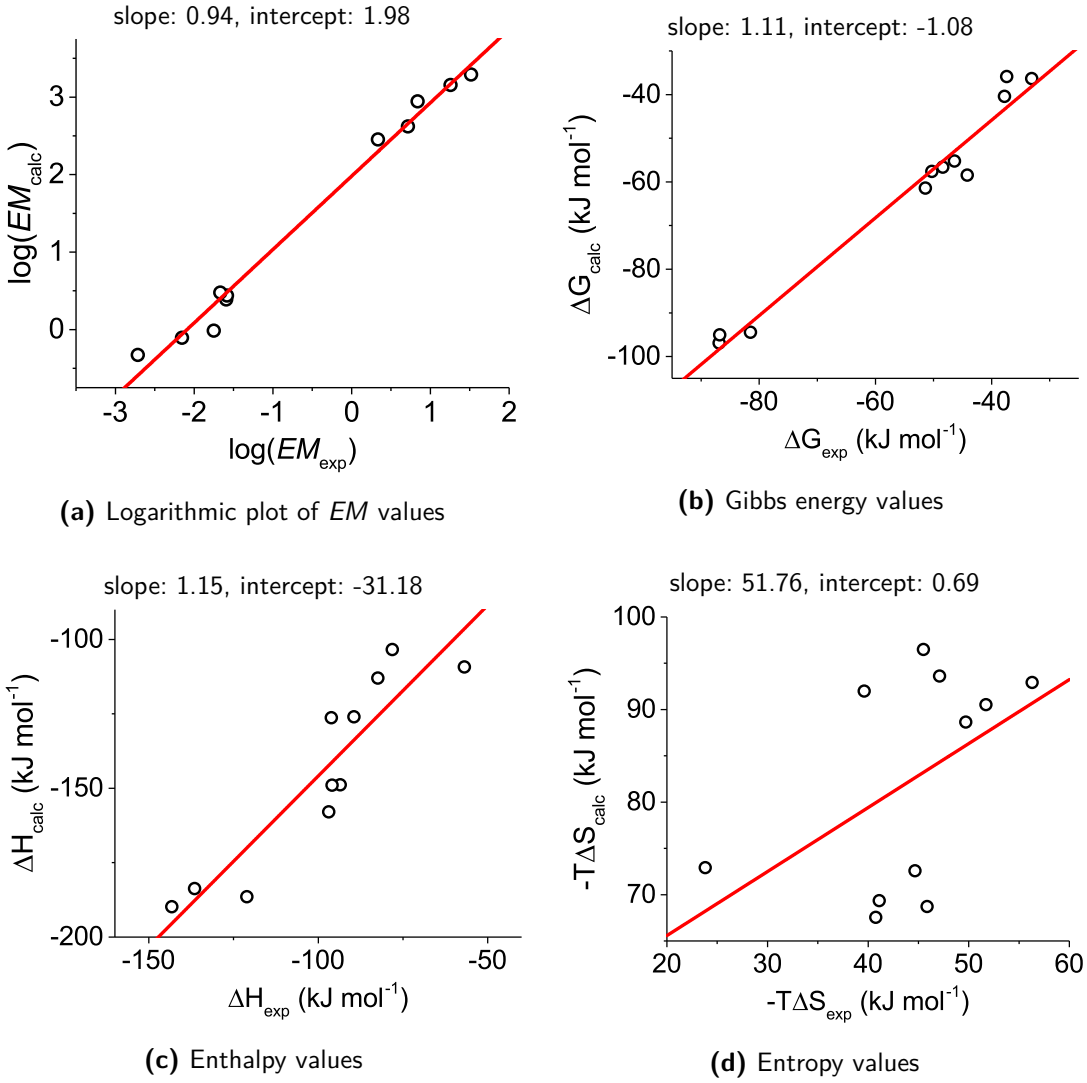

(a) Logarithmic plot of *EM* values

(b) Gibbs energy values

(c) Enthalpy values

(d) Entropy values

Figure 5.9: Plots of the on B3LYP/6-31G* calculated values (calc) against the experimentally determined ones (exp).

5.4 Solvation

As seen in Chapter 4, the host-guest library has shown deviates a surprisingly high chelation enthalpy, which could be an indication for strong interactions with solvent molecules. An extensive experimental study exploring the dependence of the cooperativity strength for ***I*-P2•A2** complex upon the solvent has revealed a strong influence of solvation on the *EM* value.[154] Depending on the solvent, the *EM* value for this system changes over an order of magnitude (*EM* varies from 0.015 M in *m*-xylene to 0.18 M in 1,2-dichloroethane) which shows that the solvent contribution to the cooperativity is significant.

An overview of the tested solvents is shown in Table 5.4. While the change in *EM* value is significant, no clear qualitative relationship could be determined to other experimental

or empirical parameter. Correlation attempts included specific solvent properties, like the solvent polarity or the solvent size.

Two empirical solvent parameters showed a slight correlation to the *EM* values: ET(30) and the structuredness. ET(30) is an empirical parameter of solvent polarity which is determined via the change in wavelength in the Vis/NIR absorption band for a pyridinium-*N*-phenolate betaine dye in a large series of solvents.[239] The structuredness is defined as the ratio of the cohesive pressure, which relates energy required to form cavities, to the internal pressure, which is the difference in internal energy if the solvent experience isothermal expansion.[240] Both parameters showed a correlation, but no straight-forward way of combining those parameters provided a sufficient correlation between the *EM* values and the empirical parameters.[154]

Table 5.4: Denaturation constant (K_{DN}) and *EM* of the ***I*-P2•A2** complex for different solvents.[154]

Solvent	K_{DN}		(M^{-2})	*EM* (M)
m-Xylene	67.7	±	2.0	0.02
Toluene	43.3	±	0.15	0.02
Iodobenzene	37.9	±	0.75	0.03
Benzene	36.5	±	0.2	0.03
Ethylbenzene	33.1	±	1.9	0.03
1,2-Dichlorobenzene	31.8	±	0.4	0.03
Chlorobenzene	26.3	±	0.2	0.04
Fluorobenzene	24.2	±	0.35	0.04
tert-Butylbenzene	12.9	±	0.3	0.08
CH_2Cl_2	12.7	±	0.3	0.08
n-Hexane	10.4	±	0.1	0.1
CCl_4	9.9	±	0.25	0.1
n-Heptane	9.6	±	0.05	0.1
Decaline (mixture of isomers)	8.7	±	0.015	0.12
Decamethylcyclopentasiloxane	7.1	±	0.55	0.14
$CDCl_3$ (0.5% Ethanol)	6.9	±	0.50	0.15
Cyclohexane	6.4	±	0.15	0.16
1,2-Dichloroethane	5.7	±	0.06	0.18

To combine the influence of solvent structure, polarity, and the solvation cavity, different approaches were tested to describe the change in solvent dependent change *EM* theoretically. As a quantity to relate the theoretical calculations, the difference in Gibbs energy between

the divalent ***I*-P2•A2** and two times the monovalent ***I*-P1•A1** was used (Eq. 5.11, termed as Gibbs energy of chelation solvation ΔG_{solv}).

$$\Delta G_{solv} = \Delta G_{\textit{I}\text{-}\mathbf{P2{\bullet}A2}} - 2 \times \Delta G_{\textit{I}\text{-}\mathbf{P1{\bullet}A1}} \tag{5.11}$$

Therefore, a relationship between the calculated Gibbs energy of chelation solvation and the experimentally determined effective molarity value should obey the following function:

$$\Delta G_{solv} = a - b \times RT \ln(EM) \tag{5.12}$$

with a and b as empirical parameters to correct any offset of a qualitative correlation.

Attempts to correlate experimental solvation to simple continuum solvation models (SMD, PCM, and COSMO in combination with M05-2X/6-31G*/LANL2DZ) on DFT level failed. The representative plot of ΔG_{solv} against the experimental EM values in different solvents for the M05-2X/6-31G*/LANL2DZ method using SMD illustrates this result (Fig. 5.10). Interestingly, solvent polarizability, a parameter relating the degree of distortion a molecule experiences by an electric field, appears to dominate the calculated solvation energy as the similarity between Figure 5.10 and Figure 5.13a (Appendix) illustrates. However, there was no clear relationship found between the experimental EM values and the solvent polarizability (see Appendix Fig. 5.13b).

Based on the evaluation of empirical parameters, the solvent effect on cooperativity seems to be heavily influenced by the the size and the structure of the solvent. Explicit solvent models are computationally too demanding to determine solvent effects for very subtle changes. However, an alternative approach is the conductor-like screening model for real solvents (COSMO-RS) solvation model.[241,242] The solvation model was used within the Amsterdam density functional (ADF) framework with re-optimised solvation model parameters.[241] Based on the benchmark in this study, COSMO-RS showed poor performance in the prediction of exact Gibbs energies of binding. A reason for the poor performance might be that COSMO-RS parameters are optimised for the BP86 functional. This functional is not suitable for the determination of binding energies in the presented host-guest systems. However, calculating the solvation energy for one specific system with varying solvents might benefit from error cancellation. While exact determination of Gibbs energies is still very challenging, a qualitative comparison allowing the determination of relevant solvent

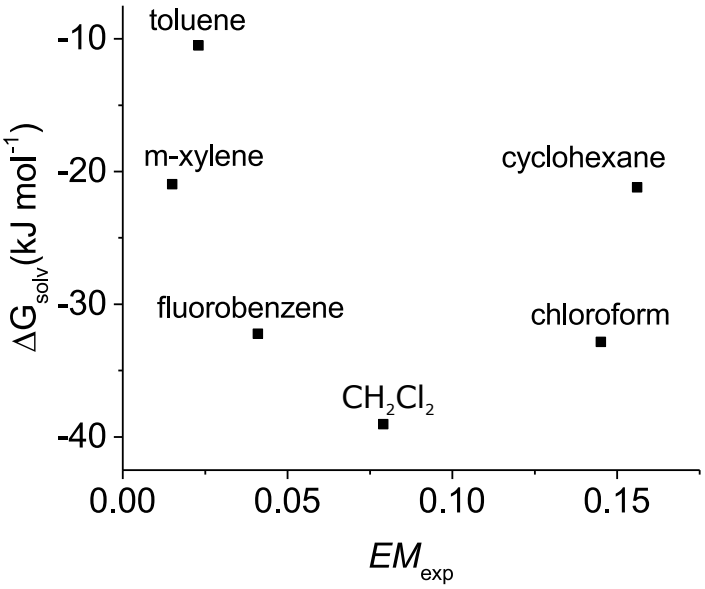

Figure 5.10: Plot of theoretical (statistically non-corrected) Gibbs energies ΔG_{solv} against the experimental effective molarities (EM_{exp}) in different solvents. ΔG_{solv} determined at the M05-2X/6-31G*/LANL2DZ level using SMD.

effects could be useful. The comparison experimental results with empirical parameters is specifically motivating; the observed slight correlation of polarity, and structuredness is an indication that the COSMO-RS approach could be successful for a qualitative comparison between different solvents.

For the COSMO-RS calculation, an electrostatic map of a molecule is constructed based on a semi-empirical or DFT approach to determine the charge and the surface of a compound. The same is done for the solvent. Interaction points are created which dictate the distance and the electrostatic interaction that two molecules can feel. In the actual COSMO-RS calculation, the solvent molecule is placed around a geometric and electrostatic approximation of the compound to achieve the lowest energetic structure. Assuming infinite dilution and no actual change in the molecular geometry, the free energy of solvation can be calculated. All reaction components were optimised using the semi-empirical PM7 approach in MOPAC[169] utilising the MOZYME[168] approximation. In the COSMO calculation the Delley type of cavity construction is chosen with an infinite dielectric constant. The radius of the probing sphere to determine the solvent excluded part of the surface was set to 1.3 Å. The solvents were optimised with the Becke Perdew exchange correlation functional (GGA), the scalar relativistic ZORA Hamiltonian, a TZP basis set with a small frozen core, and a good integration accuracy (as defined by ADF). The COSMO calculation uses the same parameter set as used for the reaction components.

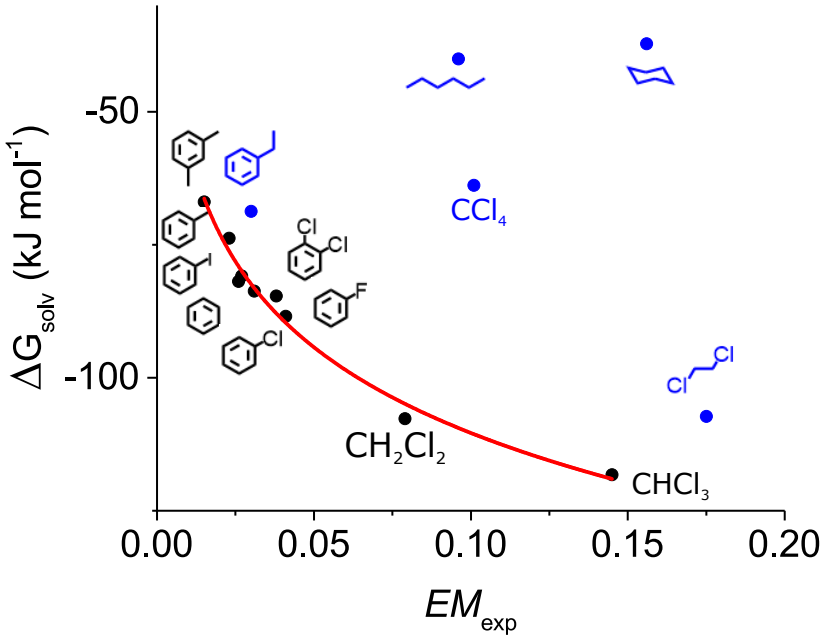

Figure 5.11: Plot of theoretical (statistically non-corrected) Gibbs energies ΔG_{solv} against the experimental effective molarities (EM_{exp}) in different solvents. ΔG_{solv} determined by PM7/COSMO-RS.

The correlation between the experimentally measured effective molarity and the calculated cooperative free energy ($\Delta\Delta G_{solv}$) is shown in Figure 5.11. Rigid solvents (shown in black) follow the logarithmic dependency expected based on Equation 5.12. Flexible solvents (illustrated in blue) show more deviation. Excluding the blue solvents, the remaining data show an excellent correlation to the logarithmic function ($R^2 = 0.98$, Eq. 5.13).

$$\Delta G_{solv} = -39.176 - 5.56 \times ln(EM_{exp}) \tag{5.13}$$

Inherent in the COSMO-RS model, the most stable (solvent) conformer is considered in the calculation and approximated as a rigid structure. However, this approximation does not describe accurately the reality of solvation for solvents that can adopt multiple configurations. This hypothesis is supported by the observed deviations. For slightly flexible solvents (like ethyl benzene), the deviations from the logarithmic trend line are small while *n*-hexane shows no correlation between the theoretical and experimental values. Due to the high number of free parameters in the optimisation, flexible solvents cannot form the most stable solvation shell around the compounds resulting in an underestimated solvation energy. The exception from this correlation is CCl_4 which requires further investigation.

To understand the observations in Chapter 4, Equation 5.11 was expanded for N intramolecular interactions (Eq. 5.14).

$$\Delta G_{solv} = \Delta G_{complex} - N \times \Delta G_{singel-site} \tag{5.14}$$

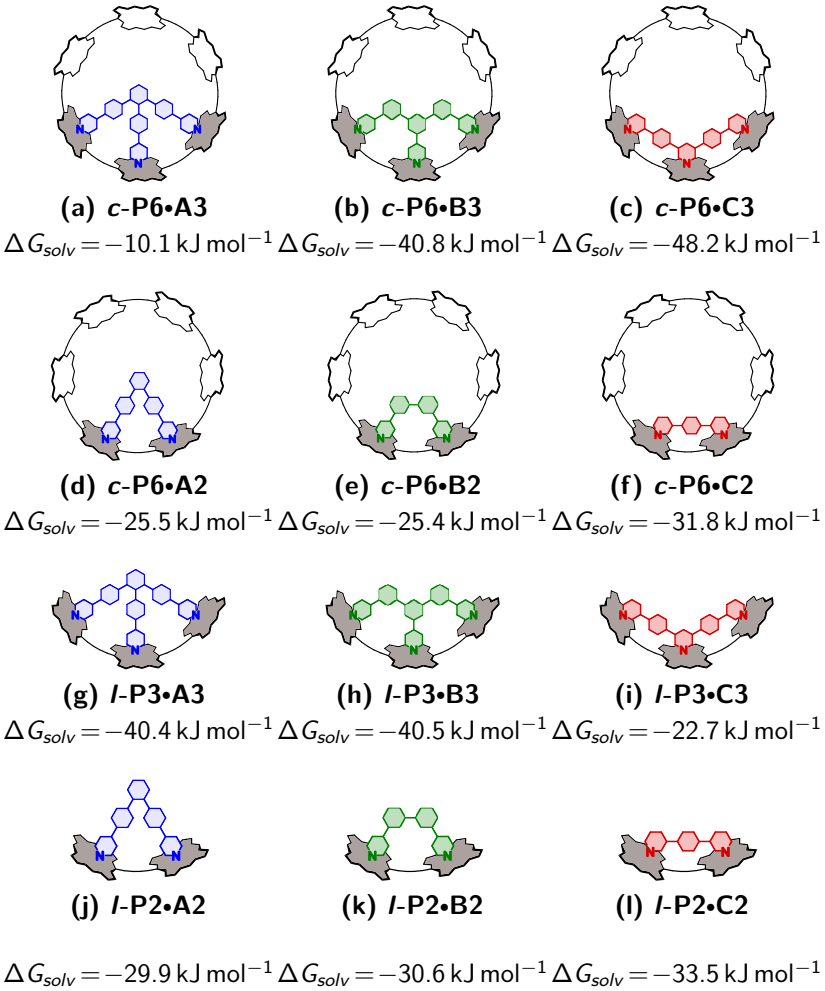

Figure 5.12: Calculated ΔG_{solv} energies for the ***l*-P2**, ***l*-P3**, and ***c*-P6** complexes with the three series of guests using COSMO-RS

The overview of the calculated energies is shown in Figure 5.12. For the bidentate ligands, the difference between the individual systems is minor. The total solvation energy is negative in all cases, indicating that the solvation contribution exhibits constructive chelate cooperativity. The complexes involving **C2** are slightly better solvated than the other ligands. Differences are observed for the tridentate ligands. The ***c*-P6•A3** complex shows a more unfavourable solvation energy than the other two cyclic complexes. For the linear oligomers, the ***l*-P3•C3** complex shows a slightly less favourable solvation energy compared to the other tridentate complexes. The difference in ΔG_{solv} for the tridentate ligands indicates that the solvation of the complexes has a significant contribution to the

effective molarity and therefore influences the cooperativity strength. This might be an explanation why the observed results appear to be less systematic than expected.

5.5 Conclusion

The theoretical prediction of effective molarities has shown promising results. A two-step benchmark was conducted to determine the most suitable method for calculation of theoretical binding energies. The first step was the evaluation of a model system, involving nine functionals in combination with two different basis sets and three different solvation models. Overall, two method combinations outperformed the rest: B3LYP/6-31G* (gas phase) and M05-2X/6-31G*/LANL2DZ (SMD). The M05-2X functional was tested against several monovalent porphyrin-based host-guest complexes and showed excellent agreement with the experimentally determined binding energies.

However the second step of the benchmark revealed instabilities. The M05-2X functional showed two types of scaling issues. First, an increase of binding interactions results in a higher deviation between the experimental and theoretical binding energies which is most likely caused by an increase in BSSE. Second, reaching convergence and optimising the structure within symmetry was more challenging with an increase in system size. Therefore, not all structures could be optimised and B3LYP was used to test the prediction of *EM* values.

Based on these results, B3LYP/6-31G* can be used in the determination of Gibbs energies. The fast and robust optimisation of molecular structures leads to an excellent starting point for further calculations. These could include single-point calculations with B3LYP/TZVP and Grimme's dispersion correction. Additionally, the differences in bond length between the gas phase molecular structure and the ones optimised using a solvation model are minor. Hence the single-point calculations could include further parameters to account for solvent effects.

The theoretical exploration of solvation effects on chelate cooperativity showed promising results. For rigid solvents, a strong correlation between the solvation energy determined via the COSMO-RS solvation model was found. In contrast to that, the solvation effects of flexible solvents could not be correlated to theoretical results.

A sensible next step would be to optimise these parameters for the application of (suitable) DFT methods. Optimising the solvation model would be a very important step in the prediction of *EM* values and hence would have a significant impact on the design of host-guest systems.

5.6 Appendix

The calculated bond length and angles are shown in Table 12 to Table 17. The differences (Δ) shown in the tables are the difference between the experimental and the calculated values. Not all basis set, functional, and solvent model combinations led to an optimised ground state structure due to convergence issues.

Table 5.5: Comparison of bond length and angles calculated with different functionals using the 6-31G*/LANL2DZ basis set in gas phase.

Functional	N_{ax}–Zn	N_1–Zn	N_2–Zn	$\alpha 1$	$\alpha 2$	ΔN_{ax}	ΔN_1	ΔN_2	$\Delta\alpha 1$	$\Delta\alpha 2$
B3LYP	2.293	2.101	2.103	160.5	162.1	0.150	0.034	0.024	−0.9	0.7
CAM-B3LYP-D3BJ	2.223	2.082	2.083	163.7	164.5	0.080	0.015	0.004	2.3	3.1
M05-2X	2.212	2.083	2.084	163.7	163.8	0.069	0.016	0.005	2.3	2.4
M06	2.237	2.083	2.080	164.5	163.6	0.094	0.016	0.001	3.1	2.2
M06-L	2.243	2.089	2.089	164.0	164.1	0.100	0.022	0.010	2.6	2.7
mPW1PW91	2.259	2.089	2.091	161.0	162.5	0.116	0.022	0.012	−0.4	1.1
PBE0-D3BJ	2.215	2.083	2.084	164.4	164.7	0.072	0.016	0.005	3.0	3.3
PBE-D3BJ	2.234	2.101	2.101	164.0	164.3	0.091	0.034	0.022	2.6	2.9
wB97XD	2.228	2.084	2.084	164.0	164.2	0.085	0.017	0.005	2.6	2.8
Experimental[235]	2.143	2.067	2.079	161.4						

Table 5.6: Comparison of bond length and angles calculated with different functionals using the 6-31G* basis set in gas phase. *a correctly optimised structure corresponding to the ground state in symmetry could not be found

Functional	N_{ax}–Zn	N_1–Zn	N_2–Zn	$\alpha 1$	$\alpha 2$	ΔN_{ax}	ΔN_1	ΔN_2	$\Delta\alpha 1$	$\Delta\alpha 2$
B3LYP	2.180	2.084	2.086	159.3	159.2	0.037	0.017	0.007	−2.1	−2.2
B3LYP-D3BJ	2.131	2.076	2.076	161.9	162.0	−0.012	0.009	−0.003	0.5	0.6
CAM-B3LYP-D3BJ	2.122	2.066	2.066	161.3	161.7	−0.021	−0.001	−0.013	−0.1	0.3
M05-2X	2.136	2.074	2.075	160.8	161.1	−0.007	0.007	−0.004	−0.6	−0.3
M06	2.142	2.066	2.065	161.3	160.3	−0.001	−0.001	−0.014	−0.1	−1.1
M06-L	2.144	2.073	2.073	160.7	160.9	0.001	0.006	−0.006	−0.7	−0.5
mPW1PW91	2.150	2.071	2.071	159.4	160.5	0.007	0.004	−0.008	−2.0	−0.9
PBE0-D3BJ	2.118	2.066	2.067	161.6	161.9	−0.025	−0.001	−0.012	0.2	0.5
PBE-D3BJ*	2.115	2.077	2.081	160.6	161.6	−0.028			−0.8	0.2
PBE-D3BJ*	2.115	2.077	2.085	160.6	161.6	−0.028			−0.8	0.2
wB97XD*	2.132	2.065	2.069	161.0	161.8	−0.011			−0.4	0.4
wB97XD*	2.132	2.066	2.073	161.0	161.8	−0.011			−0.4	0.4
Experimental[235]	2.143	2.067	2.079	161.4						

Table 5.7: Comparison of bond length and angles calculated with different functionals using the 6-31G*/LANL2DZ basis set and the PCM solvation model.

Functional	N_{ax}–Zn	N_1–Zn	N_2–Zn	$\alpha 1$	$\alpha 2$	ΔN_{ax}	ΔN_1	ΔN_2	$\Delta\alpha 1$	$\Delta\alpha 2$
B3LYP	2.287	2.103	2.105	160.2	161.5	0.144	0.036	0.026	−1.2	0.1
CAM-B3LYP-D3BJ	2.216	2.084	2.085	163.6	164.0	0.073	0.017	0.006	2.2	2.6
M05-2X	2.209	2.085	2.085	163.5	163.6	0.066	0.018	0.006	2.1	2.2
M06	2.231	2.085	2.082	163.9	163.2	0.088	0.018	0.003	2.5	1.8
M06-L	2.243	2.090	2.090	164.2	164.1	0.100	0.023	0.011	2.8	2.7
mPW1PW91	2.256	2.090	2.092	161.2	162.2	0.113	0.023	0.013	−0.2	0.8
PBE0-D3BJ	2.211	2.085	2.085	164.0	164.3	0.068	0.018	0.006	2.6	2.9
PBE-D3BJ	2.232	2.102	2.102	164.1	164.2	0.089	0.035	0.023	2.7	2.8
wB97XD	2.226	2.086	2.086	164.0	164.1	0.083	0.019	0.007	2.6	2.7
Experimental[235]	2.143	2.067	2.079	161.4						

Table 5.8: Comparison of bond length and angles calculated with different functionals using the 6-31G* basis set and the PCM solvation model.

Functional	N_{ax}–Zn	N_1–Zn	N_2–Zn	$\alpha 1$	$\alpha 2$	ΔN_{ax}	ΔN_1	ΔN_2	$\Delta\alpha 1$	$\Delta\alpha 2$
B3LYP	2.179	2.087	2.088	158.2	158.9	0.036	0.020	0.009	−3.2	−2.5
B3LYP-D3BJ	2.126	2.078	2.078	161.4	161.4	−0.017	0.011	−0.001	0.0	0.0
CAM-B3LYP-D3BJ	2.117	2.068	2.069	161.0	161.1	−0.026	0.001	−0.010	−0.4	−0.3
M05-2X	2.132	2.076	2.077	160.4	160.7	−0.011	0.009	−0.002	−1.0	−0.7
M06	2.133	2.069	2.067	160.7	159.7	−0.010	0.002	−0.012	−0.7	−1.7
M06-L	2.138	2.075	2.075	160.2	160.4	−0.005	0.008	−0.004	−1.2	−1.0
mPW1PW91	2.149	2.073	2.075	159.1	159.6	0.006	0.006	−0.004	−2.3	−1.8
PBE0-D3BJ	2.113	2.068	2.069	161.3	161.3	−0.030	0.001	−0.010	−0.1	−0.1
PBE-D3BJ	2.111	2.081	2.081	160.5	160.6	−0.032	0.014	0.002	−0.9	−0.8
Experimental[235]	2.143	2.067	2.079	161.4						

Table 5.9: Comparison of bond length and angles calculated with different functionals using the 6-31G* basis set and the SMD solvation model.

Functional	N_{ax}–Zn	N_1–Zn	N_2–Zn	$\alpha 1$	$\alpha 2$	ΔN_{ax}	ΔN_1	ΔN_2	$\Delta\alpha 1$	$\Delta\alpha 2$
B3LYP-D3BJ	2.126	2.081	2.082	160.6	160.7	−0.017	0.014	0.003	−0.8	−0.7
CAM-B3LYP-D3BJ	2.117	2.071	2.072	160.3	160.3	−0.026	0.004	−0.007	−1.1	−1.1
M05-2X	2.132	2.078	2.079	159.9	159.9	−0.011	0.011	0.000	−1.5	−1.5
M06-L	2.140	2.078	2.079	159.7	159.6	−0.003	0.011	0.000	−1.7	−1.8
mPW1PW91	2.145	2.076	2.080	157.7	158.6	0.002	0.009	0.001	−3.7	−2.8
PBE0-D3BJ	2.114	2.071	2.072	160.5	160.6	−0.029	0.004	−0.007	−0.9	−0.8
PBE-D3BJ	2.110	2.084	2.084	159.9	160.0	−0.033	0.017	0.005	−1.5	−1.4
wB97XD	2.121	2.072	2.073	160.1	160.0	−0.022	0.005	−0.006	−1.3	−1.4
Experimental[235]	2.143	2.067	2.079	161.4						

Table 5.10: Comparison of bond length and angles calculated with different functionals using the 6-31G*/LANL2DZ basis set and the SMD solvation model.

Functional	N_{ax}–Zn	N_1–Zn	N_2–Zn	$\alpha 1$	$\alpha 2$	ΔN_{ax}	ΔN_1	ΔN_2	$\Delta\alpha 1$	$\Delta\alpha 2$
M05-2X	2.212	2.087	2.088	163.4	163.4	0.069	0.020	0.009	2.0	2.0
M06-L	2.237	2.096	2.096	162.3	162.1	0.094	0.029	0.017	0.9	0.7
mPW1PW91	2.257	2.097	2.097	159.5	160.3	0.114	0.030	0.018	−1.9	−1.1
PBE-D3BJ	2.228	2.107	2.108	162.2	162.5	0.085	0.040	0.029	0.8	1.1
ω**B97XD**	2.226	2.086	2.086	164.1	164.1	0.083	0.019	0.007	2.7	2.7
Experimental[235]	2.143	2.067	2.079	161.4						

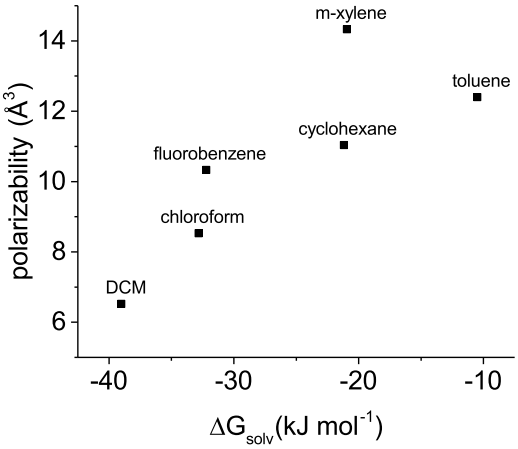

(a) Calculated solvation energy against polarisability.

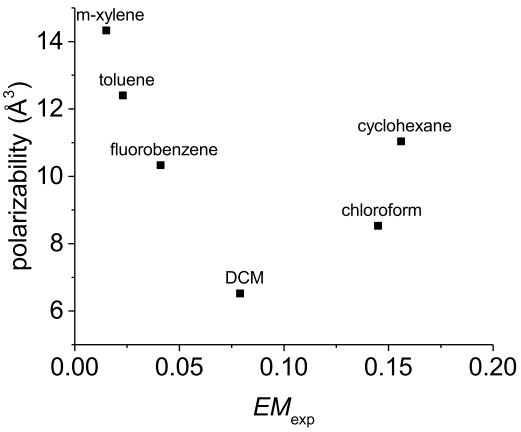

(b) Calculated solvation energy against polarisability.

Figure 5.13: Comparison of solvent polarizability, calculated solvation energy, and experimental EM values. Solvent polarizability used from Reference [243].

References

1. J. Lehn, 'Supramolecular Chemistry—Scope and Perspectives Molecules, Supermolecules, and Molecular Devices (Nobel Lecture)', *Angew. Chemie Int. Ed. English*, 1988, **27**, 89–112.
2. D. J. Cram, 'Preorganization—From Solvents to Spherands', *Angew. Chemie Int. Ed. English*, 1986, **25**, 1039–1057.
3. J. W. Steed, J. L. Atwood and P. A. Gale, in *Supramol. Chem.* John Wiley & Sons, Ltd, Chichester, UK, 2012.
4. M. F. Perutz, 'Mechanisms of cooperativity and allosteric regulation in proteins', *Q. Rev. Biophys.*, 1989, **22**, 139–237.
5. S. Shinkai, M. Ikeda, A. Sugasaki and M. Takeuchi, 'Positive allosteric systems designed on dynamic supramolecular scaffolds: Toward switching and amplification of guest affinity and selectivity', *Acc. Chem. Res.*, 2001, **34**, 494–503.
6. A. Mulder, J. Huskens and D. N. Reinhoudt, 'Multivalency in supramolecular chemistry and nanofabrication', *Org. Biomol. Chem.*, 2004, **2**, 3409.
7. C. A. Hunter and H. L. Anderson, 'What is Cooperativity?', *Angew. Chem. Int. Ed.*, 2009, **48**, 7488–7499.
8. B. Nagel, H. Dellweg and L. M. Gierasch, 'Glossary for chemists of terms used in biotechnology (IUPAC Recommendations 1992)', *Pure Appl. Chem.*, 1992, **64**, 143–168.
9. J. M. Berg, J. L. Tymoczko and L. Stryer, *Stryer Biochemie*, W.H. Freeman, 2015.
10. G. A. Lawrance, *Introduction to Coordination Chemistry*, John Wiley & Sons, Ltd, Chichester, UK, 2009, pp. 1–290.
11. L. K. S. von Krbek, C. A. Schalley and P. Thordarson, 'Assessing cooperativity in supramolecular systems', *Chem. Soc. Rev.*, 2017, **46**, 2622–2637.
12. A. Whitty, *Cooperativity and biological complexity*, 2008.
13. J.-P. Changeux, 'Allostery and the Monod-Wyman-Changeux Model After 50 Years', *Annu. Rev. Biophys.*, 2012, **41**, 103–133.
14. D. E. Koshland, J. G. Nemethy and D. Filmer, 'Comparison of Experimental Binding Data and Theoretical Models in Proteins Containing Subunits', *Biochemistry*, 1966, **5**, 365–385.
15. M. J. Cloninger, B. Bilgiçer, L. Li, S. L. Mangold, S. T. Phillips and M. L. Wolfenden, in *Supramol. Chem.* John Wiley & Sons, Ltd, Chichester, UK, 2012.
16. G. Ercolani and L. Schiaffino, 'Allosteric, Chelate, and Interannular Cooperativity: A Mise au Point', *Angew. Chem. Int. Ed. Engl.*, 2011, **50**, 1762–1768.
17. M. L. Caspers, 'Frontiers in supramolecular organic chemistry and photochemistry, Hans-Jorg Schneider and Heinz Durr, eds., VCH, New York, 1991, 485 pp.', *J. Polym. Sci. Part A Polym. Chem.*, 2003, **31**, 593–593.
18. P. Thordarson, 'Determining association constants from titration experiments in supramolecular chemistry.', *Chem. Soc. Rev.*, 2011, **40**, 1305–1323.
19. D. Brynn Hibbert and P. Thordarson, 'The death of the Job plot, transparency, open science and online tools, uncertainty estimation methods and other developments in supramolecular chemistry data analysis', *Chem. Commun.*, 2016, **52**, 12792–12805.

20. P. N. Taylor and H. L. Anderson, 'Cooperative self-assembly of double-strand conjugated porphyrin ladders', *J. Am. Chem. Soc.*, 1999, **121**, 11538–11545.

21. S. Leavitt and E. Freire, 'Direct measurement of protein binding energetics by isothermal titration calorimetry', *Curr. Opin. Struct. Biol.*, 2001, **11**, 560–566.

22. M. Rickert, M. J. Boulanger, N. Goriatcheva and K. C. Garcia, 'Compensatory energetic mechanisms mediating the assembly of signaling complexes between interleukin-2 and its α, β, and γcreceptors', *J. Mol. Biol.*, 2004, **339**, 1115–1128.

23. T. K. Dam, R. Roy, S. K. Das, S. Oscarson and C. F. Brewer, 'Binding of Multivalent Carbohydrates to Concanavalin A and Dioclea grandiflora Lectin', *J. Biol. Chem.*, 2000, **275**, 14223–14230.

24. A. Brown, 'Analysis of cooperativity by isothermal titration calorimetry', *Int. J. Mol. Sci.*, 2009, **10**, 3457–3477.

25. G. T. Morgan and H. D. K. Drew, 'Researches on residual affinity and co-ordination. Part II. Acetylacetones of selenium and tellurium', *J. Chem. Soc., Trans.*, 1920, **117**, 1456–1465.

26. T. Christensen, D. M. Gooden, J. E. Kung and E. J. Toone, 'Additivity and the Physical Basis of Multivalency Effects: A Thermodynamic Investigation of the Calcium EDTA Interaction', *J. Am. Chem. Soc.*, 2003, **125**, 7357–7366.

27. S. Monfette and D. E. Fogg, 'Equilibrium Ring-Closing Metathesis', *Chem. Rev.*, 2009, **109**, 3783–3816.

28. G. Illuminati and L. Mandolini, 'Ring closure reactions of bifunctional chain molecules', *Acc. Chem. Res.*, 1981, **14**, 95–102.

29. L. Mandolini, 'Intramolecular Reactions of Chain Molecules', *Adv. Phys. Org. Chem.*, 1986, **22**, 1–111.

30. P. Motloch and C. Hunter, in *Adv. Phys. Org. Chem.* 2016, vol. 50, pp. 77–118.

31. A. J. Kirby, in *Adv. Phys. Org. Chem.* Academic Press, 1980, vol. 17, pp. 183–278.

32. A. S. Mahadevi and G. N. Sastry, 'Cooperativity in Noncovalent Interactions', *Chem. Rev.*, 2016, **116**, 2775–2825.

33. M. I. Page and W. P. Jencks, 'Entropic Contributions to Rate Accelerations in Enzymic and Intramolecular Reactions and the Chelate Effect', *Proc. Natl. Acad. Sci.*, 1971, **68**, 1678–1683.

34. A. D. Hamilton, E. Fan, S. V. Arman, S. J. Geib and J. Yang, *The Chemistry of Biological Molecular Recognition*, tech. rep. 1674, 1993, pp. 57–66.

35. H. L. Anderson, 'Conjugated Porphyrin Ladders', *Inorg. Chem.*, 1994, **33**, 972–981.

36. G. D. Van Duyne, R. F. Standaert, P. A. Karplus, S. L. Schreiber and J. Clardy, 'Atomic structure of FKBP-FK506, an immunophilin-immunosuppressant complex.', *Science*, 1991, **252**, 839–42.

37. S. Claude, J.-M. Lehn, F. Schmidt and J.-P. Vigneron, 'Binding of nucleosides, nucleotides and anionic planar substrates by bis-intercaland receptor molecules', *J. Chem. Soc. Chem. Commun.*, 1991, 1182.

38. C. Montoro-García, J. Camacho-García, A. M. Lõpez-Pérez, N. Bilbao, S. Romero-Pérez, M. J. Mayoral and D. González-Rodríguez, 'High-fidelity noncovalent synthesis of hydrogen-bonded macrocyclic assemblies', *Angew. Chem. - Int. Ed.*, 2015, **54**, 6780–6784.

39. H. J. Hogben, J. K. Sprafke, M. Hoffmann, M. Pawlicki and H. L. Anderson, 'Stepwise effective molarities in porphyrin oligomer complexes: Preorganization results in exceptionally strong chelate cooperativity', *J. Am. Chem. Soc.*, 2011, **133**, 20962–20969.

40. M. Hoffmann, J. Kärnbratt, M.-H. Chang, L. M. Herz, B. Albinsson and H. L. Anderson, 'Enhanced πConjugation around a Porphyrin[6] Nanoring', *Angew. Chem. Int. Ed.*, 2008, **47**, 4993–4996.

41. C. Montoro-García, J. Camacho-García, A. M. López-Pérez, M. J. Mayoral, N. Bilbao and D. González-Rodríguez, 'Role of the Symmetry of Multipoint Hydrogen Bonding on Chelate Cooperativity in Supramolecular Macrocyclization Processes', *Angew. Chem. Int. Ed.*, 2016, **55**, 223–227.

42. P. Liu, P. Neuhaus, D. V. Kondratuk, T. S. Balaban and H. L. Anderson, 'Cyclodextrin-Templated Porphyrin Nanorings', *Angew. Chem.*, 2014, **126**, 7904–7907.

43. P. Parkinson, C. E. I. Knappke, N. Kamonsutthipaijit, K. Sirithip, J. D. Matichak, H. L. Anderson and L. M. Herz, 'Ultrafast energy transfer in biomimetic multistrand nanorings', *J. Am. Chem. Soc.*, 2014, **136**, 8217–8220.

44. J. Cremers, S. Richert, D. V. Kondratuk, T. D. W. Claridge, C. R. Timmel and H. L. Anderson, 'Nanorings with copper and zinc centers: forcing copper porphyrins to bind axial ligands in heterometallated oligomers', *Chem. Sci.*, 2016, **7**, 6961–6968.

45. K. M. Kadish, K. M. Smith and R. Guilard, *The porphyrin handbook*, Academic Press, 2000.

46. P. Hambright, 'Aspects of metal incorporation into porphyrin molecules', *Ann. N. Y. Acad. Sci.*, 1973, **206**, 443–452.

47. I. Beletskaya, V. S. Tyurin, A. Y. Tsivadze, R. Guilard and C. Stern, 'Supramolecular chemistry of metalloporphyrins', *Chem. Rev.*, 2009, **109**, 1659–1713.

48. S. K. Samanta, D. Samanta, J. W. Bats and M. Schmittel, 'DABCO as a Dynamic Hinge between Cofacial Porphyrin Panels and Its Tumbling inside a Supramolecular Cavity', *J. Org. Chem.*, 2011, **76**, 7466–7473.

49. L. Favereau, A. Cnossen, J. B. Kelber, J. Q. Gong, R. M. Oetterli, J. Cremers, L. M. Herz and H. L. Anderson, 'Six-Coordinate Zinc Porphyrins for Template-Directed Synthesis of Spiro-Fused Nanorings', *J. Am. Chem. Soc.*, 2015, **137**, 14256–14259.

50. S. Mehdi, D. Brisbin and W. McBryde, 'The stability of porphyrin and metalloporphyrin molecular complexes in solution', *Biochim. Biophys. Acta - Gen. Subj.*, 1976, **444**, 407–415.

51. S. J. Cole, G. C. Curthoys, E. A. Magnusson and J. N. Phillips, 'Ligand Binding by Metalloporphyrins. 111. Thermodynamic Functions for the Addition of Substituted Pyridines to Nickel(II) and Zinc(II) Porphyrins', *Inorg. Chem.*, 1972, **11**, 1024–1028.

52. J. R. Miller and G. D. Dorough, 'Pyridinate Complexes of Some Metallo-derivatives of Tetraphenylporphine and Tetraphenylchlorin 1', *J. Am. Chem. Soc.*, 1952, **74**, 3977–3981.

53. J. E. Falk, J. N. Phillips and E. A. Magnusson, 'Metal-ligand bonding in iron-porphyrins and oxyhaemoglobin', *Nature*, 1966, **212**, 1531–1533.

54. C. H. Kirksey, P. Hambright and C. B. Storm, 'Stability constants and proton magnetic resonance studies of zinc .alpha.,.beta.,.gamma.,.delta.-tetraphenylporphin and substituted pyridines', *Inorg. Chem.*, 1969, **8**, 2141–2144.

55. M. Sakuragi, K. Ichimura and H. Sakuragi, 'Photosensitized Oxygenation of olefins with Zn tetraphenyl porphine complex', *Bull. Chem. Soc. Jpn.*, 1992, **65**, 1944–1949.

56. H. Imai, S. Nakagawa and E. Kyuno, 'Recognition of Axial Ligands by a Zinc Porphyrin Host on the Basis of Nonpolar Interligand Interaction', *J. Am. Chem. Soc.*, 1992, **114**, 6719–6723.

57. P. Bhyrappa, V. Krishnan and M. Nethaji, 'Solvation and axial ligation properties of (2,3,7,8,12,13,17,18-octabromo-5,10,15,20-tetraphenylporphyrinato)zinc(II)', *J. Chem. Soc. Dalt. Trans.*, 1993, **0**, 1901–1906.

58. G. Ercolani, 'Thermodynamics of metal-mediated assemblies of porphyrins', *Struct. Bond.*, 2006, **121**, 167–215.

59. N. Kamonsutthipaijit, 'Self-Assembly and Template-Directed Synthesis in Multi-Strand Porphyrin Arrays', Ph.D. Thesis, University of Oxford, 2016.

60. D. P. Arnold, A. W. Johnson and M. Mahendran, 'Some reactions of meso-formyloctaethylporhyrin', *J. Chem. Soc. Perkin Trans. 1*, 1978, **543**, 366.

61. D. P. Arnold and L. J. Nitschinsk, 'Porphyrin Dimers Linked by Conjugated Butadiynes', *Tetrahedron*, 1992, **48**, 8781–8792.

62. D. P. Arnold and D. A. James, 'Dimers and Model Monomers of Nickel(II) Octaethylporphyrin Substituted by Conjugated Groups Comprising Combinations of Triple Bonds with Double Bonds and Arenes. 1. Synthesis and Electronic Spectra', *J. Org. Chem.*, 1997, **62**, 3460–3469.

63. D. P. Arnold, D. A. James, C. H. L. Kennard and G. Smith, 'Dimeric porphyrins linked by conjugated groups containing triple bonds: the crystal structure of the nickel octaethylporphyrin dimer bridged by 2,5-diethynylthiophene', *J. Chem. Soc. Chem. Commun.*, 1994, 2131.

64. H. Lee, K.-I. Hong and W.-D. Jang, 'Design and applications of molecular probes containing porphyrin derivatives', *Coord. Chem. Rev.*, 2018, **354**, 46–73.

65. D. P. Arnold, 'Two Rings Are Better Than One: Adventures in Porphyrin Chemistry', *Synlett*, 2000, **2000**, 296–305.

66. P. Neuhaus, A. Cnossen, J. Q. Gong, L. M. Herz and H. L. Anderson, 'A Molecular Nanotube with Three-Dimensional π-Conjugation', *Angew. Chem. - Int. Ed.*, 2015, **54**, 7344–7348.

67. M. C. O. Sullivan, 'Template Directed Synthesis of Porphyrin Nanorings', Ph.D. Thesis, University of Oxford, 2011.

68. P. Liu, 'New templates for porphyrin nanorings', DPhil thesis, University of Oxford, 2015.

69. W. John, R. Peveler and C. Church, 'Porphyrin Nanorings', 2011.

70. M. Peeks, 'Electronic delocalisation in linear and cyclic porphyrin oligomers', Ph.D. Thesis, 2016.

71. M. D. Peeks, T. D. W. Claridge and H. L. Anderson, 'Aromatic and antiaromatic ring currents in a molecular nanoring', *Nature*, 2017, **541**, 200–203.

72. R. van Grondelle, J. P. Dekker, T. Gillbro and V. Sundstrom, 'Energy transfer and trapping in photosynthesis', *Biochim. Biophys. Acta - Bioenerg.*, 1994, **1187**, 1–65.

73. G. McDermott, S. M. Prince, A. A. Freer, A. M. Hawthornthwaite-Lawless, M. Z. Papiz, R. J. Cogdell and N. W. Isaacs, 'Crystal structure of an integral membrane light-harvesting complex from photosynthetic bacteria', *Nature*, 1995, **374**, 517–521.

74. M. U. Winters, E. Dahlstedt, H. E. Blades, J. Craig, M. J. Frampton, H. L. Anderson, B. Albinsson and C. J. Wilson, 'Probing the Efficiency of Electron Transfer through Porphyrin-Based Molecular Wires Probing the Efficiency of Electron Transfer through Porphyrin-Based Molecular Wires', *J. Am. Chem. Soc.*, 2007, 4291–4297.

75. M. D. Peeks, P. Neuhaus and H. L. Anderson, 'Experimental and computational evaluation of the barrier to torsional rotation in a butadiyne-linked porphyrin dimer', *Phys. Chem. Chem. Phys.*, 2016, **18**, 5264–5274.

76. J. K. Sprafke, D. V. Kondratuk, M. Wykes, A. L. Thompson, M. Hoffmann, R. Drevinskas, W. H. Chen, C. K. Yong, J. Kärnbratt, J. E. Bullock, M. Malfois, M. R. Wasielewski, B. Albinsson, L. M. Herz, D. Zigmantas, D. Beljonne and H. L. Anderson, 'Belt-shaped π-systems: Relating geometry to electronic structure in a six-porphyrin nanoring', *J. Am. Chem. Soc.*, 2011, **133**, 17262–17273.

77. F. C. Grozema, C. Houarner-Rassin, P. Prins, L. D. a. Siebbeles and H. L. Anderson, 'Supramolecular control of charge transport in molecular wires', *J. Am. Chem. Soc.*, 2007, **129**, 13370–13371.

78. J. B. Wittenberg and L. Isaacs, in *Supramol. Chem.* John Wiley & Sons, Ltd, Chichester, UK, 2012.

79. D. Cram, 'The Design of Molecular Hosts, Guests, and Their Complexes (Nobel Lecture)', *Angew. Chem. Int. Ed.*, 1988, **27**, 1009–1112.

80. D. J. Cram and J. M. Cram, *Container Molecules and Their Guests*, Royal Society of Chemistry, Cambridge, 1994.

81. D. K. Cabbiness and D. W. Margerum, *Macrocyclic Effect on the Stability of Copper(II) Tetramine Complexes*, 1969.

82. G. W. Gokel, D. M. Goli, C. Minganti and L. Echegoyen, 'Clarification of the Hole-Size Cation-Diameter Relationship in Crown Ethers and a New Method for Determining Calcium Cation Homogeneous Equilibrium Binding Constants', *J. Am. Chem. Soc.*, 1983, **105**, 6786–6788.

83. C. J. Pedersen, 'The Discovery of Crown Ethers (Noble Lecture)', *Angew. Chemie Int. Ed. English*, 1988, **27**, 1021–1027.

84. V. Balzani, M. Clemente-León, A. Credi, J. N. Lowe, J. D. Badjić, J. F. Stoddart and D. J. Williams, 'Controlling Multivalent Interactions in Triply-Threaded Two-Component Superbundles', *Chem. - A Eur. J.*, 2003, **9**, 5348–5360.

85. J. D. Badjić, A. Nelson, S. J. Cantrill, W. B. Turnbull and J. F. Stoddart, 'Multivalency and Cooperativity in Supramolecular Chemistry', *Acc. Chem. Res.*, 2005, **38**, 723–732.

86. W. Jiang, K. Nowosinski, N. L. Löw, E. V. Dzyuba, F. Klautzsch, A. Schäfer, J. Huuskonen, K. Rissanen and C. A. Schalley, 'Chelate Cooperativity and Spacer Length Effects on the Assembly Thermodynamics and Kinetics of Divalent Pseudorotaxanes', *J. Am. Chem. Soc.*, 2012, **134**, 1860–1868.

87. J. W. Lee, S. Samal, N. Selvapalam, H. J. Kim and K. Kim, 'Cucurbituril homologues and derivatives: New opportunities in supramolecular chemistry', *Acc. Chem. Res.*, 2003, **36**, 621–630.

88. S. Liu, C. Ruspic, P. Mukhopadhyay, S. Chakrabarti, P. Y. Zavalij and L. Isaacs, 'The cucurbit[n]uril family: Prime components for self-sorting systems', *J. Am. Chem. Soc.*, 2005, **127**, 15959–15967.

89. C. Márquez, R. R. Hudgins and W. M. Nau, 'Mechanism of Host-Guest Complexation by Cucurbituril', *J. Am. Chem. Soc.*, 2004, **126**, 5806–5816.

90. L. K. von Krbek, A. J. Achazi, S. Schoder, M. Gaedke, T. Biberger, B. Paulus and C. A. Schalley, 'The Delicate Balance of Preorganisation and Adaptability in Multiply Bonded Host–Guest Complexes', *Chem. - A Eur. J.*, 2017, **23**, 2877–2883.

91. H. Adams, E. Chekmeneva, C. A. Hunter, M. C. Misuraca, C. Navarro and S. M. Turega, 'Quantification of the effect of conformational restriction on supramolecular effective molarities.', *J. Am. Chem. Soc.*, 2013, **135**, 1853–63.

92. M. C. Misuraca, T. Grecu, Z. Freixa, V. Garavini, C. A. Hunter, P. W. N. M. van Leeuwen, M. D. Segarra-Maset and S. M. Turega, 'Relationship Between Conformational Flexibility and Chelate Cooperativity', *J. Org. Chem.*, 2011, **76**, 2723–2732.

93. K. Goto, in *Compr. Supramol. Chem. II*, Elsevier, Second Edi, 2017, vol. XXIV, pp. 61–71.

94. S. Mecozzi and J. Rebek, Jr., 'The 55 % Solution: A Formula for Molecular Recognition in the Liquid State', *Chem. - A Eur. J.*, 1998, **4**, 1016–1022.

95. H. Sun, C. A. Hunter, C. Navarro and S. Turega, 'Relationship between chemical structure and supramolecular effective molarity for formation of intramolecular H-bonds', *J. Am. Chem. Soc.*, 2013, **135**, 13129–13141.

96. C. A. Hunter, M. C. Misuraca and S. M. Turega, 'Solvent effects on chelate cooperativity', *Chem. Sci.*, 2012, **3**, 589–601.

97. S.-J. J. Su, D. Tanaka, Y.-J. J. Li, H. Sasabe, T. Takeda and J. Kido, 'Novel four-pyridylbenzene-armed biphenyls as electron-transport materials for phosphorescent OLEDs', *Org. Lett.*, 2008, **10**, 941–944.

98. A. Suzuki, 'Cross-Coupling Reactions Of Organoboranes: An Easy Way To Construct C-C Bonds (Nobel Lecture)', *Angew. Chem. Int. Ed.*, 2011, **50**, 6722–6737.

99. J. Cremers, S. Richert, D. V. Kondratuk, T. D. W. Claridge, C. R. Timmel and H. L. Anderson, 'Nanorings with copper and zinc centers: forcing copper porphyrins to bind axial ligands in heterometallated oligomers', *Chem. Sci.*, 2016, **7**, 6961–6968.

100. M. Zoellner, J. Wutke and M. Bukhardt, *Phosphorescent OLED and hole transporting materials for phosphorescent OLEDs*. 2014.

101. M. Schmittel, B. He and P. Mal, 'Supramolecular Multi-Component Self-Assembly of Shape Adaptive Nanoprisms : Wrapping up C 60 with Three Porphyrin Units Supporting Information', 2008, **2**, 5814–5816.

102. K. L. Billingsley, T. E. Barder and S. L. Buchwald, 'Palladium-catalyzed borylation of aryl chlorides: Scope, applications, and computational studies', *Angew. Chem. Int. Ed.*, 2007, **46**, 5359–5363.

103. M. Jäger, L. Eriksson, J. Bergquist and O. Johansson, 'Synthesis and Characterization of 2,6-Di(quinolin-8-yl)pyridines. New Ligands for Bistridentate Ru II Complexes with Microsecond Luminescent Lifetimes', *J. Org. Chem.*, 2007, **72**, 10227–10230.

104. A. F. Littke and G. C. Fu, 'Palladium-catalyzed coupling reactions of aryl chlorides.', *Angew. Chem. Int. Ed. Engl.*, 2002, **41**, 4176–4211.

105. S.-b. Yu, X.-p. Hu, J. Deng, J.-d. Huang, D.-y. Wang, Z.-C. Duan and Z. Zheng, 'Ferrocence-based phosphine–triazine ligands for highly efficient Suzuki–Miyaura cross-coupling reaction of aryl chlorides', *Tetrahedron Lett.*, 2008, **49**, 1253–1256.

106. C. E. Tait, P. Neuhaus, M. D. Peeks, H. L. Anderson and C. R. Timmel, 'Transient EPR Reveals Triplet State Delocalization in a Series of Cyclic and Linear π-Conjugated Porphyrin Oligomers', *J. Am. Chem. Soc.*, 2015, **137**, 8284–8293.

107. M. Schulze, V. Kunz, P. D. Frischmann and F. Würthner, 'A supramolecular ruthenium macrocycle with high catalytic activity for water oxidation that mechanistically mimics photosystem II', *Nat. Chem.*, 2016, **8**, 576–583.

108. F. Porter, 'Templates For Nanoring Catenanes, PartII thesis', Part II thesis, University of Oxford, 2015.

109. P. Scheiner, E. Stockel, D. Cruset and R. Noto, 'Ditetrazolylbenzene dianions. Potential precursors of the phenylenedimethylenes', *J. Org. Chem.*, 1972, **37**, 4207–4209.

110. B. J. Littler, M. A. Miller, C. H. Hung, R. W. Wagner, D. F. O'Shea, P. D. Boyle and J. S. Lindsey, 'Refined synthesis of 5-substituted dipyrromethanes', *J. Org. Chem.*, 1999, **64**, 1391–1396.

111. M. J. Plater, S. Aiken and G. Bourhill, 'A new synthetic route to donor-acceptor porphyrins', *Tetrahedron*, 2002, **58**, 2405–2413.

112. C. A. Hunter, 'Quantifying intermolecular interactions: Guidelines for the molecular recognition toolbox', *Angew. Chem. - Int. Ed.*, 2004, **43**, 5310–5324.

113. C. E. Housecroft and A. G. Sharpe, *Inorganic chemistry*, Pearson, 2012, p. 1213.

114. F. Eblinger and H.-J. J. Schneider, 'Stabilities of hydrogen-bonded supramolecular complexes with various numbers of single bonds: Attempts to quantify a dogma in host-guest chemistry', *Angew. Chem. - Int. Ed.*, 1998, **37**, 826–829.

115. M. Mammen, E. I. Shakhnovich, G. M. Whitesides and G. Ercolani, 'Using a Convenient, Quantitative Model for Torsional Entropy To Establish Qualitative Trends for Molecular Processes That Restrict Conformational Freedom', *J. Org. Chem.*, 1999, **63**, 3350–3353.

116. S. Liu, D. V. Kondratuk, S. a. L. Rousseaux, G. Gil-Ramírez, M. C. O'Sullivan, J. Cremers, T. D. W. Claridge and H. L. Anderson, 'Caterpillar Track Complexes in Template-Directed Synthesis and Correlated Molecular Motion', *Angew. Chem. Int. Ed.*, 2015, **54**, 5355–5359.

117. S. W. Benson, 'Statistical Factors in the Correlation of Rate Constants and Equilibrium Constants', *J. Am. Chem. Soc.*, 1958, **125**, 5151–5154.

118. M. K. Gilson and K. K. Irikura, 'Symmetry Numbers for Rigid, Flexible, and Fluxional Molecules: Theory and Applications †', *J. Phys. Chem. B*, 2010, **114**, 16304–16317.

119. D. M. Bishop and K. J. Laidler, 'Symmetry Numbers and Statistical Factors in Rate Theory', *J. Chem. Phys.*, 1965, **42**, 1688–1691.

120. A. B. C. Deutman, C. Monnereau, J. A. A. W. Elemans, G. Ercolani, R. J. M. Nolte and A. E. Rowan, 'Mechanism of Threading a Polymer Through a Macrocyclic Ring', *Science (80-.).*, 2008, **322**, 1668–1671.

121. W. F. Bailey and A. S. Monahan, 'Statistical effects and the evaluation of entropy differences in equilibrium processes. Symmetry corrections and entropy of mixing', *J. Chem. Educ.*, 1978, **55**, 489.

122. D. F. DeTar, 'Theoretical ab Initio Calculation of Entropy, Heat Capacity, and Heat Content', *J. Phys. Chem. A*, 1998, **102**, 5128–5141.

123. R. Zellner, 'S.W. Benson: Thermochemical Kinetics, 2nd Ed. John Wiley', *Berichte der Bunsen-gesellschaft für Phys. Chemie*, 1977, **81**, 877–878.

124. G. Ercolani, C. Piguet, M. Borkovec and J. Hamacek, 'Symmetry Numbers and Statistical Factors in Self-Assembly and Multivalency', *J. Phys. Chem. B*, 2007, **111**, 12195–12203.

125. H. Motulsky and A. Christopoulos, *Fitting Models to Biological Data Using Linear and Nonlinear Regression: A Practical Guide to Curve Fitting*, Oxford University Press, 2004.

126. H. Motulsky and A. Christopoulos, 'Fitting models to biological data using linear and nonlinear regression', *Pharm. Stat.*, 2005, **4**.

127. J. Tellinghuisen, 'Statistical Error Propagation', *J. Phys. Chem. A*, 2001, **105**, 3917–3921.

128. T. C. Bruice and U. K. Pandit, 'The Effect of Geminal Substitution Ring Size and Rotamer Distribution on the Intramolecular Nucleophilic Catalysis of the Hydrolysis of Monophenyl Esters of Dibasic Acids and the Solvolysis of the Intermediate Anhydrides', *J. Am. Chem. Soc.*, 1960, **82**, 5858–5865.

129. T. C. Bruice and F. C. Lightstone, 'Ground state and transition state contributions to the rate of intramolecular and enzymic reactions', *Acc. Chem. Res.*, 1999, **32**, 127–136.

130. J. Rao, J. Lahiri, R. M. Weis and G. M. Whitesides, 'Design, Synthesis, and Characterization of a High-Affinity Trivalent System Derived from Vancomycin', *J. Am. Chem. Soc.*, 2000, **122**, 2698–2710.

131. A. E. Martell, R. D. Hancock and R. J. Motekaitis, 'Factors affecting stabilities of chelate, macrocyclic and macrobicyclic complexes in solution', *Coord. Chem. Rev.*, 1994, **133**, 39–65.

132. H. Sun, C. A. Hunter and E. M. Llamas, 'The flexibility–complementarity dichotomy in receptor–ligand interactions', *Chem. Sci.*, 2015, **6**, 1444–1453.

133. T. L. Hill and D. Publications, *An Introduction to Statistical Thermodynamics*, Dover Publications, 1986, p. 508.

134. S. Fowler, R. Roush, J. Wise and OpenStax College, 'Concepts of Biology', *Am. Biol. Teach.*, 1996, **58**, 186–186.

135. H.-X. Zhou and M. K. Gilson, 'Theory of Free Energy and Entropy in Noncovalent Binding', *Chem. Rev.*, 2009, **109**, 4092–4107.

136. B. Tidor and M. Karplus, 'The Contribution of Vibrational Entropy to Molecular Association: The Dimerization of Insulin', *J. Mol. Biol.*, 1994, **238**, 405–414.

137. S. Di Stefano and L. Mandolini, 'The canonical behavior of the entropic component of thermodynamic effective molarity. An attempt at unifying covalent and noncovalent cyclizations', *Phys. Chem. Chem. Phys.*, 2019, **21**, 955–987.

138. B. S. Hudson, 'Inelastic Neutron Scattering: A Tool in Molecular Vibrational Spectroscopy and a Test of ab Initio Methods', *J. Phys. Chem. A*, 2001, **105**, 3949–3960.

139. E. Balog, T. Becker, M. Oettl, R. Lechner, R. Daniel, J. Finney and J. C. Smith, 'Direct determination of vibrational density of states change on ligand binding to a protein', *Phys. Rev. Lett.*, 2004, **93**, 028103–1.

140. L. Zidek, M. V. Novotny and M. J. Stone, 'Increased protein backbone conformational entropy upon hydrophobic ligand binding', *Nat. Struct. Biol.*, 1999, **6**, 1118–1121.

141. A. L. Lee, S. A. Kinnear and A. J. Wand, 'Redistribution and loss of side chain entropy upon formation of a calmodulin-peptide complex', *Nat. Struct. Biol.*, 2000, **7**, 72–77.

142. S. Arumugam, G. Gao, B. L. Patton, V. Semenchenko, K. Brew and S. R. Van Doren, 'Increased backbone mobility in β-barrel enhances entropy gain driving binding of N-TIMP-1 to MMP-3', *J. Mol. Biol.*, 2003, **327**, 719–734.

143. T. Wiesman, S. Williston and J. F. Brandts, 'Rapid Measurement of Binding Constants and Heats of Binding using ITC', *Anal. Biochem.*, 1989, **179**, 131–137.

144. C. A. Schalley, *Analytical Methods in Supramolecular Chemistry*, ed. C. Schalley, Wiley-VCH Verlag GmbH & Co. KGaA, Weinheim, Germany, 2006, pp. 55–78.

145. A. Arnaud and L. Bouteiller, 'Isothermal Titration Calorimetry of Supramolecular Polymers', *Langmuir*, 2004, **20**, 6858–6863.

146. I. Herrera and M. a. Winnik, 'Differential binding models for isothermal titration calorimetry: Moving beyond the Wiseman isotherm', *J. Phys. Chem. B*, 2013, **117**, 8659–8672.

147. T. Liu, Y. Lin, X. Wen, R. N. Jorissen and M. K. Gilson, 'BindingDB: A web-accessible database of experimentally determined protein-ligand binding affinities', *Nucleic Acids Res.*, 2007, **35**, D198–D201.

148. J. Tellinghuisen, 'Van't Hoff analysis of K°(T): How good. . . or bad?', *Biophys. Chem.*, 2006, **120**, 114–120.

149. M. Origin, 'Microcal software', *Inc., Northampton, USA*, 1991.

150. E. Muñoz and A. Piñeiro, 'AFFINImeter Software: from its Beginnings to Future Trends- A Literature review', *J. Appl. Bioanal.*, 2018, **4**, 124–139.

151. Y. Vignollet, J. C. Maire and M. Witanowski, 'Interaction between a phenyl ring and silicon atom. the nitrogen-14 nuclear magnetic resonance of nitrophenyltrimethylsilanes', *Chem. Commun.*, 1968, 1187.

152. P. S. Bols and H. L. Anderson, 'Shadow Mask Templates for Site-Selective Metal Exchange in Magnesium Porphyrin Nanorings', *Angew. Chem. Int. Ed.*, 2018, **57**, 7874–7877.

153. J. D. Chodera and D. L. Mobley, 'Entropy-Enthalpy Compensation: Role and Ramifications in Biomolecular Ligand Recognition and Design', *Annu. Rev. Biophys.*, 2013, **42**, 121–142.

154. A. Jeppesen, 'Croconic acid derivatives for laser welding and anion recognition', Ph.D. Thesis, 2017.

155. C. J. Cramer, *Essentials of computational chemistry : theories and models*, Wiley, 2013, p. 624.

156. W. Koch and M. C. Holthausen, *A chemist's guide to density functional theory*, Wiley-VCH, 2001, vol. 2, p. 313.

157. F. Jensen, *Introduction to Computational Chemistry*, John Wiley & Sons, 2014, p. 620.

158. A. Szabo and N. Ostlund, *Modern quantum chemistry : introduction to advanced electronic structure theory*, Dover Publications, 2018, p. 466.

159. A. K. Rappe and C. J. Casewit, *Molecualr Mechanics across Chemistry*, University Science Books, 1997, p. 444.

160. L. Pauling, *The nature of the chemical bond and the structure of molecules and crystals : an introduction to modern structural chemistry*, Cornell University Press, New York, 1960, p. 644.

161. K. S. Pitzer, 'The Nature of the Chemical Bond and the Structure of Molecules and Crystals: An Introduction to Modern Structural Chemistry.', *J. Am. Chem. Soc.*, 1960, **82**, 4121–4121.

162. M. Huš and T. Urbic, 'Strength of hydrogen bonds of water depends on local environment', *J. Chem. Phys.*, 2012, **136**, 144305.

163. L. J. Prins, D. N. Reinhoudt and P. Timmerman, *Noncovalent synthesis using hydrogen bonding*, 2001.

164. T. Clark, 'Quo Vadis semiempirical MO-theory?', *J. Mol. Struct. THEOCHEM*, 2000, **530**, 1–10.

165. J. J. P. Stewart, 'Optimization of parameters for semiempirical methods VI: more modifications to the NDDO approximations and re-optimization of parameters', *J. Mol. Model.*, 2013, **19**, 1–32.

166. G. B. Rocha, R. O. Freire, A. M. Simas and J. J. Stewart, 'RM1: A reparameterization of AM1 for H, C, N, O, P, S, F, Cl, Br, and I', *J. Comput. Chem.*, 2006, **27**, 1101–1111.

167. J. Hostaš, J. Řezáč and P. Hobza, 'On the performance of the semiempirical quantum mechanical PM6 and PM7 methods for noncovalent interactions', *Chem. Phys. Lett.*, 2013, **568-569**, 161–166.

168. J. J. Stewart, 'Application of localized molecular orbitals to the solution of semiempirical self-consistent field equations', *Int. J. Quantum Chem.*, 1996, **58**, 133–146.

169. J. J. P. Stewart, *MOPAC2016*, 2016.

170. E. Schrödinger, 'Quantisierung als Eigenwertproblem', *Ann. Phys.*, 1926, **386**, 109–139.

171. E. Schrödinger, 'Quantisierung als Eigenwertproblem', *Ann. Phys.*, 1926, **384**, 489–527.

172. E. Schrödinger, 'Quantisierung als Eigenwertproblem', *Ann. Phys.*, 1926, **384**, 361–376.

173. E. Schrödinger, 'Quantisierung als Eigenwertproblem', *Ann. Phys.*, 1926, **385**, 437–490.

174. M. Born and R. Oppenheimer, 'Zur Quantentheorie der Molekeln', *Ann. Phys.*, 1927, **389**, 457–484.

175. P. Hohenberg and W. Kohn, 'Inhomogeneous electron gas', *Phys. Rev.*, 1964, **136**, B864–B871.

176. W. Kohn and L. J. Sham, 'Self-Consistent Equations Including Exchange and Correlation Effects', *Phys. Rev.*, 1965, **140**, 1133–1138.

177. W. Kohn, A. D. Becke and R. G. Parr, 'Density functional theory of electronic structure', *J. Phys. Chem.*, 1996, **100**, 12974–12980.

178. T. A. Wesolowski, 'Development of Novel Computational Strategies to Match the Challenges of Supramolecular Chemistry, Biochemistry, and Materials Science', *Chim. Int. J. Chem.*, 2002, **56**, 707–711.

179. G. E. Scuseria, 'Linear Scaling Density Functional Calculations with Gaussian Orbitals', *J. Phys. Chem. A*, 1999, **103**, 4782–4790.

180. D. J. Cole and N. D. Hine, *Applications of large-scale density functional theory in biology*, 2016.

181. J. P. Perdew, A. Ruzsinszky, L. A. Constantin, J. Sun and G. I. Csonka, 'Some fundamental issues in ground-state density functional theory: A guide for the perplexed', *J. Chem. Theory Comput.*, 2009, **5**, 902–908.

182. N. Mardirossian and M. Head-Gordon, 'How accurate are the Minnesota density functionals for non-covalent interactions, isomerization energies, thermochemistry, and barrier heights involving molecules composed of main-group elements?', *J. Chem. Theory Comput.*, 2016, acs.jctc.6b00637.

183. N. Mardirossian and M. Head-Gordon, *Thirty years of density functional theory in computational chemistry: An overview and extensive assessment of 200 density functionals*, 2017.

184. Q. Peng, F. Duarte and R. S. Paton, 'Computing organic stereoselectivity-from concepts to quantitative calculations and predictions', *Chem. Soc. Rev.*, 2016, **45**, 6093–6107.

185. J. P. Perdew, J. Chem. Phys. 2003, vol. 577, pp. 1–20.

186. J. P. Perdew and Y. Wang, 'Accurate and simple analytic representation of the electron-gas correlation energy', *Phys. Rev. B*, 1992, **45**, 13244–13249.

187. S. H. Vosko, L. Wilk and M. Nusair, 'Accurate spin-dependent electron liquid correlation energies for local spin density calculations: a critical analysis', *Can. J. Phys.*, 2010, **58**, 1200–1211.

188. J. P. Perdew and A. Ruzsinszky, Int. J. Quantum Chem. John Wiley & Sons, Ltd, 2010, vol. 110, pp. 2801–2807.

189. J. P. Perdew, 'Density-functional approximation for the correlation energy of the inhomogeneous electron gas', *Phys. Rev. B*, 1986, **33**, 8822–8824.

190. A. D. Becke, 'Density-functional exchange-energy approximation with correct asymptotic behavior', *Phys. Rev. A*, 1988, **38**, 3098–3100.

191. J. P. Perdew, M. Ernzerhof and K. Burke, 'Rationale for mixing exact exchange with density functional approximations', *J. Chem. Phys.*, 1996, **105**, 9982–9985.

192. J. P. Perdew, 'Climbing the ladder of density functional approximations', *MRS Bull.*, 2013, **38**, 743–750.

193. J. P. Perdew, A. Ruzsinszky, G. I. Csonka, L. A. Constantin and J. Sun, 'Workhorse Semilocal Density Functional for Condensed Matter Physics and Quantum Chemistry', *Phys. Rev. Lett.*, 2009, **103**, 026403.

194. A. D. Becke, 'Density-functional thermochemistry. III. The role of exact exchange', *J. Chem. Phys.*, 1993, **98**, 5648–5652.

195. H. Kruse, L. Goerigk and S. Grimme, 'Why the standard B3LYP/6-31G* model chemistry should not be used in DFT calculations of molecular thermochemistry: Understanding and correcting the problem', *J. Org. Chem.*, 2012, **77**, 10824–10834.

196. J. P. Perdew, V. N. Staroverov, J. Tao and G. E. Scuseria, 'Density functional with full exact exchange, balanced nonlocality of correlation, and constraint satisfaction', *Phys. Rev. A - At. Mol. Opt. Phys.*, 2008, **78**, 052513.

197. J. Jaramillo, G. E. Scuseria and M. Ernzerhof, 'Local hybrid functionals', *J. Chem. Phys.*, 2003, **118**, 1068–1073.

198. D. C. Langreth and J. P. Perdew, 'The gradient approximation to the exchange-correlation energy functional: A generalization that works', *Solid State Commun.*, 1979, **31**, 567–571.

199. F. Furche, 'Molecular tests of the random phase approximation to the exchange-correlation energy functional', *Phys. Rev. B - Condens. Matter Mater. Phys.*, 2001, **64**, 195120.

200. J. Harl, L. Schimka and G. Kresse, 'Assessing the quality of the random phase approximation for lattice constants and atomization energies of solids', *Phys. Rev. B - Condens. Matter Mater. Phys.*, 2010, **81**, 115126.

201. R. Karaman, 'The effective molarity (EM) puzzle in intramolecular ring-closing reactions', *J. Mol. Struct. THEOCHEM*, 2010, **940**, 70–75.

202. R. Karaman, 'Proximity vs. strain in intramolecular ring-closing reactions', *Mol. Phys.*, 2010, **108**, 1723–1730.

203. R. Karaman, 'Effects of substitution on the effective molarity (EM) for five membered ring-closure reactions - A computational approach', *J. Mol. Struct. THEOCHEM*, 2010, **939**, 69–74.

204. A. J. Cohen, P. Mori-Sánchez and W. Yang, 'Challenges for density functional theory', *Chem. Rev.*, 2012, **112**, 289–320.

205. A. Sengupta, A. Seitz and K. M. Merz, *Simulating the Chelate Effect*, 2018.

206. S. Grimme, 'Do special noncovalent π-π stacking interactions really exist?', *Angew. Chem. - Int. Ed.*, 2008, **47**, 3430–3434.

207. M. P. Waller, H. Kruse, C. Mück-Lichtenfeld and S. Grimme, *Investigating inclusion complexes using quantum chemical methods*, 2012.

208. R. Sure and S. Grimme, 'Comprehensive Benchmark of Association (Free) Energies of Realistic Host-Guest Complexes', *J. Chem. Theory Comput.*, 2015, **11**, 3785–3801.

209. J. Antony, R. Sure and S. Grimme, 'Using dispersion-corrected density functional theory to understand supramolecular binding thermodynamics.', *Chem. Commun. (Camb).*, 2014, **51**, 1764–1774.

210. P. J. Hay and W. R. Wadt, 'Ab initio effective core potentials for molecular calculations. Potentials for K to Au including the outermost core orbitale', *J. Chem. Phys.*, 1985, **82**, 299–310.

211. C. Lee, W. Yang and R. G. Parr, 'Development of the Colle-Salvetti correlation-energy formula into a functional of the electron density', *Phys. Rev. B*, 1988, **37**, 785–789.

212. D. Margetić, R. N. Warrener, D. N. Butler and D. Officer, 'Computational study of supramolecular bis-porphyrin "molecular tweezers"', *Theor. Chem. Acc.*, 2007, **117**, 239–245.

213. S. Ehrlich, J. Moellmann and S. Grimme, 'Dispersion-corrected density functional theory for aromatic interactions in complex systems', *Acc. Chem. Res.*, 2013, **46**, 916–926.

214. S. de Visser and M. Stillman, 'Challenging Density Functional Theory Calculations with Hemes and Porphyrins', *Int. J. Mol. Sci.*, 2016, **17**, 519.

215. T. Yanai, D. P. Tew and N. C. Handy, 'A new hybrid exchange-correlation functional using the Coulomb-attenuating method (CAM-B3LYP)', *Chem. Phys. Lett.*, 2004, **393**, 51–57.

216. J. P. Perdew, K. Burke and M. Ernzerhof, 'Generalized gradient approximation made simple', *Phys. Rev. Lett.*, 1996, **77**, 3865–3868.

217. J. P. Perdew, K. Burke and M. Ernzerhof, 'Generalized Gradient Approximation Made Simple - The PBE functional', *Phys. Rev. Lett.*, 1996, **77**, 3865–3868.

218. C. Adamo and V. Barone, 'Toward reliable density functional methods without adjustable parameters: The PBE0 model', *J. Chem. Phys.*, 1999, **110**, 6158–6170.

219. M. Ernzerhof and G. E. Scuseria, 'Assessment of the Perdew-Burke-Ernzerhof exchange-correlation functional', *J. Chem. Phys.*, 1999, **110**, 5029–5036.

220. Y. Zhao, N. E. Schultz and D. G. Truhlar, 'Design of density functionals by combining the method of constraint satisfaction with parametrization for thermochemistry, thermochemical kinetics, and noncovalent interactions', *J. Chem. Theory Comput.*, 2006, **2**, 364–382.

221. Y. Zhao and D. G. Truhlar, 'The M06 suite of density functionals for main group thermochemistry, thermochemical kinetics, noncovalent interactions, excited states, and transition elements: Two new functionals and systematic testing of four M06-class functionals and 12 other function', *Theor. Chem. Acc.*, 2008, **120**, 215–241.

222. A. Sorkin, D. G. Truhlar and E. A. Amin, 'Energies, geometries, and charge distributions of ZN molecules, clusters, and biocenters from coupled cluster, density functional, and neglect of diatomic differential overlap models', *J. Chem. Theory Comput.*, 2009, **5**, 1254–1265.

223. E. A. Amin and D. G. Truhlar, 'Zn coordination chemistry: Development of benchmark suites for geometries, dipole moments, and bond dissociation energies and their use to test and validate density functionals and molecular orbital theory', *J. Chem. Theory Comput.*, 2008, **4**, 75–85.

224. M. Korth and S. Grimme, 'Mindless DFT benchmarking', *J. Chem. Theory Comput.*, 2009, **5**, 993–1003.

225. C. Adamo and V. Barone, 'Exchange functionals with improved long-range behavior and adiabatic connection methods without adjustable parameters: The mPW and mPW1PW models', *J. Chem. Phys.*, 1998, **108**, 664–675.

226. J. D. Chai and M. Head-Gordon, 'Long-range corrected hybrid density functionals with damped atom-atom dispersion corrections', *Phys. Chem. Chem. Phys.*, 2008, **10**, 6615–6620.

227. S. Grimme, 'Semiempirical GGA-type density functional constructed with a long-range dispersion correction', *J. Comput. Chem.*, 2006, **27**, 1787–1799.

228. K. S. Thanthiriwatte, E. G. Hohenstein, L. A. Burns and C. D. Sherrill, 'Assessment of the performance of DFT and DFT-D methods for describing distance dependence of hydrogen-bonded interactions', *J. Chem. Theory Comput.*, 2011, **7**, 88–96.

229. N. Ramos-Berdullas, I. Pérez-Juste, C. Van Alsenoy and M. Mandado, 'Theoretical study of the adsorption of aromatic units on carbon allotropes including explicit (empirical) DFT dispersion corrections and implicitly dispersion-corrected functionals: The pyridine case', *Phys. Chem. Chem. Phys.*, 2015, **17**, 575–587.

230. J. Ho, A. Klamt and M. L. Coote, 'Comment on the correct use of continuum solvent models', *J. Phys. Chem. A*, 2010, **114**, 13442–13444.

231. R. F. Ribeiro, A. V. Marenich, C. J. Cramer and D. G. Truhlar, 'Use of solution-phase vibrational frequencies in continuum models for the free energy of solvation', *J. Phys. Chem. B*, 2011, **115**, 14556–14562.

232. S. Grimme, J. Antony, S. Ehrlich and H. Krieg, 'A consistent and accurate ab initio parametrization of density functional dispersion correction (DFT-D) for the 94 elements H-Pu', *J. Chem. Phys.*, 2010, **132**, 154104.

233. S. Grimme, S. Ehrlich and L. Goerigk, 'Effect of the damping function in dispersion corrected density functional theory', *J. Comput. Chem.*, 2011, **32**, 1456–1465.

234. M. J. Frisch, G. W. Trucks, H. B. Schlegel, G. E. Scuseria, M. A. Robb, J. R. Cheeseman, G. Scalmani, V. Barone, G. A. Petersson, H. Nakatsuji, X. Li, M. Caricato, A. Marenich, J. Bloino, B. G. Janesko, R. Gomperts, B. Mennucci, H. P. Hratchian, J. V. Ort and D. J. Fox, *Gaussian09, Revision D.01*, Wallingford CT, 2016.

235. D. M. Collins and J. L. Hoard, 'The Crystal structure and molecular stereochemistry of a,b,y,d-tetra(4-pyridyl)prophinatomonopyridinezinc (II) An appraisal of bond strain in the Porphine skeleton.', *J. Am. Chem. Soc.*, 1970, **92**, 3761–3771.

236. M. Rickhaus, A. Vargas Jentzsch, L. Tejerina, I. Grübner, M. Jirasek, T. D. Claridge and H. L. Anderson, 'Single-Acetylene Linked Porphyrin Nanorings', *J. Am. Chem. Soc.*, 2017, **139**, 16502–16505.

237. H. Kruse and S. Grimme, 'A geometrical correction for the inter- and intra-molecular basis set superposition error in Hartree-Fock and density functional theory calculations for large systems A geometrical correction for the inter- and intra-molecular basis set superposition erro', *J. Chem. Phys.*, 2012, **154101**, 0–16.

238. L. Yang, J. B. Brazier, T. A. Hubbard, D. M. Rogers and S. L. Cockroft, 'Can Dispersion Forces Govern Aromatic Stacking in an Organic Solvent?', *Angew. Chem. Int. Ed.*, 2016, **55**, 912–916.

239. C. Reichardt and T. Welton, in *Solvents Solvent Eff. Org. Chem.* Wiley-VCH Verlag GmbH & Co. KGaA, Weinheim, Germany, 2011, pp. 425–508.

240. C. Reichardt and T. Welton, in *Solvents Solvent Eff. Org. Chem.* Wiley-VCH Verlag GmbH & Co. KGaA, Weinheim, Germany, 2011, pp. 65–106.

241. A. Klamt, V. Jonas, T. Bürger and J. C. Lohrenz, 'Refinement and parametrization of COSMO-RS', *J. Phys. Chem. A*, 1998, **102**, 5074–5085.

242. A. Klamt, 'Conductor-like screening model for real solvents: A new approach to the quantitative calculation of solvation phenomena', *J. Phys. Chem.*, 1995, **99**, 2224–2235.

243. R. Bosque and J. Sales, 'Polarizabilities of Solvents from the Chemical Composition', *J. Chem. Inf. Comput. Sci.*, 2002, **42**, 1154–1163.